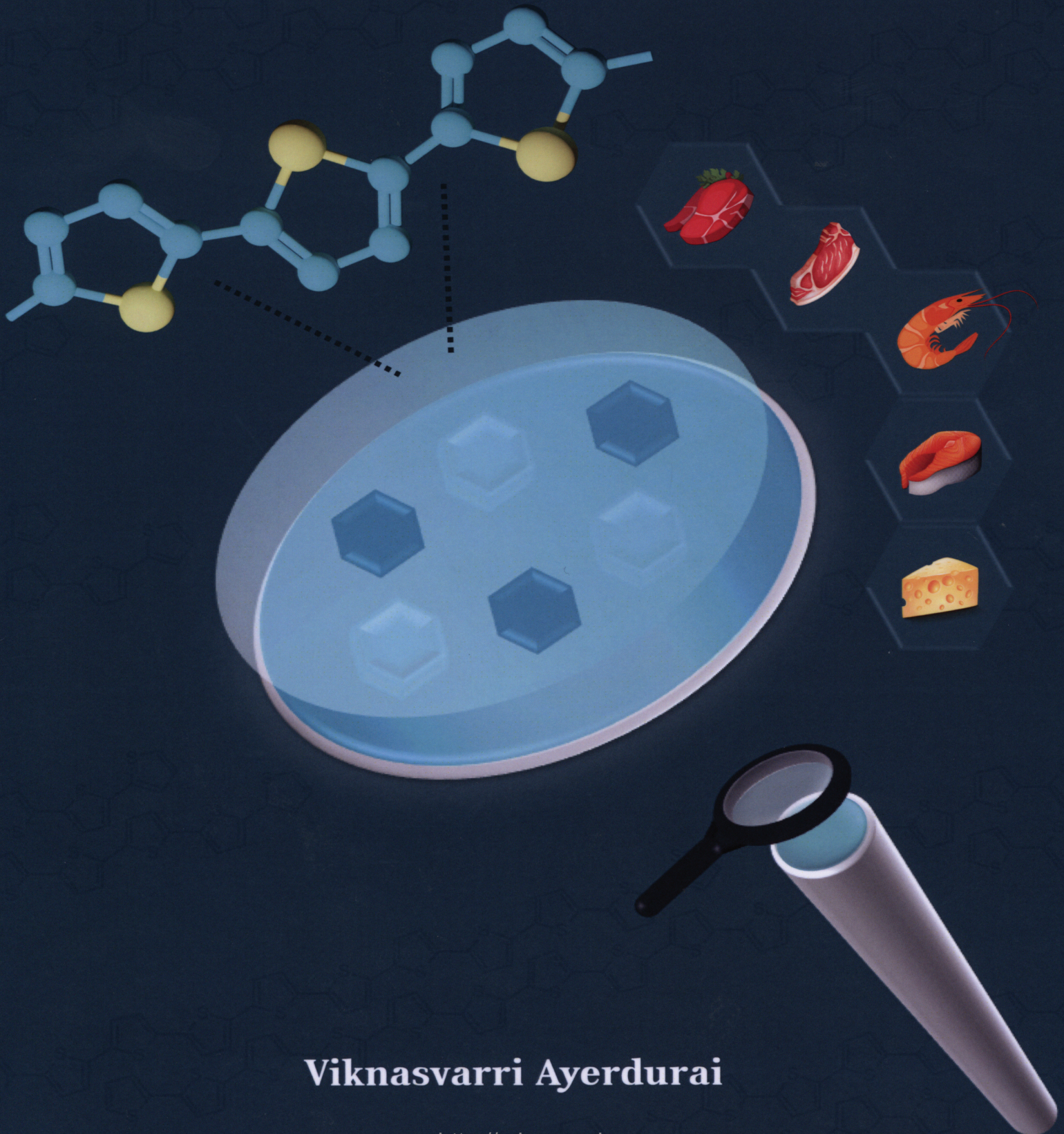


Ph.D. Thesis

# Molecularly imprinted polymers-based chemosensors for selective determination of chosen food toxins



Viknasvarri Ayerdurai

<http://rcin.org.pl>

**Ph.D. thesis**

***Molecularly imprinted polymers-based  
chemosensors for selective determination  
of chosen food toxins***

**Viknasvarri Ayerdurai**

Supervisor: Prof. Włodzimierz Kutner, Ph.D., D.Sc.  
Auxiliary supervisor: Dr. Maciej Cieplak, Eng., Ph.D.

The thesis was prepared within the International Doctoral Studies in Chemistry at the Institute of Physical Chemistry of the Polish Academy of Sciences in the Molecular Films Research group in collaboration with the Prof. Francis D'Souza group at the University of North Texas in Denton.

Warsaw, March 2022

Biblioteka Instytutu Chemii Fizycznej PAN

**F-B.553/22**



10000000109205

A-21-7  
K-9-175  
K-0-290  
K-6-216



B. 553/22

*To my family*



## *Declaration of originality*

I declare that the research included within this thesis was carried out by myself or with support from others included in the acknowledgments. I state that I have exercised care to ensure that the work is original and contains no previously published material or written by another person, except where citations have been made in the text. The content provided here does not violate any copyrights to the best of my knowledge. I accept that the Polish Academy of Sciences has the right to use plagiarism detection software to ensure the thesis's legitimacy. I certify that no part of my thesis has been or will be submitted for obtaining a degree or diploma by the Institute of Physical Chemistry, Polish Academy of Science, or any other educational institution. This thesis's copyright rests with the author, and no information derived from it may be published without the author's consent.

Warsaw, 31 March 2022



-----  
Signature

# *Acknowledgments*

My heartfelt gratitude goes to a few important people in my life, my supervisors and colleagues who encouraged me throughout my Ph.D. studies. First of all, I would like to thank my supervisor, Dr. Maciej Cieplak, for his support, understanding, supervision, and patience throughout my studies. He played a significant role in shaping my research work. He was always keen to share his knowledge and experience and encouraged me to think critically, which helped me improve myself. Most importantly, he was very supportive and understanding during different stages of my life. I am very grateful that he is very caring and kind towards his students. I have learned a lot from him, both professionally and personally, which will help me beyond this Ph.D. journey.

Next, I would like to thank Prof. Włodzimierz Kutner for giving me this opportunity to pursue my Ph.D. study under his supervision. He was always keen to share his scientific knowledge and expertise with his students. Moreover, he was always very generous in dedicating his time to teaching his students about science and personal wisdom. His guidance and critical assessment of my work played an essential role in influencing me as a better researcher. I truly value his experience and contribution to science and to shaping the young researchers' generation. Moreover, I would also like to extend my gratitude to Prof. Francis D'Souza for his support, collaboration, research advice and suggestions throughout my Ph.D. studies, as well as for providing functional monomers.

I would like to acknowledge my colleagues gratefully for their valuable time and collaboration: Dr. Piyush Sharma (fruitful collaboration and flow-cell training), Dr. Krzysztof R. Noworyta (AFM imaging), Dr. Pawel Borowicz (PM-IRRAS study), Dr. Wojciech Lisowski (XPS analysis), Prof. Francesco Sannicolò, Prof. Tiziana Benincori, and Dr. Joanna Piechowska (for synthesizing the T8 monomer), M.Sc. Jyoti and M.Sc. Jakub Kalecki (SEM imaging and training), Dr. Agnieszka Pietrzyk-Le, Dr. Alvaro Garcia-Cruz, Dr. Katarzyna Bartold, and Marianna Gajda (fruitful collaboration in tyramine and heterocyclic aromatic amine projects), and Dr. Agnieszka Lis-Cieplak and Patrycja Lach (fruitful collaboration in preparing a review article). Moreover, I would like to thank all colleagues from the research groups of Molecular Films and Functional Polymers, i.e., Dr. Piotr Pieta, Dr. Ievgen

Obraztsov, Dr. Dusan Mrdenovic, M.Sc. Valerii Malyshev, Dr. Kamila L. Lepicka, and M.Sc. Monika Charazka for their valuable discussions and suggestions throughout my Ph.D. studies.

My heartfelt gratitude and love go to my husband, Piotr, who supports me endlessly, inspires me every day, and encourages me to achieve my fullest potential. 'I truly have no words to express my gratefulness to you; thank you for everything, Pika.' Furthermore, my immense gratitude goes to my mother. I look up to her in every step of my life, and she always believed in me, time and again. I cannot begin to express how deeply she impacted my life and shaped me as a person. My father is no more. However, I am sure that I managed to come this far with his blessing and love. I am forever thankful to my parents, Ayerdurai and Mallika, for their unconditional love, care, patience, support, and faith in me. My siblings, Kavi, Selva, and Sumi, have had played a huge part in my life, and I thank them for all the love, motivation, and support they have showered me throughout my life. They always have been pillars of my life ever since I can remember. Moreover, I am very grateful to my lovely family, Stefan, Łucja, and Tomasz, here in Poland. Thank you for embracing, loving, and encouraging me as always. I cannot thank all my family members enough for their support and unwavering confidence in me.

I would also like to thank my dear friends, Alcina, Neha, Jyoti, Swaraj, Rashmi, Tanvi, and Nabila, for their companionship, care, motivation, and support throughout my journey here in Poland. I will always cherish all the late nights, good foods, laboratory times, wedding planning, festivities, parties, trips, and stories that we enjoyed together. I could not imagine this journey without all of you. A special mention to my beloved friends, brother Amr, Guna, Mages, Anitha, Sankar, Ramesh Anna, and Benny, for always being there for me all these years through thick and thin. I also would like to thank little Edgar and Antonii for continuously cheering me up. In addition, I would like to thank Prof. Yamaguchi, Dr. Alexandra, Dr. Zaitun, Dr. Aidil, Cikgu Nurul, and all the educators I cross-paths with for nurturing me as a student and an individual.

Finally, I gratefully thank the Marie Skłodowska-Curie fellowship, the Polish Ministry of Science and Higher Education, and Erasmus+ for providing me funding to realize my Ph.D. research projects and plans.



# *I. Funding*

- 1 The European Union Horizon 2020 Research and Innovation Programme under the Marie Skłodowska-Curie grant agreement no. 711859 and the Polish Ministry of Science and Higher Education for implementing an international co-financed project in the years 2017–2021.
- 2 The Polish National Science Centre, OPUS 8 grant no. 2014/15/B/NZ/01011.
- 3 Erasmus+ to Viknasvarri Ayerdurai.



Horizon 2020  
European Union Funding  
for Research & Innovation



Ministry of Science  
and Higher Education

Republic of Poland



NATIONAL SCIENCE CENTRE  
POLAND



Erasmus+

## II. Publications

- 1 **Ayerdurai, V.**, Cieplak, M., Noworyta, K. R., Gajda, M., Ziminska, A., Sosnowska, M., Piechowska, J., Borowicz, P., Lisowski, W., Shao, S., D'Souza, F., Kutner, W. Electrochemical Sensor for Selective Tyramine Determination, Amplified by a Molecularly Imprinted Polymer Film. *Bioelectrochemistry* **2021**, *138*, 107695. <https://doi.org/10.1016/j.bioelechem.2020.107695>
- 2 **Ayerdurai, V.**, Garcia-Cruz, Piechowska, J., Cieplak, M., Borowicz, P., Noworyta, K. R., Spolnik, G., Danikiewicz, W., Lisowski, W., Pietrzyk-Le, A., D'Souza, F., Kutner, W., Sharma, P. S. Selective Impedimetric Chemosensing of Carcinogenic Heterocyclic Aromatic Amine in Pork by dsDNA-Mimicking Molecularly Imprinted Polymer Film-Coated Electrodes. *J. Agric. Food Chem.* **2021**, *69*, 14689-14698. <https://doi.org/10.1021/acs.jafc.1c05084>
- 3 **Ayerdurai, V.**, Lach, P., Lis-Cieplak, A., Cieplak, M., Kutner, W., Sharma, P. S. Advantageous application of molecularly imprinted polymers in food processing and quality control. *Submitted*.
- 4 **Ayerdurai, V.**, Cieplak, M., Kutner, W. Molecularly imprinted polymers based electrochemical sensors for food contaminants determination. *In preparation*.

## III. Patent application

- 1 **Ayerdurai, V.**, Cieplak, M., Gajda, M., Ziminska, A., D'Souza, F., Kutner, W., Appl. No. PL427041, Appl. date 17 Sep 2018, Polimer wdrukowany molekularnie w postaci warstwy do oznaczania tyraminy, sposób otrzymywania takiego polimeru i zastosowanie w chemoczuJNIku do selektywnego elektrochemicznego wykrywania i/lub oznaczania analitów, zwłaszcza tyraminy ("Molecularly imprinted polymer in the form of a layer to mark tyramine , a method for the preparation of such a polymer and its use in a chemosensor for the selective electrochemical detection and / or marking analytes, in particular tyramine"). *Submitted*.

## *IV. Activity at scientific conferences*

### **Oral presentations**

- 1 **Viknasvarri Ayerdurai**, Maciej Cieplak, Piyush Sindhu Sharma, Francis D'Souza, and Wlodzimierz Kutner, 'Molecularly Imprinted Polymers for Determination of Chosen Food Toxins,' The European Materials Research Society (E-MRS), 17 - 20 September 2018, Warsaw, Poland. (*Award for successful oral presentation*)
- 2 **Viknasvarri Ayerdurai**, Alvaro Garcia-Cruz, Maciej Cieplak, Piyush Sindhu Sharma, Francis D'Souza, and Wlodzimierz Kutner, 'Electrochemical Sensor for Food Toxins with Molecularly Imprinted Polymer For Selective Determination of Heterocyclic Aromatic Amines (HAA),' PRIME 2020, 4 - 9 October 2020, Honolulu, USA. <https://doi.org/10.1149/MA2020-02683681mtgabs>
- 3 **Viknasvarri Ayerdurai**, Alvaro Garcia-Cruz, Maciej Cieplak, Piyush Sindhu Sharma, Francis D'Souza, and Wlodzimierz Kutner, 'Nucleobase-Functionalized Molecularly Imprinted Polymer (MIP) Electrochemical Sensor for Determination of Heterocyclic Aromatic Amines,' European Biosensor Symposium, 9 -11 March 2021, TH Wildau Technical University of Applied Science, Aachen, Germany.
- 4 **Viknasvarri Ayerdurai**, Alvaro Garcia-Cruz, Maciej Cieplak, Piyush Sindhu Sharma, Francis D'Souza, and Wlodzimierz Kutner, 'Capacitive Electrochemical Sensor for Food Toxins with Molecularly Imprinted Polymer for Selective Determination of Heterocyclic Aromatic Amines (HAA),' 239th Electrochemical Society Meeting and 18th International Meeting on Chemical Sensors, 30 May - 3 June 2021, Chicago, USA. <https://doi.org/10.1149/MA2021-01551363mtgabs>

### **Poster presentations**

- 1 **Viknasvarri Ayerdurai**, Maciej Cieplak, Piyush Sindhu Sharma, Francis D'Souza, and Wlodzimierz Kutner, 'Molecularly Imprinted Polymers for Determination of Chosen Food Toxins,' The European Materials Research Society (E-MRS), 17 - 20 September 2018, Warsaw, Poland. (*Award for successful poster presentation*)
- 2 **Viknasvarri Ayerdurai**, Maciej Cieplak, Piyush Sindhu Sharma, Francis D'Souza, and Wlodzimierz Kutner, 'Molecularly Imprinted Polymers for Determination of Chosen Food Toxins,' Microsymposium organized at IPC PAS, 15 - 17 January 2019, Warsaw, Poland.

- 3 **Viknasvarri Ayerdurai**, Maciej Cieplak, Piyush Sindhu Sharma, Francis D'Souza, and Wlodzimierz Kutner, 'Molecularly Imprinting Polymers for the detection of food toxins,' 6th International Conference on Bio-Sensing, 16 - 19 June 2019, Kuala Lumpur, Malaysia.
- 4 **Viknasvarri Ayerdurai**, Alvaro Garcia-Cruz, Maciej Cieplak, Piyush Sindhu Sharma, Francis D'Souza, and Wlodzimierz Kutner, 'Electrochemical Sensor for Food Toxins with Molecularly Imprinted Polymer for Selective Determination of Heterocyclic Aromatic Amines (HAA),' Microsymposium organized at IPC PAS, 19 - 20 January 2021, Warsaw, Poland.
- 5 **Viknasvarri Ayerdurai**, Alvaro Garcia-Cruz, Maciej Cieplak, Piyush Sindhu Sharma, Francis D'Souza, and Wlodzimierz Kutner, 'Molecularly Imprinting Polymers Capacitive Chemosensor for Determination of Heterocyclic Aromatic Amines,' 20 - 22 October 2021, Milan, Italy.
- 6 **Viknasvarri Ayerdurai**, Alvaro Garcia-Cruz, Maciej Cieplak, Piyush Sindhu Sharma, Francis D'Souza, and Wlodzimierz Kutner, 'Molecularly Imprinting Polymers-Based Electrochemical Sensor for Selective Determination of Heterocyclic Aromatic Amines (HAA),' The 10th International Workshop on Surface Modification for Chemical and Biochemical Sensing (SMCBS), 5 - 9 November 2021, Warsaw, Poland.
- 7 **Viknasvarri Ayerdurai**, Maciej Cieplak, Piyush Sindhu Sharma, Francis D'Souza, and Wlodzimierz Kutner, 'Selective impedimetric Chemosensing of Carcinogenic Heterocyclic Aromatic Amine in Pork by DSDNA Mimicking Molecularly Imprinted Polymer Film-Coated Electrodes,' Microsymposium organized at IPC PAS, 25 - 26 January 2022, Warsaw, Poland.

## ***V. Short training programs***

- 1 Smart materials for and from electrochemistry, Castellammare del Golfo, Sicily, Italy, organized by the Italian Chemical Society, 19 - 26 May 2019.
- 2 Market Research and Analysis, online, organized by e-Cornell, 1-14 December 2020.

## *VI. List of abbreviations*

### **A**

AFM – Atomic force microscopy

AIAs – Aminoimidazoarenes

AIBN – Azobisisobutyronitrile

APS – 3-Acryloxypropyltrimethoxysilane

APTES – 3-Aminopropyltriethoxysilane

AS – Ammonium persulphate

ATR – Attenuated total reflection

ATRP – Atom transfer radical polymerization

AuNP – Gold nanoparticle

ac – alternating current

### **B**

BIS – *N,N'*-methylenebisacrylamide

BSE – Backscattered electron

### **C**

CD – Carbon dot

CI – Capacitive impedimetry

CNSS – Graphitic-phase carbon nitride nanosheet

CS – Chitosan

CS-AgNP – Neomycin-MIP modified chitosan-silver nanoparticles

CV – Cyclic voltammetry

### **D**

DFT – Density functional theory

DMF – *N,N*-dimethylformamide

7,8-DiMeIQx – 2-amino-3,7,8-trimethyl-3*H*-imidazo[4,5-*f*]quinoxaline

DPV – Differential pulse voltammetry

ds – Double-stranded (DNA)

## **E**

EDMA – Ethylene glycol dimethacrylate

EIS – Electrochemical impedance spectroscopy

## **F**

Fc – Ferrocene

Fc<sup>+</sup> – Ferrocenium

FT – Fourier transform

FTIR – Fourier transform infrared (spectroscopy)

[Fe(CN)<sub>6</sub>]<sup>3-</sup>/[Fe(CN)<sub>6</sub>]<sup>4-</sup> – Hexacyanoferrate(III)/hexacyanoferrate(II)

## **G**

GCE – Glassy carbon electrode

GN – Graphene

GN/MIP – Graphene-modified MIP

GN-MWCNT – Graphene-(multi-walled) carbon nanotube

## **H**

HPLC – High-performance liquid chromatography

## **I**

IF – Imprinting factor

IHP – Inner Helmholtz plane

IR – Infrared

IRE – Internal reflection element

IRRAS – Infrared reflection-absorption spectroscopy

ITC – Isothermal titration calorimetry

ITO – Indium-tin oxide

## **L**

LOD – Limit of detection

LOQ – Limit of quantification

LSV – Linear sweep voltammetry

LUMO – Lowest unoccupied molecular orbital

## **M**

MAA – Methacrylic acid

MAO – Monoamine oxidase

MBA – Methylene bisacrylamide

MeA $\alpha$ C – 2-Amino-3-methyl-9*H*-pyrido[2,3-*b*]indole

MeIQ – 2-Amino-3,4-dimethylimidazo[4,5-*f*]quinoline

8-MeIQ<sub>x</sub> – 2-Amino-3,8-dimethylimidazo [4,5-*f*]quinoxaline

MEPS – Microextraction by packet sorbent

MIP-ISE – MIP membrane ion-selective electrode

MIP – Molecularly imprinted polymer

MPS – 3-Methacryloxypropyltrimethoxysilane

MPTMS – 3-(trimethoxysilyl)propyl methacrylate

MS – Mass spectrometry

1-*m*-4-MP – 1-Methyl-4-mercaptopyridine

$\gamma$ -MAPS –  $\gamma$ -Methacryloxypropyl trimethoxysilane

## **N**

NA – Noradrenaline

NaTFPB – Sodium tetrakis [3,5-bis(trifluoro-methyl)phenyl]borate

NF – Nickel nanofoam electrode

NIP – Non-imprinted polymer

NMR – Nuclear magnetic resonance

NPOE – 2-Nitrophenyloctyl ether

NP – Nanoparticle

## **O**

OHP – Outer Helmholtz plane

*o*-PD – Poly(*o*-phenylenediamine)

## **P**

PBS – Phosphate buffered saline

PEDOT : PSS – Poly(3,4-ethylene dioxythiophene): Polystyrene sulfonate

PEM – Photoelastic modulator

PhIP – 2-Amino-1-methyl-6-phenylimidazo[4,5-*b*]pyridine

PM-IRRAS – Polarization-modulation IR reflection-absorption spectroscopy

PTEOS – Phenyltriethylorthosilicate

PVC – Poly(vinyl chloride)

PZT – Piezoelectric actuator

## **Q**

QCM – Quartz crystal microbalance

## **R**

RAFT – Reversible addition-breakage chain transfer

rGO – Reduced graphene oxide

rGO-COOH – Reduced carbonylated graphene oxide

## **S**

SEM – Scanning electron microscopy

SERS – Surface-enhanced Raman spectroscopy

SPCE – Screen-printed carbon electrode

SPE – Solid-phase extraction

STM – Scanning tunneling microscope

SWV – Square wave voltammetry

*S/N* – signal-to-noise ratio

ss – Single-stranded (DNA)

## **T**

TAAR1 – Trace amine-associated receptor 1

TEMED – *N,N,N',N'*-tetramethylethylenediamine

TEOS – Tetraethylorthosilicate

THF – Tetrahydrofuran

TRIM – Trimethylolpropane trimethacrylate

Trp-P-1 – 2-amino-1,4-dimethyl-5*H*-pyrido[4,3-*b*]indole

(TBA)ClO<sub>4</sub> – Tetrabutylammonium chloride

## **U**

UHPLC – Ultra high-performance liquid chromatography

UV-vis – Ultraviolet-visible light (spectroscopy)

## **V**

VDAT – 2-Vinyl-4,6-diamino-1,3,5-triazine

VPBA – 4-Vinylphenylboronic acid

## **X**

XPS – X-ray photoelectron spectroscopy

## ***VII. List of symbols***

### **A**

$A$  – Electrode surface area,  $\text{cm}^2$

$a$  – Absorbance

### **C**

$C$  – Charge,  $\mu\text{C}$

$C_{\text{dl}}$  – Electric double-layer capacitance,  $\mu\text{C}$

$c$  – Concentration,  $\text{mg/L}$

$c_0$  – Initial concentration,  $\text{mg/L}$

### **D**

$D$  – Diffusion coefficient,  $\text{cm}^2/\text{s}$

$d$  – Optical path length,  $\text{cm}$

### **E**

$E_{\text{b}}$  – Binding energy,  $\text{eV}$

$E_{\text{kin}}$  – Photoelectron kinetic energy

$E_{\text{pa}}$  – Anodic peak potential,  $\text{V}$  vs. reference electrode

$E_{\text{pc}}$  – Cathodic peak potential,  $\text{V}$  vs. reference electrode

$E_{\text{s}}$  – Switching potential,  $\text{V}$

$E^0$  – Standard redox potential,  $\text{V}$

$E_0$  – Potential amplitude,  $\text{V}$

$\Delta E_{\text{p}}$  – Pulse amplitude,  $\text{V}$

$E$  – Electrode potential,  $\text{V}$  vs. reference electrode

$E_{\text{i}}$  – Initial potential,  $\text{V}$  vs. reference electrode

### **F**

$F$  – Faraday constant, 96,485 C/mol

## **G**

$\Delta G$  – Gibbs free energy change, kJ/mol

## **H**

$h\nu$  – electromagnetic wave energy

## **I**

$I$  – Intensity of the incident light

$I_{\text{ref}}$  – Intensity of the transmitted light

$i$  – Current, A

$i_{\text{pa}}$  – Anodic peak current, A

$i_{\text{pc}}$  – Cathodic peak current, A

$i_0$  – Current amplitude, A

## **K**

$k$  – Affinity constant

$k^0$  – Heterogeneous standard rate constant

## **N**

$n_1$  – Crystal's refractive index

$n_2$  – Sample's refractive index

$n$  – Number of electrons transferred

## **Q**

$Q$  – Amount of analyte bound to the MIP

$Q_{\text{MIP}}$  – Mass shift of MIP

$Q_{\text{NIP}}$  – Mass shift of NIP

## **R**

$R$  – Ideal molar gas constant,  $8.3144 \text{ J mol}^{-1} \text{ K}^{-1}$

$R_t$  – Total resistance,  $\Omega$

$R_{ct}$  – Charge transfer resistance,  $\Omega$

$R_s$  – Resistance of solution,  $\Omega$

## **T**

$T$  – Absolute temperature, K

$t_p$  – Pulse width, s

$t$  – Time, s

## **V**

$v$  – Volume, mL

$\nu$  – Potential scan rate, V/s

## **W**

$W_f$  – Work function

$W$  – Mass, g

## **X**

$x$  – Distance

## **Z**

$Z$  – Impedance,  $\Omega$

$Z_I$  – Imaginary impedance,  $\Omega$

$Z_R$  – Real impedance,  $\Omega$

$Z_w$  – Warburg impedance,  $\Omega$

$\alpha$  – Charge transfer coefficient

$\omega$  – Frequency, rad/s

$\theta_c$  – Critical phase angle, degree

$\varphi$  – Phase angle, degree

$\xi$  – Molar absorption coefficient, L mol<sup>-1</sup> cm<sup>-1</sup>

## VIII. Abstract (English)

The dissertation objective involves devising, fabricating, and testing molecularly imprinted polymer (MIP) film-based chemosensors to determine selectively chosen food toxins, namely, tyramine and heterocyclic aromatic amines (HAAs).

For that purpose, an electrochemical sensor was engineered for selective tyramine determination. Tyramine is generated in smoked and fermented food products. Therefore, it may serve as a marker of the rottenness of food products. Importantly, intake of large amounts of tyramine by patients treated with monoamine oxidase (MAO) inhibitors may lead to a "cheese effect," namely, a dangerous hypertensive crisis. Functional monomers were carefully selected using density functional theory (DFT) with the B3LYP/3-21G functional and basis set. Tyramine was determined using differential pulse voltammetry (DPV) and electrochemical impedance spectroscopy (EIS) with the  $\text{Fe}(\text{CN})_6^{4-}/\text{Fe}(\text{CN})_6^{3-}$  redox couple that served as the probe to observe the so-called "gate effect." The DPV and EIS limit of detection (LOD) at  $S/N = 3$  of the chemosensor was 159 and 168  $\mu\text{M}$  tyramine, respectively. The linear dynamic concentration extended from 290  $\mu\text{M}$  to 2.64 mM tyramine. The chemosensor was highly selective to the glucose, urea, and creatinine interferences. Its DPV determined apparent imprinting factor was  $IF = 5.6$ . Moreover, the prepared MIP film-coated electrode was applied for DPV tyramine determination in real Mozzarella cheese samples.

An impedimetric chemosensor was devised for selective determination of a 2-amino-3,7,8-trimethyl-3*H*-imidazo[4,5-*f*]quinoxaline (**7,8-DiMeIQx**) HAA. HAAs are generated in meat and fish processed at high temperatures. They are considered potent hazardous carcinogens. The quinoxaline HAAs readily intercalate dsDNAs, cleaving the covalent bond in the dsDNA base pairs. Hence, chronic exposure to HAAs, even at low doses, can cause lung, stomach, breast, etc., cancer. Therefore, a nucleobase-functionalized MIP as the recognition unit was devised by potentiodynamic electropolymerization of a pre-polymerization complex of two adenine- and one thymine-substituted *bis*(2,2'-bithien-5-yl)methane functional monomer molecules with one **7,8-DiMeIQx** template molecule, in the presence of the 2,4,5,2',4',5'-hexa(thiophene-2-yl)-3,3'-bithiophene cross-linking monomer. The pre-polymerization complex was studied with DFT's M06-2X/6-31G functional basis set. The fabricated MIP chemosensor allowed for a selective impedimetric determination of **7,8-DiMeIQx** in the 47 to 400  $\mu\text{M}$  linear dynamic concentration range with the LOD of 15.5  $\mu\text{M}$ . It was successfully applied for **7,8-DiMeIQx** determination in the pork meat extract as a proof of concept.

## IX. Abstract (Polish)

Celem badań opisanych w rozprawie było zaprojektowanie, wykonanie i przetestowanie chemoczuJNIKÓW z warstwami polimerów wdrukowanych molekularnie (MIP-ów) przeznaczonych do selektywnego wykrywania i oznaczania wybranych toksyn, tyraminy i 2-amino-3,7,8-trimetylo-3*H*-imidazolo[4,5-*f*]quinoksalinę, **7,8-DiMeIQx**, z grupy heterocyklicznych amin aromatycznych (HAA), w żywności.

Dlatego zaprojektowany został selektywny chemoczuJNIK do oznaczania tyraminy. Tyramina powstaje w żywności w wyniku wędzenia lub fermentacji. Dlatego może służyć za wskaźnik psucia się produktów spożywczych. Ponadto, spożywanie większych ilości tyraminy przez pacjentów przyjmujących inhibitory monoaminooxygenazy (MAO) może prowadzić do „efektu serowego”, tj. niebezpiecznego przełomu nadciśnieniowego. Dzięki symulacjom przeprowadzonym metodą teorii funkcyjonału gęstości (DFT) z zastosowaniem funkcyjonału B3LYP i bazy 3-21G wybrane zostały najbardziej odpowiednie monomery funkcyjne. Osadzone na elektrodach warstwy MIP-ów umożliwiły oznaczanie tyraminy w obecności próbnika  $\text{Fe}(\text{CN})_6^{4-}/\text{Fe}(\text{CN})_6^{3-}$  z zastosowaniem tzw. „efektu bramkowania”. Dolny limit wykrywania tyraminy za pomocą różnicowej woltamperometrii pulsowej (DPV) wynosił 159  $\mu\text{M}$  oraz 168  $\mu\text{M}$  za pomocą elektrochemicznej spektroskopii impedancyjnej (EIS). Zakres liniowej odpowiedzi chemoczuJNIKA MIP wynosił od 290  $\mu\text{M}$  do 2,64 mM. Czujnik wykazywał wysoką selektywność względem takich substancji przeszkadzających, jak glukoza, mocznik i kreatynina. Pozorny współczynnik wdrukowania wyznaczony metodą DPV wynosił 5,6. Dzięki temu, elektroda pokryta warstwą MIPu została zastosowana do oznaczeń za pomocą DPV tyraminy w próbkach sera Mozzarella.

Aby selektywnie oznaczyć **7,8-DiMeIQx** opracowano chemoczuJNIK impedymetryczny. Aminy HAA powstają w produktach mięsnych po wpływie obróbki cieplnej. Uważa się je za potencjalnie niebezpieczne kancerogeny. Interkalując podwójną nić DNA zrywają one wiązania wodorowe pomiędzy sparowanymi nukleotydami. Dlatego długotrwałe przyjmowanie tych amin, nawet w niewielkich dawkach, może wywołać wiele nowotworów, m.in., płuc, żołądka i piersi. W związku z tym, sfunkcjonalizowana zasadami azotowymi warstwa rozpoznająca MIP została osadzona na elektrodzie za pomocą elektropolimeryzacji potencjodynamicznej kompleksu prepolimeryzacyjnego **7,8-DiMeIQx** z dwoma cząsteczkami *bis*(2,2'-bitien-5-ylo)metanowego monomeru funkcyjnego mającego w swojej strukturze grupę adeninową oraz jedną cząsteczką monomeru z grupą tyminową, w obecności monomeru sieciującego, 2,4,5,2',4',5'-heksa(tiofen-2-ylo)-3,3'-bitiofenu. Struktura kompleksu prepolimeryzacyjnego została zoptymalizowana za pomocą obliczeń DFT z funkcyjonałem M06-2X oraz bazą 6-31G. Wytworzony chemosensor umożliwił impedymetryczne oznaczanie **7,8-DiMeIQx** w zakresie stężeń od 47 do 470  $\mu\text{M}$ . Dolna granica wykrywalności **7,8-DiMeIQx** wynosiła 15,5  $\mu\text{M}$ . ChemoczuJNIK ten został z powodzeniem zastosowany do oznaczania **7,8-DiMeIQx** w modelowych próbkach wieprzowiny.

# *Table of contents*

Declaration of originality .....	v
Acknowledgements .....	vi
I. Funding.....	ix
II. Publications .....	x
III. Patent application.....	x
IV. Activity at scientific conferences.....	xi
V. Short training programs.....	xii
VI. List of abbreviations.....	xiii
VII. List of symbols .....	xviii
VIII. Abstract (English) .....	xxii
IX. Abstract (Polish) .....	xxiii
Chapter 1: Literature Review.....	1
1.1 Molecularly imprinted polymers (MIPs) .....	1
1.2 Electrochemical MIP chemosensor .....	18
1.3 Food toxins - compounds of interest .....	41
1.4 Research objective .....	56
Chapter 2: Experimental .....	59
2.1 Materials and chemicals .....	59
2.2 Techniques .....	63
2.3 MIP and NIP films preparation .....	87
Chapter 3: Electrochemical sensor for selective tyramine determination with a molecularly imprinted polymer film .....	100
3.1 Introduction .....	103
3.2 Results and discussion .....	103
3.3 Conclusions .....	126
Chapter 4: Selective impedimetric chemosensing of carcinogenic heterocyclic aromatic amine by dsDNA mimicking molecularly imprinted polymer film-coated electrodes .....	129
4.1 Introduction .....	132
4.2 Results and discussion .....	132
4.3 Conclusions .....	155
Chapter 5: Summary and future prospectives.....	158
References .....	162





# *Chapter 1*

## *Literature Review*

The present chapter describes preparation methods, basic principles of operation, and application of molecularly imprinted polymers (MIPs). It in-depth discusses MIP-based electrochemical chemosensors, especially for food safety monitoring applications.

### **1.1 Molecularly imprinted polymers (MIPs)**

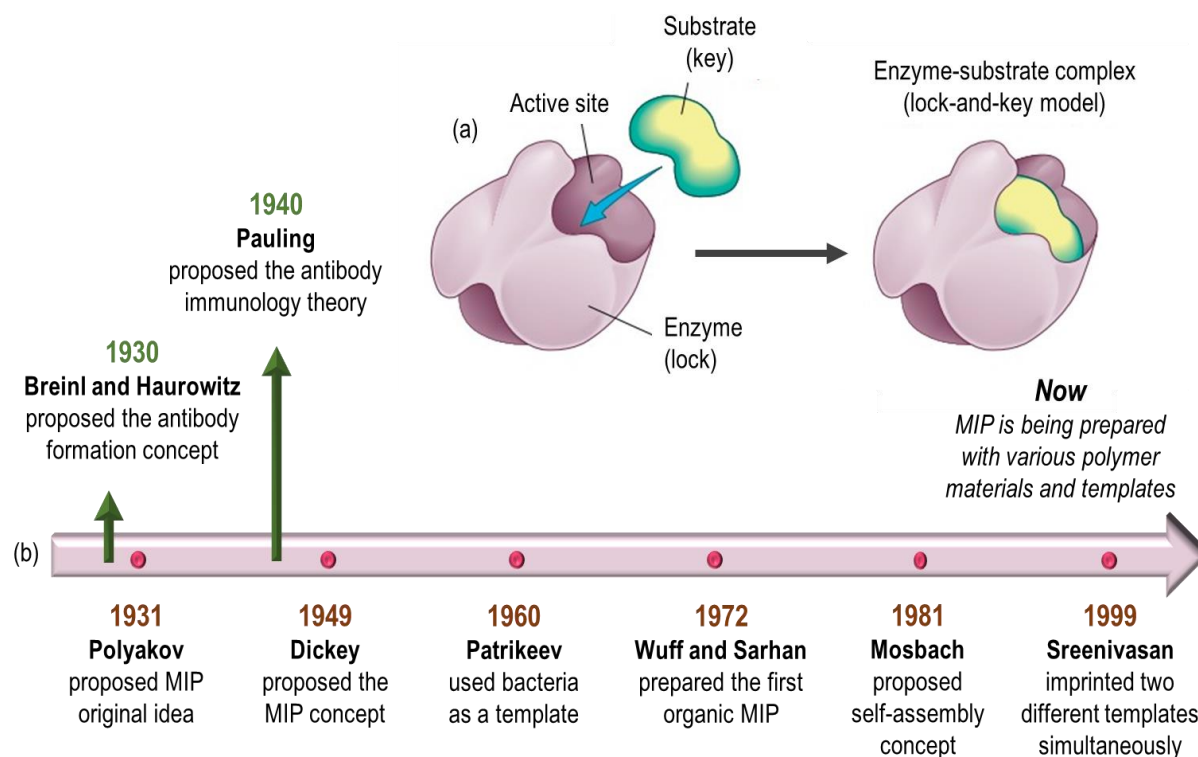
Molecularly imprinted polymers (MIPs) are artificial molecular recognition materials that mimic biological recognition entities, such as antibodies, active centers of enzymes, aptamers, etc.<sup>1</sup> In some literature reports, MIPs are referred to as artificial antibodies.<sup>2</sup> That is because molecular imprinting in polymers has a common ground with the instructional theory of antibody formation proposed by Breinl and Haurowitz<sup>3</sup> in 1930 and the antibody immunology theory proposed by Linus Pauling in 1940.<sup>4</sup> Therefore, MIP can be thought of as the synthetic analog to nature's antibody-antigen or enzyme-substrate systems, which operate based on Fischer's lock and key mechanism (Scheme 1.1-1a). In these molecular models, the receptors and their natural target molecule have geometrically complementary shapes that fit perfectly together. As a result, only the interacting molecules of the proper size, shape, and functionality would fit into the active sides of the receptors. This unique interaction yields high affinity and selectivity.

Polyakov, a Soviet chemist, first introduced imprinting in 1931.<sup>1</sup> He reported a novel procedure where the silica particles were polymerized in water using a gelating agent. An additive (toluene, benzene, or xylene) was added after two weeks, and the material was allowed to dry for 20-30 days. Subsequently, the additive was removed from the material, resulting in a memory effect that revealed the material's higher additive uptake capacity. In 1955, Dickey, a student of Pauling, reported inorganic silicates preparation similar to Polyakov's procedure. However, he prepared the material in the presence of methyl orange as a template from the start of the reaction.<sup>5</sup> Patrikeev, in 1960, used bacteria as a template and incubated it in a silica gel.<sup>6</sup>

Up to the early 70s, inorganic materials were primarily used to explore molecular imprinting. In 1972, Wulff and Sarhan prepared the first organic MIP using sugar derivatives as templates.<sup>7</sup> They further popularized the concept of covalent and non-covalent imprinting.

In 1981, Mosbach made a significant contribution to molecular imprinting by proposing the 'self-assembly' approach.<sup>8</sup> He proposed that the cavity was formed when the template and the functional monomer formed a non-covalent adduct in the 3D space. Template subsequent removal led to an empty imprinted cavity capable of analyte recognition. In 1999, Sreenivasan significantly moved forward in the field by simultaneously imprinting two template molecules, namely, salicylic acid and hydrocortisone, in poly(2-hydroxy ethyl methacrylate).<sup>9</sup>

Scheme 1.1-1b illustrates the timeline of significant contributions to molecular imprinting.



**Scheme 1.1-1.** (a) The lock-and-key interaction between the enzyme [adapted from <sup>10</sup>] and a substrate and (b) the timeline of significant contributions to the molecular imprinting field.

### 1.1.1 Bioreceptors and MIPs comparison

A bioreceptor is the recognition element/entity of biological origin. It can either be a biomolecule, such as protein, or a living object, such as tissue or cell, of a specific affinity for

a particular biological target analyte.<sup>11</sup> Bioreceptors are extensively used as recognizing units in biosensors because their target-favored interactions yield high selectivity.<sup>12</sup> However, bioreceptors suffer from many disadvantages, e.g., instability and low durability. Therefore, bioreceptors require dedicated storage conditions, application at the proper temperature (generally at human body temperature), and skilled labor to handle them. Generally, bioreceptors are not vastly available, their activity may vary from batch to batch of the same manufacturer, and their production is expensive. Thus, bioreceptors eventually increase the overall biosensor cost.

**Table 1.1.** Comparison of MIPs and bioreceptors.<sup>13</sup>

Feature	MIPs	Bioreceptors
Generality	Can be devised for nearly any template	One receptor per analyte, e.g., an antibody can specifically interact with only one antigen
Stability	Highly robust and stable in multiple conditions (high/low pHs, pressure, and temperature)	Limited stability and susceptibility to environmental changes
Cost	Inexpensive	Expensive to purchase, synthesize, and care for
Storage	Long-term storage	Days at room temperature
Synthesis	Facile	Time-demanding
Experimental conditions	Polymers for different targets can operate in the same environment	Biocompounds have unique operational requirements (pH, ionic strength, temperature, substrate)
Experimental medium	Can work in aqueous and organic solvent solutions	Poor performance in non-aqueous solvent solutions

MIPs, on the other hand, are a perfect solution to overcome the bioreceptor's weaknesses. MIPs offer high selectivity as they operate similarly to the lock and key mechanism while being highly robust. Generally, MIPs are chemically, physically, and mechanically stable. They largely remain inert in acidic and basic solutions and can operate in organic solvents,

unlike bioreceptors. Furthermore, MIPs can be stored for a long time, and generally, they do not require any particular storage conditions. Table 1.1 compares the bioreceptors and MIPs.<sup>13</sup> Evidently, MIPs are superior to bioreceptors. Therefore, they have now gained the interest of the sensor community.

### 1.1.2 Molecular imprinting principle - synthesis of MIPs

The basic principle of molecular imprinting consists of imprinting molecular cavities in synthetic materials that complementarily fit target analyte molecules' size, shape, and distribution. MIP synthesis (Scheme 1.1-2a) involves three consecutive steps.<sup>14</sup>

- (i) The first involves forming stable pre-polymerization complexes (or adducts) of the target analyte, which at this step plays the role of a template, with selected functional monomers in solution. Depending on the chemical functionalities of these monomers, they can interact with the template/analyte molecules by forming covalent or non-covalent bonds, i.e., hydrogen bonds, electrostatic attractions,  $\pi$ - $\pi$  stacking, hydrophobic, van der Waals interactions, etc. Table 1.2 compares these two bonding types.
- (ii) The second step involves polymerizing the template-(functional monomers) complex/adduct in solution in the presence of the cross-linking monomer(s). During polymerization, the polymer net grows around the pre-polymerization complex molecules. That causes imprinting of the target analyte in the polymer matrix. As a result, the rigid MIP matrix would now have the memory of the imprinted molecular cavity.
- (iii) The third step is removing the template from the MIP, thus vacating molecular cavities. Those resemble the target analyte molecules' shapes, sizes, and functionality distribution. Therefore, these molecular cavities can only recognize complementary analyte molecules, thus contributing to the MIP selectivity.

Different MIPs can be synthesized following the same principle by changing the templates, as well as functional and cross-linking monomers.

Non-imprinted polymer (NIP) is prepared similarly but without the target analyte (Scheme 1.1-2b). In effect, there is no arrangement of the functional monomers matching the

binding sites of the target analyte. That causes the synthesized NIP not to have imprinting cavities and, thus, no recognition ability. Therefore, an NIP is mainly used as the reference control to the counterpart, an MIP.

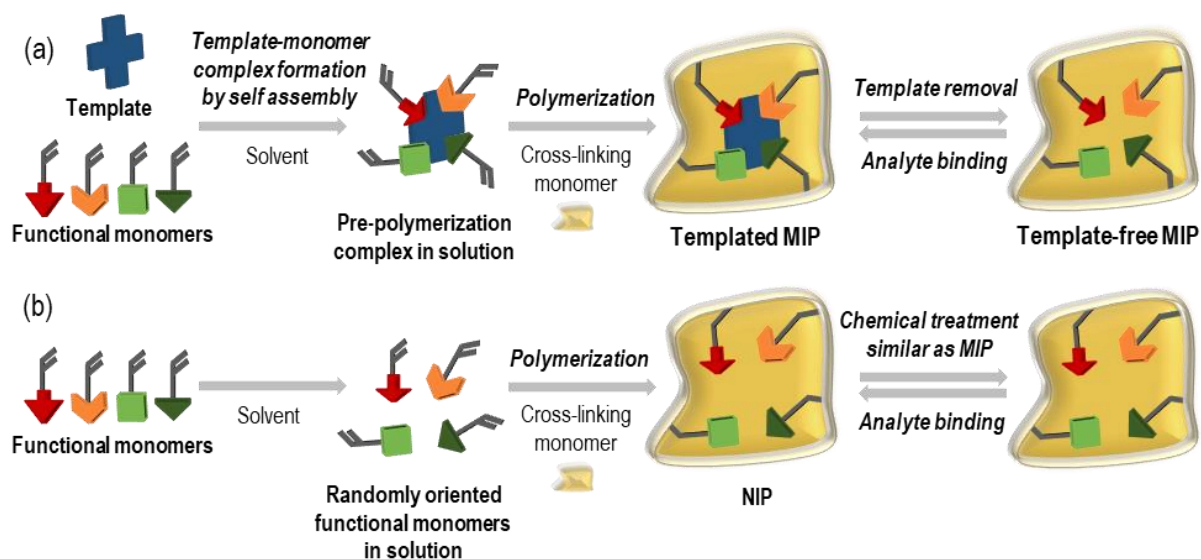
**Table 1.2.** Comparison of different strategies to molecular imprinting based on interactions between the template and the functional monomer.<sup>15</sup>

Type of imprinting	Advantage	Disadvantage
Covalent (known as the pre-organization approach)	Stable template-(functional monomers) adduct formation due to strong covalent bonds.  Homogeneous distribution and the maximum population of imprinted cavities are ensured during polymerization.	Breaking the covalent bonds of the template-(functional monomers) adduct is difficult. Thus, template extraction and analyte binding are challenging.
Non-covalent (known as the self-assembly approach)	Simple and easy synthesis.  Simple template extraction, then analyte binding.  Resembles natural recognition.  Many different templates are capable of non-covalent bonding the functional monomers.	Formation of non-specific recognizing sites during polymerization due to excessive monomers' use.  Highly influenced by the solvent used. More polar solvent facilities stronger non-polar interactions. A less polar solvent facilities hydrogen bonding.  The distribution and interaction of the functional monomer and template molecules may be inhomogeneous.

### 1.1.3 Crucial parameters of MIP synthesis

Multiple parameters influence the morphology, properties, and performance of the synthesized MIPs. The most critical parameter is the template molecule structure. Ideally, a template molecule's binding sites should promote establishing appropriate interactions with the functional monomers to organize them around itself. In MIPs syntheses, molecules of any size can be used as templates. Notably, for some types of polymerizations, e.g., free-radical and

electrochemical polymerization, an inert template without any functional groups that can disturb the polymerization is preferred. Moreover, the template should neither decompose nor be chemically transformed during polymerization. If that requirement is not met, then a structural analog of the target analyte molecule is used as the "dummy template" instead of the target analyte itself.<sup>16</sup> So far, macromolecular biological compounds, including proteins,<sup>17</sup> hormones,<sup>18</sup> nucleotides,<sup>19</sup> as well as carbohydrates,<sup>20</sup> pesticides,<sup>21</sup> drugs,<sup>22</sup> and different contaminants,<sup>23</sup> etc., were used as templates.



**Scheme 1.1-2.** Basics of synthesis (a) molecularly imprinted polymer (MIP) and (b) non-imprinted polymer (NIP).

The other significant parameter is the structure of functional monomers. Functional monomer (Scheme 1.1-3a) interacting with the target analyte via covalent or non-covalent bonds generates unique pre-polymerization complexes in solution, leading to template-selective molecular cavities after polymerization. The non-covalent interaction is the most popular choice due to the simplicity of the MIP synthesis. The selectivity and affinity of the MIP are influenced by intermolecular interactions between functional monomers and templates.<sup>24</sup> For stable pre-polymerization complex formation in solution, it is vital that the functional monomer strongly interacts with the template. However, each non-covalent bond is relatively weak. But they all, concertedly, lead to monomer-template strong interactions.

Stable pre-polymerization complexes aid the formation of homogenous imprinted cavities. In the case of the unstable pre-polymerization complexes, however, some fraction of functional monomer molecules is not involved in the complex formation. Nevertheless, those molecules are randomly copolymerized in the polymer matrix, forming undesired and random binding sites, like those in NIP. Recently, to avoid those problems, template-(functional monomers) interactions have been studied by ultraviolet-visible (UV-vis) spectroscopy,<sup>25</sup> nuclear magnetic resonance (NMR) spectroscopy,<sup>26</sup> or isothermal titration calorimetry (ITC) titration.<sup>27</sup> Alternatively, the template-(functional monomer) pre-polymerization complex structure can be optimized via computational simulations before laboratory experiments. The most significant advantage of those simulations is the laboratory work time shortening, effort-saving, and decreasing consumption of chemicals.

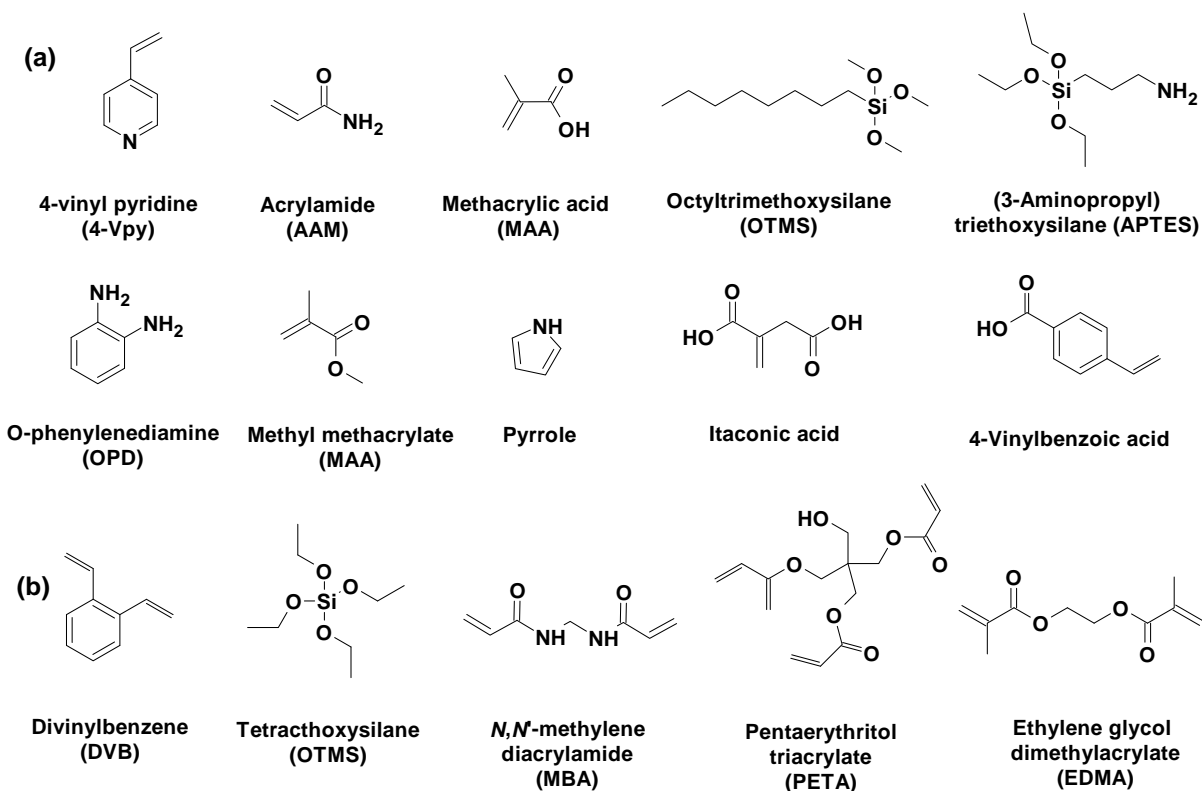
Computational simulation combines the theoretical basis of quantum chemistry and statistical mechanics to predict a molecule's static structures and dynamic motions.<sup>4b</sup> First, the computer software simulates changes in the molecule's static structure and dynamic motion. This simulation causes the molecule to have different forms, each characterized by different formation energy. Then, these energies are calculated and mutually compared to understand the intermolecular interactions between molecules and their different forms that occur in the pre-polymerization complex mixture. That allows the computer program to predict the mechanism of action at the molecular level accurately.

The density functional theory (DFT) method is often used to predict possible hydrogen bonding between functional monomers and template molecules depending on their distance from each other.<sup>28</sup> A common method for selecting the most appropriate functional monomers is comparing the Gibbs free energy change of formation of the pre-polymerization complexes with different functional monomers at different stoichiometry. The equilibrium of template-(functional monomer) complex formation by self-assembly is under thermodynamic control, precisely, the negative Gibbs free energy gain upon complex formation.<sup>29</sup> A complex with the most negative Gibbs free energy change is generally preferred as it is the most stable.<sup>30</sup> Thus, it has the highest chance of surviving polymerization, then forming imprinted molecular cavities in the resulting MIPs.

The third crucial parameter is the nature of the cross-linking monomer. That monomer (Scheme 1.1-3b) has three functions in the MIP synthesis. (i) It stabilizes the spatial

distribution of the imprinted cavities, (ii) controls MIP's morphology, and (iii) ensures the mechanical stability of the MIP matrix. Moreover, the selectivity and binding ability of the MIP are primarily affected by the type and quantity of the cross-linking monomer.<sup>31</sup> That quantity used in the MIP synthesis influences the polymer stability. The MIP stability decreases because of functional monomer shedding when a low amount of cross-linking monomer is incorporated into the MIP during the synthesis. Therefore, a high cross-linking monomer molar ratio to the template and the functional monomer is typically used to ensure a rigid MIP formation. Such a robust polymer matrix can maintain the stability of the imprinted cavities. It can retain the shape and functionality of the three-dimensional structure of the cavity even after harsh template extraction treatment. The most common template-to-(cross-linking monomer) ratio appears to be 1 : 5 for a successful cavity imprinting.<sup>32</sup>

The final important parameter is the nature of the porogenic solvent. The primary role of such a solvent is to dissolve the selected functional and cross-linking monomers and templates and facilitate the formation of the porous structure in the polymer matrix. In the case of the non-covalent interaction of the template with the functional monomer, the porogenic solvent must be selected carefully. Generally, organic solvents with low polarities, such as chloroform, toluene, and acetonitrile, are opted to minimize interferences during template-(functional monomer) complex formation and simultaneously promote hydrogen bonding in the complex.<sup>33</sup> The MIP synthesized in the mixed (low-polar organic)-aqueous solvent solution, e.g., acetonitrile and water, exhibits a strong ion-ion and hydrogen bonding of the template, e.g., phosphoric acid, with the monomer, e.g., vinyl pyridine and methacrylic acid (MAA).<sup>34</sup> Moreover, MIP preparation by polymerization in the presence of porogenic solvent promotes the porosity of the resulting polymer. The calculated pore size was 4 nm for both the MIP and NIP when these polymers were prepared using the same volume of the tetrahydrofuran (THF) solvent.<sup>25a</sup> THF, acetonitrile, *N,N*-dimethylformamide (DMF), methanol, dichloromethane, chloroform, toluene, and water are some of the most commonly used porogenic solvents in MIP syntheses.



**Scheme 1.1-3.** Commonly used (a) functional monomers and (b) cross-linking monomers in MIP preparation.<sup>35</sup>

#### 1.1.4 MIP synthesis methods

MIP morphology is a crucial feature influencing MIP's binding capacity and detection sensitivity and, therefore, its application. Depending on the desired application, an MIP morphology is carefully designed using different preparation and or synthesis methods, i.e., free-radical polymerization, controlled/living polymerization, sol-gel process, surface synthesis method, or electropolymerization. The first is most commonly used in MIP preparation (Scheme 1.1-4). It is a rapid reaction conducted under mild conditions, i.e., below 80 °C in the bulk solution at atmospheric pressure. It mainly involves functional monomers and an initiator. An initiator, e.g., azobisisobutyronitrile (AIBN), potassium persulfate, *tert*-butyl hydroperoxide, benzoyl peroxide, etc., homolytically decompose, producing free radicals. Thermal or photochemical initiation is employed to trigger this decomposition. Then, the generated free radicals react with monomers present in the solution and, thus, initiate polymerization. This polymerization method is generally rapid and straightforward, not requiring sophisticated or expensive instrumentation.

Typically, MIPs are prepared as blocks, then crushed, ground, and sieved to result in particles of the desired size range (mainly in micrometers) depending on the application.<sup>36</sup> This process is time-consuming and may foul high-affinity imprinted cavities. Moreover, the size and shape of final particles are irregular, directly influencing the heterogeneous distribution of imprinted cavities, limiting MIP's application only as a selective adsorbent for solid-phase extraction (SPE)<sup>37</sup> and chromatographic separation.<sup>36a</sup> To overcome these drawbacks, researchers opted for different polymerization strategies, including the suspension,<sup>38</sup> emulsion,<sup>39</sup> seed,<sup>40</sup> and precipitation<sup>41</sup> polymerizations.

In suspension polymerization, MIP is prepared by suspending the pre-polymerization mixture droplets in the presence of a surfactant as a stabilizer in a continuous liquid phase. Upon suspension, a mini-bulk reaction occurs in each droplet, resulting in polydisperse spherical MIP particles. The resultant spherical shape promotes easier template extraction than that of irregular grains.<sup>42</sup> Moreover, water is generally used as a continuous phase.<sup>43</sup> Maybe, this is a disadvantage, especially in a non-covalent approach, as the water presence can weaken electrostatic interactions and hydrogen bonding between the functional monomer and template molecules. Therefore, mineral oil<sup>38</sup> or perfluorocarbon liquid<sup>44</sup> were used instead of water. A surfactant is still required for polymerization in other continuous phases, except for polymerization in mineral oil. That could be a drawback as a surfactant may cause unwanted interactions with the functional monomer and template molecules.

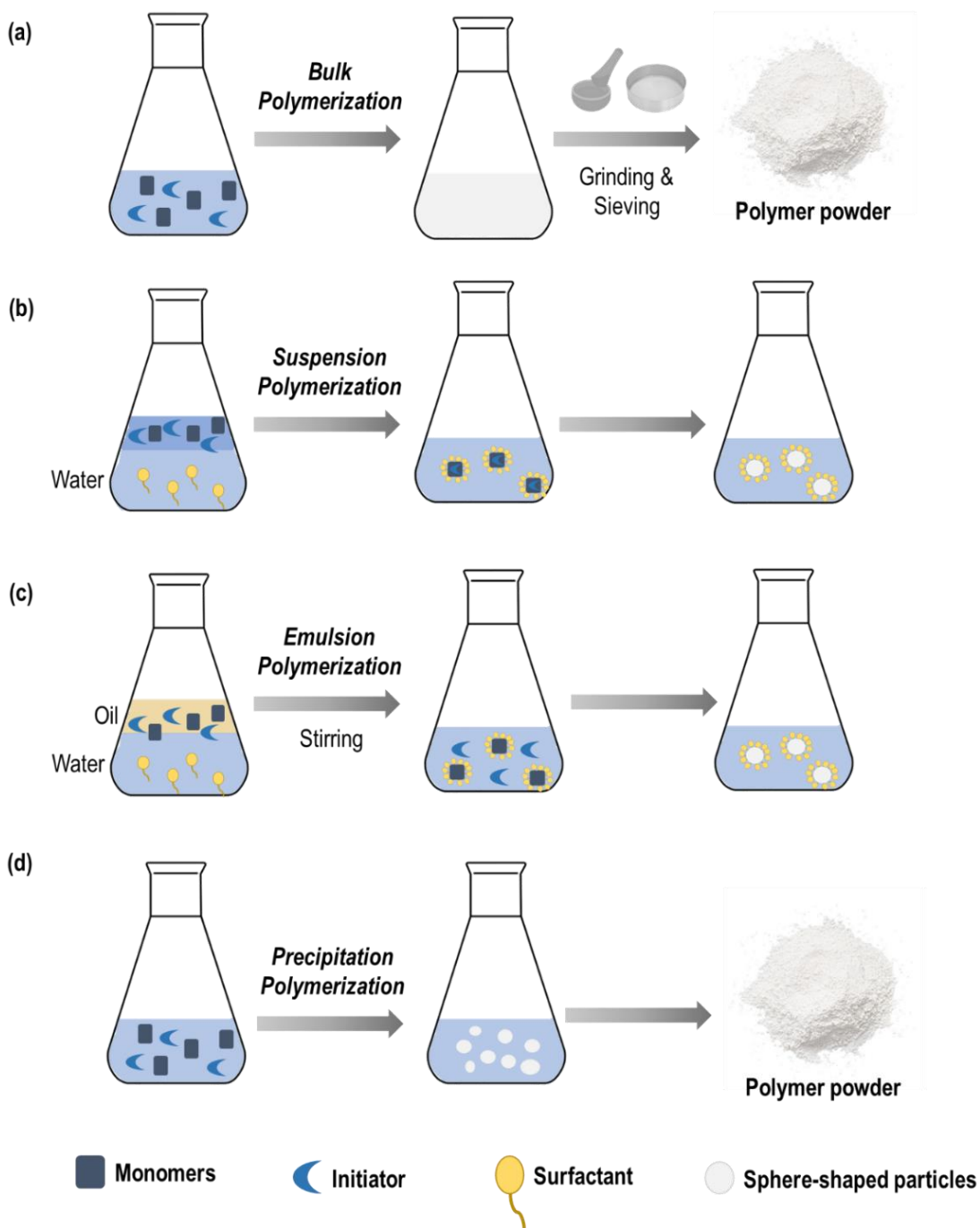
In emulsion polymerization, MIP is prepared by polymerization in a two-phase medium, e.g., oil-in-water.<sup>45</sup> In water, in the continuous phase, surfactants are dissolved. The monomers and initiators are dissolved in the other medium, used as the dispersed phase. A vigorous stirring or sonication emulsifies the two phases where the stable monomer micelles are formed. The micelles' droplets are then polymerized. The emulsion polymerization is relatively simple, and it often results in a high yield of monodispersed particles with homogeneously distributed imprinted cavities. This strategy deficiency is the excessive use of chemicals, e.g., surfactants, that may favor the unwanted interaction between the monomer and template molecules.<sup>46</sup> The surfactant may act as a pollutant, contaminating the final polymer product. Therefore, a time-consuming polymer purification step is required.

The seed polymerization involves multi-step swelling and polymerizing in water as a continuous phase. Particles such as polystyrene, titanium dioxide, etc., are usually used as

seeds for polymer growth. The seeds are then swelled multiple times in batches in the presence of functional and cross-linking monomers and diluents in water. The initiator forms initiator radicals which then develop into oligomer radicals. These radicals promote polymer growth on the seeds' surface.<sup>47</sup> The major advantage of seed polymerization is the high yield of the monodispersed MIP particles. The drawbacks are the time-consuming preparation and water use, which can weaken the interaction between the template and functional monomer molecules.

The last free-radical polymerization method is precipitation polymerization. MIP is prepared by bulk polymerization in the excess solvent. In this solvent, all monomers, templates, and initiators are dissolved. The polymer precipitates when its chain has grown large enough to become insoluble in the reaction mixture.<sup>48</sup> The polymer is then collected after washing then centrifuging. Among the above methods, precipitation polymerization is the most promising. Its advantages include a simple synthesis procedure and high uniformity in the resultant polymer particles prepared without surfactant. Moreover, the particle diameters can easily be controlled by manipulating polymerization conditions, such as porogen's volume and polarity, stirring rate, and polymerization temperature.<sup>49</sup> The only disadvantage is the use of solvent excess, which is not environmentally friendly.

Alternative to conventional radical polymerization is the controlled/living polymerization, such as reversible addition-fragmentation chain-transfer (RAFT) polymerization and atom transfer radical polymerization (ATRP). In RAFT polymerization, a chain-transfer agent, whereas in ATRP, a transition metal catalyst ensures uniform polymer growth with controlled molecular weight and polydispersity. Therefore, the resulting polymer is well-defined, has a predicted molecular weight, and is homogeneous. Moreover, this polymer has controlled composition and functionality, translating into superior binding parameters.<sup>50</sup> Pan et al. demonstrated that MIPs synthesized by RAFT precipitation polymerization reveal a superior binding capacity and a higher binding constant than MIPs prepared by conventional precipitation polymerization.<sup>51</sup> The disadvantage of living polymerization is that it requires using protic solvents, oxygen, and polar functional groups, making this approach extremely prone to produce unwanted reactions, demanding stringent conditions to prevent the side reactions.<sup>52</sup>

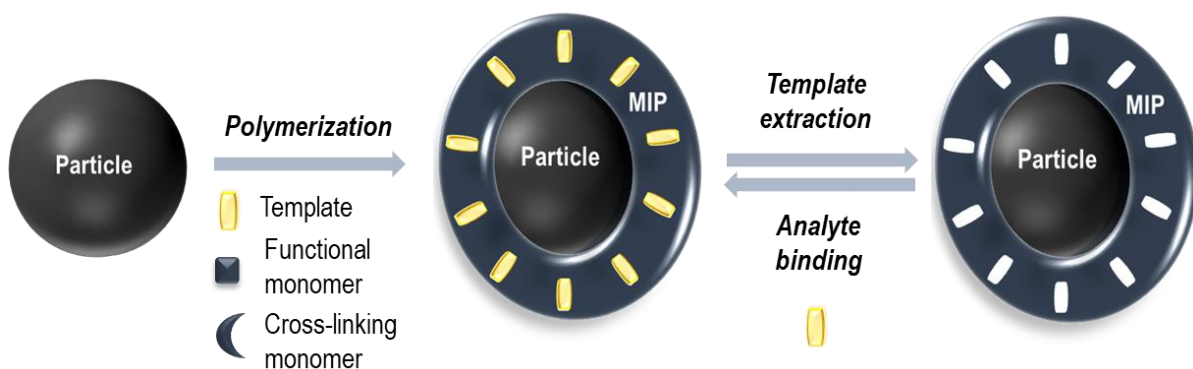


**Scheme 1.1-4.** The flowchart of MIP synthesis by free-radical (a) bulk, (b) suspension, (c) emulsion, and (d) precipitation polymerization [adapted from <sup>42</sup>].

In the sol-gel method, hydrolysis and condensation of metal oxide precursors, such as methyl orthosilicate,<sup>53</sup> ethyl orthosilicate,<sup>54</sup> or titanium dioxide<sup>55</sup> in an acidic or basic solution, result in the formation of a highly stable inorganic-based polymer. When a template is used in

this process, a cavity is imprinted in the media during polymerization. This method is advantageous compared the free-radical polymerization. The procedure is simple. The final product is transparent, highly porous, and homogeneous. Moreover, a sol-gel material is very versatile as it has high thermal and mechanical stability because of the metal oxide presence.<sup>56</sup> The mechanical stability is particularly enhanced due to the extensive formation of cross-linking polymer network that can preserve and maintain the shape of the cavity even after harsh extraction treatment. Initiators or surfactants, which are generally expensive, are not required in this method and, therefore, it is cost-effective. Despite its advantages, the polymer prepared with this method is generally studied using complex analytical techniques, such as high-performance liquid chromatography (HPLC) for application purposes which is a form of limitation. Low sensitivity and delayed response time in drug delivery studies were the disadvantages of the MIP prepared via the sol-gel method.<sup>57</sup>

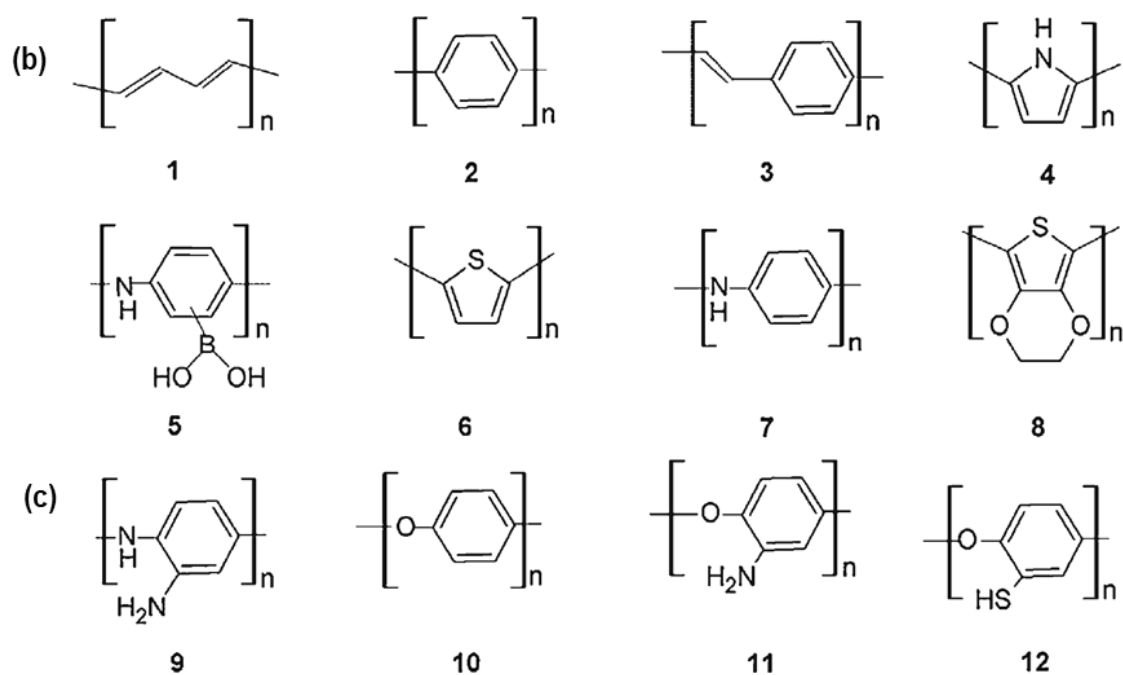
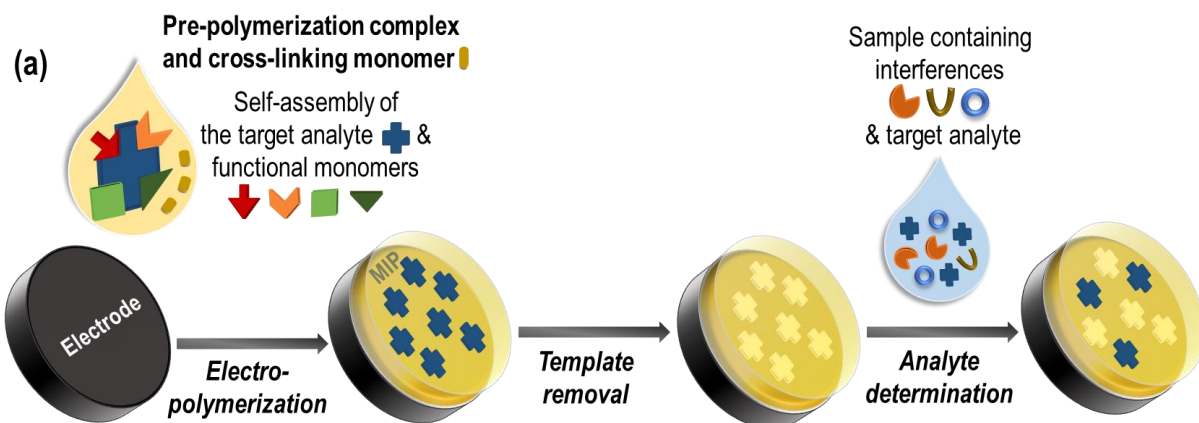
In grafting thin MIP films on the support particle surface, the MIP is synthesized directly on this surface (Scheme 1.1-5), resulting in a core-shell nanoparticle. Depending on the nature of the support particles, i.e., magnetic nanoparticles,<sup>58</sup> carbon nanomaterials,<sup>59</sup> silica nanobeads,<sup>60</sup> etc., properties of the final material wildly varied. For instance, an MIP film on a magnetic nanoparticle offers magnetically-aided separation. This separation is relatively simple and highly efficient. Living polymerization is often used to control the MIP film thickness, a significant parameter that influences the MIP performance.<sup>51</sup> The grafting disadvantage is the extensive procedure requiring additional modification of the support material before MIP polymerization. That may increase the cost and use of chemicals.



**Scheme 1.1-5.** Grafting of the MIP film on the particle surface.

An MIP thin film can be deposited on a transducer surface by electropolymerization (Scheme 1.1-6a). There are three different electropolymerization methods. One is the pH-induced polymer film formation.<sup>61</sup> The other is the reductive electropolymerization, e.g., fullerene derivatives.<sup>62</sup> However, the most widely used is oxidative electropolymerization (Scheme 1.1-6b).<sup>63</sup> Pyrrole, aniline, and diaminobenzene are among the most popular monomers to prepare MIPs due to their commercial availability and low cost. In recent decades, thiophene derivative monomers have gained attention as well.<sup>64</sup> That is because of polythiophenes' high mechanical and chemical stability. Therefore, they can maintain the shape and size of imprinted cavities even under harsh template extraction conditions compared to other polymers, e.g., polypyrrole. Moreover, polythiophenes are highly conductive and processable in both doped and undoped states. The procedure of MIP preparation via anodic oxidation is described in detail in Chapter 2, Sections 2.3.1, 2.3.4, and 2.3.5, below.

The main advantage of electropolymerization is that the polymer films can be grown on the surface of any conductive or semiconductive, chemically inert material of any shape and size, e.g., on electrodes of surface plasmon resonance chips or quartz crystal resonators for electrochemical quartz crystal microbalance (QCM).<sup>65</sup> Particularly, MIP film deposition on the electrode surface for sensor application provides direct communication between the MIP and the electrode, making the signal transduction more straightforward. Moreover, it helps in miniaturizing a sensor without compromising its analytical integrity.<sup>65</sup> Furthermore, appropriately adjusted electropolymerization parameters can easily control the polymer nucleation and growth rate.<sup>63</sup> The polymer thickness can readily be controlled by controlling the charge transferred, e.g., by controlling the number of potential cycles and potential scan range in potentiodynamic deposition or the potential and time in potentiostatic deposition. Furthermore, the film morphology can be adjusted by selecting an appropriate porogenic solvent and supporting electrolyte. However, this method's significant deficiency is that the template should be electroinactive in the applied potential range to ensure successful imprinting.<sup>66,67</sup> That may limit the choice of templates. Table 1.3 summarizes MIP preparation methods.



**Scheme 1.1-6.** (a) The flowchart of MIP preparation by electropolymerization and electroactive monomers polymerizing to form (b) conductive: polyacetylene **1**, polyphenylene **2**, polyphenylenevinylene **3**, polypyrrole **4**, poly(aminophenylboronic acid) **5**, polythiophene **6**, polyaniline **7**, and polyethylenedioxythiophene (PEDOT) **8**, and (c) insulating: polyphenylenediamine **9**, polyphenol **10**, polyaminophenol **11**, and polythiophenol **12** polymers [adapted from <sup>63</sup>].

**Table 1.3.** MIP synthesis methods.<sup>42, 49, 68</sup>

Method	Morphology	Advantage	Disadvantage
Bulk polymerization	Irregular	<ul style="list-style-type: none"><li>- Rapid and simple preparation</li><li>- No sophisticated instrumentation needed</li><li>- No solvent excess required</li><li>- Cost-effectiveness</li></ul>	<ul style="list-style-type: none"><li>- Time-consuming post-treatment involving crushing, grinding, and sieving to obtain an MIP powder</li><li>- Inhomogeneous distribution of imprinted cavities</li><li>- Risk of the destruction of high-affinity imprinted cavities</li><li>- Difficulty in template extraction</li><li>- A large template amount required as only 30-40% of the polymer is usable after grinding</li></ul> Limited applications
Suspension polymerization	Sphere	<ul style="list-style-type: none"><li>- Simple one-step preparation</li><li>- High porosity polymer</li></ul>	<ul style="list-style-type: none"><li>- Polydisperse particles</li><li>- Require both aqueous and organic phase</li><li>- Water may weaken the interaction between template molecules and functional monomers</li><li>- May favor unwanted interaction between surfactants, template, and functional monomers</li><li>- Additional purification is required because of surfactant contamination</li></ul>
Emulsion polymerization	Sphere	<ul style="list-style-type: none"><li>- Simple preparation</li><li>- High stability of the dispersion system</li><li>- High yield of monodispersed particles</li><li>- Homogeneous distribution of imprinted cavities</li></ul>	<ul style="list-style-type: none"><li>- May favor unwanted interaction between surfactants, template, and functional monomers</li><li>- Additional purification may be needed because of surfactant contamination</li></ul>
Seed polymerization	Sphere	<ul style="list-style-type: none"><li>- Monodispersed particles</li><li>- Homogeneous distribution of imprinted cavities</li></ul>	<ul style="list-style-type: none"><li>- Tedious, time-consuming preparation</li></ul>

Precipitation polymerization	Sphere	<ul style="list-style-type: none"> <li>- Simple and easy preparation</li> <li>- Uniform and controllable particle size</li> <li>- Free of surfactant or stabilizer</li> <li>- Excellent size controlling ability</li> </ul>	<ul style="list-style-type: none"> <li>- Water may weaken the interaction between the template and functional monomers</li> <li>- A large amount of solvent needed</li> <li>- Possible dilution of the pre-polymerization complex</li> </ul>
Living polymerization	Varies	<ul style="list-style-type: none"> <li>- Uniform polymer growth</li> <li>- Material homogeneity</li> <li>- Controlled composition and functionality</li> <li>- Control over MIP film thickness on a support material</li> </ul>	<ul style="list-style-type: none"> <li>- Possible side reactions in the presence of protic solvents, oxygen, and moieties with polar functional groups</li> </ul>
Sol-gel process	Sphere	<ul style="list-style-type: none"> <li>- Simple and easy preparation</li> <li>- Material homogeneity and high porosity</li> <li>- High mechanical and thermal stability</li> <li>- Higher binding capacity</li> <li>- Cost-effectiveness</li> </ul>	<ul style="list-style-type: none"> <li>- Sophisticated instrumentation required for application studies</li> </ul>
MIP grafting	Sphere	<ul style="list-style-type: none"> <li>- Simple and highly efficient procedure</li> <li>- Easy template extraction</li> <li>- High binding capacity</li> </ul>	<ul style="list-style-type: none"> <li>- Additional modification step before MIP synthesis may be required</li> </ul>
Electro-polymerization	Film	<ul style="list-style-type: none"> <li>- Simple one-step preparation</li> <li>- Fast preparation</li> <li>- Easy control over the polymer thickness, rate of nucleation, and growth</li> <li>- An initiator not required</li> <li>- Control over film morphology</li> </ul>	<ul style="list-style-type: none"> <li>- Limited template selection</li> </ul>

### 1.1.5 Application of MIPs

MIPs are highly chemically and mechanically stable, durable, and selective. They are easy and inexpensive to prepare. Due to their significant advantages, MIPs were primarily utilized in analytical separation and purification, i.e., SPE,<sup>69</sup> chromatography,<sup>70</sup> environmental

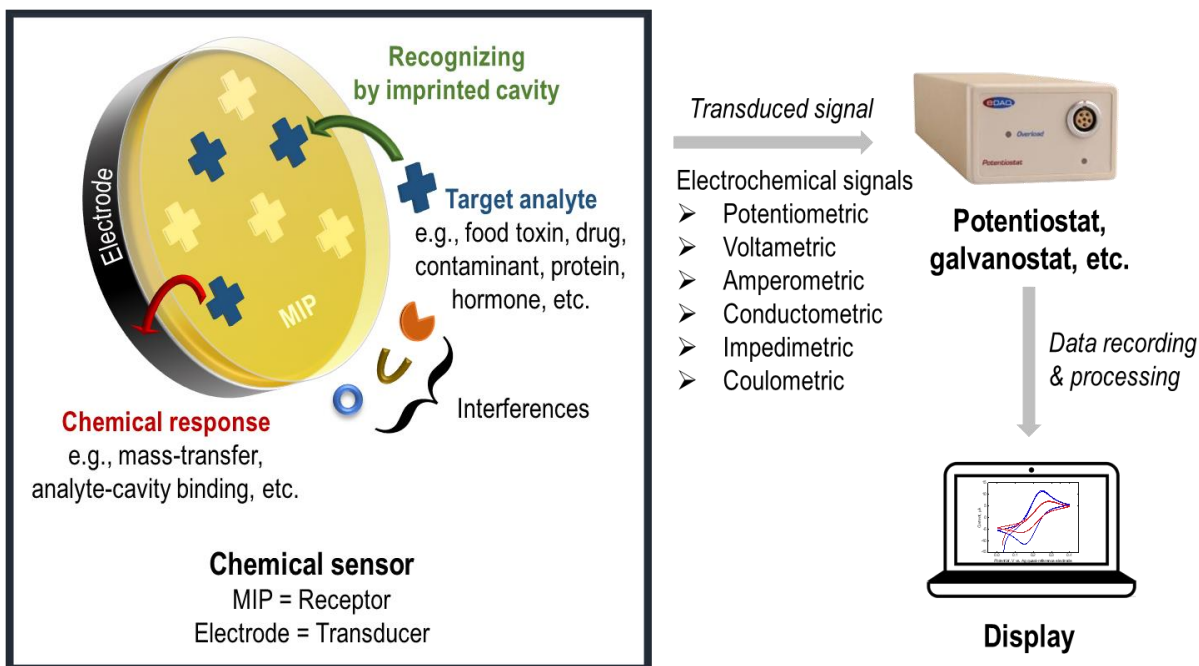


analysis,<sup>71</sup> food analysis,<sup>72</sup> etc. In recent years, extensive research in the MIP field further diversified MIPs application in clinical analysis,<sup>73</sup> drug delivery,<sup>74</sup> and catalysis.<sup>75</sup> Moreover, MIPs are commonly used as electrochemical, colorimetric, fluorescent, etc., chemosensors' selective recognizing units.<sup>76</sup> The aforementioned is the scope of the present thesis, discussed in detail in Section 1.2 of the present chapter.

## 1.2 Electrochemical MIP chemosensor

In the early years of development, MIPs were primarily used as stationary phases in liquid chromatography. Researchers began to utilize them as an alternative to antibodies in immunosensors in the early 1990s. Vlatakis et al. in 1993 reported the first ligand-binding assay, demonstrated by the chemically prepared MIP instead of the traditional biocompounds.<sup>77</sup> MIP was prepared in bulk using MAA as the functional monomer, theophylline and diazepam as templates, ethylene glycol dimethacrylate (EDMA) as the cross-linking monomer, and AIBN as the initiator. This MIP was studied using a radio-labeled and fluorescence-labeled analyte for the molecularly imprinted sorbent assay and enzyme-multiplied immunoassay. Then, in 1995 Hutsins and Bachas combined the imprinting technology with electrochemical transduction.<sup>78</sup> They electropolymerized polypyrrole in sodium nitrate aqueous solution on a glassy carbon electrode (GCE) to deposit an MIP film for nitrate detection. Although subsequently, the template was not removed, the MIP film was applied for sensing purposes. Notably, these significant contributions to imprinting opened another promising application of the MIP as a chemosensor.

An MIP chemosensor is composed of two components, i.e., a receptor and a transducer (Scheme 1.2-1). MIP serves as the chemical recognition element, i.e., an artificial receptor in this chemosensor. The transducer converts a chemical response, i.e., analyte-cavity binding, mass transfer, etc., into a readable analytical signal. An electrode used as the transducer in the electrochemical chemosensor converts chemical recognition events from the receptor into a quantifiable analytical signal, i.e., the current, charge, potential, capacity, impedance, or conductivity change.<sup>79</sup> Ideally, an electrode should be inert in the potential range applied for measurements.



**Scheme 1.2-1.** The MIP electrochemical chemosensor; its components and operation.

The imprinting factor (*IF*) is an essential parameter of an MIP chemosensor. It provides information on whether the imprinting of the template, i.e., the formation of selective molecular cavities in the polymer, is successful. This value can be used to evaluate the interaction strength between the cavity and the target analyte molecule.<sup>80</sup> The *IF* is determined by comparing the binding capacity of MIP and NIP in the extraction experiments.<sup>81</sup> For a QCM experiment using an MIP thin film, the direct readout of the resonance frequency change proportional to the mass change upon the target analyte sorption in the MIP film is the final result.<sup>82</sup> Therefore, for such an experiment, the binding capacity of the MIP and NIP can be determined as given by Equation 1.1.<sup>83</sup> However, most of the other electrochemical transduction methods only indirectly estimate the amount of analyte sorbed in the MIP. Therefore, the 'apparent imprinting factor' is determined for such experiments instead.

There are two ways to calculate the apparent *IF* according to Equation 1.2. The first is by dividing the slope of the calibration plot of the target analyte's response to the MIP over NIP. The second method is by dividing the affinity constant, *k* (target analyte-MIP interaction strength) of the MIP over the NIP.<sup>84</sup> The MIP's ability to retain a particular binding site for the target analyte is often indicated by higher *IF* values.<sup>85</sup> Likewise, a lower *IF* indicates a low

imprinting effect (almost negligible if IF is equal to 1). Low IF often results from non-specific binding such as surface interaction between MIP and target analyte.

Moreover, the imprinting event can be evaluated by performing a selectivity study using common interferences and compounds whose molecules are structural analogs of the target analyte using MIPs and NIPs.<sup>86</sup> In fact, selectivity is the essential feature of a chemical sensor, as in reality, there are no interference-free samples. Furthermore, a selectivity study can reveal if the resultant response arises from binding the target analyte to the cavity or not. The MIP selectivity is calculated according to Equation 1.3. Recently, an MIP, primarily used for sensing applications, has been fused with metal particles, such as gold, silver, and silica particles, sometimes in the carbon nanotubes' presence. Metal particles offer high conductivity and a highly developed surface, which improves the chemosensor's performance.<sup>87</sup>

$$Q = \frac{(c_0 - c)v}{W}, \quad IF = \frac{Q_{MIP}}{Q_{NIP}} \quad \text{Equation 1.1}$$

The  $Q$  symbol is the amount of target analyte bound to the MIP,  $c_0$  (mg/L) is the initial concentration of the target analyte,  $c$  (mg/L) is the final concentration of the target analyte after the sorption,  $v$  (mL) is the volume of the target analyte added, and  $W$  (g) is the mass of the MIP or NIP.  $IF$  is the imprinting factor, and  $Q_{MIP}$  and  $Q_{NIP}$  are the MIP and NIP mass change.

$$\text{Apparent IF} = \frac{\text{Calibration plot slope}_{MIP}}{\text{Calibration plot slope}_{NIP}} \text{ or } \frac{k_{MIP}}{k_{NIP}} \quad \text{Equation 1.2}$$

$$\text{Selectivity} = \frac{\text{Calibration plot slope}_{MIP}}{\text{Calibration plot slope}_{Interference}} \quad \text{Equation 1.3}$$

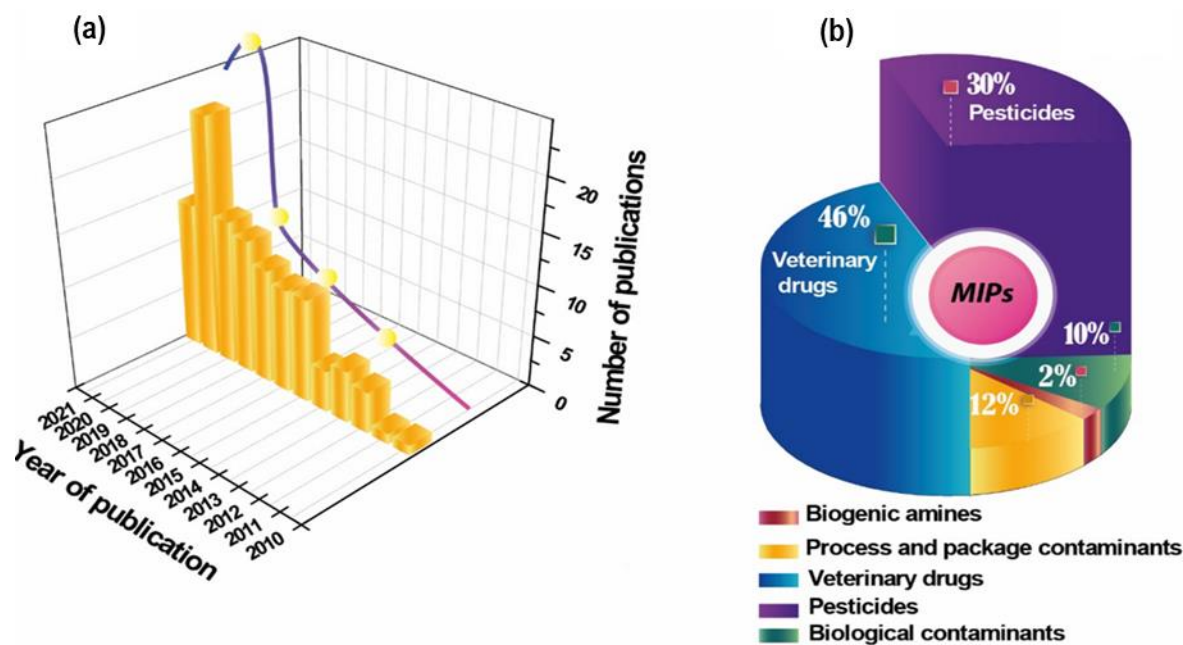
### 1.2.1 Application of electrochemical MIP chemosensors in food analysis

The human population has continued to boom for a long time. That has contributed to the significant increase in demand for food products and their variety. Unfortunately, this demand is not met, and thus low food supply is a huge problem worldwide. This scenario had cultivated dishonest farmers, food producers, and suppliers to produce unsafe products to meet the market demand. Industrialization and globalization of the world economy further worsen this situation.<sup>88</sup> As a result, in the past decade, food products have been contaminated with dangerous chemicals, i.e., artificial chemical fertilizers, pesticides, herbicides, antibiotics,

antifungals or hormones, heavy metal ions, and food additives used by the food industry, including preservatives, food dyes, and artificial fragrances of adverse effects on the consumers' health.

Despite active governmental efforts to control and monitor food quality, this task is not easy. Traditionally, qualified personnel in certified laboratories perform food quality and safety tests using sophisticated, time-consuming, and expensive analytical techniques, e.g., HPLC combined with mass spectrometry (HPLC-MS)<sup>89</sup> and methods, e.g., (polymerase chain reaction)-(gas chromatography) combined with mass spectrometry.<sup>90</sup> However, this strategy suffers from deficiencies. It has recently failed because of the diversity of chemical contaminants and low residue limits.<sup>91</sup> Therefore, a cost-effective, rapid detection and determination with a high-throughput method is in demand. Moreover, newly developed analytical methods should easily be integrated with portable, hand-held devices, thus enabling on-spot sample analysis.<sup>92</sup>

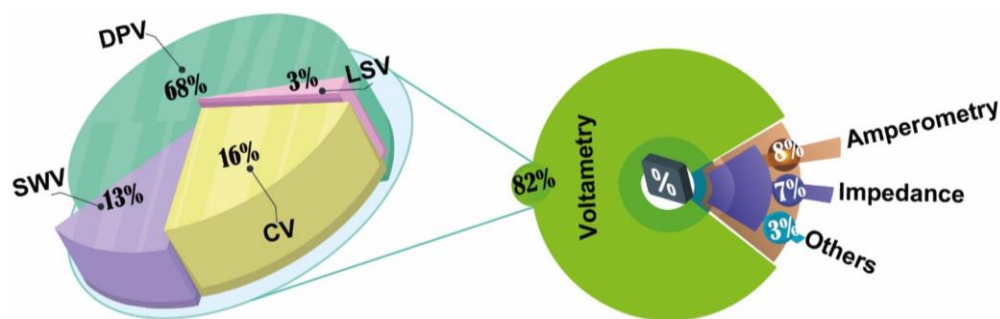
MIP electrochemical chemosensing can overtake conventional detection and determination methods as it fulfills all the requirements for a food quality and safety monitoring strategy. MIP chemosensors can detect analytes efficiently, sensitively, and inexpensively with small, portable equipment.<sup>91,93</sup> Moreover, MIPs are very stable under harsh chemical and physical conditions, offering highly selective molecular recognition. Therefore, MIP electrochemical chemosensors are promising in determining food contaminants (Scheme 1.2-2b).<sup>88</sup> Various food contaminants, including veterinary drugs (46%), pesticides (30%), biological contaminants (10%), and biogenic amines (2%), have been determined using MIP chemosensors from the year 2010 to 2021. Moreover, the number of publications on MIP electrochemical chemosensors for food safety and quality monitoring application significantly increased in recent years (denoted with vertical bars in Scheme 1.2-2a).<sup>88</sup> Interestingly, in 2020, the number of journals publishing papers on food contaminants' determination using MIP electrochemical sensors was doubled compared to that of the previous 2019 year. This high increase in the publication number substantiates that the MIP electrochemical chemosensors' application for food safety and quality monitoring is a hot research topic that continues to evolve and expand.



**Scheme 1.2-2.** (a) The number of publications on food safety monitoring and (b) food contaminants determination between 2010 and 2021 using MIP electrochemical chemosensors.<sup>88</sup>

### 1.2.2 MIP electrochemical chemosensors used in food analysis

The electrochemical chemosensors are classified based on the mode of transduction, i.e., current (A), charge (C), potential (V), capacitance ( $\mu\text{F}$ ), impedance ( $\Omega$ ), and conductivity (S), used to quantify the physicochemical phenomena accompanying analyte-cavity binding.<sup>94</sup> Various MIP chemosensors have recently been proposed for food safety applications.<sup>88,95</sup> Elfadil et al. reported a detailed analysis of the publication numbers of MIP electrochemical chemosensors concerning different electrochemical techniques used, i.e., voltammetry (82%), amperometry (8%), impedimetry (7%), and other (3%) for food safety between the year 2010 and 2021 (Scheme 1.2-3).<sup>88</sup> MIP voltammetric chemosensors are the most reported, especially those using DPV (68%). The subsequent most reported voltammetry technique is cyclic voltammetry, CV (16%), followed by square wave voltammetry, SWV (13%). The least reported voltammetry technique used is linear sweep voltammetry, LSV (3%). Apparently, potentiometric and conductometric MIP chemosensors are some of the least reported chemosensors in food safety research.



**Scheme 1.2-3.** The number of publications on food safety studied between 2010 and 2021 using MIP electrochemical chemosensors.<sup>88</sup>

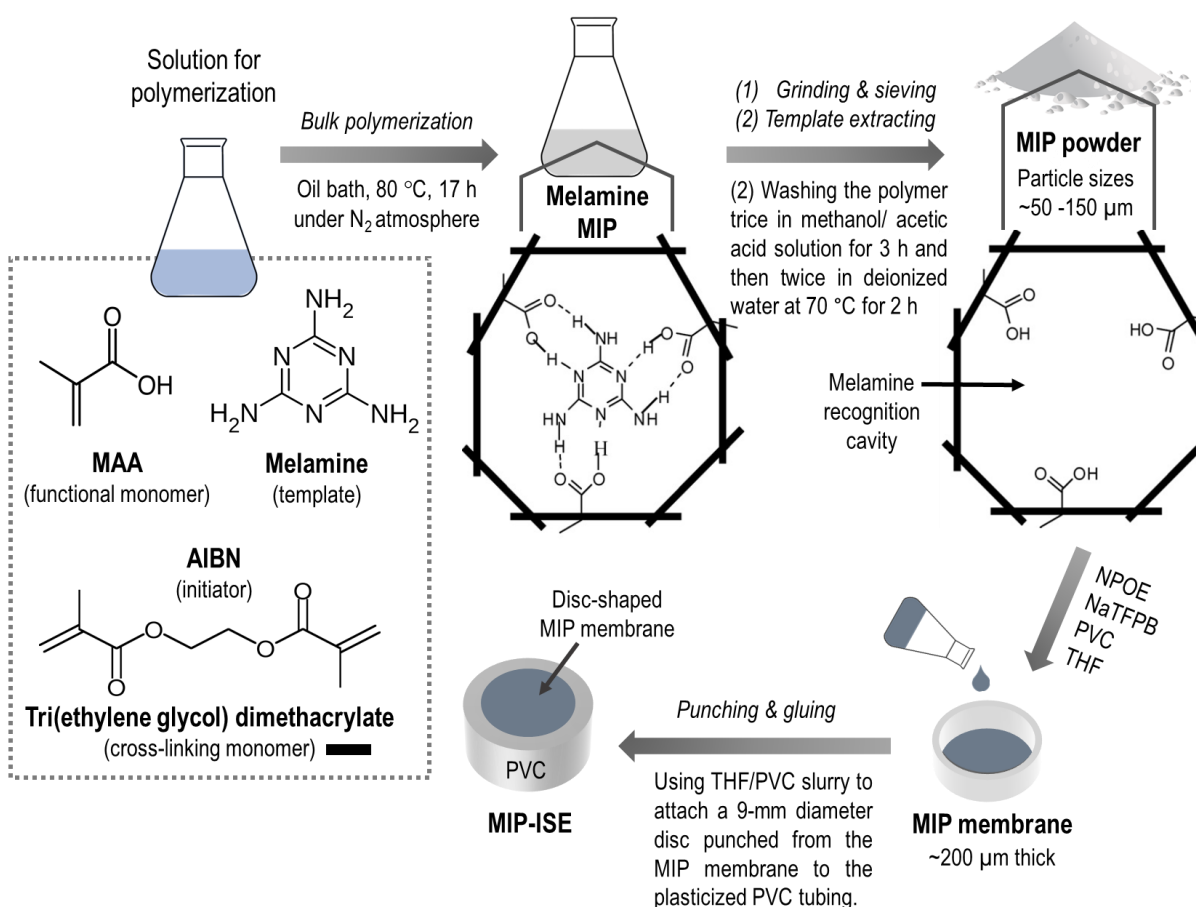
Potentiometric chemosensors measure the potential difference between the reference and working electrode, mainly under the zero-current condition. The charge accumulated by the MIP film generates the potential difference. This difference can be generated without the need for the target analyte to diffuse through the MIP film.<sup>96</sup> Generally, the reference electrode potential is constant, and the working electrode potential varies depending on the examined solution composition. The potential difference correlates with the ion activity, equivalent to the concentration, but only at very low concentrations. The potentiometric chemosensor's response is linear against the logarithm of the analyte ion concentration, covering a broad concentration range, as estimated by the Nikolsky-Eisenman equation. Potentiometric chemosensors' advantages include their high selectivity, relatively short response time, easy use, and inexpensive preparation. The downside is their insensitivity to small changes in analyte concentrations as they linearly respond to the logarithm of analyte concentration.

Liang et al. reported melamine determination using an MIP membrane ion-selective electrode (MIP-ISE).<sup>97</sup> The pre-polymerization complex of the melamine template with the MAA functional monomer in benzene was prepared in solution by self-assembly (Scheme 1.2-4). Then, the complex was polymerized in bulk in the presence of the AIBN initiator and the EDMA cross-linking monomer. The resulting MIP block was ground then sieved to obtain the desired-size MIP particles. Subsequent melamine template removal resulted in vacating cavities capable of selective recognizing the target melamine molecules. The MIP membrane was prepared by dissolving the melamine-extracted MIP powder in 2-nitrophenyloctyl ether (NPOE), sodium tetrakis [3,5-bis(trifluoro-methyl)phenyl]borate (NaTFPB), and poly(vinyl chloride) in THF solvent. The mixture was poured into a glass ring, then dried overnight to

obtain a ~200  $\mu\text{m}$  thick membrane. The membrane was then punched to a disc shape and mounted to PVC tubing.

NaTFPB was incorporated to decrease anionic interferences and membrane resistance, and improve chemosensor selectivity, whereas NPOE was a plasticizer. The MIP-ISE chemosensor was subjected to melamine ion detection in the flow analytical system. Melamine is a weak base ( $\text{p}K_{\text{a}}=5.05$ ). Therefore, it can easily be protonated in a solution of low pH and directly determined by potentiometry. The determined melamine linear dynamic concentration range was  $5.0 \times 10^{-6} - 1.0 \times 10^{-2}$  M. The chemosensor response was fast (16 s), and its stability was high (over two months). Moreover, the chemosensor was applied for melamine determination in a milk sample. It was highly selective to melamine ions in this application, discriminating against other common ions in milk ( $\text{Na}^+$ ,  $\text{K}^+$ , and  $\text{Ca}^{2+}$ ). The recovery ranged from 95 to 110%.

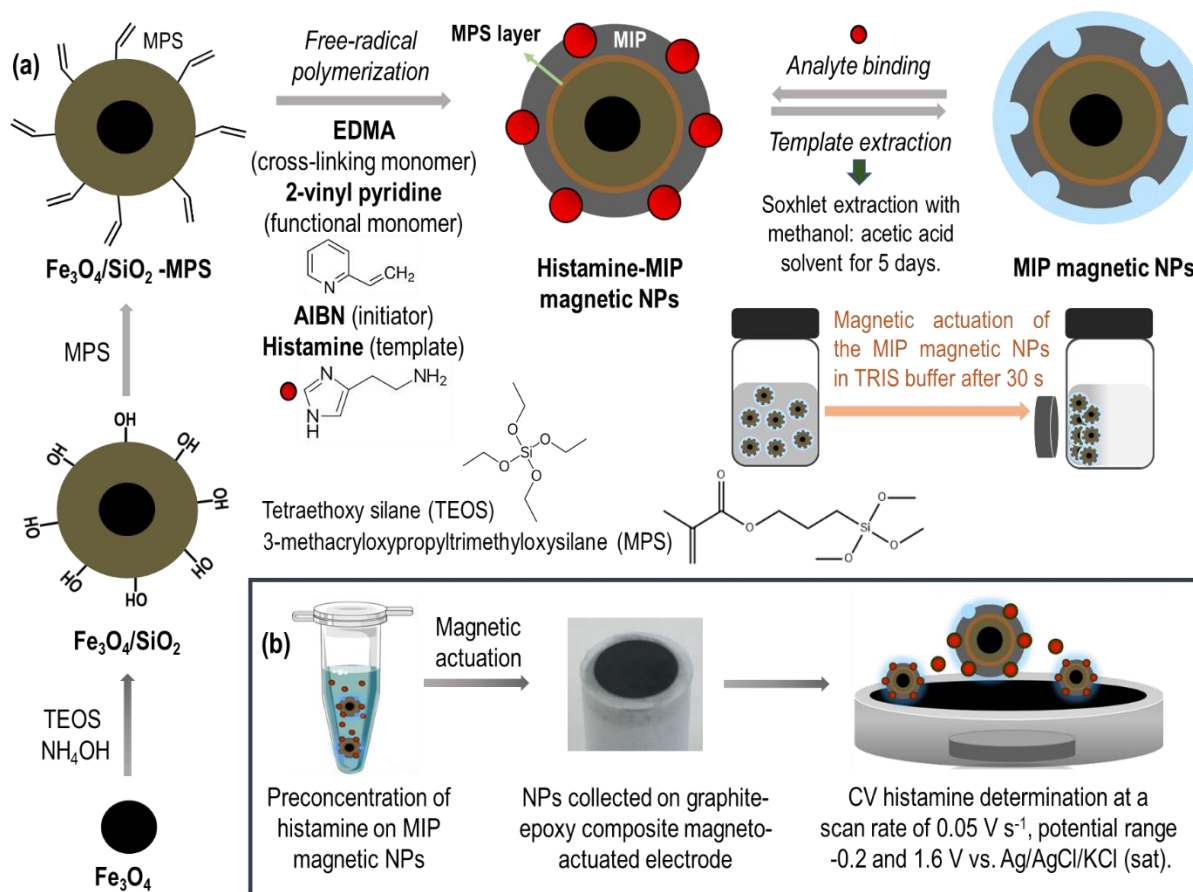
Voltammetric chemosensors are the most prevalent among electrochemical chemosensors as they offer fast and sensitive determination accompanied by simple preparation at a low cost. They measure the faradic current of a redox reaction at an appropriate potential. The faradic current measured linearly depends on the concentration of the analyte undergoing electrochemical reaction.<sup>98</sup> There are a few modes of potential modulating (e.g., linear scanning with time, non-linear modulating with a pulse or sinusoidal excitation, etc.). Depending on the type of potential agitation, voltammetric techniques fall into the category of linear sweep voltammetry (LSV),<sup>99</sup> CV,<sup>100</sup> pulse voltammetry, e.g., DPV<sup>101</sup> and square-wave voltammetry (SWV),<sup>102</sup> etc. Particularly, the DPV technique has recently gained enormous attention as it offers a high signal-to-noise ratio and, therefore, sensitivity higher than other techniques.<sup>96</sup>



**Scheme 1.2-4.** The flowchart of MIP membrane ion-selective electrode (MIP-ISE) preparation by punching and gluing the MIP membrane, prepared in a glass ring by dissolving the melamine-extracted MIP powder, prepared by bulk polymerization in 2-nitrophenyloctyl ether (NPOE), sodium tetrakis [3,5-bis(trifluoro-methyl)phenyl]borate (NaTFPB), and poly(vinyl chloride) (PVC), in THF solvent, to a PVC tubing [adapted from <sup>97</sup>].

Hassan et al. reported CV histamine determination with MIP magnetic  $\text{Fe}_3\text{O}_4$  nanoparticles (NPs).<sup>100</sup> First, the  $\text{Fe}_3\text{O}_4$  NPs' surface was modified with hydroxyl groups of tetraethylorthosilicate (TEOS). The hydroxyl modified  $\text{Fe}_3\text{O}_4/\text{SiO}_2$  NPs were further modified with 3-methacryloxypropyltrimethyloxysilane (MPS). MPS provided the NPs with an activated C=C group, making the NPs suitable for MIP polymerization. The histamine MIP magnetic NPs were synthesized by free-radical polymerization using histamine as the template, 2-vinyl pyridine as the functional monomer, EDMA as the cross-linking monomer, and AIBN as the initiator in the presence of MPS-modified  $\text{Fe}_3\text{O}_4/\text{SiO}_2$  NPs (Scheme 1.2-5a). Afterward, the histamine template was extracted, thus emptying cavities imprinted in the MIP. The MIP magnetic NPs were gently shaken in a concentrated histamine solution for 60 min, allowing

the MIP to bind to the histamine analyte. The NPs with the pre-concentrated histamine were collected on the graphite-epoxy composite magneto-actuated electrode by applying a magnetic field. Histamine was determined directly with CV (Scheme 1.2-5b) in the concentration range of 0 to 11.1 mg L<sup>-1</sup>. However, the chemosensor response was non-linear. Advantageously, it negligibly responded to interferences, including tryptamine, cadaverine, and putrescine, thus revealing high selectivity to histamine. This chemosensor was applied to histamine determination in the real fish sample (tuna); its recovery ranged between 96.8 and 102.0%. The MIP magnetic NPs chemosensor exhibited high binding capacity. Furthermore, it was easily separated from any solution using a magnetic field.



**Scheme 1.2-5.** (a) MIP magnetic NPs synthesis [adapted from <sup>100,103</sup>]. (b) CV determination of pre-concentrated histamine on magnetic-MIP [adapted from <sup>100</sup>].

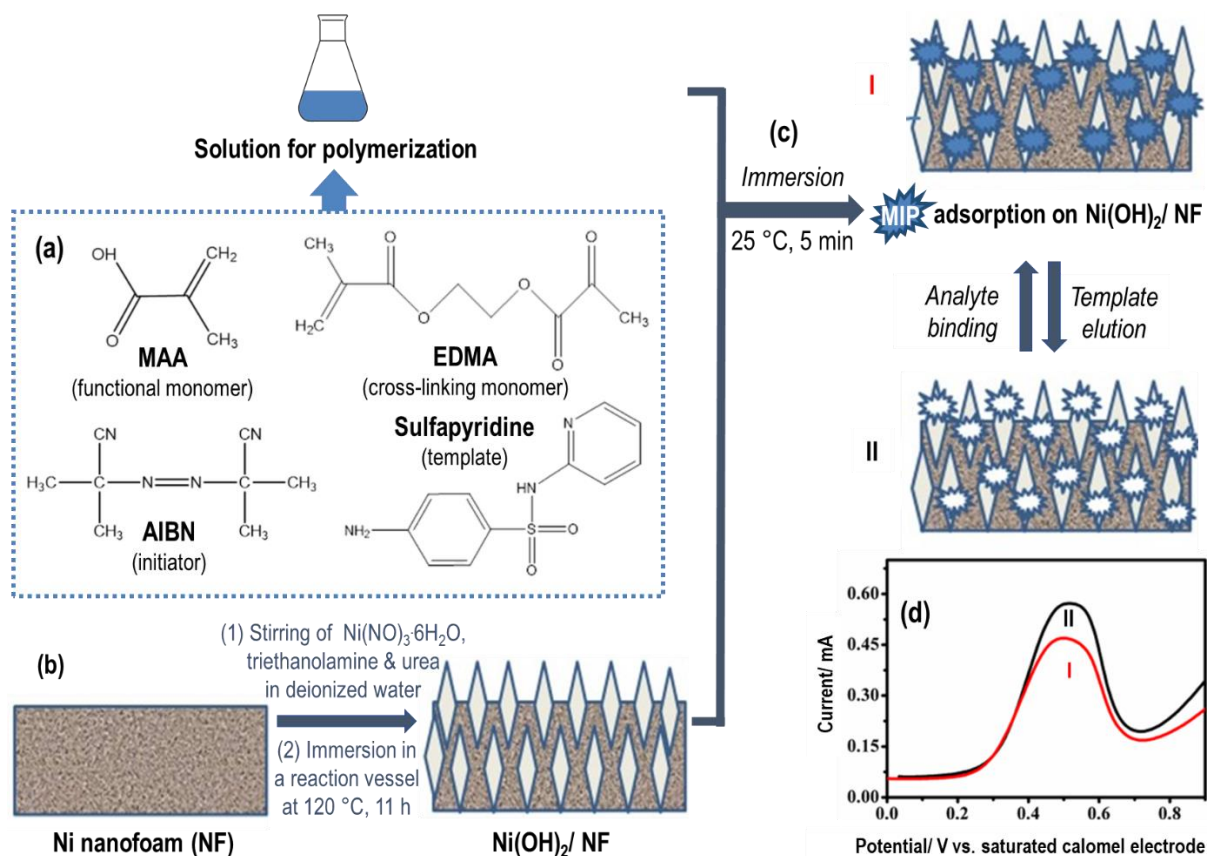
Liu et al. proposed an MIP film-coated electrode nanoarray for sulfapyridine, a sulfanilamide antibacterial medication, determination with DPV.<sup>101</sup> The Ni(OH)<sub>2</sub> nanoarrays

were grown in situ on a nickel nanofoam (NF) electrode by the hydrothermal method (Scheme 1.2-6b). Next, the solution for polymerization containing the sulfapyridine template, MAA functional monomer, EDMA cross-linking monomer, and AIBN initiator (Scheme 1.2-5a) was used to fabricate an MIP film on the Ni(OH)<sub>2</sub>/NF electrode (Scheme 1.2-6c). The sulfapyridine template was eluted to expose imprinted cavities. Subsequently, the extracted MIP/Ni(OH)<sub>2</sub>/NF electrode was immersed in a sulfapyridine solution for 5 min. Analyte binding was indirectly studied with the use of potassium hexacyanoferrate(III), K<sub>3</sub>[Fe(CN)<sub>6</sub>], redox probe using DPV (Scheme 1.2-5d). The Ni(OH)<sub>2</sub> nanoarray was applied to improve the MIP chemosensor's repeatability, stability, and sensitivity. This nanoarray features a large surface area, high mass transfer rate, operability, and sensitivity. As a result, the prepared chemosensor exhibited high selectivity and repeatability. The sulfapyridine linear dynamic concentration range was  $5.9 \times 10^{-7}$ – $1.34 \times 10^{-3}$  M. Moreover, the chemosensor discriminated interferences, including sulfadiazine, sulfathiophene, and sulfasalazine. It was stable for at least 9 days. The chemosensor was applied to determine sulfapyridine in real freshwater fish samples, and the recovery was 98 to 98.6%.

Capoferri et al. reported an MIP chemosensor for dimethoate organophosphate insecticide determination using SWV.<sup>102</sup> The MIP was deposited on a GCE electrode in the phosphate-buffer solution containing the dimethoate template and pyrrole functional monomer (Scheme 1.2-7b). Cavities in the MIP were emptied after templates molecules were removed with HCl. The template-extracted MIP film-coated electrode was dipped in dimethoate solutions of different concentrations, and subsequently, dimethoate was indirectly determined using SWV. The SWV measurement was performed in the presence of the K<sub>3</sub>[Fe(CN)<sub>6</sub>] redox probe. The determined dimethoate dynamic concentration range was linear from 0.1 to 1 nM.

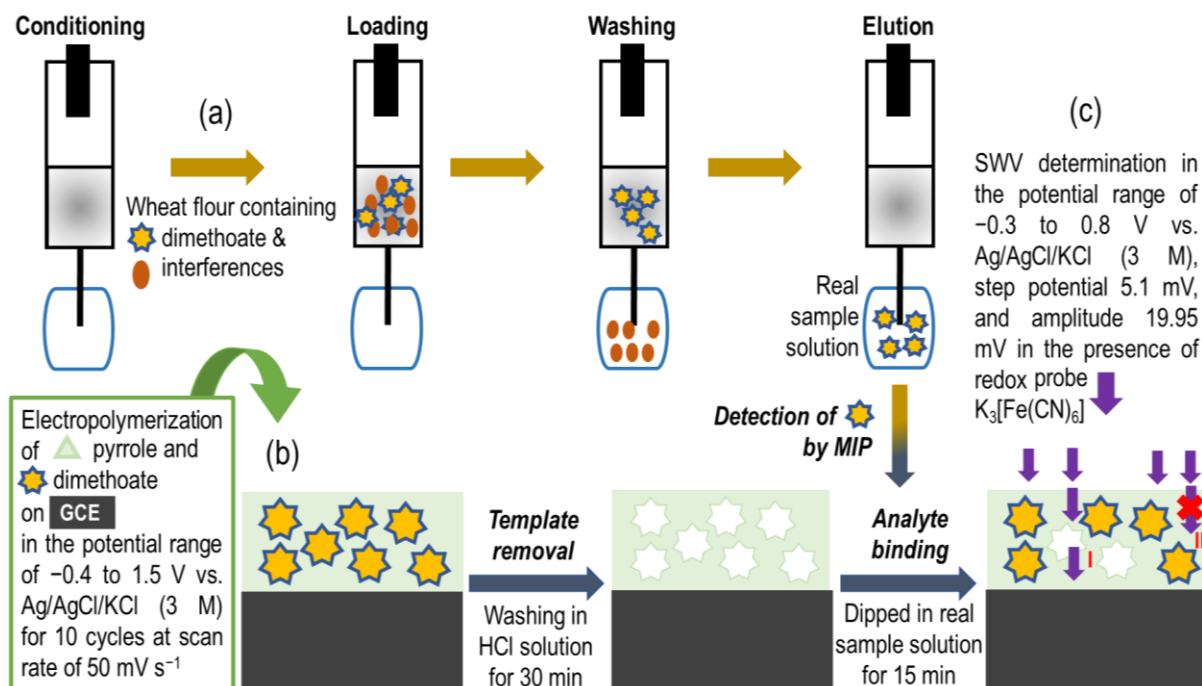
The chemosensor selectivity was examined using other organophosphate pesticides, viz., omethoate, malathion, parathion, and paraoxon. The response to omethoate of the molecular structure is similar to that of dimethoate was 23%, whereas responses to all other interferences were negligible at the concentration range same as that of dimethoate. The chemosensor was applied to determine dimethoate in real wheat flour samples. The analyte samples were prepared by selectively extracting dimethoate from wheat flour using microextraction by packed sorbent, MEPS (Scheme 1.2-7a), which is a miniaturized version of a traditional SPE. The extracted dimethoate was then determined using the MIP chemosensor. The dimethoate

analyte recovery, examined using MIPs combined with MEPS, was comparable to those determined via UHPLC-MS/MS. Moreover, the devised chemosensor's reproducibility, repeatability, and selectivity were excellent.



**Scheme 1.2-6.** (a) Solution for polymerization. (b) Modification of nickel nanofoam electrode (NF) with  $\text{Ni}(\text{OH})_3 \cdot 6\text{H}_2\text{O}$  (c) MIP adsorption on the  $\text{Ni}(\text{OH})_2/\text{NF}$ , then template elution, and then analyte binding. (d, I) Analyte-cavity binding, resulting in a decrease in the DPV peak for the  $\text{K}_3[\text{Fe}(\text{CN})_6]$  redox probe, and (d, II) elution of the analyte from the MIP cavity, increasing the DPV peak for the  $\text{K}_3[\text{Fe}(\text{CN})_6]$  redox probe [adapted from <sup>101</sup>].

Zhang et al. reported MIP-modified graphene deposition on GCE (GCE/GN/MIP) for an imidacloprid systemic insecticide determination (Scheme 1.2-8).<sup>99</sup> First, graphene (GN) was modified with the *p*-vinylbenzoic acid functional monomer through  $\pi$ - $\pi$  interactions in DMF. The imidacloprid template was added to the resulting solution to promote pre-polymerization complex formation via interfacial hydrogen bonding.

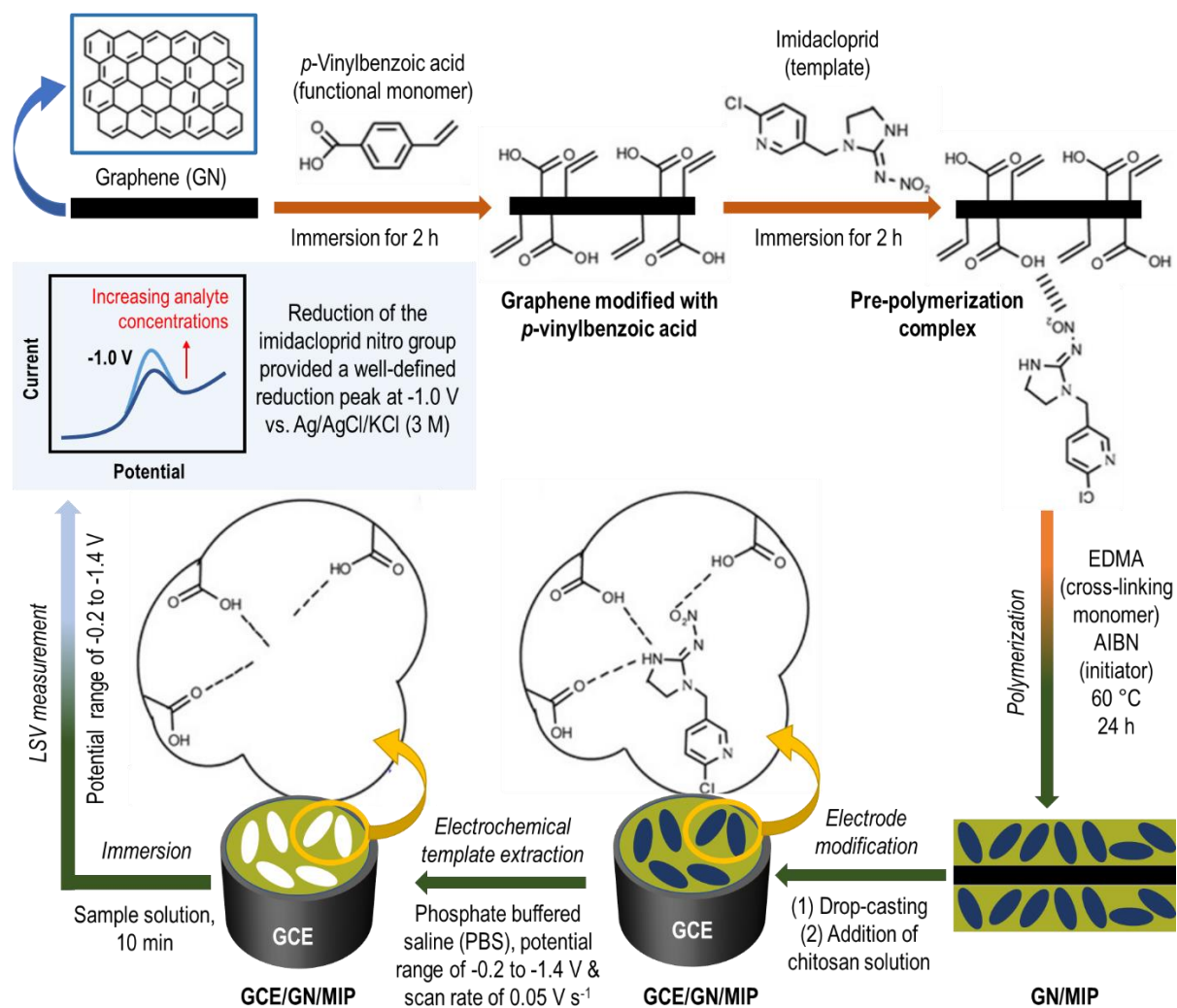


**Scheme 1.2-7.** (a) Preparation of the sample of dimethoate extracted from wheat flour using microextraction by packet sorbent, MEPS. (b) MIP preparation by electropolymerization, followed by template removal, and then analyte binding using dimethoate samples extracted from wheat flour. (c, I) The empty cavity allowed diffusion of the K<sub>3</sub>[Fe(CN)<sub>6</sub>] redox probe through the MIP, whereas (c, II) analyte-cavity binding blocked this diffusion [adapted from <sup>102</sup>].

Subsequently, the EDMA cross-linking monomer and AIBN initiator were added to this solution, and then the free-radical polymerization was initiated thermally. The prepared GN/MIP suspension was dropped on a GCE, and then a chitosan solution was added to prevent the frail membrane from falling off. The template was electrochemically extracted from GCE/GN/MIP, and then the electrode was immersed in phosphate-buffered saline (PBS) containing different imidacloprid concentrations. Imidacloprid was directly determined with LSV using the GCE/GN/MIP chemosensor.

The determined imidacloprid dynamic concentration range was 0.5 – 15 μM, with two linear segments at 0.5 – 4.0 μM and 4.0 – 15 μM. The chemosensor's selectivity against interferences, vis., neodinotefuran, nitenpyram, thiamethoxam, clothianidin, acetamiprid, and thiacloprid, was examined. There were no LSV responses to acetamiprid and thiacloprid because of the nitro group absence in their structures. The responses to other interferences were low in the concentration range, same as that of imidacloprid. Moreover, the chemosensor

was applied to imidacloprid determination in rice samples with a 75 to 78% recovery. GN-based materials have unique properties of well-defined tubular nano-sized structures, functional surfaces, appreciable chemical stability, high electrocatalytic activity, and excellent biocompatibility. Therefore, these materials are excellent for composing and supporting imprinted sensing films. Furthermore, the GN incorporation in the MIP significantly improved the chemosensor sensitivity, especially in the imidacloprid recognition. Additionally, the chemosensor selectivity and reproducibility were high.

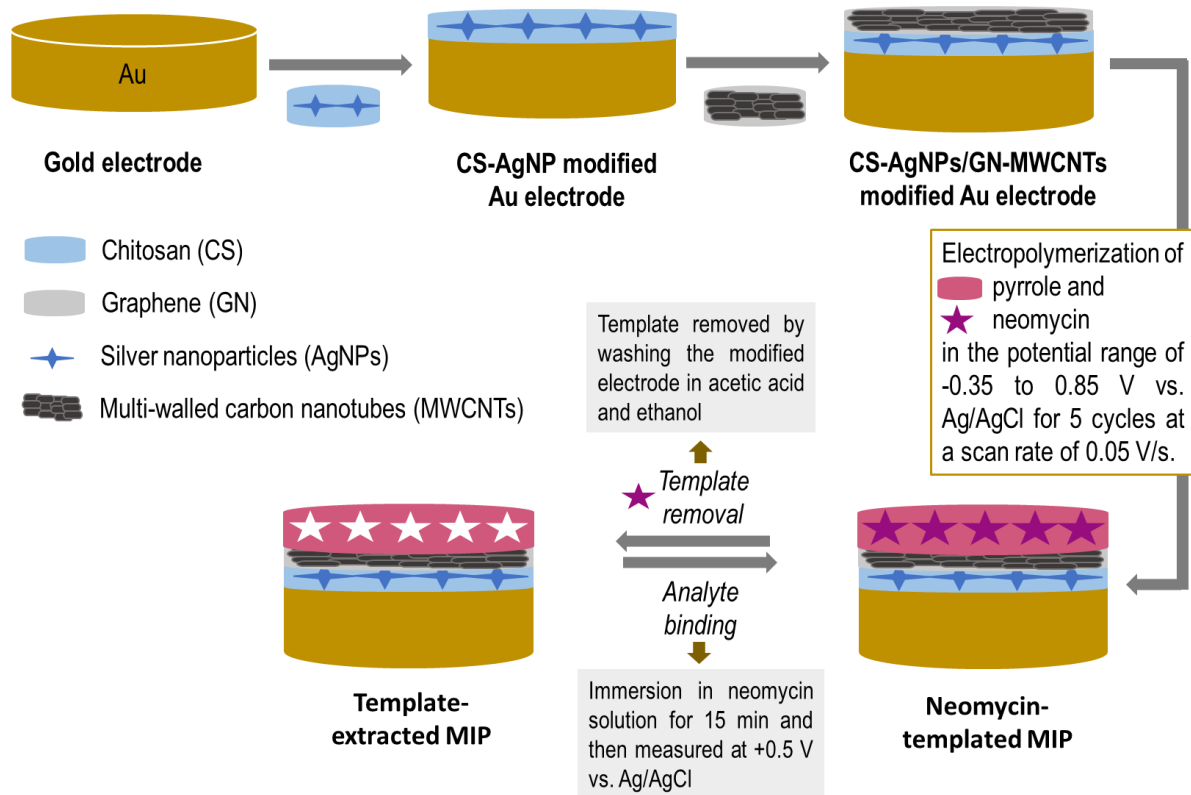


**Scheme 1.2-8.** Graphene-modified MIP preparation on a glassy carbon electrode (GCE/GN/MIP) and selective electrochemical imidacloprid determination using LSV [adapted from <sup>99</sup>].

The amperometric and chronoamperometric chemosensors measure the current change with time resulting from the electrode process of analyte diffusing to the MIP film-coated electrode from the bulk solution. The difference between these two techniques is that the amperometric measurement is performed at a constant voltage, whereas a potential jump is applied in the latter.<sup>104</sup> In both techniques, the current is measured as a function of time. These techniques help measure the current for the diffusion-rate controlled redox process, which linearly increases with the analyte concentration. Furthermore, they are simple yet sensitive, not requiring analyte labeling.

Lian et al. reported deposition of MIP, templated with the neomycin natural antibiotic, on modified chitosan-(silver nanoparticles) (CS-AgNPs)/graphene-(multi-walled) carbon nanotubes (GN-MWCNTs) on the gold electrode.<sup>105</sup> First, the CS-AgNPs suspension was applied to the gold electrode, then dried at room temperature. Next, this procedure was repeated with GN-MWCNTs. Subsequently, MIP was prepared by electropolymerization of the pyrrole functional monomer in the neomycin template presence on the CS-AgNPs/GN-MWCNTs modified gold electrode (Scheme 1.2-9). Afterward, the template was extracted from the modified electrode then used for neomycin indirect determination using the  $K_3[Fe(CN)_6]$  redox probe.

The amperometric neomycin response of the thus prepared chemosensor was linear in the concentration range of  $9.0 \times 10^{-9} - 7.0 \times 10^{-6}$  M. Moreover, the chemosensor was selective, discriminating interferences, vis., gentamicin sulfate, streptomycin, kanamycin sulfate, and erythromycin. The chemosensor was applied for neomycin determination in natural milk and honey samples; the recovery ranged from 97.1 to 103%. AgNPs are biocompatible conductors with unique electrical and catalytic properties. CS is a biocompatible material with high mechanical strength, adhesion, and film-forming ability. It is often used to enhance nanoparticles' stability as immobilization matrices.<sup>106</sup> Moreover, the AgNPs incorporation in CS increases the effective surface area of the electrode and thus enhances the faradic current signal. GN has a large surface area with high mechanical stability and electric conductivity. MWCNTs have a unique electric property promoting electron transfer. Therefore, the prepared chemosensor was selective, and its signal was repeatable due to the synergistic effects of the high electric conductivity of CS-AgNPs and GN-MWCNTs.



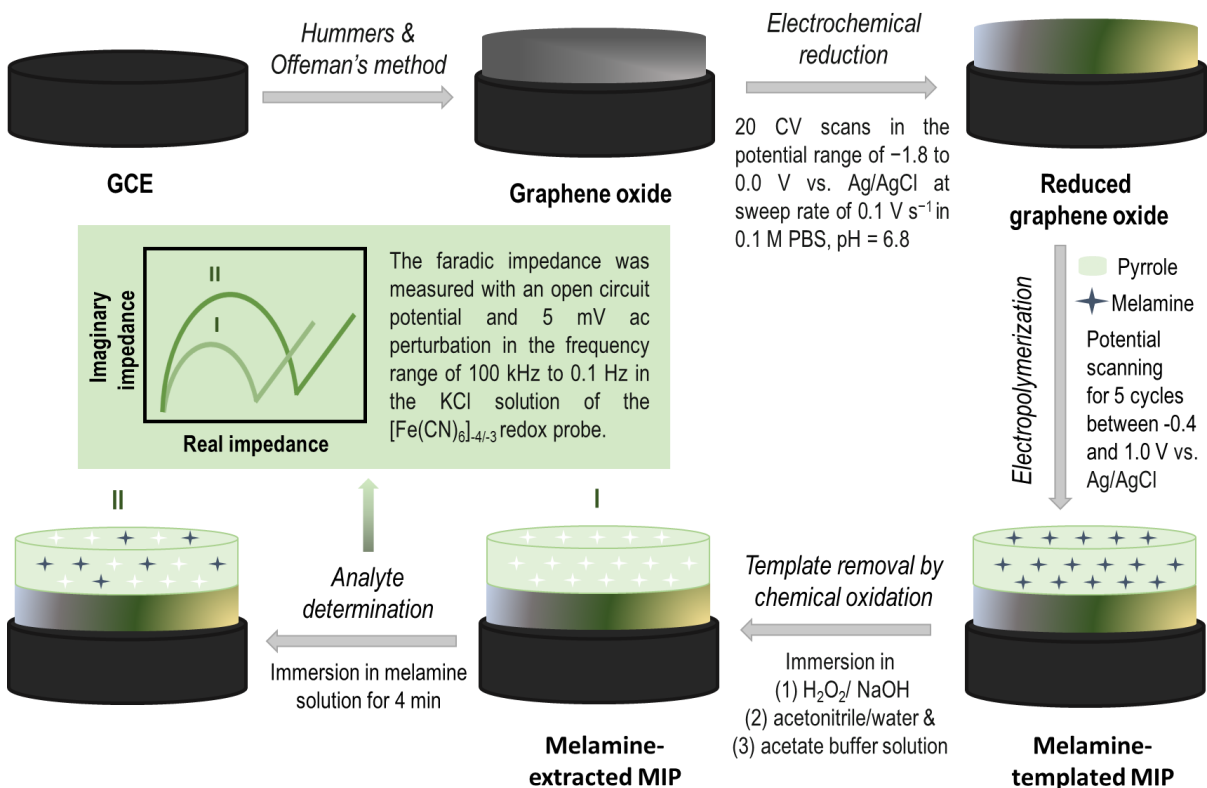
**Scheme 1.2-9.** The flowchart of neomycin-templated and template-extracted MIP fabrication [adapted from <sup>105</sup>].

The impedimetric sensor measures the change in the MIP film impedance or capacitance upon applying a range of frequencies. Impedimetry is helpful for monitoring changes in film thickness and electric properties, including the change of electric permittivity of the electric double layer originating from analyte-cavity recognition events.

Shamisur et al. proposed melamine determination using an impedimetric chemosensor with an MIP film deposited on electrochemically reduced graphene oxide (rGO) modified GCE (Scheme 1.2-10).<sup>107</sup> The graphene oxide (GO) suspension was cast on the GCE, then electroreduced. Then, the melamine-templated MIP film was prepared by electropolymerization of the pyrrole functional monomer, in the melamine template presence, on the rGO-modified GCE. The chemical oxidation of the melamine-templated MIP using the H<sub>2</sub>O<sub>2</sub>-NaOH solution resulted in the melamine template removal, forming radical cations (polarons) in the polypyrrole film (Scheme 1.2-11). The chemosensor was immersed in

solutions of different melamine concentrations, and, subsequently, its electric property was indirectly examined using EIS in the presence of  $[\text{Fe}(\text{CN})_6]^{4-/3-}$ .

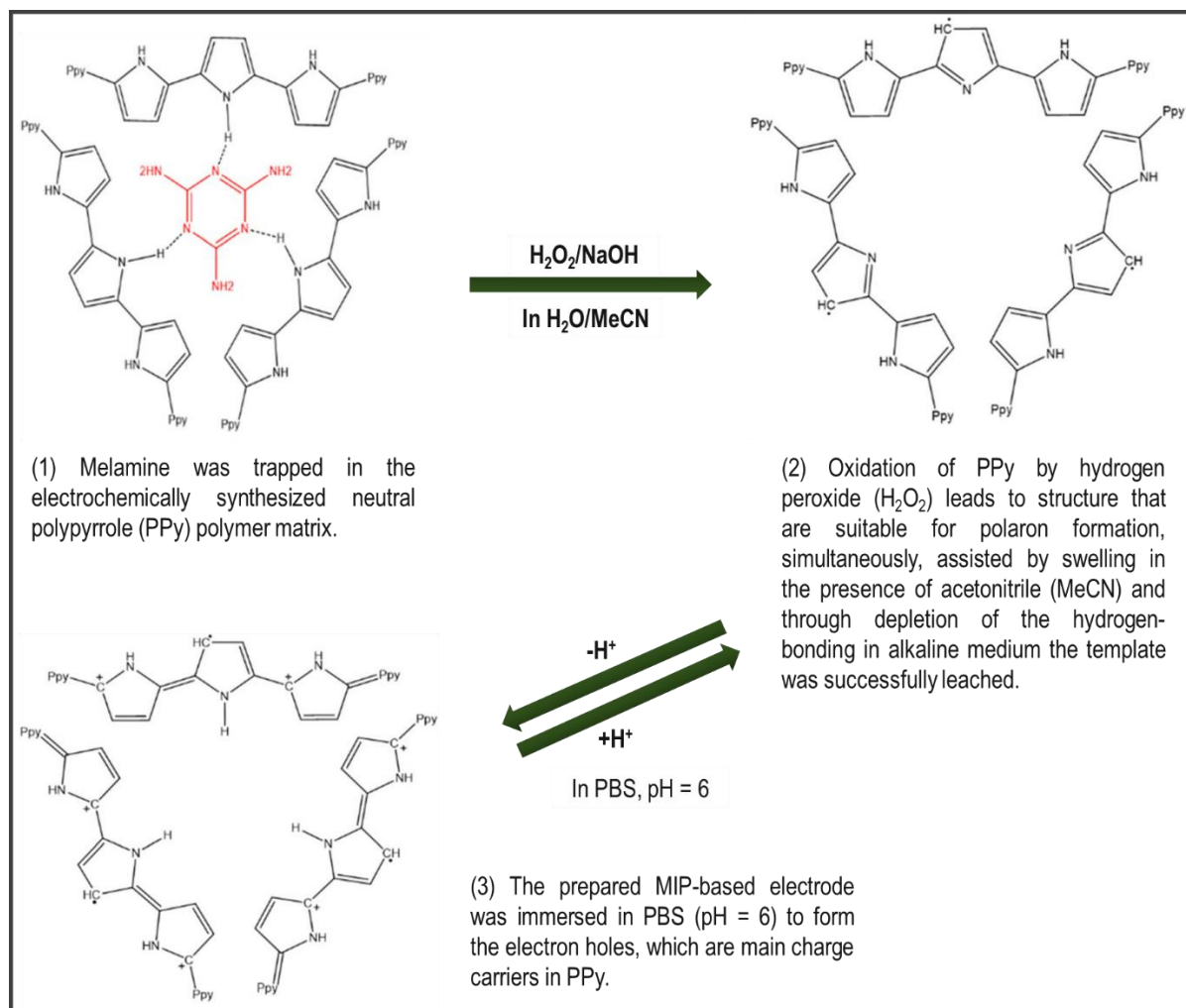
The chemosensor linearly responded to the melamine 4.0 to 240 nM concentration range. It discriminated interferences, namely, glycine, phenylalanine, tryptophan, histidine, tyrosine, and ascorbic acid. Moreover, the chemosensor determined melamine in a multiple concentration-spiked milk sample. Its sensitivity, selectivity, reproducibility, and repeatability were high owing to the rGO layer presence. The rGO increased the number of imprinted cavities by providing a developed surface for MIP film deposition. Furthermore, it amplified the detection signal. Besides, the polarons' formation improved the electron transfer properties and, thus, the conductivity of the electroactive polypyrrole film.



**Scheme 1.2-10.** (a) The flowchart illustrating melamine-templated MIP film preparation on the (reduced graphene)-modified GCE [adapted from <sup>107</sup>].

The conductometric sensor measures conductivity if the alternating current (ac) is applied in a diluted electrolyte solution between two electrodes. The ac causes the migration of ions,

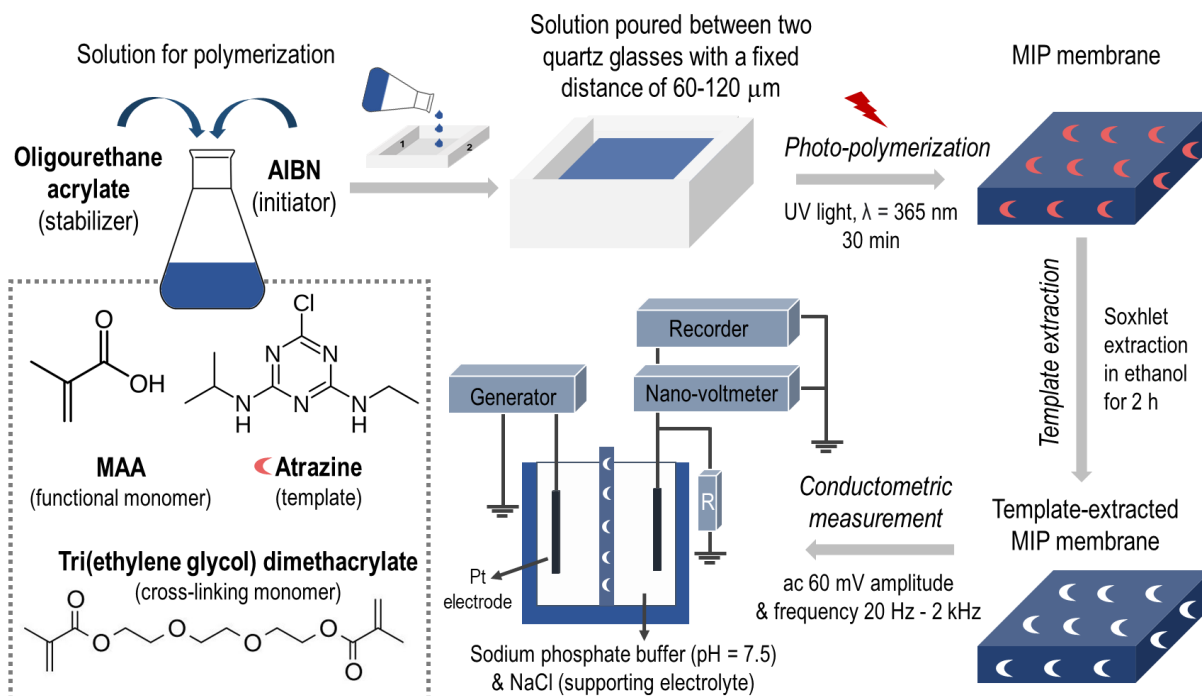
resulting in a current flow. The MIP conductivity chemosensor devised relied on MIP preparation as a membrane.



**Scheme 1.2-11.** Melamine template removal from the MIP molecular cavity by chemical oxidation [adapted from <sup>107</sup>].

In 1999, Sergeyeva et al. reported an atrazine-sensitive conductometric MIP chemosensor.<sup>108</sup> The MIP was prepared by photopolymerization using atrazine as the template, MAA as the functional monomer, tri(ethylene glycol) dimethacrylate as the cross-linking monomer, AIBN as the initiator, and oligourethane acrylate as the film stabilizer (Scheme 1.2-12). The solution for polymerization was cast between two quartz plates to obtain a 60-120  $\mu\text{m}$  thick membrane. Subsequently, the template was extracted, exposing the imprinted cavity. The template-extracted MIP membrane was used for conductometric atrazine determination. Chemosensor

detectability was high, with the LOD of 5 nM atrazine, and the response time was 6 to 15 min. Moreover, its selectivity to interferences, namely, atrazine, triazine, simazine, and promertyn, was high.



**Scheme 1.2-12.** The flowchart of preparation of atrazine-imprinted MIP membrane for conductometric atrazine determination [adapted from <sup>108</sup>].

Among all signal transduction methods, conductometry is the least sensitive. Therefore, MIP conductometric chemosensors are rarely used. That is because it is almost impossible to discriminate between ions as ion conductivity is additive.<sup>96</sup> Small differences in ionic limiting molar conductance are insufficient to distinguish between species. Furthermore, if the concentration of one ion is exceptionally high, it may mask other ions.

### 1.2.3 Factors governing the selection of the MIP electrochemical chemosensor's assay

The selection of the assay/transduction method depends on the target analyte's nature and the suitability of the detection technique. For instance, potentiometry is more suited for detecting charged molecules, e.g.,  $\text{Hg}^{2+}$ ,<sup>109</sup> whereas chronoamperometry can readily quantify an electroactive target compound, such as butyrate hydroxylamine.<sup>110</sup>

Although the only electroactive component of the sample must be the target compound in the studied potential range, which is a substantial drawback of this sensor, that disadvantage can be overcome by selecting the voltammetric technique. However, in the voltammetric technique, the undesired capacity currents overlap the faradic current resulting from an electrode process. Alternatively, the DPV or SWV technique, which subtracts the undesired capacity currents, can eliminate the above measurement complication. Often, DPV is applied for determining electroactive analytes, e.g., sunset yellow dye.<sup>111</sup>

Moreover, the sensing approach, direct and indirect, plays an essential role in choosing the chemosensor's assay. Electroactive analytes are directly determined in the potential range of their electroactivity.<sup>110</sup> The faradaic current of the electrode process of an electroactive analyte is the output signal. In contrast, an indirect analytical signal measurement is performed with an external redox probe, e.g., hexacyanoferrate(III)/hexacyanoferrate(II),  $[\text{Fe}(\text{CN})_6]^{3-}/[\text{Fe}(\text{CN})_6]^{4-}$ , ferrocene, etc., in the test solution for the determination of electroinactive analytes, e.g., metronidazole<sup>112</sup> and sulfonamide.<sup>101</sup> The measurement is performed in the potential range, in which the redox probe is electroactive, and the faradaic current of the redox probe is the output signal.

Yoshimi et al. were the first in 2001 to describe the indirect approach, exemplified with theophylline determination using the theophylline-imprinted poly(methacrylic acid-co-ethyleneglycol di-methacrylate).<sup>113</sup> The MIP was deposited on the MPS film-coated indium-tin-oxide (ITO) electrode using the theophylline template, MAA functional monomer, EDMA cross-linking monomer, and AIBN initiator by free-radical polymerization (Scheme 1.2-13a). Removing the template from the MIP by ultrasonication in water for 1 h resulted in emptying the imprinted cavities (Scheme 1.2-13a, I). The cavity-analyte binding was examined by CV in the presence of a potassium hexacyanoferrate redox probe. The analyte-cavity binding causes the MIP film to swell and its pores to widen (Scheme 1.2-13a, II). That swelling enhances the permeability through the film of the redox probe, thus significantly increasing the probe's faradaic currents (Scheme 1.2-13a, IV).<sup>114</sup>

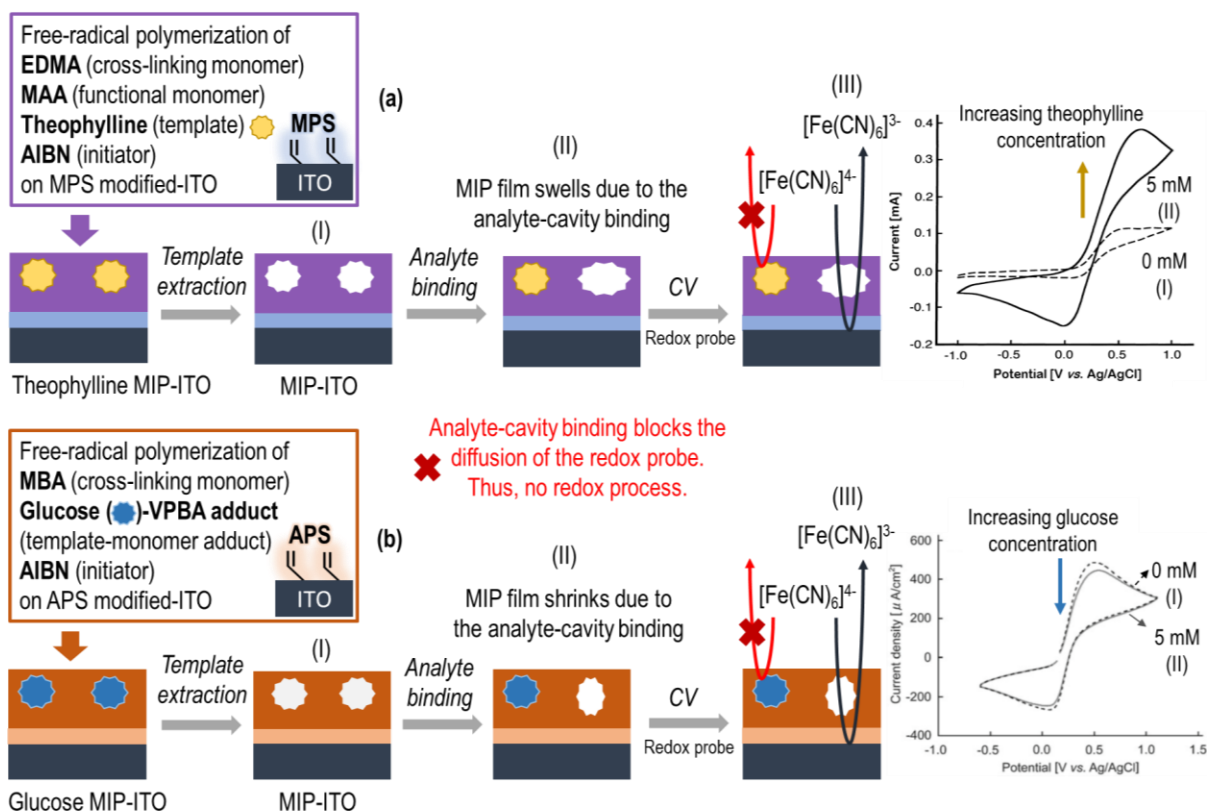
In 2009, Yoshimi et al. reported an enzyme-free glucose MIP chemosensor.<sup>115</sup> The pre-polymerization complex was synthesized by esterifying glucose template with 4-vinylphenylboronic acid (VPBA) functional monomer. Then, MIP was deposited on the 3-acryloxypropyltrimethoxysilane (APS) modified ITO electrode using this complex in the

presence of the methylene bisacrylamide (MBA) cross-linking monomer and AIBN initiator (Scheme 1.2-13b). The template was extracted from the MIP with the HCl solution for 1 h (Scheme 1.2-132b, I) and then studied with CV in the presence of a potassium hexacyanoferrate redox probe. Notably, the probe's faradaic current was decreased because of the cavity-analyte binding. Apparently, this binding caused the MIP film to shrink (Scheme 1.2-13b, II), enhancing probe diffusion through the film to the electrode surface (Scheme 1.2-13b, III). Furthermore, when the template-extracted MIPs were subjected to binding electroinactive target analytes at different concentrations, the MIP film porosity decreased proportionally to the redox probe permeability.<sup>88</sup> Therefore, a decrease in the probe's faradic current or increase of the chemosensor impedance is likely.

This indirect approach is known as the "gate effect." The "gate effect" mechanism of enhancing or more often hindering the redox probe diffusion caused by MIP film swelling or shrinking due to analyte-cavity binding is widely adopted to account for the operation of MIP chemosensors.<sup>101, 107, 110</sup>

Moreover, this effect may serve as a sensitive transduction method for analyte determination if combined with an electrochemical technique, such as DPV or EIS.<sup>107,116</sup> In some advanced chemosensor fabrications, electroinactive analytes, e.g., *p*-synephrine, were determined using self-reporting MIP film. This film was prepared by electropolymerization of functional monomers of *bis*-bithiophene, derivatized with carboxyl and ferrocene moieties, in the *p*-synephrine template presence.<sup>117</sup> The co-polymerized in the MIP film ferrocene moiety eliminated the need for using an external redox probe because this moiety served as the internal redox probe.

It has recently been reported that the "gate effect" mechanism is different for conductive MIP film-coated electrodes.<sup>118</sup> That is, the cavity-analyte binding causes a decrease in the polymer film conductivity, directly corresponding to the decrease in the faradaic current of the redox probe. Obviously, this current decrease does not arise from the redox probe's hindered diffusion through the conductive MIP. Table 1.4 summarizes the MIP electrochemical chemosensor's application in food analysis.



**Scheme 1.2-13.** Indirect CV analyte determination with the potassium hexacyanoferrate(II),  $[\text{Fe}(\text{CN})_6]^{4-}$  redox probe using (a) theophylline [adapted from <sup>113</sup>] and (b) glucose [adapted from <sup>115</sup>] templated MIP film deposited on 3-methacryloxypropyltrimethyloxysilane (MPS) and 3-acryloxypropyltrimethyloxysilane (APS), respectively, modified-ITO electrode. Removal of templates resulted in cavity vacation (a & b, I). Analyte-cavity binding caused the MIP films to swell (a, II) or to shrink (b, II), leading to pore widening and thus enhancing the diffusion of the  $[\text{Fe}(\text{CN})_6]^{3/4-}$  (a & b, III).

**Table 1.4.** Examples of electrochemical MIP chemosensors' application for the contaminants sensing in food samples.

Assay type	Group of contaminants	Specific target	Linear dynamic concentration range	Limit of detection (LOD)	Food product analyzed	Ref.
Potentiometry	Chemical contamination	Melamine	$5.0 \times 10^{-6}$ – $1.0 \times 10^{-2}$ M <sup>a</sup>	$1.6 \times 10^{-6}$ M	Milk	97
	Heavy metal ion	Hg <sup>2+</sup>	$4.00 \times 10^{-9}$ – $1.30 \times 10^{-3}$ M <sup>a</sup>	$1.95 \times 10^{-9}$ M	Tuna and shrimp	109
Chrono-amperometry	Antibiotic	Neomycin	$9.0 \times 10^{-9}$ – $7.0 \times 10^{-6}$ M	$7.63 \times 10^{-9}$ M	Milk and honey	105
	Preservative	Butyrate hydroxylamine	$9.0 \times 10^{-8}$ – $7.0 \times 10^{-5}$ M	$7.63 \times 10^{-8}$ M	Potato chips	110
Cyclic voltammetry	Antiprotozoal agent	Metronidazole	$6 \times 10^{-14}$ – $4 \times 10^{-13}$ M and $4.0 \times 10^{-13}$ – $4 \times 10^{-12}$ M	$2 \times 10^{-14}$ M	Fish	112
	Biogenic amine indicate of food rottenness	Histamine	$0$ – $2.2 \times 10^4$ mg L <sup>-1</sup> and $0$ – $11.1$ mg L <sup>-1</sup> with histamine preconcentration <sup>b</sup>	$1.6 \times 10^{-6}$ mg L <sup>-1</sup>	Fish	100
Linear sweep voltammetry	Flavor	Eugenol	$5.0 \times 10^{-7}$ – $2.0 \times 10^{-5}$ M	$1.0 \times 10^{-7}$ M	Curry	119
Square wave voltammetry	Pesticide	Dimethoate	$0.1$ – $1$ nM	$0.5$ nM	Wheat flour	102

Differential pulse voltammetry (DPV)	Dye	Sunset yellow	2.2 nM – 4.64 $\mu$ M	1.4 nM	Jelly, fruit drink, chocolate, instant juice powder, ice cream, and candy	111
	Antibiotic	Sulfonamide	$5.9 \times 10^{-7}$ – $1.34 \times 10^{-3}$ M	$3.57 \times 10^{-7}$ M	Fish	101
	Hazardous dietary supplement	<i>p</i> -Synephrine	0.2 – 8.8 nM	0.57 nM	Dietary supplement for body-builders	117
Electrochemical impedance spectroscopy (EIS)	Chemical contamination	Melamine	4.0 – 240 nM	0.83 nM	Milk	107
DPV EIS	Mycotoxin	Fumonisin B1	1 fM – 10 pM <sup>a</sup> 1 fM – 10 pM <sup>a</sup>	0.03 fM 0.7 fM	Maise -	116

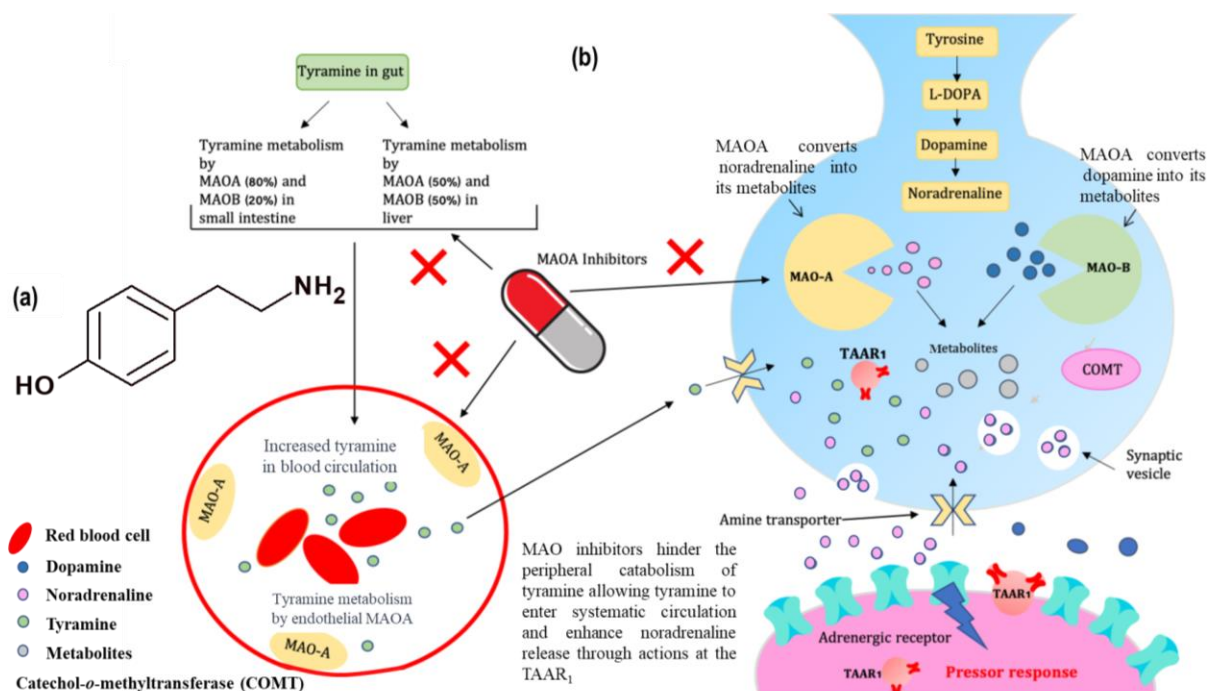
<sup>a</sup> Linear response in a semi-log scale.

<sup>b</sup> Non-linear response.

## 1.3 Food toxins - compounds of interest

### 1.3.1 Tyramine

Tyramine (Scheme 1.3-1a) is a common biogenic primary amine. Living organisms produce it through tryptophan decarboxylation. It can also be found in smoked and fermented food products. Food rich in tyramine includes pickles, cheese, yogurt, fish, meat products, and fruits, including cacao seeds, bananas, avocados, figs, and pineapples.<sup>120</sup> Tyramine in the mammalian brain is present in nanomolar concentrations and generally decomposes by monoamine oxidase (MAO) A and B in the gut wall and liver.<sup>121</sup> Therefore, patients taking monoamine oxidase (MAO) inhibitors or antidepressants could be at risk if they consume a large amount of tyramine.



**Scheme 1.3-1.** (a) Tyramine structural formula and (b) illustration of the "cheese reaction" [adapted from <sup>121</sup>].

The MAO inhibitor hinders the tyramine metabolism and causes the circulatory system to absorb the unchanged tyramine. The unchanged tyramine act as a substrate for the noradrenaline (NA) transporter, i.e., trace amine-associated receptor 1 (TAAR<sub>1</sub>), inducing excessive NA release. That often leads to a severe hypertensive crisis known as the "cheese

reaction" (Scheme 1.3-1b).<sup>122</sup> Moreover, trace amine, such as tyramine, has a similar structure and functionality to catecholamines. Therefore, chronically high tyramine levels in the blood can lead to migraines, other types of headaches, and hypertension. Besides, Parkinson's disease, depression, and schizophrenia are often associated with imbalanced tyramine levels.<sup>123</sup> Table 1.5 shows the tyramine content in food products that are deemed unhealthy for the patients taking MAO inhibitors.<sup>124</sup>

**Table 1.5.** Tyramine content in food products considered not to be recommended for patients treated with MAO inhibitors or antidepressants.<sup>124</sup>

Food product	Sample size	Tyramine content, mg	Tyramine content, $\mu\text{mol}$	Tyramine concentration, $\text{mM}^a$
Canadian cheddar	28 g	43	314	11.2
Camembert cheese	28 g	38	277	9.9
Bleu/Blue cheese	28 g	28	204	4.7
Gorgonzola	28 g	1.6	11	0.42
Cottage cheese, fresh	112 g	0	0	0
Tap beer	355 mL	38	277	0.78
Chicken livers, aged	28 g	60	438	15.6
Sauerkraut	112 g	3.5 - 14	25 - 102	0.23 - 0.91
Soy sauce	5 mL	0.05 - 4.7	3.6 - 34	0.073 - 6.86
Thai fish sauce	5 mL	0 - 3.7	27	5.4

<sup>a</sup> Tyramine concentration was calculated assuming that the food product density equals that of water.

Currently, chromatography is frequently opted for determining biogenic amines in food matrices.<sup>125,126</sup> The advantage of this technique is its high accuracy. However, its application requires costly instrumentation, skilled operators, vast quantities of expensive chemicals, and often it is time-consuming. These disadvantages highlight the importance of developing reliable, fast, low-cost, and simple determination procedures. MIP-based chemosensors demonstrated their usefulness for that. Several ways of tyramine imprinting have been attempted to circumvent the drawbacks of traditional tyramine determination. That is, tyramine was imprinted using sol-gel systems<sup>127,128,129,130</sup> and acrylic polymers.<sup>131,132,133</sup> Those polymers were used as packaging materials for SPE columns or as selective recognition units for optical<sup>131,134</sup> and electrochemical<sup>127,128,130,134</sup> chemosensors.

Atta et al. reported tyramine imprinted sol-gel material synthesized using the TEOS and phenyltriethylorthosilicate (PTEOS) functional monomers and the tyramine template (Scheme 1.3-2a).<sup>127</sup> The material was spin-coated on a GCE (Scheme 1.3-2a, II). Then, the tyramine template was extracted by cycling the MIP film-coated electrode in the potential range of tyramine electroactivity. Next, the electrode was immersed in a 50  $\mu$ M tyramine solution for 15 min. Subsequently, tyramine was directly determined using SWV at 0.70 V vs. Ag/AgCl. The SWV peak measured for the tyramine-imprinted MIP film-coated electrode after dipping in the tyramine solution was low, equalling 0.8  $\mu$ A. Thence, it was essential to modify the electrode surface with nanomaterials and the conducting polymers' composites to improve the chemosensor sensitivity.

Huang et al. deposited MIP on a GCE modified with the (multi-walled carbon nanotube)-gold nanoparticle (MWCNT-AuNP) composites and chitosan (Scheme 1.3-2b).<sup>130</sup> Tyramine-imprinted sol-gel material was synthesized using silicic acid tetraethyl ester and triethoxyphenylsilane as the functional monomers and tyramine as the template. MWCNT-AuNPs were incorporated to enhance the electronic transmission and sensitivity of the chemosensor, whereas the chitosan layer's role was to connect the composite and imprinted sol-gel material layers. Then, the tyramine template was extracted using PBS solution. Afterward, the tyramine analyte was indirectly determined by amperometry at 0.50 V vs. Ag/AgCl/KCl (saturated) using solutions of different tyramine concentrations in the  $[\text{Fe}(\text{CN})_6]^{3-}/[\text{Fe}(\text{CN})_6]^{4-}$  redox probe presence. The chemosensor enabled selective tyramine determining in a broad linear dynamic concentration range of  $1.08 \times 10^{-7}$  to  $1 \times 10^{-5}$  M.

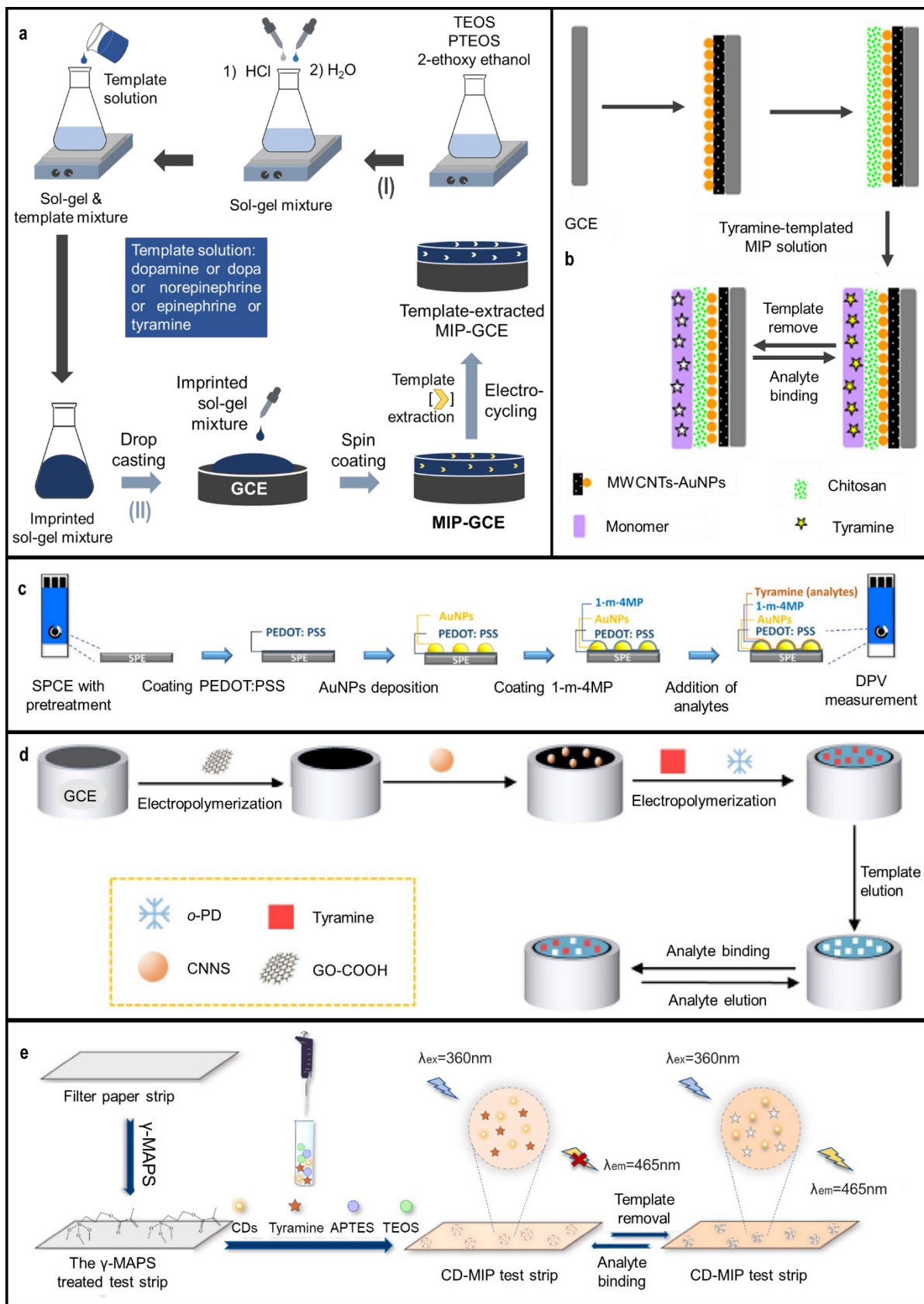
Li et al. combined SPE with MIP particles to isolate tyramine selectively and then electrochemically determined the pre-concentrated tyramine on the modified screen-printed carbon electrodes (SPCEs), thus improving the chemosensing sensitivity.<sup>134</sup> The MIP for SPE was prepared by free-radical polymerization using MAA as the functional monomer, trimethylolpropane trimethacrylate (TRIM) as the cross-linking monomer, and AIBN as the initiator. Following that, the MIP was ground to a fine powder. Then, the tyramine template was chemically extracted by sonification of the powder in the (acetic acid)-methanol solution. Subsequently, this powder was dried in a vacuum oven and used to isolate tyramine. The tyramine analyte was then determined using modified SPCEs.

SPCEs were modified with a poly(3,4-ethylene dioxythiophene) : poly(styrene sulfonate) (PEDOT : PSS) conducting polymer composite to enhance electron transfer (Scheme 1.3-2c).<sup>134</sup> Then, AuNPs were electrochemically deposited on these modified electrodes to increase the electrodes' conductivity. Finally, the surface-enhanced Raman spectroscopy (SERS)-active substrate, 1-methyl-4-mercaptopyridine (1-m-4-MP), was immobilized on the AuNPs' surface through the gold-sulfur bond. The 4-MP further amplified the sensor signal by interacting with the metal through a lone pair of electrons of N and S atoms or  $\pi$  electrons. Subsequently, the isolated tyramine samples on the MIP particles-packed SPE cartridge were electrochemically analyzed. DPV was used to determine tyramine phenolates (negatively charged) interaction with 1-m-4-MP (positively charged) under alkaline solution conditions (0.1 M NaOH, pH = 13). The chemosensor allowed selective tyramine determining in a linear dynamic concentration range of 5 to 100 nM.

Recently, Liu et al. proposed an indirect electrochemiluminescent tyramine sensing procedure (Scheme 1.3-2d).<sup>135</sup> In this procedure, graphitic-phase carbon nitride (g-C<sub>3</sub>N<sub>4</sub>) nanosheets (CNSS) were deposited on the reduced carbonylated graphene oxide (rGO-COOH) support. Next, the thus modified electrode was coated with the poly(*o*-phenylenediamine) (*o*-PD) film imprinted with tyramine. The film was deposited by electropolymerization using six potentiodynamic cycles between 0 and 0.8 V vs. saturated calomel electrode. Next, the tyramine template was extracted with ethanol for 20 min. The prepared MIP/CNNS/(rGO-COOH) electrochemiluminescence chemosensor exhibited a dual recognition effect. One originated from tyramine recognition by MIP, and the other from tyramine luminescence quenching arising from MIP film binding the tyramine analyte. Integrating rGO-COOH with

CNNS promoted electron transfer between the nanosheets and the electrode surface, amplifying the signal measured. The g-C<sub>3</sub>N<sub>4</sub> material is a new metal-free semiconductor with unique electronic properties, thermal stability, and low toxicity.<sup>136</sup> It is promising as a luminophore. The reported chemosensor enabled selective tyramine determination in a linear dynamic concentration range of 10 nM to 1 mM. However, despite the use of advanced techniques of tyramine determination, the simplicity of the measurement is rarely addressed.

In 2021, Qiao et al. reported carbon dots (CDs)-MIP fluorescent test strips for rapid, highly selective, and sensitive on-site tyramine detection.<sup>137</sup> To this end, a filter paper was treated with  $\gamma$ -methacryloxypropyl trimethoxysilane ( $\gamma$ -MAPS). The CDs-MIP was then grafted on the pre-treated filter paper by in-situ synthesis (Scheme 1.3-2e). To this end, the MIP was prepared using the sol-gel process with the 3-aminopropyltriethoxysilane (APTES) functional monomer, TEOS cross-linking monomer, and tyramine template. The tyramine template was then extracted with ethanol. The extraction was continued until no tyramine was detected by UV-vis spectrophotometry in the extracting solvent. The filter papers were treated with  $\gamma$ -MAPS for two reasons. The first was to provide an even distribution of the recognition film. The other was to enable interaction between the  $\gamma$ -MAPS methacrylate group and the template via the hydrogen and hydrophobic interactions. Moreover, CDs served as fluorescent sensing substance. The fabricated test strips were highly selective, with the fluorescence intensity linearly quenched with the tyramine concentration increase from 0.5 to 10.0 mg L<sup>-1</sup>. The test strips were applied for tyramine determination in rice vinegar and white rice vinegar. The recovery exceeded 90.9%. Evidently, this fast and straightforward tyramine determination in food technique is in demand.



**Scheme 1.3-2.** (a, I) MIP synthesis with the sol-gel method using the 3-aminopropyltriethoxysilane (APTES) functional monomer and the TEOS cross-linking monomer in the 2-ethoxyethanol solvent and (a, II) spin-coating of the extracted sol-gel MIP material on a glassy carbon electrode (GCE) [adapted from <sup>127</sup>]. (b) MIP on the GCE modified with multi-walled carbon nanotube-gold nanoparticle composites and chitosan [adapted from <sup>130</sup>]. (c) Screen-printed carbon electrode (SPCE) modification with the poly(3,4-ethylene dioxothiophene) : polystyrene sulfonate (PEDOT: PSS) conductive polymer, gold nanoparticles (AuNPs), and a 1-methyl-4-mercaptopyridine (1-m-4-MP) Raman-active substrate, for tyramine determination, selectively isolated using MIP prepared for solid-phase extraction (SPE) [adapted from <sup>133</sup>]. (d) Deposition of the film of poly(*o*-phenylenediamine) (*o*-PD), imprinted with tyramine, on the GCE modified with carbonylated reduced graphene oxide (rGO-COOH) and graphitic-phase carbon nitride (g-C<sub>3</sub>N<sub>4</sub>) nanosheets (CNSS) [adapted from <sup>135</sup>]. (e) Carbon dots (CDs)-MIP grafted on a filter paper pre-treated with  $\gamma$ -methacryloxypropyl trimethoxysilane ( $\gamma$ -MAPS) [adapted from <sup>137</sup>].

### 1.3.2 Quinoxaline heterocyclic aromatic amine (HAA)

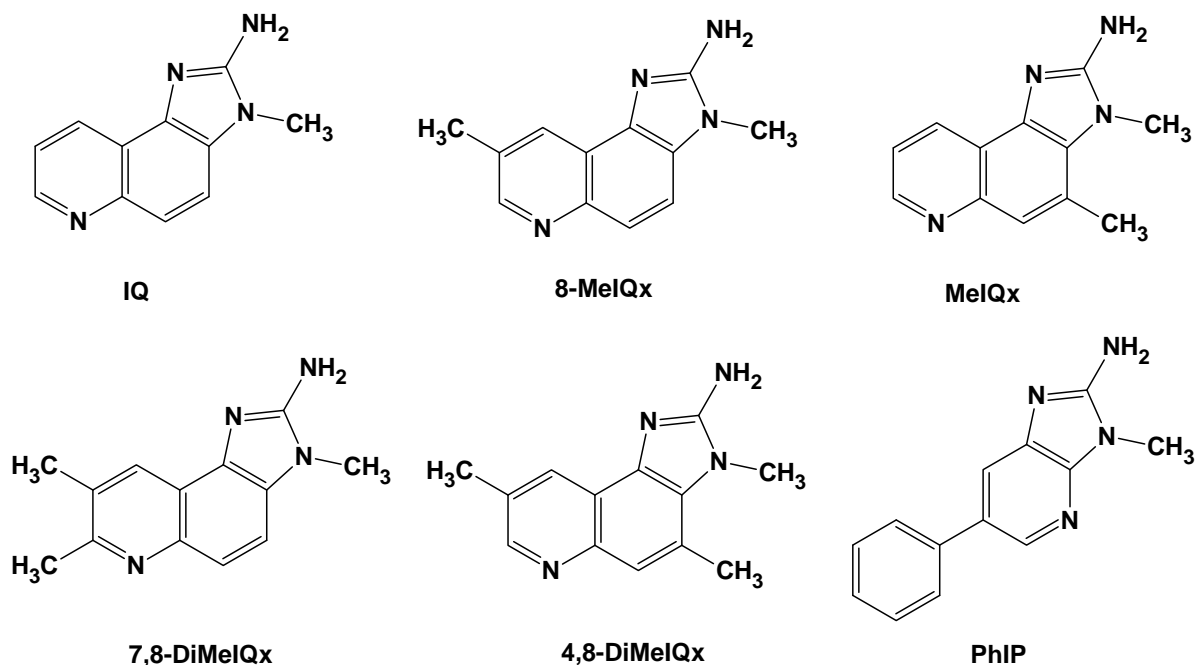
Quinoxaline heterocyclic aromatic amines, HAAs, are mutagens and potent carcinogens exposed to humans continuously through dietary intake and surroundings. HAAs are generated in heat-processed protein-rich food, such as meat and fish at the nanograms.<sup>138,139,140</sup> Moreover, they were found in tobacco smoke, cooking fumes, and environmental sources, i.e., river water, air, and rain.<sup>141</sup> To date, more than 25 different HAAs are identified in heat-processed foods. They are categorized into two major classes depending on their structures.<sup>142</sup>

One class is known as aminoimidazoarenes (AIAs) or thermic HAAs, e.g., 2-amino-3-methylimidazo[4,5-*f*]quinoline (IQ), 2-amino-3,7,8-trimethyl-3*H*-imidazo[4,5-*f*]quinoxaline (7,8-DiMeIQ<sub>x</sub>), etc. These HAAs originate from creatinine condensation with hexoses, pyrazine, and pyridine derivatives at 150-250 °C.

The other class is known as pyrolytic HAAs, e.g., 2-amino-1,4-dimethyl-5*H*-pyrido[4,3-*b*]indole (Trp-P-1), 2-amino-3-methyl-9*H*-pyrido[2,3-*b*]indole (MeAαC), etc. These HAAs are formed from the amino acid or protein pyrolysis at above 300 °C. The type of HAAs generated is highly dependent on several factors, vis., the meat type (fish, poultry, beef, lamb, pork, etc.), type of cooking (grilling, barbecuing, roasting, frying, broiling, smoking, etc.), cooking temperature, cooking duration, and pH.<sup>143</sup> Examples of HAAs are summarized in Scheme 1.3-3.

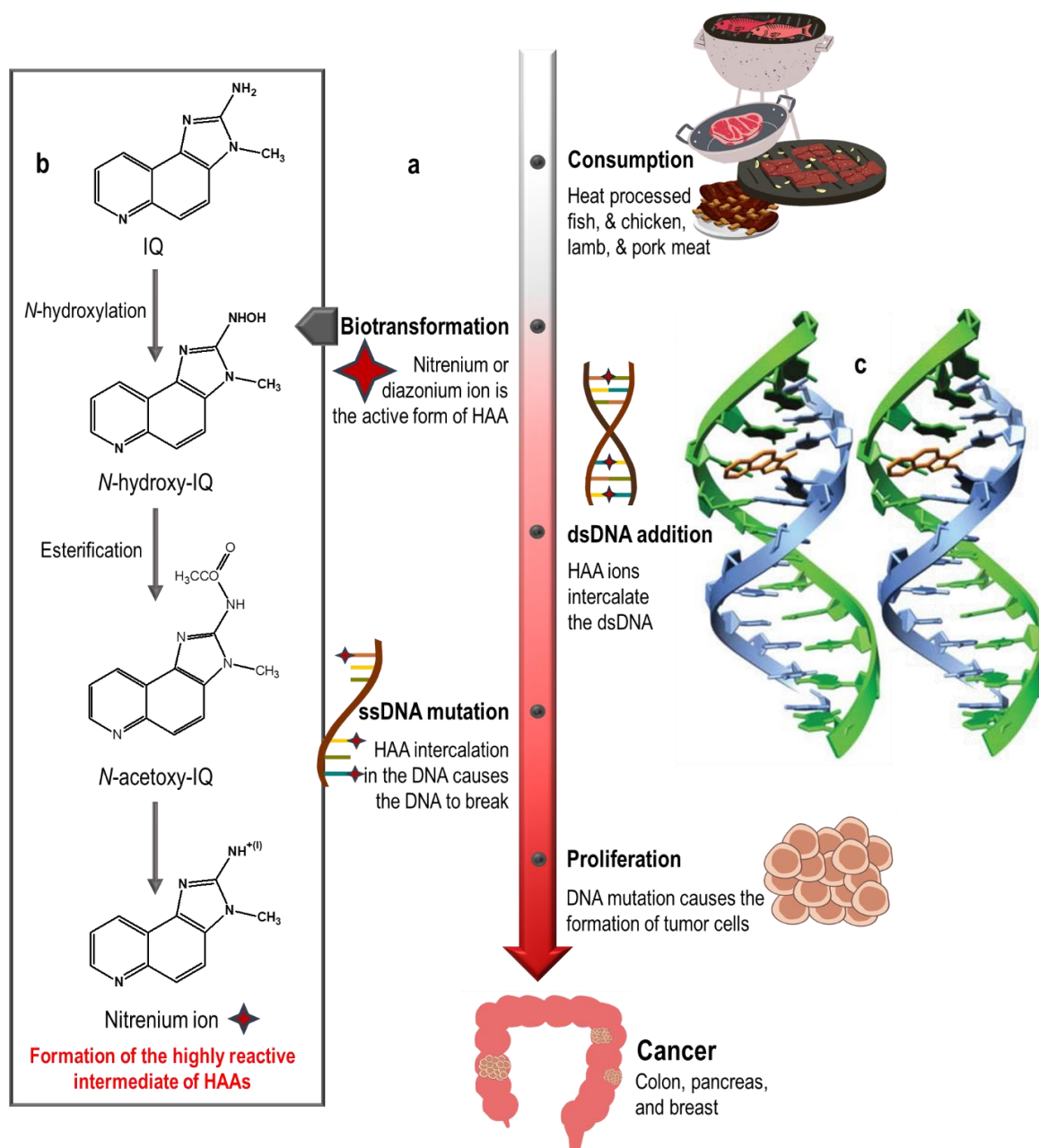
HAAs are not carcinogenic themselves. They undergo enzymatic transformations inside the organism (Scheme 1.3-4a).<sup>139,144</sup> HAAs biotransform to *N*-hydroxy-HAAs and then to highly

unstable *N*-acetyltransferases or sulfotransferases in extrahepatic tissues or liver (Scheme 1.3-4b).



**Scheme 1.3-3.** Structural formulas of HAAs, namely, 2-amino-3-methylimidazo[4,5-*f*]quinoline (**IQ**), 2-amino-3,8-dimethylimidazo [4,5-*f*]quinoxaline (**8-MeIQx**), 2-amino-3,4-dimethylimidazo[4,5-*f*]quinoline (**MeIQx**), 2-amino-4,8-trimethylimidazo[4,5-*f*]quinoxaline (**4,8-DiMeIQx**), 2-amino-3,7,8-trimethyl-3H-imidazo[4,5-*f*]quinoxaline (**7,8-DiMeIQx**), and 2-amino-1-methyl-6-phenylimidazo[4,5-*b*]pyridine (**PhIP**).

These HAAs' metabolites then biotransform into highly reactive nitrenium and diazonium ions, intercalating the double-stranded (ds) DNA (dsDNA) and covalently binding nucleobases (Scheme 1.3-4c).<sup>145,146</sup> Moreover, the resulting adduct structure is stabilized by a hydrogen bond with the oxygen atom of the 5'-phosphodiester linkage. The HAA intercalation results in nucleobase displacement in the dsDNA structure. The consequence of this displacement is the development of cancer diseases, i.e., colorectal, pancreatic, and breast cancers. Therefore, one should limit HAAs intake to 2 up to 25 ng/kg per day for precaution.



**Scheme 1.3-4.** Heterocyclic aromatic amine's (a) mechanism of action inside the human body [adapted from <sup>88</sup>] and (b) pathway of reactive intermediate formation [adapted from <sup>147,148</sup>]. (c) Intercalation of 2-amino-3-methylimidazo[4,5-f]quinoline (IQ) in the dsDNA.<sup>145</sup>

Clearly, HAAs are not beneficial to human health and, therefore, their intake must be regulated. However, determining HAAs in food matrices is difficult because of their low concentration. Different pre-concentration/isolation techniques combined with HPLC are currently being used to accomplish the challenging HAAs determination.<sup>149,150,151</sup> Unfortunately, the procedures are rather complex and time-consuming. Besides, fluorescence

spectroscopy was used for the determination of 2-amino-3,4,8-trimethyl-3H-imidazo[4,5-f]quinoxaline (4,8-DiMeIQx) with CDs.<sup>152,153</sup> However, the obtained results were pH-dependent, and in both reports, the detectability of the analytical system was insufficiently low. That is, the reported LOD<sup>152</sup> or limit of quantification (LOQ)<sup>153</sup> were very high, namely, equal to 1.3 and 0.36 mg L<sup>-1</sup>, respectively. Those values were far above the average concentration of HAAs in food.

Alternatively, an MIP-based chemosensor can be beneficial for HAAs determination as it offers simplicity and high sensitivity even in nano-concentration ranges. Frandsen et al. prepared to date the only MIP for HAAs (Scheme 1.3-5).<sup>154</sup> They devised an MIP for the SPE application that selectively extracted 2-amino-1-methyl-6-phenylimidazo[4,5-b]pyridine (PhIP). This MIP was prepared by free-radical polymerization using PhIP as the template, pentaerythritol tetra-acrylate, and 2-acrylamido-2-methyl propane sulfonic acid as functional monomers, and AIBN as the initiator. After bulk polymerization, the MIP block was ground to a fine powder, and the template was then extracted. This powder was used as the SPE column packing material, and the urine and feces samples of rodents spiked with PhIP were studied. After separation, the extracted samples were analyzed using HPLC, which showed a linear dose-response relationship in rats orally dosed with PhIP and the amount of 5-hydroxy-PhIP (a product of nitrenium ion) found in feces. So far, MIP electrochemical chemosensor for HAA determination is not reported to the best of our knowledge.

MIPs have successfully mimicked natural receptors and were applied to sensing devices as recognizing units for determining dsDNA.<sup>155</sup> Thus, MIPs capable of DNAs mimicking were also proposed.<sup>156,157</sup> Slinchenko et al. reported the first DNA-MIP to identify dsDNA of the verotoxin gene (Scheme 1.3-6).<sup>156</sup> The solution for MIP polymerization was prepared using the HEPES buffer solution containing verotoxin gene as the template, 2-vinyl-4,6-diamino-1,3,5-triazine (VDAT), and acrylamide as functional monomers, *N,N'*-methylenebisacrylamide (BIS) as the cross-linking monomer. The MIP solution was drop cast on a silanized glass, covered, then left at room temperature for 1 h. After template extraction from the deposited MIP thin film, the film identified functionalized dsDNA using fluorescence. This MIP was highly sensitive to the target verotoxin dsDNA. The MIP selectivity was tested with a non-target DNA with the ds structure and length similar to the target analyte.

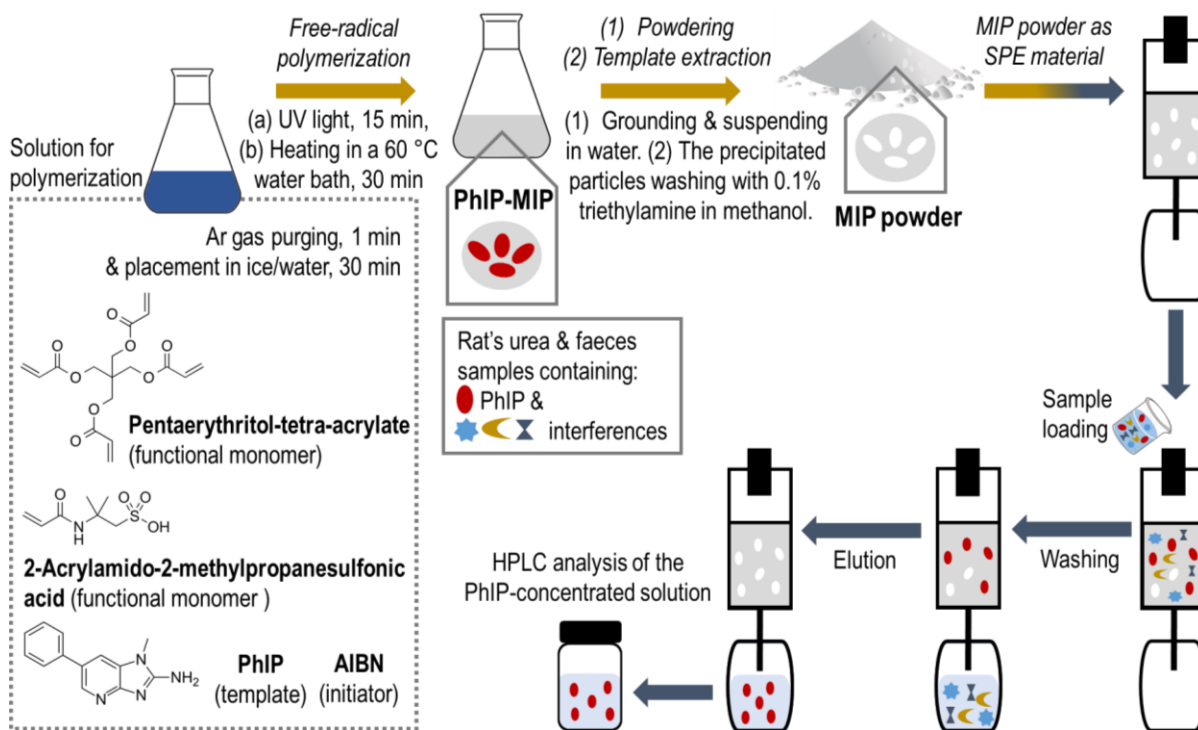
Unfortunately, this MIP discriminated against that interference, and the selectivity was relatively low.

Ogiso et al. reported MIP gel imprinted with a dsDNA of a specific sequence selected as the matrix for the gel electrophoresis (Scheme 1.3-7).<sup>157</sup> The pre-polymerization complex was prepared by self-assembly of the poly(deoxyadenylic acid)·poly(thymidylic acid) sodium salt template and the VDAT functional monomer in the HEPES buffer solution. Next, TEMED, acrylamide, and BIS were added to this solution and then polymerized in a glass tube. Subsequently, the dsDNA template was removed from the MIP gel by pre-running the electrophoresis. Then, the template-extracted MIP gel was used as the matrix to capture the dsDNA during the electrophoresis. The migration of the target dsDNAs was hindered by their strong interaction with the MIP cavities, which resulted in the target dsDNA separation from the sample mixture containing dsDNA chains with various lengths. Moreover, the MIP gel identified single-stranded (ss) and dsDNAs in the sample mixtures. Unfortunately, this gel did not differentiate adenine-thymine base pairs from thymine-adenine base pairs.

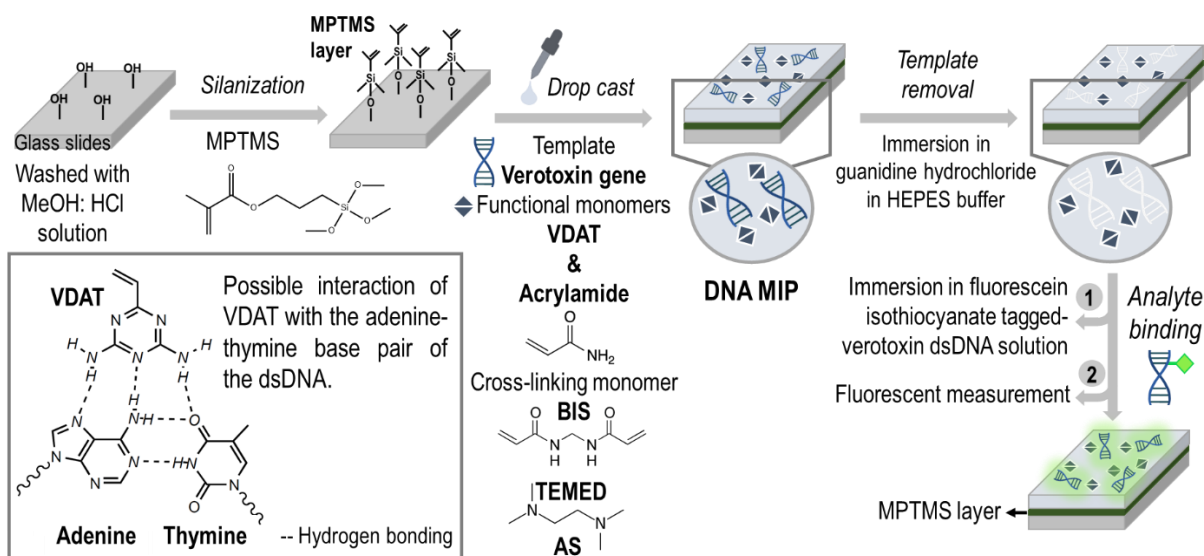
Moreover, DNA of a specific nucleotides' sequence imprinting on a polythiophene matrix (Scheme 1.3-8) was proposed by Bartold et al. from Kutner's group.<sup>158</sup> The ssDNA of a six-nucleotide sequence, namely, the TATAAA oligonucleotide (Scheme 1.3-9, 13), was imprinted in the polythiophene matrix using the thiophene based-functional monomers with adenine (Scheme 1.3-9, 15) and thymine (Scheme 1.3-9, 16) nucleobase moiety. The template, the thiophene-based functional, and cross-linking monomers (Scheme 1.3-9, 17) were allowed to self-assembly in solution. Subsequently, they were electropolymerized to form an MIP film on an electrode. The ssDNA-imprinted MIP was then subjected to template extraction, where the ssDNA-shaped cavities were formed. The resulting ssDNA-extracted MIP film-coated electrode was used to recognize the target ssDNA by Watson-Crick nucleobase pairing selectively. The selectivity of the ssDNA-extracted MIP electrode was examined under flow-injection analysis (FIA) conditions by capacitive impedimetry (CI) without any external redox probe. The MIP chemosensor was highly sensitive to the target dsDNA and discriminative against other interfering oligonucleotides of a sequence similar to the target ssDNA analyte within 2 min. The linear dynamic concentration range was 0.05 to 2.0  $\mu\text{M}$  ssDNA with the LOD as low as  $\sim 5$  nM ssDNA.

Furthermore, Huynh et al. from Kutner's group proposed an MIP bearing adenine functional monomer to determine 5-fluorouracil antitumor drug substance using the Watson-Crick-like interaction between adenine and uracil (Scheme 1.3-10).<sup>159</sup> The adenine-based functional monomer was allowed to self-assemble with the 5-fluorouracil target and a thiophene-based cross-linking monomer. The pre-polymerization complex solution was then used to deposit an MIP thin film on platinum and ITO electrodes and a gold glass slide by potentiodynamic electropolymerization. The 5-fluorouracil template was subsequently extracted from the MIP, and the imprinted cavities were exposed. Then, the 5-fluorouracil target drug was determined under the steady-state solution and FIA conditions using three different transductions, vis., DPV, CI, and piezoelectric microgravimetry. The chemosensors' LOD was 56 nM, 75 nM, and 0.26 mM, respectively, suitable for clinical 5-fluorouracil assays. The capacitive impedimetric chemosensor was more sensitive to the 5-fluorouracil target drug than its 5-fluorouridine metabolite and other interferences, including cytosine and thymine.

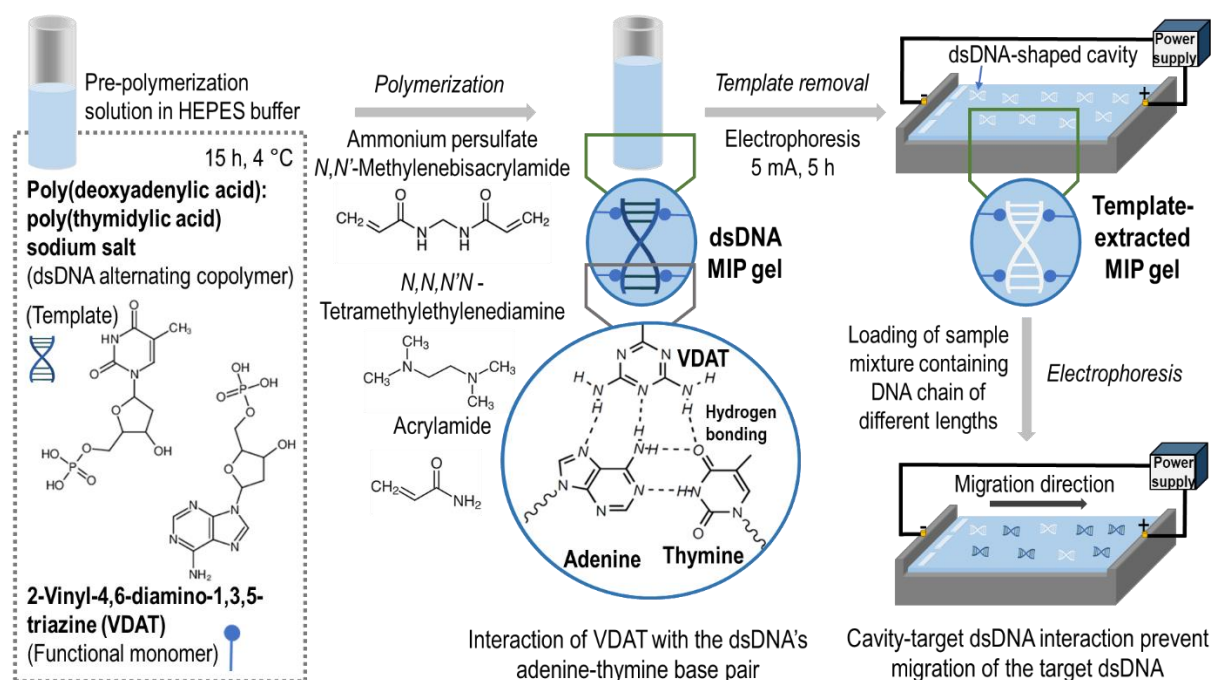
Other examples proposed by Kutner's group are MIPs with cytosine-substituted *bis*-bithiophenes, which were used for selective recognizing 6-neopterin<sup>160</sup> and 6-thioguanine.<sup>161</sup> All these analytes were recognized with MIPs only by hydrogen bonds. To our best knowledge, the dsDNA-mimicking MIP has not yet been applied for intercalating template molecules.



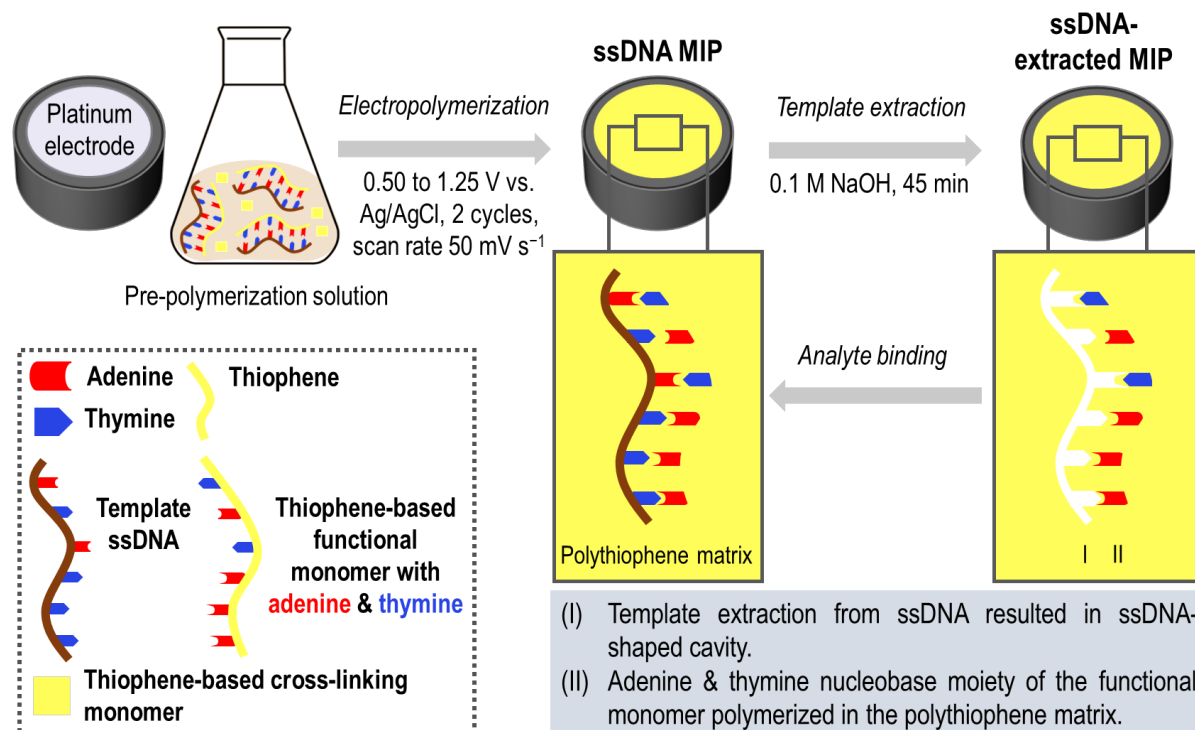
**Scheme 1.3-5.** The flowchart of synthesis of an MIP powder used as the solid phase extraction (SPE) material for selective determination of 2-amino-1-methyl-6-phenylimidazo[4,5-b]pyridine (PhIP) [adapted from <sup>145</sup>].



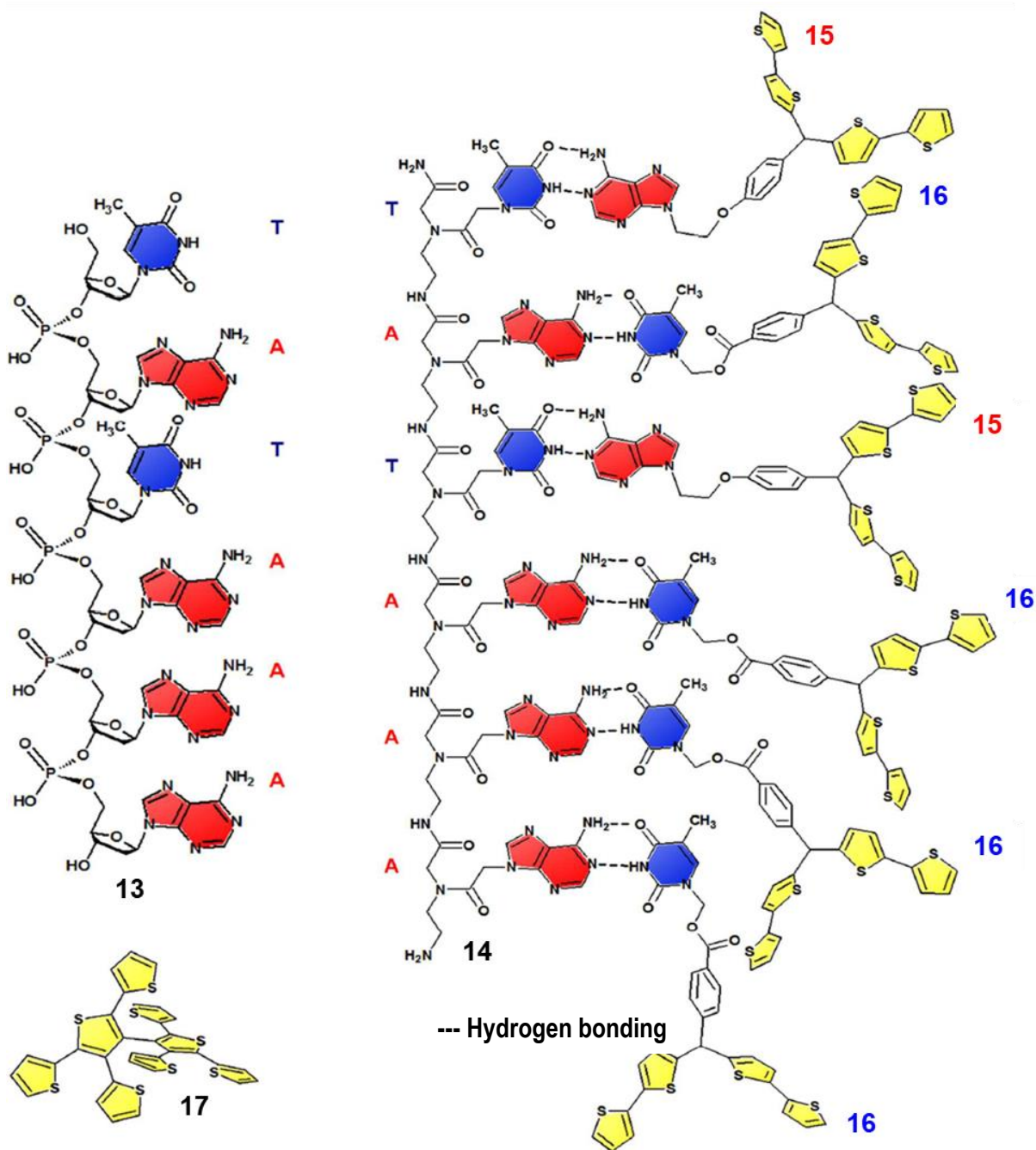
**Scheme 1.3-6.** The flowchart of dsDNA-templated MIP thin film deposition on 3-(trimethoxysilyl)propyl methacrylate (MPTMS) film-modified glass slide using the verotoxin gene template, the 2-vinyl-4,6-diamino-1,3,5-triazine (VDAT) and acrylamide functional monomers, *N,N'*-methylenebisacrylamide (BIS) cross-linking monomer, *N,N,N',N'*-tetramethylethylenediamine (TEMED) and ammonium persulphate (AS) [adapted from <sup>146</sup>].



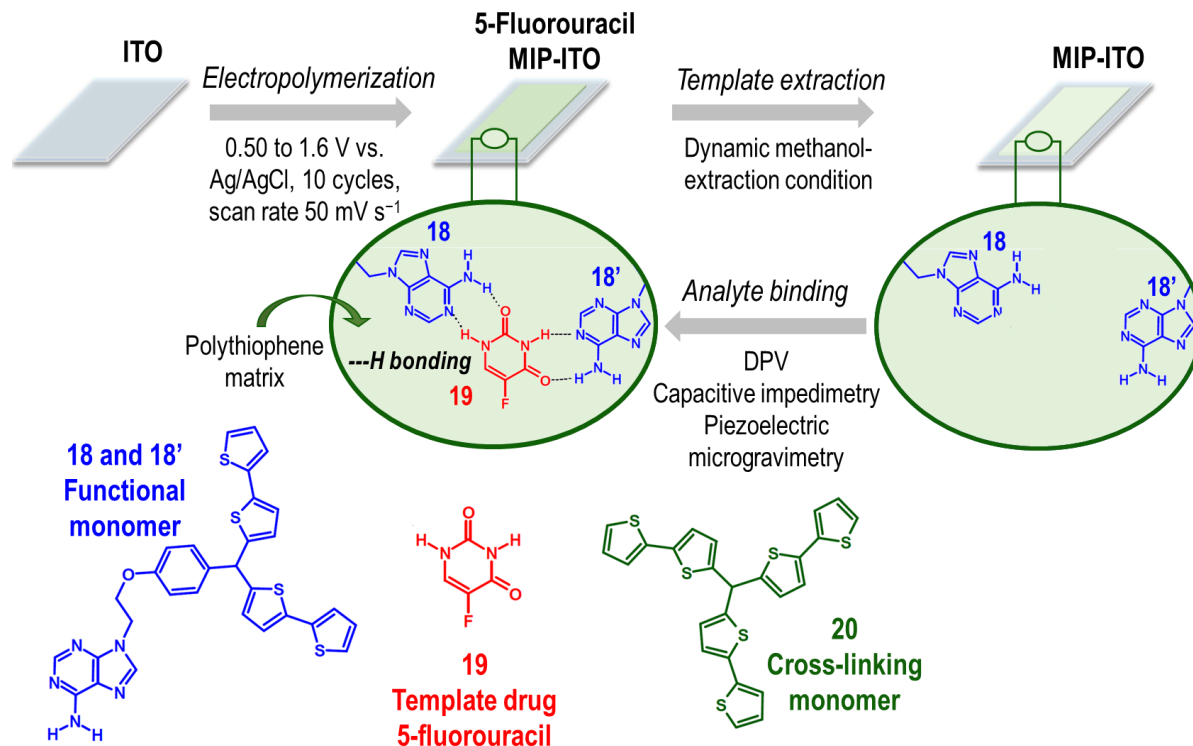
**Scheme 1.3-7.** The flowchart of the synthesis of the dsDNA-templated MIP gel and this gel application as the matrix for gel electrophoresis [adapted from <sup>148</sup>].



**Scheme 1.3-8.** The flowchart of ssDNA imprinting on a polythiophene matrix [adapted from <sup>149</sup>].



**Scheme 1.3-9.** Structural formulas of the TATAAAA oligonucleotide **13** template, peptide nucleic acid **14** (analog of the template with the same nucleobase sequence), thiophene-based functional monomers, namely, 4-bis(2,2'-bithien-5-yl)methylphenyl-2-adenine ethyl ether **15** and 4-bis(2,2'-bithien-5-yl)methylphenyl thymine-1-acetate **16** and the 2,4,5,2',4',5'-hexa(thiophene-2-yl)-3,3'-bithiophene **17** cross-linking monomer [adapted from <sup>149</sup>].



**Scheme 1.3-10.** The flowchart of deposition by potentiodynamic electropolymerization of a (5-fluorouracil)-templated MIP film on the ITO glass slide and structural formulas of the 4-[2-(6-amino-9H-purin-9-yl)ethoxy]phenyl-4-[bis(2,2'-bithienyl)methane] functional monomer **18** and **18'**, the 5-fluorouracil target drug **19** and the tris([2,2'-bithiophen]-5-yl)methane **20** cross-linking monomer [adapted from <sup>150</sup>].

## 1.4 Research objective

The demand for safe food increases with the increase of public awareness of potential food product toxicity and health risks. However, food toxicity monitoring is not easy. Significant amounts of financial expenditures are spent by government and private parties on research and analysis of food toxins and contaminants to keep high-quality standards of food products. The surge in the number and diversity of food pollutants has resulted in more stringent laws. Now, methods requiring expensive instruments, such as gas and liquid chromatographs, are utilized. Moreover, these methods require excessive chemicals, extensive experimental time, and experienced labor. Therefore, they are not convenient for in-field and on-spot practical applications. As a result, the demand for fast and cheap food analysis procedures has increased significantly. Researchers have extensively utilized chemosensors to fulfill this demand.

The objective of the current projects is to devise, fabricate, and test chemosensors of high selectivity against selected food toxins. For that purpose, films of MIPs were used as recognition units of the chemosensors. Two cancer-triggering food toxins, namely tyramine, and chosen HAA representative, were selected as target analytes to prepare MIP films on electrode surfaces to fulfill the objective of the thesis. A faster and low-cost sensing approach with simplified chemosensor preparation and measurement procedures and the possibility for these toxins determination in real samples were heavily weighed while designing our chemosensors.

The thesis is divided into five chapters. The present Chapter 1, entitled: "Literature review," describes the known electrochemical MIP chemosensors' preparation, construction, and application in the food safety and monitoring field.

Next is Chapter 2, "Experimental." It pronounces the chemicals and materials used, MIP and NIP film preparation procedures, and the signal transduction techniques applied.

Subsequent Chapter 3, "Electrochemical sensor for selective tyramine determination with a molecularly imprinted polymer film," is devoted to preparing the tyramine-templated MIP electrochemical chemosensor studied using the "gate effect" with the help of an external redox probe. Here, the influence of functional monomers on the performance of the MIP is discussed in length. Moreover, the tyramine-templated MIP is characterized by AFM, FTIR, SEM, and C/H/S/O elemental analysis, along with the results of MIP chemosensor application to tyramine determination in cheese samples.

Then, Chapter 4, "Selective impedimetric chemosensing of carcinogenic heterocyclic aromatic amine by dsDNA mimicking molecularly imprinted polymer film-coated electrodes," provides the method of label-free MIP chemosensor preparation using HAA as the template. The unique design of this chemosensor utilizes the ability of the HAA to intercalate double-stranded DNA. The influence of different transduction techniques on the MIP performance is discussed. Furthermore, the MIP is characterized using AFM, FTIR, SEM, and C/H/S/O elemental analysis, along with the results of MIP chemosensor application for HAA determining in pork samples.

Finally, Chapter 5, "Summary and future prospectives," compiles the thesis content, providing the most critical conclusions drawn based on the research accomplished and research prospectives.



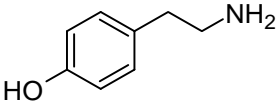
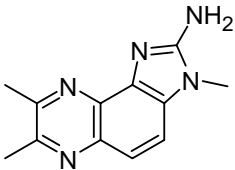
# Chapter 2

## Experimental

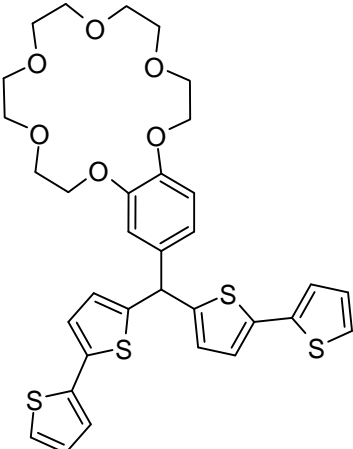
The present section describes the materials and chemicals, techniques, experimental procedures, and instruments used to prepare and characterize the MIP films.

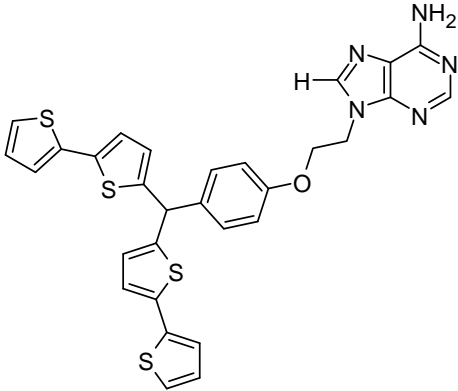
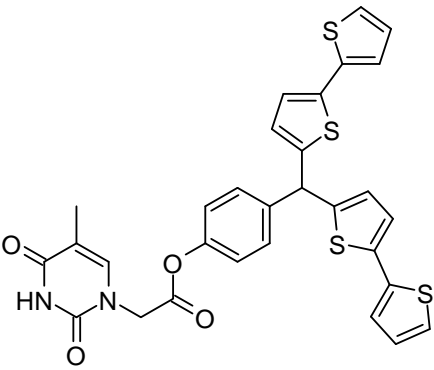
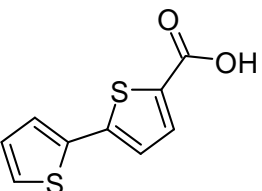
### 2.1 Material and chemicals

**Table 2.1-1.** Chemicals used as templates.

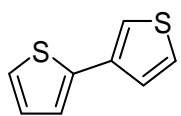
No.	Name, abbreviation, and function	Structural formula	Source
1	Tyramine		Sigma Aldrich
2	2-Amino-3,7,8-trimethyl-3 <i>H</i> -imidazo[4,5- <i>f</i> ]quinoxaline, 7,8-DiMeIQ <sub>x</sub>		Toronto Research Chemicals

**Table 2.1-2.** Chemicals used as functional monomers.

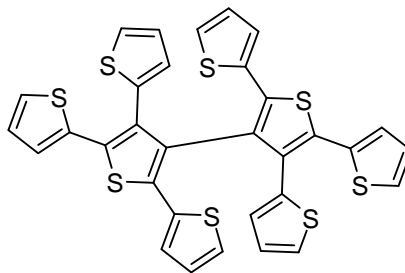
No.	Name, abbreviation, and function	Structural formula	Source
1	<i>Bis</i> (2,2'-bithienyl)-benzo-[18-crown-6] methane, FM2 Functional monomer for the tyramine chemosensor		Synthesized at the University of North Texas, Denton TX, USA

<p><b>2</b> 4-Bis(2,2'-bithien-5-yl)methylphenyl 2-adenine ethyl ether, ABT</p> <p>Functional monomer for the 7,8-DiMeIQx chemosensor</p>		<p>Synthesized at the University of North Texas, Denton TX, USA</p>
<p><b>3</b> 4-Bis(2,2'-bithien-5-yl)methylphenyl thymine-1-acetate, TBT</p> <p>Functional monomer for the 7,8-DiMeIQx chemosensor</p>		<p>Synthesized at the University of North Texas, Denton TX, USA</p>
<p><b>4</b> (5-Thiophen-2-yl)thiophene-2-carboxylate, FM1</p> <p>Functional monomer for the tyramine chemosensor</p>		<p>Sigma Aldrich</p>

**Table 2.1-3.** Chemicals used as cross-linking monomers.

No.	Name, abbreviation, and function	Structural formula	Source
1	2,3-Bithiophene Cross-linking monomer for the tyramine chemosensor		Sigma Aldrich

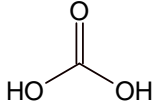
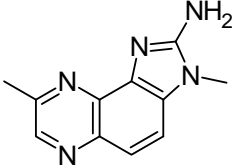
- 2 2,4,5,2',4',5'-  
Hexa(thiophene-2-yl)-3,3'-  
bithiophene, T8  
Cross-linking monomer for  
the 7,8-DiMeIQx  
chemosensor



Synthesized at the  
Università degli  
Studi  
dell'Insubria,  
Milan, Italy, and  
the Institute of  
Physical  
Chemistry, Polish  
Academy of  
Sciences, Warsaw,  
Poland.

**Table 2.1-4.** Chemicals used as interferences.

No.	Name, abbreviation, and function	Structural formula	Source
1	Adrenaline Interference for the tyramine chemosensor study		Sigma Aldrich
2	Creatinine Interference for the tyramine and 7,8-DiMeIQx chemosensor studies		Sigma Aldrich
3	D-Phenylalanine Interference for the tyramine chemosensor study		Sigma Aldrich
4	Glucose Interference for the tyramine and 7,8-DiMeIQx chemosensor studies		Sigma Aldrich
5	L-Tyrosine Interference for the tyramine chemosensor study		Sigma Aldrich
6	Tryptamine Interference for the tyramine chemosensor study		Sigma Aldrich

7	Urea Interference for the tyramine and 7,8-DiMeIQx chemosensor studies		Sigma Aldrich
8	2-Amino-3,8-dimethylimidazo[4,5-f]quinoxaline, 8-MeIQx Interference for the 7,8-DiMeIQx chemosensor studies		Toronto Research Chemicals

---

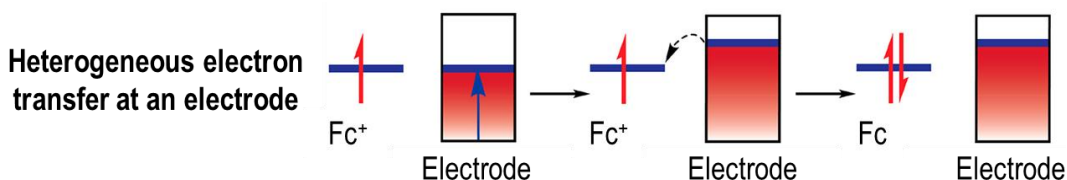
**Other chemicals used in the experiments are listed below.**

- Acetonitrile (sure seal), CH<sub>3</sub>CN – Sigma Aldrich
- Dimethyl sulfoxide (≥ 99%), DMSO – Sigma-Aldrich
- Disodium phosphate (analytical grade), Na<sub>2</sub>HPO<sub>4</sub> – POCH
- Isopropanol (analytical grade) – CHEMPUR
- Methanol (analytical grade), CH<sub>3</sub>OH – STANLAB
- Methanol (analytical grade), CH<sub>3</sub>OH – STANLAB
- Monopotassium phosphate (analytical grade), KH<sub>2</sub>PO<sub>4</sub> – POCH
- Potassium chloride (analytical grade), KCl – POCH
- Potassium fluoride (analytical grade, KF – Sigma Aldrich
- Potassium hexacyanoferrate(II), K<sub>4</sub>Fe(CN)<sub>6</sub> – CHEMPUR
- Potassium hexacyanoferrate(III), K<sub>3</sub>Fe(CN)<sub>6</sub> – Sigma-Aldrich
- Sodium chloride (analytical grade), NaCl – POCH
- Sodium hydroxide (analytical grade), NaOH – POCH
- Tetra-n-butylammonium perchlorate (electrochemical grade), (TBA)ClO<sub>4</sub> –Merck
- Toluene (sure seal) – Sigma Aldrich
- Triethylamine (≥ 99%), – Sigma-Aldrich

## 2.2 Techniques

### 2.2.1 Voltammetry fundamentals

In the simplest configuration, an electrode reaction is the heterogeneous charge transfer between an electroactive species in solution and the working electrode driven by an external power source, e.g., a potentiostat/galvanostat.<sup>162</sup> The electrode material can be an electric conductor or semiconductor. The energy level of the electrons in the electrode is controlled through the potential applied. Hence, an electron from the electrode is transferred to the electroactive species when the energy of the electrons in the electrode is higher than the lowest unoccupied molecular orbital (LUMO) of an electroactive species and vice versa (Scheme 2.2-1). Current resulting from the oxidation or reduction of the redox species, i.e., the faradic current, is limited by factors such as the rate of mass transport of the electroactive species to the electrode or the rate of the charge transfer between the electrode and the redox species. A redox system is categorized as reversible or irreversible depending on the relative charge transfer kinetics. If the charge transfer is faster than the mass transport, the system's equilibrium is often re-established, resulting in a reversible process. On the other hand, the transfer of an electron slower than the mass transport results in an irreversible system.



**Scheme 2.2-1.** The energy difference between the LUMO of the ferrocenium,  $\text{Fc}^+$ , and the electrode, controlled by an applied potential, causes heterogeneous reduction of  $\text{Fc}^+$  to ferrocene,  $\text{Fc}$ .<sup>162</sup>

A voltammetric technique is a primary tool to understand the current-potential relationship as the current is measured by linearly varying potential with time. The behavior of the electroactive species upon potential stimulation can be described by the Nernst and Butler-Volmer equations and Fick's laws.<sup>163</sup> Nernst equation (Equation 2.2-1) describes the relationship between the applied potential and the concentration of the electroactive species in its oxidized,  $c_{\text{Red}}$ , and reduced,  $c_{\text{Ox}}$ , form for a reversible system.

$$E = E^0 - \frac{RT}{nF} \ln \frac{c_{\text{Red}}}{c_{\text{Ox}}} \quad [\text{Equation 2.2-1}]$$

where  $E$  is the electrode potential in V,  $E^0$  is the standard redox potential for the electroactive species in V,  $R$  is the ideal molar gas constant,  $8.3144 \text{ J mol}^{-1} \text{ K}^{-1}$ ,  $T$  is the absolute temperature in K,  $n$  is the number of electrons participating in the redox reaction, and  $F$  is the Faraday constant,  $96485 \text{ C/mol}$ . The  $\frac{c_{\text{Red}}}{c_{\text{Ox}}}$  ratio changes with the applied potential to satisfy Equation 2.2-1. For instance, if a negative potential is applied, the redox species is reduced, resulting in a larger ratio and vice versa. The Butler-Volmer equation (Equation 2.2-2) generally defines the relationship between current, potential, and concentration.

$$\frac{i}{nFA} = k^0 \{c_{\text{Ox}} \exp[-\alpha\theta] - c_{\text{Red}} \exp[(1 - \alpha)\theta]\} \quad [\text{Equation 2.2-2}]$$

Where  $\theta = \frac{nF(E-E^0)}{RT}$ ,  $k^0$  is the heterogeneous standard rate constant,  $\alpha$  is the charge transfer coefficient, and  $A$  is the electrode area.

In electrochemistry, the first Fick's law (Equation 2.2-3) relates the current (referred to as the faradic current) resulting from the electrode activity of the electroactive species to their flux at the electrode-solution interface. The second Fick's law (Equation 2.2-4) correlates concentration changes of the oxidized or reduced species with time at a certain distance from the electrode surface.

$$J = -D \frac{dc}{dx}, \text{ the Fick's first law} \quad [\text{Equation 2.2-3}]$$

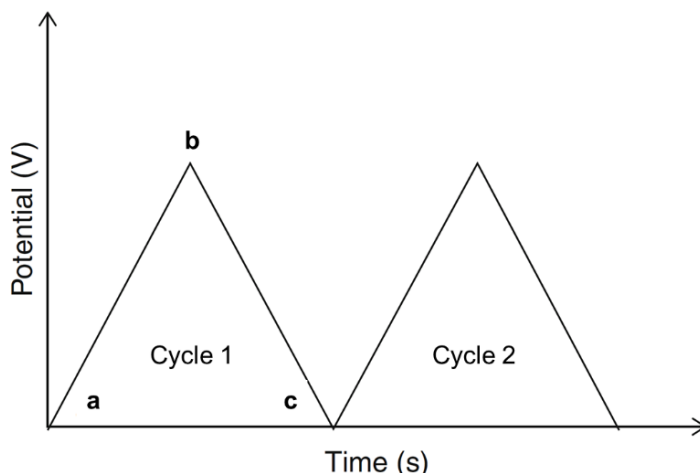
$$\frac{dc}{dt} = D \frac{d^2c}{dx^2}, \text{ the Fick's second law} \quad [\text{Equation 2.2-4}]$$

In these equations,  $J$  is the diffusional flux of the species,  $D$  is its diffusion coefficient,  $x$  is the distance from the electrode surface, and  $t$  is time. Typically, the generated current directly depends on the flux of the electroactive species to or from the electrode surface. A concentration gradient is generated when more oxidized or reduced species are produced at the electrode surface. Thus, the diffusion is promoted between the electrode surface and the solution bulk.<sup>164</sup> Moreover, the redox species adsorption on the electrode surface often contributes to this concentration gradient. Nevertheless, the concentration gradient at the solution bulk and electrode surface is responsible for the redox species diffusion, thus strongly influencing the resulting current.

### 2.2.2 Cyclic voltammetry (CV)

In MIP studies, current-potential experiments are used for two purposes, i.e., (i) electropolymerization under potentiodynamic conditions of the pre-polymerization complex in the presence of a cross-linking monomer and (ii) the CV qualitative analysis of electrochemical reactions over a polymer film-coated electrode, independently or combined with other techniques. CV measurements provide crucial information, including the redox potential of the couple, electrochemical reaction mechanism and kinetics, and other chemical reactions associated with electrode processes, e.g., electrocatalytic activity.<sup>165</sup>

A linear triangle potential ramp is provided as an excitation signal for CV measurement. Then the potential is scanned between the lower and the upper potential limits. First, the starting potential is applied (point a in Scheme 2.2-2). It is then linearly ramped positively or negatively until it reaches the preselected final potential (point b in Scheme 2.2-2). At point b, the applied potential is sufficient to oxidize or reduce the electroactive species. The potential scan is then switched at point b and scanned back to point c. The CV excitation signal is an isosceles triangle whose slope describes the potential scan rate.



**Scheme 2.2-2.** The excitation signal of the CV experiment where (a) is the starting potential, (b) is the potential extremum (also known as switching potential) where the redox process of the electroactive species occurs, and (c) is the point where the potential is scanned back to its starting value.<sup>166</sup>

A typical cyclic voltammogram for a reversible electrode process of an electroactive species present in the solution is the current-potential curve shown in Scheme 2.2-3. In this

scheme, the potential scanning starts then proceeds towards positive potentials. The oxidation occurs from A, the starting potential, to C, the switching potential, which results in an anodic peak current,  $i_{pa}$ . The anodic current increases with the potential from A to B as more substrate molecules are oxidized. When all the substrate at the working electrode surface oxidizes, the anodic peak of the  $E_{pa}$  potential is developed. Thus, from B to C, the current decreases due to the diffusion layer thickness increase. At point C, the potential scan is switched back to negative potentials. Here, the reduction is dominant from C to A, resulting in the cathodic peak. Complete depletion of the oxidized species during the negative scan results in a peak denoted as D in Scheme 2.2-3. That is the cathodic peak of the  $E_{pc}$  potential. This cycle can be repeated multiple times.

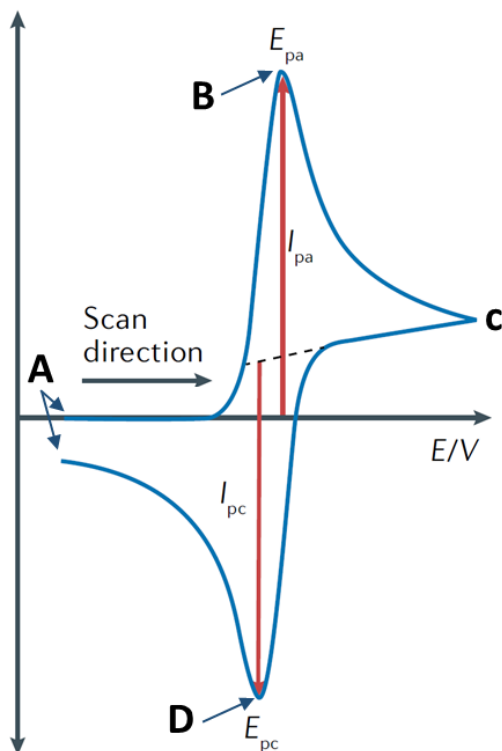
The following equations describe the potential ramp of a CV experiment.<sup>167</sup>

$$E = E_i + vt, \text{ for a positive scan} \quad [\text{Equation 2.2-5}]$$

$$E = E_s - vt, \text{ for a negative scan} \quad [\text{Equation 2.2-6}]$$

where  $E$  is the electrode potential,  $E_i$  is the initial point,  $E_s$  is the potential at the switching point,  $v$  is the potential scan rate, and  $t$  is the time.

The scan rate is a crucial parameter in CV measurement. It elucidates the speed at which the potential is linearly varied with time. Hence, it controls the duration of the experiment. The range of typical scan rates applied for an analytical electrode, i.e., 1- or 2-mm diameter disk electrode, is 1 – 1000 mV s<sup>-1</sup>.<sup>168</sup> By altering the scan rate, the kinetics of an electrochemical reaction of the electroactive species can be investigated. Other factors influencing CV measurement are the transport of the electroactive species to the electrode surface and the electron transfer.<sup>169</sup> The characteristics of CV curves for reversible, irreversible, and quasi-reversible electrode reactions are well defined.



**Scheme 2.2-3.** A CV current-potential curve for a reversible electrode process of an electroactive species.  $E_{pa}$  and  $E_{pc}$  stand for the anodic and cathodic peak potential, respectively, while  $i_{pa}$  and  $i_{pc}$  are the respective anodic and cathodic peak currents.<sup>170</sup>

First, the peak-to-peak potential separation ( $\Delta E_p$ ) provides information about the relative diffusion rate of the redox analyte. For a reversible system, the  $\Delta E_p$  and its relation to the Nernst equation at 25 °C for all scan rates is given by Equation 2.2-7 below. The  $\Delta E_p$  for a quasi-reversible system is higher than Equation 2.2-7 predicts. Then, the  $\Delta E_p$  for an irreversible system is even higher. Only one peak, either anodic or cathodic, is often seen during the CV experiment for an irreversible system.

$$\Delta E_p = E_{pa} - E_{pc} = \frac{0.0565}{n} \quad \text{[Equation 2.2-7]}$$

where  $n$  is the number of electrons participating in the redox reaction.

The anodic-to-cathodic peak ratio reveals the nature of the system, i.e., reversible, irreversible, or quasi-reversible. In the case of a reversible system, this ratio is  $\sim 1$  for all scan rates (Equation 2.2-8). That means that the  $i_{pa}$  and  $i_{pc}$  values are nearly equal. For a quasi-reversible and irreversible system, this ratio differs from 1.

$$\frac{i_{pa}}{i_{pc}} = 1 \quad \text{[Equation 2.2-8]}$$

Finally, the peak current,  $i_p$ , of a reversible process is described by the Randles-Ševčík equation (Equation 2.2-9). This equation relates the  $i_p$  to the concentration of the electroactive species at the working electrode surface and the square root of the potential scan rate.

$$i_p = 2.72 \times 10^5 n^{2/3} D^{1/2} A v^{1/2} c \quad \text{[Equation 2.2-9]}$$

Here,  $n$  is the number of electrons participating in the redox reaction,  $A$  is the electrode surface area in  $\text{cm}^2$ ,  $D$  is the diffusion coefficient of the electroactive species in  $\text{cm}^2/\text{s}$ ,  $v$  is the scan rate in  $\text{V/s}$ , and  $c$  is the concentration of the electroactive species in the solution bulk.

The peak increases with the scan rate increase (Figure 2.2-4a) because the diffusion layer thickness decreases; hence the concentration gradient increases. As a result, the flux of the redox species to the electrode increases. The Randles-Ševčík equation predicts that the peak is proportional to the concentration of the redox species ( $i_p \propto c$ ). The linear relationship of  $i_p$  and  $v^{1/2}$ , predicted by Equation 2.2-9, is illustrated by the Randles-Ševčík plot (Figure 2.2-4b). A non-linear  $i_p$  dependence on  $v^{1/2}$  plot suggests that the system is quasi-reversible or a surface redox process is involved.

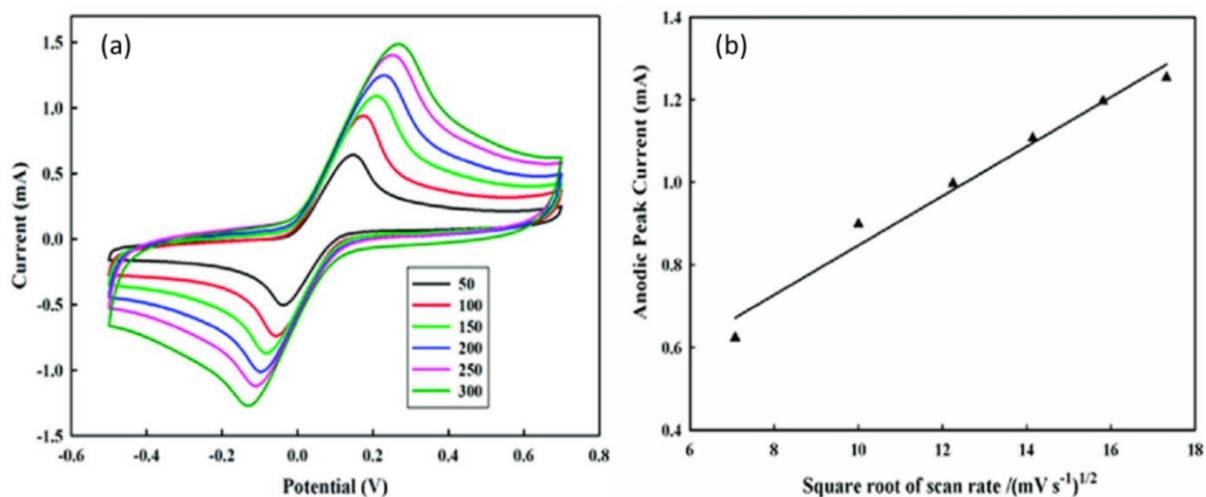


**Figure 2.2-4.** (a) The scan rate effect on CV curves recorded at the poly(3,4-ethylenedioxythiophene) film-coated pencil lead electrode for the determination of 6 mM hydroquinone in 100 mM PBS (pH = 7.4), and (b) the Randles-Ševčík plot.<sup>171</sup>

### 2.2.3 Differential pulse voltammetry (DPV)

A potential applied to the electrode promotes the charge exchange between the electroactive species and the electrode. Simultaneously, it also charges or discharges the electrical double layer (EDL) formed at the electrode-electrolyte solution interface.<sup>172</sup> That charging or discharging generates the undesired capacitive current flow. Unlike rapid scanning CV, which introduces a sizeable capacitive current in the background, DPV can discriminate against it. The pulse voltammetry technique relies on the difference in the decay rate of the capacitive and the faradaic currents following a potential step (pulse).<sup>173</sup> For a diffusion-controlled reaction, the faradic current decays according to the Cottrell equation with  $\frac{1}{t^{1/2}}$  while the capacity current decays exponentially. Thus, the capacitive current decays considerably faster than the faradic current. Therefore, only the faradic current is measured by sampling the current at the end of the potential pulses applied.

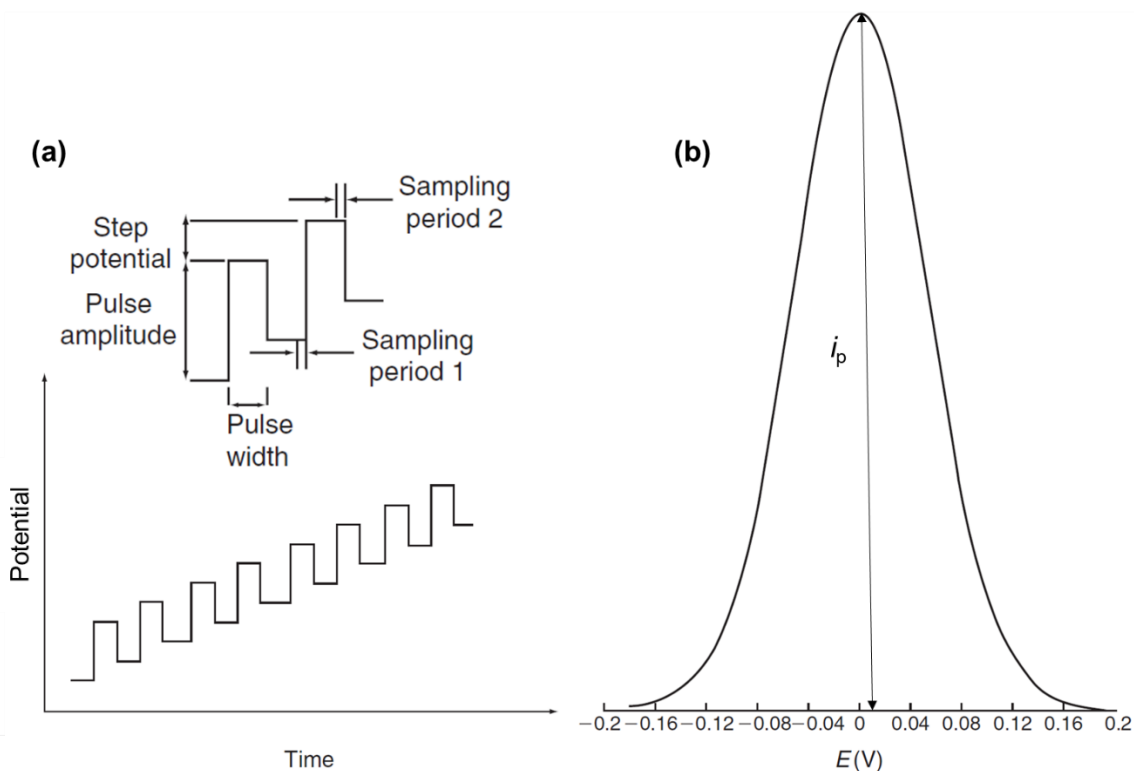
In the DPV waveform, small pulses of constant amplitude (10-100 mV) are periodically superimposed on the linear potential ramp.<sup>174</sup> The current is then measured twice for each cycle during each pulse (Scheme 2.2-5a). Typically, the current is sampled just before the pulse application and at the pulse end. The difference in currents sampled for each pulse,  $\Delta I$ , is plotted against the potential applied (Scheme 2.2-5b). The resultant peak-shaped voltammogram reveals information about the redox activities of the electroactive species at the working electrode. Thus, the peak current,  $I_p$ , is directly proportional to the concentration of the electroactive species in the solution bulk, as predicted by the Osteryoung-Parry equation.<sup>175</sup>

$$I_p = \frac{nFA}{4RT} \left( \frac{D_{\text{Red}}}{\pi t_p} \right)^{1/2} C_{\text{Red}} \Delta E_p \quad \text{[Equation 2.2-10]}$$

In the above equation,  $\Delta E_p$  is the pulse amplitude (potential pulse height) and  $t_p$  is the pulse width (potential pulse duration). Both  $\Delta E_p$  and  $t_p$  are essential parameters in the DPV technique. Higher  $\Delta E_p$  causes the peak to be broader. Moreover, the inhibited diffusion of the electroactive species to the electrode surface can be seen in the DPV measurement if the increase of the electroactive species concentration at a constant  $\Delta E_p$  increases the  $t_p$ .

The peak potential,  $E_p$ , can be calculated using Equation 2.2-1, 1 below.

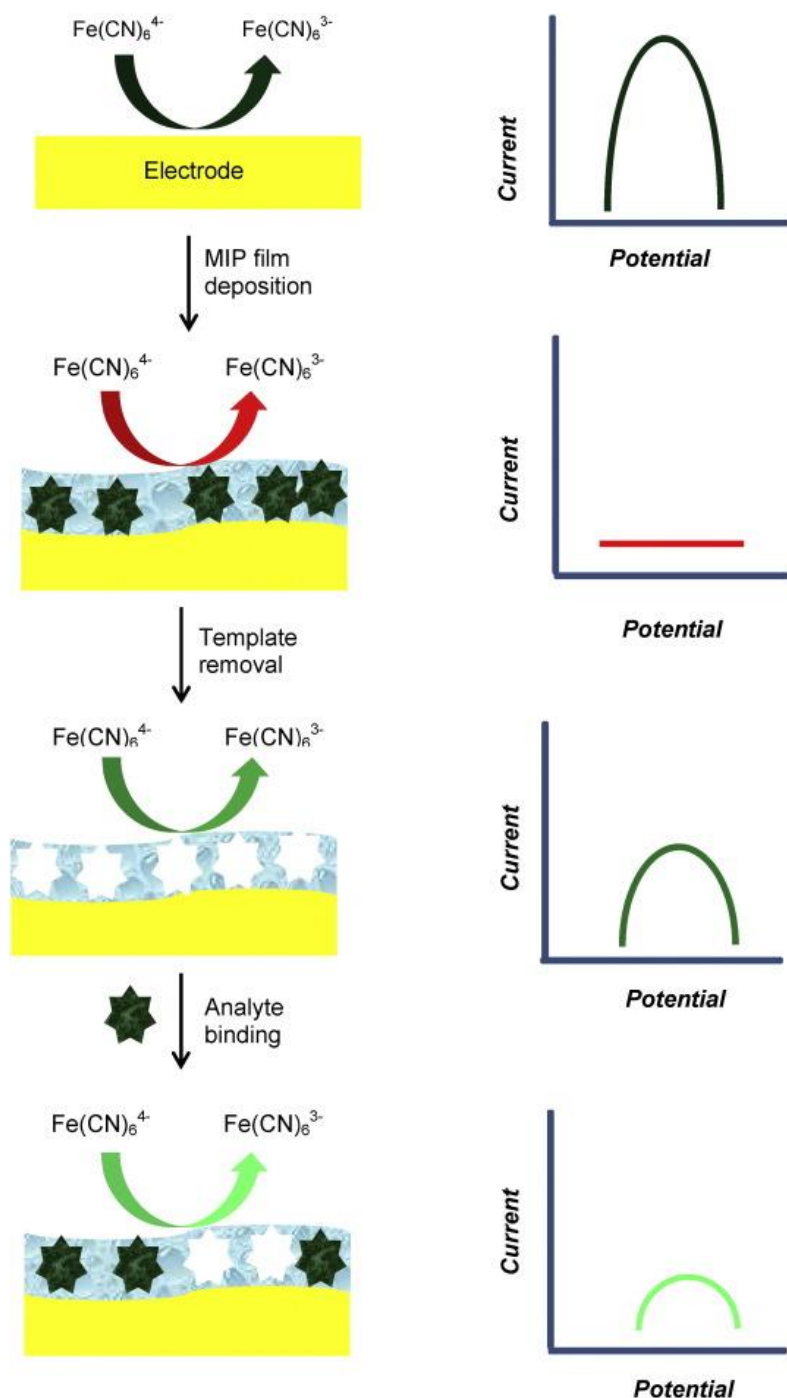
$$E_p = E_{p/2} - \frac{\Delta E_p}{2} \quad \text{[Equation 2.2-11]}$$



**Scheme 2.2-5.** The differential pulse voltammetry (DPV) (a) potential waveform and (b) voltammogram.<sup>172</sup>

The DPV technique enhances the sensitivity and selectivity of the measurement; consequently, the analyte concentration as low as  $10^{-8}$  M can be detected. Thus, in DPV, a lower LOD can be achieved than in CV. In MIP studies, DPV serves as a quantitative tool for confirming template imprinting and then extracting. Moreover, it is applied for electroinactive analyte determination using the so-called "gate effect" (Scheme 2.2-6).

The "gate effect" increases or decreases faradic currents resulting from the oxidation or reduction of a redox probe as the MIP film binds to the target analyte. The resulting faradic current depends upon MIP film permeability changes for the redox probe when the analyte binds to the MIP cavity. Therefore, the "gate effect" is used for signal transduction in the DPV measurements.



**Scheme 2.3-6.** The DPV measurement on an uncoated and MIP film-coated Pt electrode. The oxidation-reduction of  $[\text{Fe(CN)}_6]^{3-/4-}$  redox probe on the electrode surface. This process results in a well-defined DPV peak. Upon MIP film coating of the electrode surface, the charge transfer of the redox probe is hindered; thus, there is no DPV response. Then, the template is removed from the MIP film, allowing the redox probe diffusion to result in a DPV peak. However, the binding of the analyte to the empty cavities partially blocks this diffusion; hence, the DPV peak is lower.<sup>176</sup>

#### 2.2.4 Electrochemical impedance spectroscopy (EIS)

In an electric circuit, the measure of the opposition to the current flow is known as resistance. As defined by Ohm's law (Equation 2.2-12), resistance is the ratio of voltage to current. A resistor obeying Ohm's law for all currents and voltages and independent of frequency is ideal. The current response of an ideal resistor to the applied ac voltage is sinusoidal at the same phase. The electrochemical reaction at the electrode-electrolyte is complex and has additional components that the traditional Ohm's law does not describe. Therefore, impedance is used to describe a complex system instead. Impedance is the measure of total opposition to the electric current in a circuit, taking into account the contribution of resistors, capacitors, and inductors.<sup>177</sup>

$$r = \frac{V}{I}, \text{ for an ideal resistor} \quad [\text{Equation 2.2-12}]$$

Typically, the electrochemical impedance is measured by applying constant ac voltage with a small amplitude over a pre-determined frequency range to an electrochemical cell. As a result, the current flowing through the cell is measured. The applied ac voltage, expressed as a function of time, is described by Equation 2.2-13.<sup>178</sup>

$$E(t) = E_0 \sin(\omega t) \quad [\text{Equation 2.2-13}]$$

Here,  $E(t)$  is the potential at time  $t$ ,  $E_0$  is the potential amplitude,  $\omega = 2\pi f$  is the radial frequency, and  $t$  is time. Applying a small-amplitude ac signal, e.g., 10 mV, causes the cell's response to be linear or pseudo linear. For such a system, the sinusoidal current response to an applied ac voltage has the same frequency as the input signal; however, it is shifted in phase (Scheme 2.3-7a), as described by Equation 2.2-14.

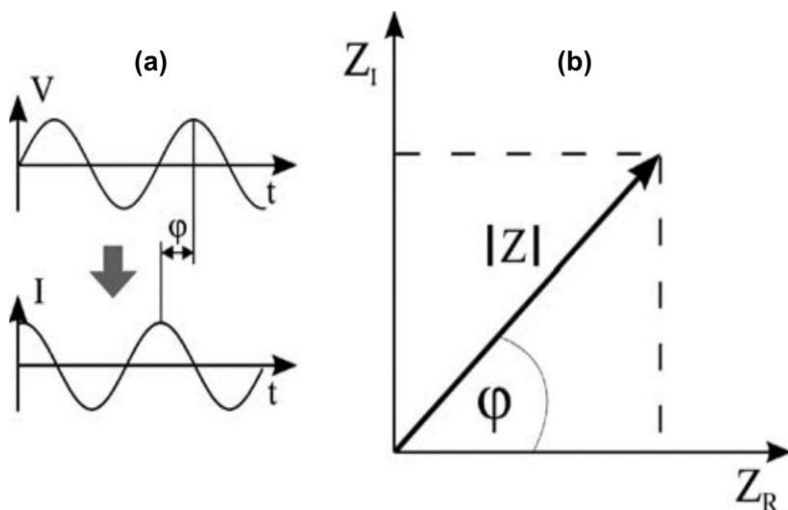
$$i(t) = i \sin(\omega t + \varphi) \quad [\text{Equation 2.2-14}]$$

where  $i(t)$  is the current at time  $t$ ,  $i_0$  is the current amplitude,  $\varphi$  is the phase angle difference between the potential and current. In an electrochemical cell, the capacitive and the resistive effects are responsible for the phase shift.

The frequency-dependent impedance,  $Z(\omega)$  of a system, is expressed by Equation 2.2-15.

$$Z(\omega) = \frac{E(t)}{I(t)} = |Z| \exp(j\varphi) = Z_R + j Z_I \quad [\text{Equation 2.2-15}]$$

where  $|Z|$  is the absolute magnitude of the impedance,  $j = \sqrt{-1}$  is the imaginary number, and  $Z_R$  and  $Z_I$  is the real and imaginary impedance components, respectively. Impedance is a vector quantity expressed either in Cartesian or polar coordinates. Scheme 2.2-7b shows impedance in Cartesian coordinates, revealing resistance as the real component. The sum of capacitance and inductance are often denoted as the imaginary part of the impedance.



**Scheme 2.2-7.** (a) The sinusoidal voltage-time and current-time responses, and (b) impedance expressed in Cartesian coordinates where  $|Z|$  is the absolute magnitude of the impedance,  $\phi$  is the phase angle,  $Z_R$  and  $Z_I$  is the real and imaginary component of impedance, respectively.<sup>179</sup>

Four critical parameters govern the impedance of an electrochemical system. The first is the charge-transfer resistance revealing the electrochemical reaction rates, described by Equation 2.2-16. Any surface modification that results in electrode blockages, such as adsorption and film formation, affects the charge-transfer resistance. Therefore, the charge-transfer resistance is of great interest in MIP studies as it is used to investigate the analyte-cavity interaction and polymer film deposition on an electrode surface

$$R_{ct} = \frac{nF}{RTJ_0} \quad \text{[Equation 2.2-16]}$$

where  $J_0$  is the exchange current density.

The second parameter is the solution resistance (ohmic resistance) between the working and reference electrodes, often compensated by the three-electrode potentiostat system. Generally, an accurate charge-transfer resistance value is obtained by subtracting the solution resistance. Solution resistance depends on several factors, namely, the type and concentration

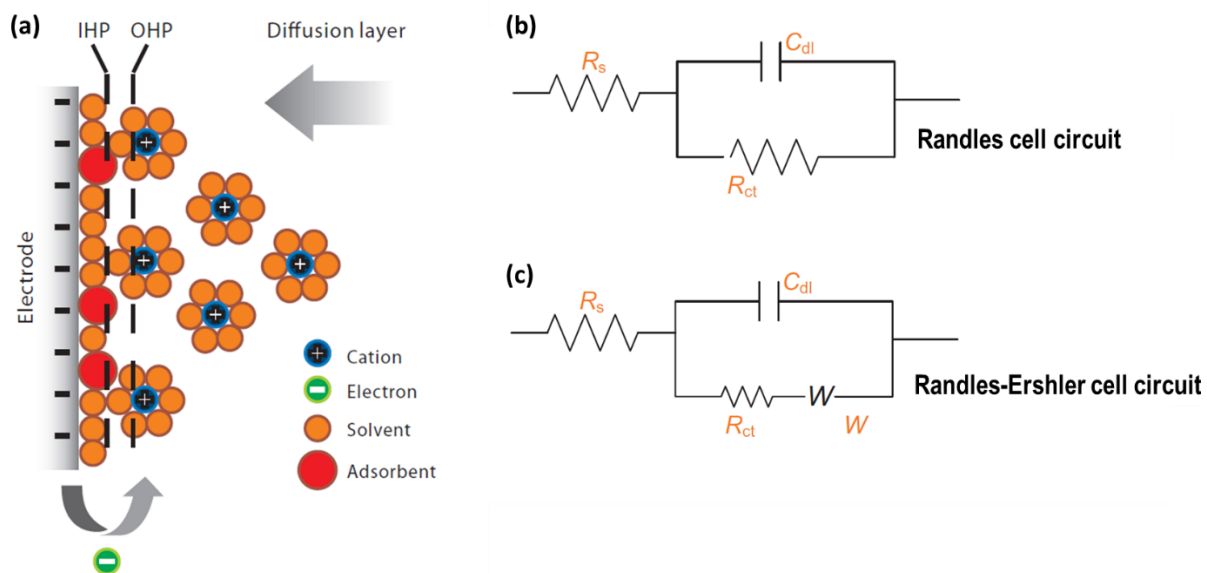
of ions and temperature. Both the charge transfer and solution resistance arise from a faradic current flow.

The third parameter is the electric double-layer capacity,  $C_{dl}$ . An electrode-electrolyte solution interface behaves as a thin flat-parallel capacitor when the electrode and the counter ions adjacent to it are oppositely charged (Scheme 2.2-8a). This resistance arises from the non-faradic current flow. Therefore, the  $C_{dl}$  can be calculated from its relationship to the imaginary impedance component at low frequency, described by Equation 2.2-17. The  $C_{dl}$  provides information on the adsorption and desorption of the chemical species on an electrode surface when measured in the absence of the redox species. It depends on the electrode surface area and ion size. (Redox probe)-free sensors often use capacitance measurement as an analytical signal. However, the capacitance measurements in some systems may not represent the  $C_{dl}$ . Instead, it imparts information such as film thickness or the surface integrity of an organic coating.

$$Z_I = \frac{1}{\omega A C_{dl}} \quad \text{[Equation 2.2-17]}$$

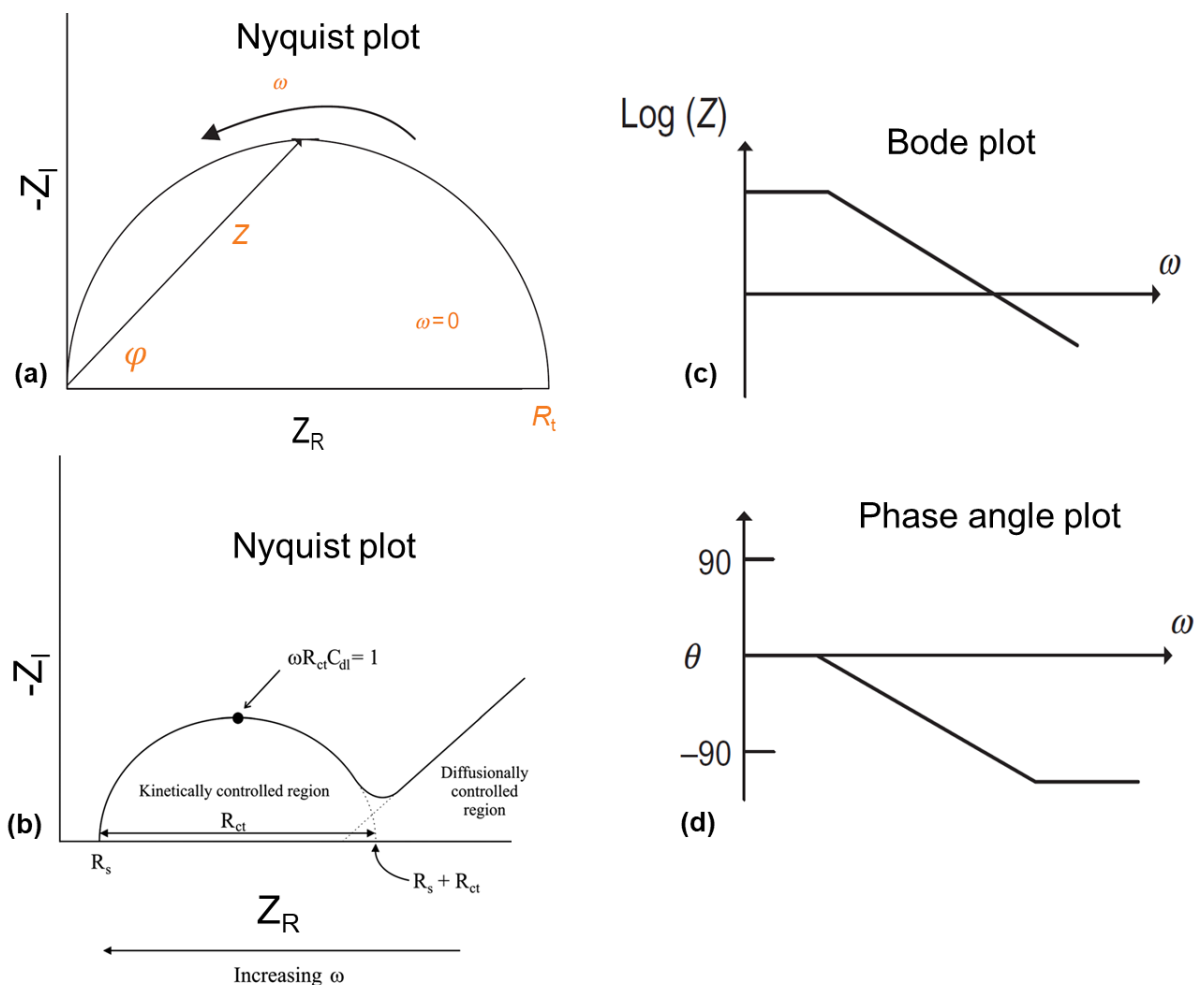
In this equation,  $A$  is the electrode surface area.

The fourth parameter is the Warburg impedance. It accounts for the mass transport of the ions (also referred to as diffusion control) at the electrode surface. A Randles-Ershler equivalent electric circuit comprises these four parameters impart critical information about the electrical properties of the system (Scheme 2.2-8c).



**Scheme 2.2-8.** (a) Formation of the electric double layer at the interface of a negatively charged electrode and the Helmholtz double-layer (IHP - inner Helmholtz plane and OHP - outer Helmholtz plane) and (b) the Randles simple equivalent electric circuit omitting the contribution of the diffusion, and (c) the Randles-Ershler equivalent electric circuit of an electrochemical cell comprising four important impedance parameters, where  $R_s$  is the solution resistance,  $C_{dl}$  is the electric double-layer capacitance,  $R_{ct}$  is the charge transfer resistance, and  $Z_w$  is the Warburg impedance.<sup>178,180</sup>

Nyquist and Bode's plots are two typical graphs used in data analysis of EIS measurements. The imaginary impedance component plotted against the real impedance component is the Nyquist plot (Scheme 2.2-9a and 2.2-9b). The measurement is initiated at a low-frequency region (on the right-hand side) and is terminated at a high-frequency region (on the left-hand side). Each data point in the Nyquist plot is a measurement of impedance at a given frequency. However, the frequency responses are not available in Nyquist plots. Instead, the Bode plot is employed to obtain the frequency-related information. In the Bode plot, the impedance or its logarithm (Scheme 2.2-9c) or the phase angle (Scheme 2.2-9d) is presented as a function of frequency. A logarithmic scale is particularly beneficial if plotting functions that change by several orders of magnitude.



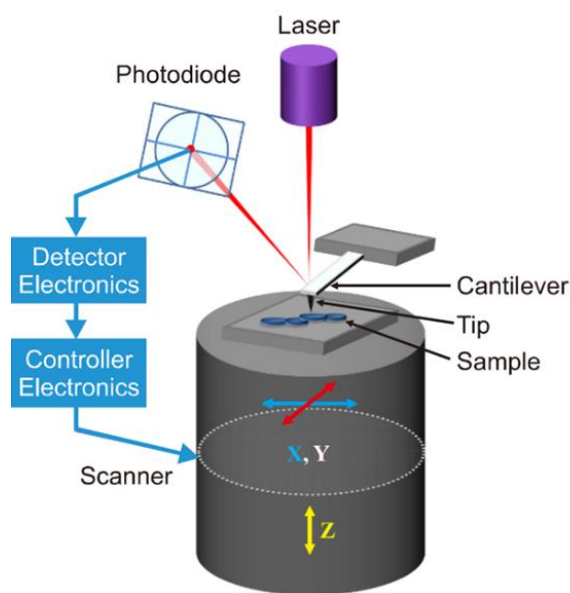
**Scheme 2.2-9.** Graphical representations of the electrochemical impedance spectroscopy (EIS) measurements expressed by the Nyquist plot for (a) the Randles and (b) Randles-Ershler equivalent electric circuit.  $Z_R$  and  $Z_I$  is the real and imaginary component of impedance, respectively,  $Z$  is the impedance,  $\varphi$  is the phase angle,  $\omega$  is the angular frequency ( $\omega = 0$  at high-frequency region),  $R_t$  is total resistance and  $R_{ct}$  is the charge transfer resistance, and the Bode (c) logarithm of impedance vs. frequency, and (d) phase angle vs. frequency graphs.<sup>178-179</sup>

### 2.2.5 Atomic force microscopy (AFM)

Atomic force microscopy (AFM) is an accurate, non-destructive, high-resolution imaging tool used to study surface topography at the nanoscale with minimum sample preparation. The resultant AFM images are atomically resolved with the angstrom scale resolution. Unlike a scanning tunneling microscope (STM), which can only image semiconductive and conductive surfaces, AFM can image almost any non-conducting surface, including glass, composites, ceramics, polymers, and biological samples. Apart from imaging, AFM also provides a

quantitative evaluation of the surface properties, i.e., resistance, film thickness, friction, conductivity, surface potential, capacitance, electric forces, magnetic forces, etc., which makes AFM a crucial tool in materials science.<sup>181</sup>

AFM uses a sharp cantilever tip to probe the region of interest of a material surface in a raster pattern ( $x$ ,  $y$ , and  $z$  directions in Scheme 2.2-10).<sup>182</sup> A commonly used cantilever is made from Si and  $\text{Si}_3\text{N}_4$  material with a tip radius of 10 to 40 nm.<sup>183</sup> The basic principle of AFM measurement relies on the tip-sample interaction. During measurement, the cantilever is brought closer to the sample causing the cantilever to deflect towards the surface due to the attractive force between the tip and surface. Conversely, the repulsion force causes the cantilever to deflect away from the surface when the cantilever is brought further close to the sample. A laser beam monitors this deflection when the cantilever interacts with the sample. A position-sensitive photodiode then detects the reflected incident beam from the cantilever's top. As a result of laser and photodiode interaction, an electric potential is generated, revealing critical information about the sample surface.

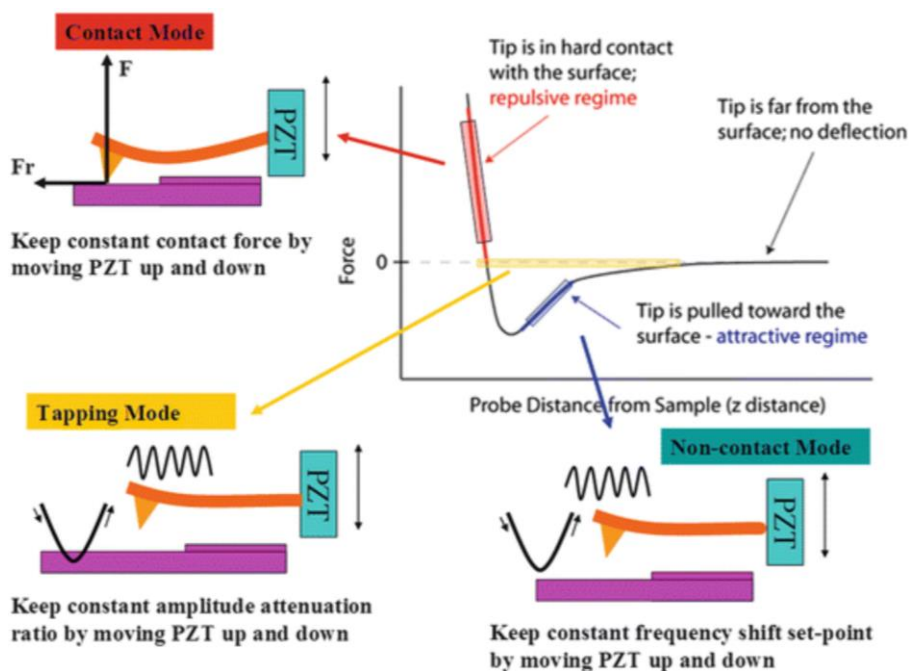


**Scheme 2.2-10.** Schematic illustration of atomic force microscope and the principle of its operation.<sup>182</sup>

Moreover, the laser position on the detector is heavily influenced by the cantilever deflection because of the tip-sample interactions. When the cantilever deflects from its pre-

determined setpoint value, the laser position also changes. Therefore, a feedback loop is triggered to compensate for the extensive cantilever deflections. The piezoelectric element moves vertically to control the height of the tip above the surface ( $z$ -direction in Scheme 2.2-10) and causes a constant laser position. This protocol is repeated throughout the scanning, then the coordinates that the tip scanned are combined, resulting in a three-dimension topography AFM image.

The modes of AFM operation are contact, non-contact, and tapping (Scheme 2.2-11). The cantilever tip scans the area of interest in the contact mode while maintaining constant contact with the sample.<sup>184</sup> The repulsive force dominates in the contact mode. The contact mode is realized by maintaining the constant cantilever deflection by keeping a constant interaction force between the sample and the tip using the feedback signal. In the non-contact mode, the tip is oscillated by a piezoelectric actuator (PZT) very close to the sample surface ( $\sim 1-10$  nm). The attraction force, such as the van der Waals force, dominates in this mode.



**Scheme 2.2-11.** Principles of the contact, non-contact, and tapping modes of AFM operation.<sup>185</sup>

In the tapping mode, the oscillating tip intermittently makes contact with the sample surface. The repulsive force dominates in the tapping mode. The feedback signal controls the

vertical movement of the cantilever tip to maintain a constant cantilever oscillation. The sample surface topography is constructed by measuring the amplitude, phase, and cantilever oscillation frequency changes. The tapping mode is well suited for imaging soft and delicate samples such as polymer film-coated electrodes. Therefore, in MIP studies, the tapping mode of the AFM is used to image the film's surface and to determine the thickness of films deposited on an electrode surface (see Section 2.3.7, below).

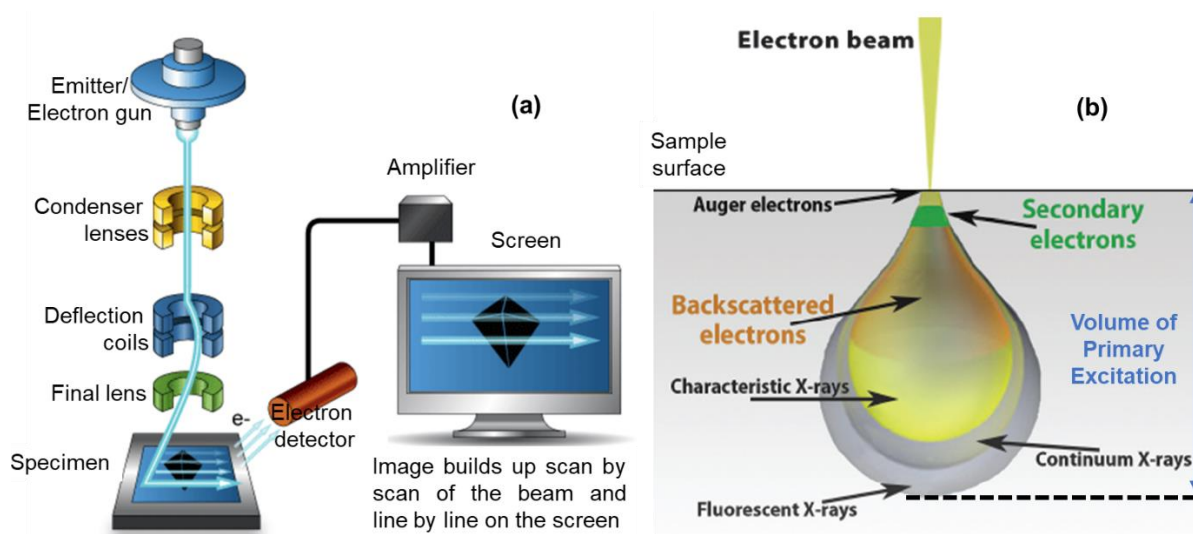
### **2.2.6 Scanning electron microscopy (SEM)**

Scanning electron microscopy (SEM) generates high-resolution images of fine structures. SEM utilizes a high-energy electron beam instead of visible light as a source for imaging purposes. This beam wavelength is shorter, offering higher resolution, allowing the visibility of nanoscale structures. The SEM resolution is 10 nm, and magnification is possible up to 3,000,000 times.<sup>186</sup> Furthermore, SEM allows for a three-dimensional observation because it produces images with a deeper focal depth. As a result, SEM informs about the surface topography, morphology, and chemical composition, such as a material's crystallographic, magnetic, and electrical characteristics. Moreover, it provides information on film uniformity in the MIP study and, possibly, confirms the cavity formation after template extracting.

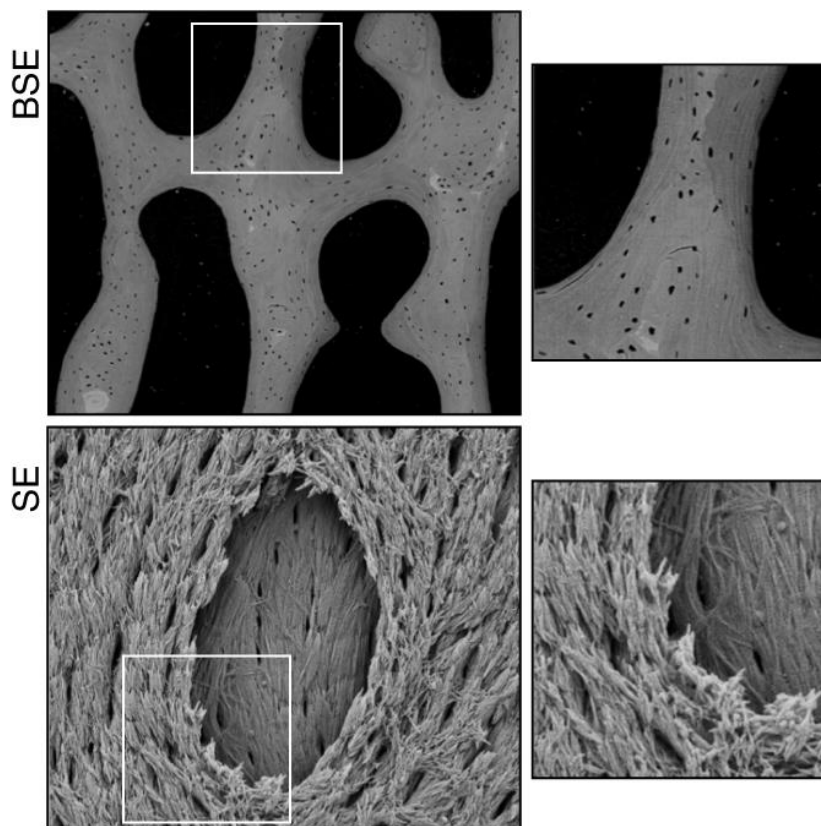
The SEM microscope consists of an electron source, a vacuum system, an optical column, an electron detector, a sample chamber, and imaging software (Scheme 2.2-12a). SEM measurements are carried out using a high vacuum setup ( $10^{-4}$  Pa). A focused (a few nanometers in diameter) electron beam with an energy of 0.2 - 40 keV is formed as electrons pass through lenses and apertures. The high-energy electron beam is used to scan across the sample's surface in a raster pattern resulting in various signals. The electron detector collects these signals and converts them to an electrical signal, and then the signal is amplified via a scintillator and photomultiplier. Subsequently, the software processes the electric signal, constructing the image.

The signals produced during SEM measurements are secondary electrons (SEs), backscattered electrons (BSEs), different types of X-rays, and cathodoluminescence (Scheme 2.2-12b). The type of signal generated depends on several factors, including sample form, element composition in the sample, the substance's density, and an accelerating voltage of the beam. The most common signals used for SEM measurement are BESs and SEs (Scheme 2.2-

13). BSEs come from the deeper region (a few micrometers) of the sample because of the elastic scattering of the primary electrons. For comparison, SEs come from the surface region (10 nm) because of the inelastic interaction between the beam and the sample.<sup>187</sup> The BSEs signal is often used to study sample compositions, while that of SEs is used to obtain topography information. An SEM image constructed from a SEs signal shows brightness variation on a black-and-white display, and its resolution is higher than that of the BSEs signal.



**Scheme 2.2-12.** (a) A sketch of scanning electron microscopy (SEM) setup and (b) different signals produces when the electron beam penetrates the sample.<sup>186</sup>



**Scheme 2.2-13.** Scanning electron microscopy (SEM) images of a bone recorded using backscattered electron (BSE) and secondary electron (SE) signals.<sup>188</sup>

### 2.2.7 X-ray photoelectron spectroscopy (XPS)

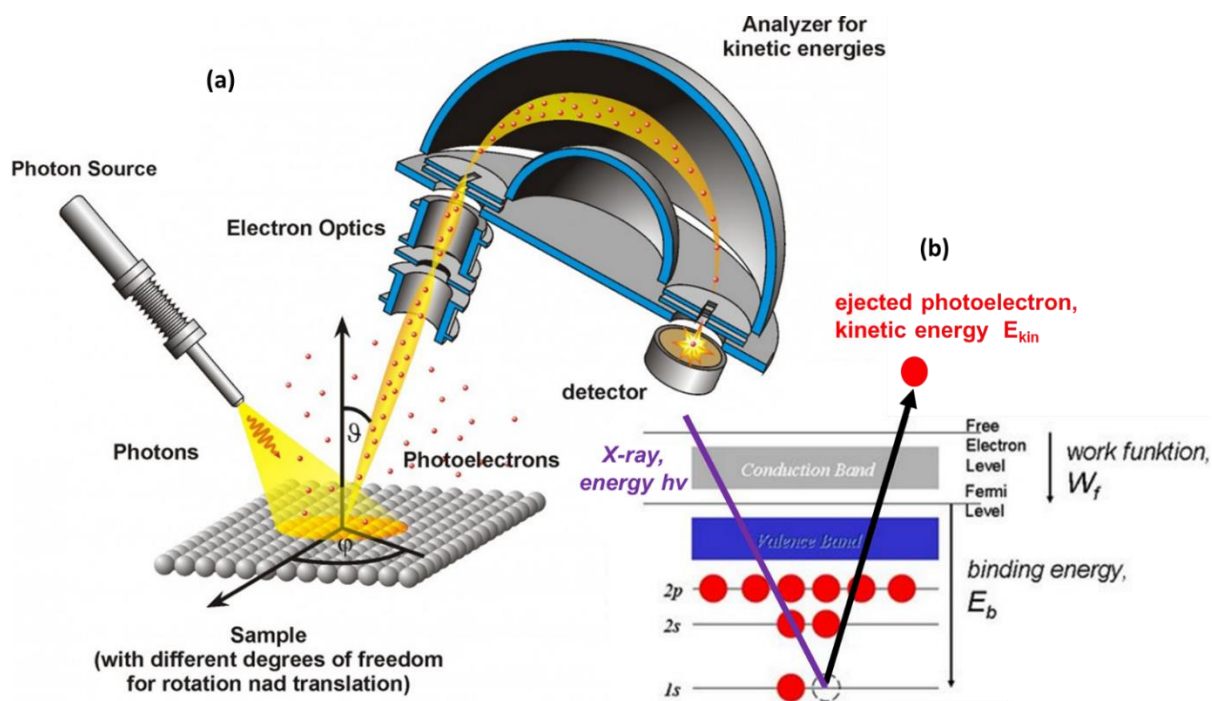
X-ray photoelectron spectroscopy (XPS) is a surface-sensitive characterization and qualitative analysis technique used to study a solid material's surface (1-20 nm). For non-destructive profiling, an XPS probe has an average of ~5 nm penetration depth of a sample under an ultrahigh vacuum condition. An XPS measurement is based on the photoelectric effect (Scheme 2.2-14b), where electrons are emitted from the surface region due to inelastic interaction between the high energy (10–2000 eV) photons (Al-K $\alpha$  or Mg-K $\alpha$  X-rays) and the sample.<sup>189</sup> Each photoelectron has different kinetic energy depending on the photon energy and electron binding energy. The electron analyzer measures the photoelectron's kinetic energy. XPS determines the photoelectron binding energy (Equation 2.2-18), revealing critical information, including surface elemental composition and quantity, empirical formula, chemical, and electronic states. In MIP studies, XPS is used to study the difference in MIP and NIP film surface composition before and after template extraction.

A typical XPS spectrum represents the photoelectron intensity dependence on the binding energy

$$E_b = h\nu - E_{kin} - W_f \quad [\text{Equation 2.2-18}]$$

where  $E_b$  is the binding energy (energy required to remove one electron from the atom),  $h\nu$  is the energy of the X-ray,  $E_{kin}$  is the photoelectron kinetic energy, and  $W_f$  is the work function (energy that must be overcome to remove one electron from the atom).

Depth (or destructive) profiling is sometimes carried out to obtain information about the sample subsurface.<sup>190</sup> First, the sample is analyzed using a narrow energy range. Then, energetic inert gas ions (Ar and Xe) are sputtered over the sample to etch the sample. These procedures are repeated until the desired depth (typically a few microns) is acquired, followed by spectrum recording. For a material such as a polymer film, C<sub>60</sub> is preferred over Ar or Xe because of much smaller sample damage.



**Scheme 2.2-14.** (a) Schematic illustration of an X-ray photoelectron spectroscopy (XPS) setup consisting of an X-ray source, sample holder, an electron analyzer, a detector, and data processing software, and (b) a principle of XPS operation.<sup>191</sup>

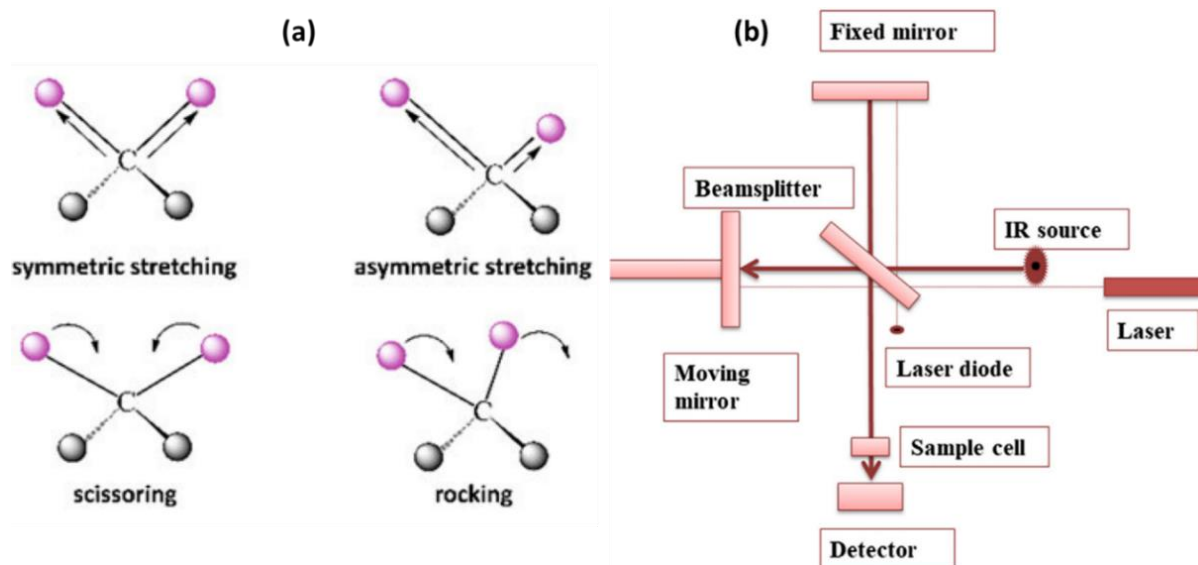
### 2.2.8 Fourier transform infrared (FTIR) spectroscopy

Fourier transform infrared (FTIR) spectroscopy is a non-destructive, fast, and inexpensive technique to study sample structure. Several parameters characterize an FTIR spectrum, including band position, intensity, width, and the spectra's shape. These unravel information about the molecular functional groups and bonding ('molecular fingerprint' of a chemical compound) in organic, inorganic, and polymeric samples. Therefore, an FTIR spectroscopy measurement is often adopted to identify an unknown sample and detect decomposition products, contaminants, and additives in a sample. In MIP studies, FTIR spectroscopy is used to identify the composition of an MIP before and after template extraction, which can indirectly confirm cavity formation.

The FTIR spectroscopy measurement utilizes the spring-like behavior of the chemical bonds. A chemical bond in a molecule at room temperature is not rigid. Instead, it constantly vibrates by bending, twisting, and stretching (Scheme 2.2-15a), each motion having its own frequency.<sup>192</sup> Hence, when the infrared (IR) radiation hits the molecule and supposes the frequency of the incident IR matches with the frequency of the molecular bond vibration, the molecule will absorb the radiation energy. Then, it excites the molecule to its higher vibration energy state, causing an increment in the vibration amplitude while remaining at the same frequency. The difference between the new and old vibration energy states represents the energy absorbed by the molecule at that particular wavenumber. The FTIR spectrophotometer measures the intensity and wavenumber of the IR radiation absorbed by a molecule. A typical FTIR spectrum is an IR radiation absorbance or transmittance plot vs. the wavenumber. Each spectrum band represents IR absorption by the molecule at a specific wavenumber, revealing information about the chemical bonding. Moreover, the chemical environment highly influences the IR radiation absorption by the molecule. Therefore, an FTIR spectrum is unique and different for each chemical compound.

In a modern FTIR spectrophotometer (Scheme 2.2-15b), a Michelson interferometer present consists of a beamsplitter (half-transparent window), and there is one movable and one stationary mirror.<sup>193</sup> A laser monitors the position of the moving mirror. The beamsplitter splits the incident IR radiation into two beams, causing the beams to travel in different paths toward the moving or fixed mirror. Then the beams return to the beamsplitter either in-phase (constructive interference) or out-of-phase (destructive interference) and are detected by the

detector. This signal is represented as an interferogram which is a time-domain spectrum. After that, this light is passed through the sample and detected by the detector. The interferogram is converted to the frequency-domain spectrum by applying a Fourier transform (FT). The final absorbance spectrum is obtained after comparing the spectrum with a background (reference measurement). A few notable advantages of FTIR spectra include a high signal-to-noise ratio, short measurement time, high resolution, wide wavenumber scan range, and high wavenumber accuracy.



**Scheme 2.2-15.** (a) Different vibration modes of a chemical bond and (b) schematic illustration of an FTIR spectrophotometer consisting of an IR light source, sample chamber, interferometer, amplifier, analog-to-digital converter, detector, and computer.<sup>192-193</sup>

Transmission and attenuated total reflection (ATR) are the two most common FTIR sampling modes to study bulk samples. In the transmission mode (Scheme 2.2-16a), IR radiation hits the potassium bromide (KBr)-pellet containing sample. The detector then detects the radiation transmitted by the sample. Liquid samples are often diluted with a transparent solvent, e.g., carbon tetrachloride, before measurement and, in some cases, measured directly. The relationship between absorbance,  $a$ , the sample concentration,  $c$  (in mol cm<sup>-1</sup>), and the optical path length,  $d$  (in cm), is given by Equation 2.2-19 (the Beer-Lambert law) below.

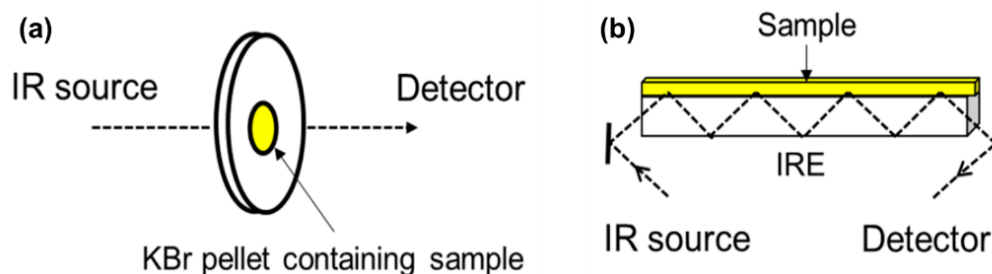
$$a = -\log\left(\frac{I}{I_{\text{ref}}}\right) = \xi c d \quad \text{[Equation 2.2-19]}$$

Where  $I$  and  $I_{\text{ref}}$  are the intensities of the incident and transmitted light, and  $\xi$  is the molar absorption coefficient in  $\text{L mol}^{-1} \text{cm}^{-1}$ .

The major disadvantages of IR spectroscopy include tedious sample preparation and the requirement for the sample to be thin ( $<15 \mu\text{m}$ ) and sufficiently transparent to enable light permeation through the sample. Moreover, the transmission mode is not surface sensitive. These transmission mode deficiencies are overcome by adapting the attenuated total reflection (ATR) mode. The ATR-FTIR was utilized in the present study. In ATR (Scheme 2.2-16b), the sample is pressed on an internal reflection element (IRE) such as diamond, germanium, or zinc selenide. Then, the IR radiation passes through the IRE at a certain angle and is subsequently reflected. At this time, some light (evanescent wave) penetrates the sample (a few micrometers deep). This phenomenon is known as the total internal reflection. The total internal reflection happens in two situations, i.e., (i) when the angle of incident,  $\theta$ , exceeds the critical angle,  $\theta_c$ , and (ii) when the crystal's refractive index,  $n_1$ , is higher than the sample's refractive index,  $n_2$ . Equation 2.2-20 defines the critical angle. An ATR spectrum is recorded during the light penetration, where the sample absorbs the energy at the wavenumber at which the beam loses its energy.

$$\sin\theta_c = \frac{n_2}{n_1}$$

[Equation 2.2-20]



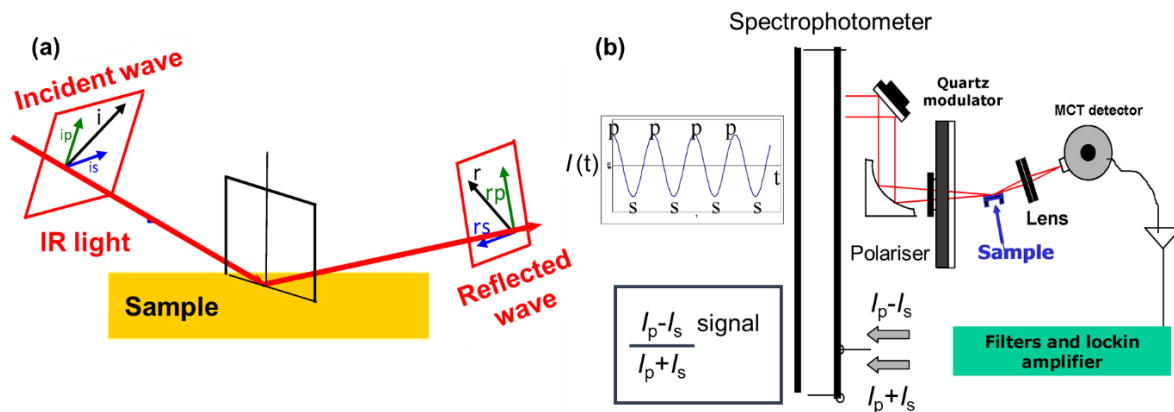
**Scheme 2.2-16.** Fourier transform infrared (FTIR) spectroscopy analysis modes of (a) transmission and (b) attenuated total reflection (ATR); IRE is the internal reflection element.<sup>194</sup>

### 2.2.9 Polarization-modulation infrared reflection-absorption spectroscopy (PM-IRRAS)

Polarization-modulation infrared reflection-absorption spectroscopy (PM-IRRAS) is a surface-sensitive molecular structural analyzing IR technique. It is the reflection-absorption sampling mode of the FTIR. This mode is adapted to obtain molecular-level information, which is often unattainable in a traditional FTIR spectroscopy measurement. Chemical bonds, orientation, conformation, geometry, the degree of hydration, and coordination of the molecules adsorbed on a thin layer of a reflecting substrate (gold, silver, platinum, or water) are some of the information that can be acquired from a PM-IRRAS spectrum.<sup>195</sup>

The optical constant of a thin film and the reflecting material, the incidence angle, and the polarization of the incident IR radiation are three essential parameters in a PM-IRRAS measurement. The sample's surface is focused with an incident *IR* beam at a grazing incidence (typically 80°), subsequently reflected by the substrate. A high-frequency photoelastic modulator (PEM) modulates the incident and reflected polarized radiation concerning the plane of the incident, generating two-radiation components; parallel (p-) and perpendicular (s-) to the reflection plane-polarized radiation (Scheme 2.2-17a). The p-polarized radiation strongly interacts with the sample's surface at an anisotropic interface, while the s-polarized radiation does not. Nevertheless, both p- and s-polarized radiation equally interacts at the isotropic background.<sup>196</sup> Thus, two different signals are measured simultaneously in PM-IRRAS, vis., (i) an intensity difference between p- and s-polarized radiation ( $\Delta I = I_p - I_s$ ), and (ii) the sum of p- and s-polarized radiation signals ( $\Sigma I = I_p + I_s$ ). The differential reflectivity spectrum of a chemical species in a thin layer is expressed by Equation 2.2-19.

$$\frac{\Delta I}{\Sigma I} = \frac{I_p - I_s}{I_p + I_s} \quad \text{[Equation 2.3-19]}$$



**Scheme 2.2-17.** (a) A basic principle of polarization-modulation infrared reflection-absorption spectroscopy (PM-IRRAS) measurement and (b) schematic illustration of a PM-IRRAS setup consisting of a spectrophotometer, optical system, photoelastic (quartz) modulator, polarizer, and a mercury-cadmium-telluride, MCT, detector.<sup>197</sup>

The s-polarized light reflectivity is a reference in the PM-IRRAS measurement because it is insensitive to the chemical species deposited on a substrate. Thus, the time of the experiment is reduced significantly via this technique. Other than that, the conventional infrared reflection-absorption spectroscopy (IRRAS) sensitivity is enhanced by using the polarization-modulation technique. It allows eliminating the environmental adsorption (carbon dioxide or water vapor), enabling a comprehensive molecular level measurement.<sup>198</sup>

## 2.3 MIP and NIP films preparation

### 2.3.1 General procedure of preparation of molecularly imprinted polymers

A general procedure of MIP preparation involves five steps. The first is the pre-selection of functional and cross-linking monomers for a given template. That may be accomplished based on chemical intuition, procedures previously reported in the literature, and the availability of the functional monomers. The target analyte or its close analog is used as the template.

The second step involves computational modeling of the pre-polymerization complexes. The essential step in modeling is to optimize the structures and calculate the Gibbs free energy change of formation of the template and functional monomers molecules. Next is to calculate and optimize the negative Gibbs free energy change,  $\Delta G$ , accompanying the formation of possible functional monomer pre-polymerization complexes with the template. The last step

in modeling calculates the  $\Delta G$  of the pre-polymerization complexes with different compositions and stoichiometries. Moreover, possible dimerization of molecules should be considered. The most negative  $\Delta G$  value indicates the most stable and vital complex for successfully forming the desired MIP with high selectivity. Therefore, this set of functional monomers is selected for further studies.

The third step is to dissolve the template, functional and cross-linking monomers of choice, in one or a mixture of appropriate solvents to form a pre-polymerization complex. There are two main approaches to the pre-polymerization complex preparation, i.e., the preorganization and self-assembly approach. The aforementioned is often used in MIP preparation, including the work reported in the present thesis, due to the simplicity of the preparation and extraction procedures and the possibility of interaction between available functional monomers with a wide variety of templates.

The fourth step in our study is the electrochemical MIP film deposition under potentiodynamic conditions on an electrode surface. For that, the electrode is immersed in a template-monomer pre-polymerization complex solution of a supporting electrolyte. The pre-polymerization complexes are oxidized or reduced at predefined potentials and subsequently deposited on the electrode surface. Afterward, the resulting polymer film is rinsed with the same abundant solvent to dissolve any unbound template, functional monomers, pre-polymerization complex, and excessive supporting electrolyte.

The fifth final step is template extraction. The template can be extracted either chemically or electrochemically, depending on the nature of template-film interactions. The extraction leads to emptying cavities in the MIP, thus making it suitable to serve as a chemosensor recognition unit. Finally, the reversible analyte-cavity binding is studied.

NIP preparation entails polymerizing the selected functional and cross-linking monomers in the absence of the template under the same conditions as MIP film preparation. An NIP polymer serves as a control material. It is used to determine the extent of imprinting, whose quantitative measure is an apparent imprinting factor.

### **2.3.2 Computational modeling**

First, the 3D structures of the (i) template molecule, (ii) functional monomers' molecules and (iii) their dimers, and (iv) pre-polymerization complex of functional monomers with a template

were drawn with Gauss View or Avogadro software. Then, the DFT calculation, performed using Gaussian 2009 software (Gaussian, Inc., Wallingford CT, USA),<sup>199</sup> was used to run all calculations. Independently, each 3D structure was optimized using the functional and basic quantum-chemical modeling using the B3LYP/3-21G or M06-2X/6-31G set, and then  $\Delta G$  was calculated. The solvent effect was approximated with the polarizable continuum model (PCM). Finally, the changes in Gibbs free energy,  $\Delta G$ , due to complex formation were acquired by comparing  $\Delta G$  values calculated for the complex with those calculated for its components alone.

### 2.3.3 Electrode cleaning

The 0.75-mm diameter Pt or 1-mm diameter Au disk electrode was cleaned for 10 min in a "piranha" solution before polymer film deposition. (*Warning. The "piranha" solution is hazardous if it comes in contact with skin or eyes.*) The electrodes were first polished using the 1.0, 0.3, and 0.05- $\mu\text{m}$  alumina slurry then rinsed with abundant deionized water. Next, the electrode was roughed with 1000 grit sandpaper to enhance the polymer film adhesion to the electrode surface. The electrode was then rinsed with abundant deionized water, then acetone.

For the ATR-FTIR spectroscopy, PM-IRAAS, and XPS measurements as well as SEM and AFM imaging, MIP films were coated on a 0.5-cm<sup>2</sup> area Au-glass slides (Institute of Electronic Materials Technology, Warsaw, Poland). The Au film (100 nm thick) was vapor-deposited over the Ti (15 nm thick) underlayer; glass slides were cleaned by 15-min ultrasonication in acetone. Then the slides were dried in an Ar stream before polymer film deposition.

### 2.3.4 Preparing the polymer imprinted with tyramine

Two MIPs with different functional monomers and film thicknesses were prepared and examined. The pre-polymerization complex of **MIP-1** was prepared using a 50  $\mu\text{M}$  **tyramine**, 100  $\mu\text{M}$  **FM1**, 500  $\mu\text{M}$  **2,3'-bithiophene**, and 100 mM (TBA)ClO<sub>4</sub> acetonitrile solution. **MIP-1** was prepared by electropolymerization under potentiodynamic conditions using five potential cycles over the potential range of 0 to 1.30 V vs. Ag quasi-reference electrode at a potential scan rate of 50 mV/s at a 0.75-mm diameter Pt disk electrode.

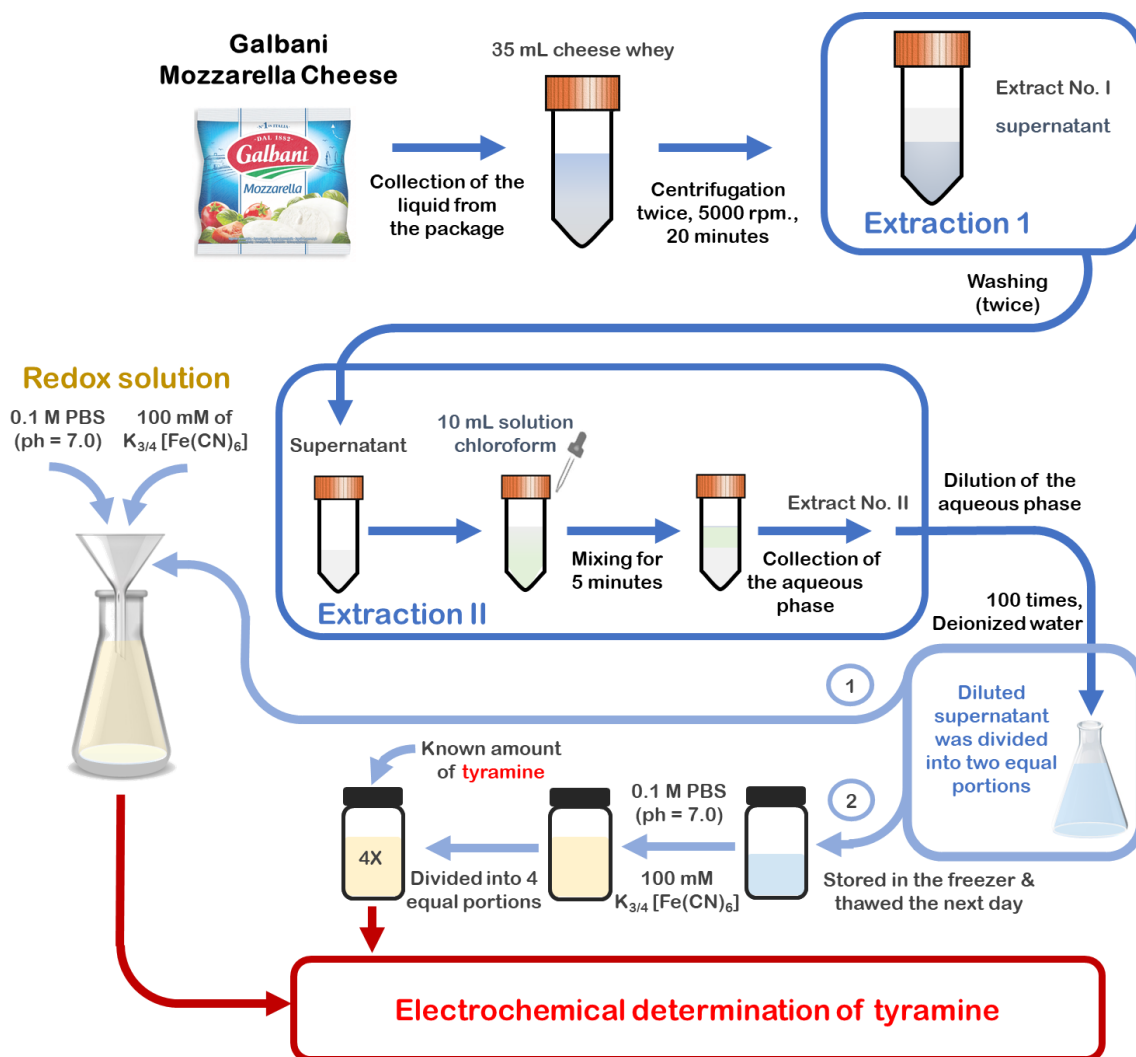
The pre-polymerization complex of **MIP-2** was prepared using a 50  $\mu\text{M}$  **tyramine**, 100  $\mu\text{M}$  **FM1**, 50  $\mu\text{M}$  **FM2**, 500  $\mu\text{M}$  **2,3'-bithiophene**, and 100 mM (TBA)ClO<sub>4</sub> acetonitrile solution. **MIP-2** was prepared by electropolymerization under potentiodynamic conditions using two potential cycles over the potential range of 0 to 1.30 V vs. Ag quasi-reference electrode at a potential scan rate of 50 mV/s at a 0.75-mm diameter Pt disk electrode.

The resulting films were thrice rinsed with acetonitrile to remove the tetrabutylammonium perchlorate salt and unreacted monomers residue after the electropolymerization. The tyramine template was removed from the **MIP-1** and **MIP-2** films by immersing the film-coated electrodes in 0.1 M NaOH and magnetically stirred for 150 min at room temperature. After template extraction, the MIP film was rinsed with abundant acetonitrile to remove the extracting solution and then dried in air for 10 min. A stable DPV peak of  $\sim 45 \mu\text{A}$  for the redox probe marker shows the complete extraction of the template from the MIP film. The MIP films were re-extracted several times using the same extraction solution and conditions for 10 to 90 min after each tyramine determination. The **NIP-1** and **NIP-2** control films were prepared similarly to **MIP-1** and **MIP-2** films, however, without the template, and then extracted in the same manner as the MIP films.

### **Preparing Mozzarella cheese whey as a food sample**

A package of Galbani Mozzarella cheese was purchased from a local supermarket. The cheese whey sample (35 mL) from a freshly opened package was collected and centrifuged twice (20 min, 10,000 rpm) to remove any solid contaminants. Next, the supernatant was collected and washed twice with chloroform (10 mL). Subsequently, the collected aqueous phase was diluted with deionized water 100 times. This solution was then divided into two equal portions. To one, the 0.1 M PBS (pH = 7.0) solution with 100 mM K<sub>3</sub>[Fe(CN)<sub>6</sub>] and 100 mM K<sub>4</sub>[Fe(CN)<sub>6</sub>] redox probe was added. This redox probe concentration is the same as that used to study the MIP chemosensor. The prepared solutions were then applied for DPV tyramine determinations in the same way as that described in Chapter 2 (Sections 2.3.4 and 2.3.6) to construct calibration plots. The other portion was transferred to a clean bottle and stored in the freezer. The next day, this portion was thawed, and the 0.1 M PBS (pH = 7.0) solution of the K<sub>3</sub>[Fe(CN)<sub>6</sub>] and K<sub>4</sub>[Fe(CN)<sub>6</sub>] was added, as before. Then, it was divided into four samples. Each of these samples was spiked with a known amount of tyramine. Finally,

tyramine was determined in these samples using a freshly prepared **MIP-2** film coated electrode. Scheme 2.3.1 illustrates the preparation of the Mozzarella cheese whey.



**Scheme 2.3-1.** The redox solution and the Mozzarella cheese whey samples preparation for tyramine determination using the MIP film-coated electrode.

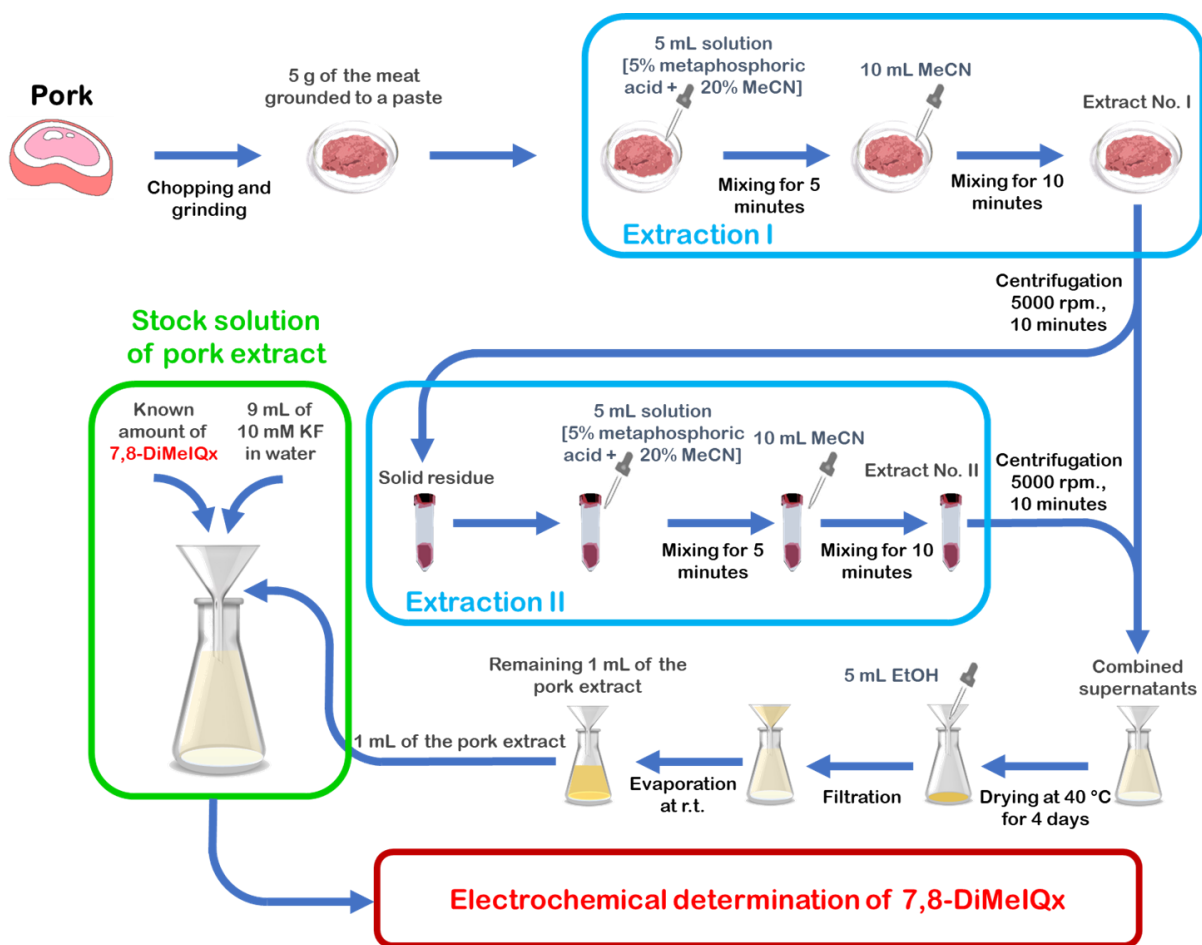
### 2.3.5 Preparing a polymer imprinted with 7,8-DiMeIQx

The MIP pre-polymerization complex was prepared using an acetonitrile solution of 20  $\mu$ M **7,8-DiMeIQx**, 40  $\mu$ M **Abt**, 20  $\mu$ M **Tbt**, 40  $\mu$ M **CrI T8**, and 20 mM (TBA)ClO<sub>4</sub>. The MIP film was prepared by electropolymerization under potentiodynamic conditions for two and five potential cycles over the potential range of 0 to 1.25 V vs. Ag quasi-reference electrode at a potential scan rate of 50 mV/s using a 1-mm Au disk electrode.

Subsequently, the MIP film-coated electrode was thrice rinsed with acetonitrile to remove the unreacted pre-polymerization complex, monomers, and electrolyte salt. Finally, the **7,8-DiMeIQx** template was extracted by immersing the MIP film-coated electrode in 10 mM trimethylamine in acetonitrile and magnetic stirring for 20 min at room temperature. After the extraction, the MIP film was rinsed with abundant acetonitrile to remove the extracting solution. Before further measurement, the MIP film-coated Au electrode was dried in air for 20 min. The control NIP films were prepared as MIP films but without the target **7,8-DiMeIQx** analyte and then extracted in the same manner as the MIP films.

### **Preparing a pork meat extract as a food sample**

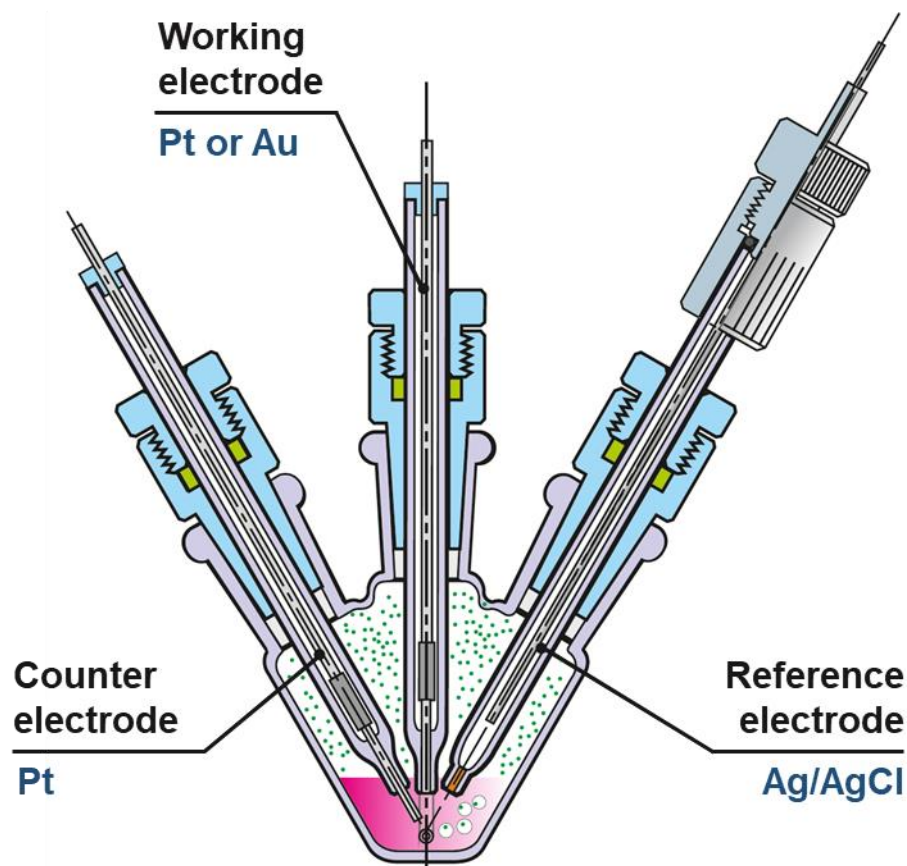
The pork meat extracts were prepared according to a slightly modified procedure reported by Yang et al.<sup>200</sup> That is, a 5-g pork meat sample was purchased from a local market and ground to a paste using a high-speed food blender. A 5 mL of a 5% metaphosphoric acid and 20% acetonitrile solution was added to this paste, then mixed for 5 min, followed by adding 10 mL acetonitrile, then mixing for another 10 min. Afterward, the mixture was transferred to a 100-mL centrifuge tube, then centrifuged at 500 rpm for 10 min. Subsequently, the supernatants were collected. Following that, the residue was extracted in the same manner as above. The resultant supernatants were combined and transferred to a glass dish where it was set to evaporate at 40 °C for 4 days. Later, the residue was dissolved in a 5-mL sample of methanol, then filtered on a Whatman™ chromatography paper. The filtered solution was collected in a flask and evaporated at room temperature until the sample volume was decreased to 1 mL. Then the 1 mL pork extract solution was spiked with 4.99 mg of **7,8-DiMeIQx** and then diluted with 10 mM KF to achieve the 1 mM concentration. Finally, this stock solution was applied to test the devised MIP-based chemosensor for **7,8-DiMeIQx**. Scheme 2.3-2 illustrates the procedure of preparing the pork meat extract.



**Scheme 2.3-2.** The pork meat sample preparation procedure for 7,8-DiMeIQx determination using the MIP film-coated electrode.

### 2.3.6 Instrumentation, experimental setup, and electrochemical measurements' procedures

Electrochemical experiments were performed with an SP 300 electrochemistry system of Bio-Logic Science Instruments controlled by the EC-lab computer program of the same manufacturer. A 0.5-mL three-electrode V-shaped glass mini vessel served as the electrochemical cell (Scheme 2.3-3). A 0.75-mm diameter Pt or 1-mm diameter Au disk electrode or Au-layered glass slide were used as working electrodes, while the Pt and Ag wire was used as the auxiliary and Ag quasi-reference electrode, respectively, in the CV, DPV, EIS, and the steady-state CI measurements.



**Scheme 2.3-3.** A cross-sectional view of the three-electrode electrochemical mini vessel designed by the Institute of Physical Chemistry PAS (Warsaw, Poland). The glass minicell was custom-manufactured by Labit sp. z o.o. (Stare Babice, Poland).

Template removal from the MIP films and the sensitivity and selectivity of the MIP chemosensor was investigated by DPV and EIS or CI. These measurements were performed at room temperature using the electrochemical minicell (Scheme 2.3-3) in the following experimental media:

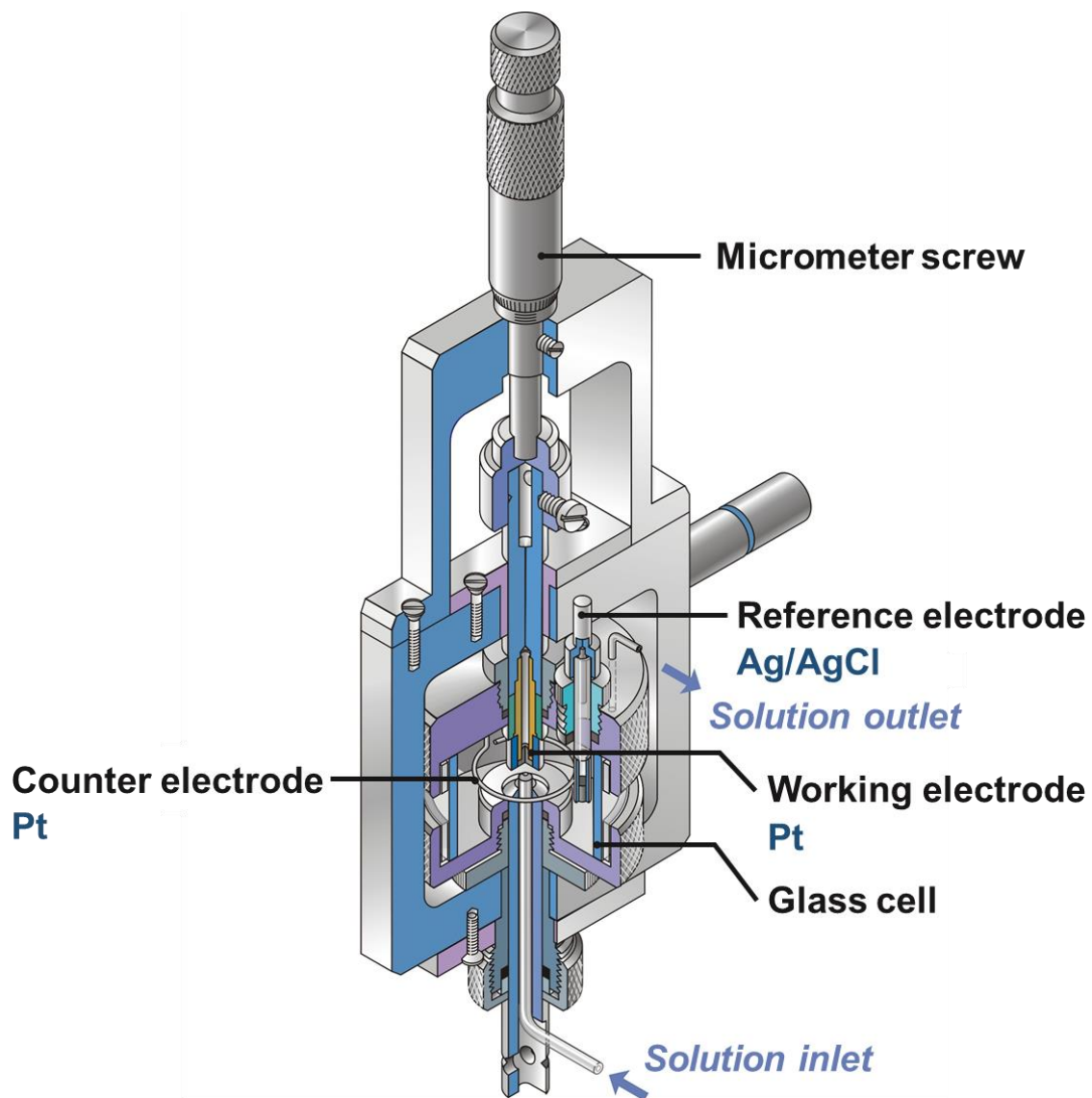
- (a) phosphate-buffered saline, PBS, (pH = 7.0) solution of the 100 mM  $K_3[Fe(CN)_6]$  and 100 mM  $K_4[Fe(CN)_6]$  redox probe for MIP-tyramine, and
- (b) phosphate-buffered saline, PBS, (pH = 7.4) solution of the 100 mM  $K_3[Fe(CN)_6]$  and 100 mM  $K_4[Fe(CN)_6]$  redox probe, or
- (c) 1 mM ferrocene, 0.1 M (TBA)ClO<sub>4</sub>, in acetonitrile, or
- (d) 10 mM KF for MIP-7,8-DiMeIQ<sub>x</sub>.

For DPV determinations, the potential scan range, potential step, pulse amplitude, and pulse duration were 0 to 0.60 V, 5 mV, 50 mV, and 50 ms, respectively. A drop of the redox probe

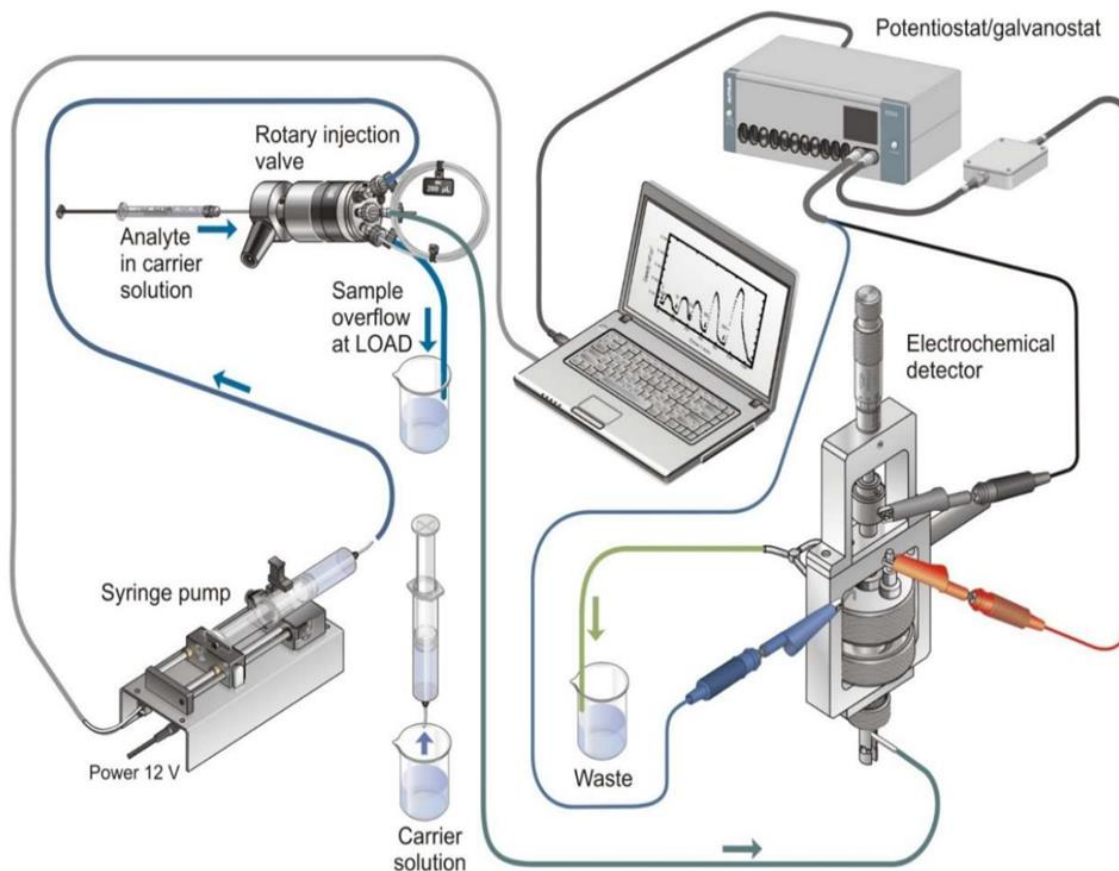
faradaic current served as the analytical signal.<sup>114</sup> The EIS spectra were recorded in the 1 MHz to 100 mHz or 100 mHz to 200 kHz frequency range at a constant potential of 0.20 V or 0.50 V vs. Ag quasi-reference electrode for **MIP-tyramine** and **MIP-7,8-DiMeIQx**, respectively, at the 10-mV sinusoidal amplitude. The EIS experimental data were fitted using the Randles-Ershler equivalent electric circuit (see Section 2.2.4, above) with EC-lab V10.44 software of Bio-Logic to determine the charge transfer resistance ( $R_{ct}$ ) of the  $K_3[Fe(CN)_6]/K_4[Fe(CN)_6]$  redox probe. The target analyte samples were dissolved in the experimental medium for analyte recognition, and the DPV and EIS measurements were performed.

The CI measurements were carried out under both the steady-state solution and FIA conditions. The electrochemical minicell (Scheme 2.3-3) was used for the steady-state CI measurements. The FIA experiments were performed using a homemade radial-flow thin-layer 35-mL electrochemical cell (Scheme 2.3-4).<sup>201</sup> The cell was designed and manufactured in the mechanical workshop of the Institute of Physical Chemistry PAS in Warsaw (Schemes 2.3-4 and 2.3-5). The 1-mm diameter Pt disk working electrode was axially mounted, opposite the inlet capillary, at the (capillary outlet)-to-electrode distance of 500  $\mu\text{m}$ . A Pt wire loop and an Ag/AgCl electrode were used as the auxiliary and reference electrode, respectively (Scheme 2.3-4). The cell was filled with the 10 mM KF carrier solution prepared using deionized water without any redox probe. The carrier solution was continuously pumped with a KDS100 syringe pump of KD Scientific, Inc. (Holliston MA, USA) at a flow rate of 30  $\mu\text{L min}^{-1}$  throughout the experiments. The target analyte samples of different concentrations were prepared using a solution of the same composition as the carrier solution. Then, 100  $\mu\text{L}$  of the prepared analyte solutions samples were applied for the CI measurements.

The CI measurements determined the electric double-layer capacity,  $C_{dl}$ , of the MIP film-coated Pt electrode and the carrier solution interface by measuring the imaginary component of impedance,  $Z_{im}$ . The CI measurements were carried at a constant potential and frequency of 0.21 V vs. Ag/AgCl and 500 Hz, respectively, at the 10-mV ac amplitude. Under these conditions, no faradaic process occurred at the electrode. Therefore, the non-faradaic impedance was measured. Moreover, the diffuse part of the double layer was negligibly small because of using a concentrated supporting electrolyte solution, i.e., 10 mM KF. As a result, the  $C_{dl}$  change was directly influenced only by  $Z_{im}$ .



**Scheme 2.3-4.** Cross-sectional view of electrodes and the inlet capillary orifice of the 35-mL radial-flow thin-layer electrochemical cell [adapted from <sup>201</sup>].



**Scheme 2.3-5.** Illustration of the experimental setup used for CI measurements, under FIA conditions, at the MIP film-coated Pt disk electrode.

### 2.3.7 Instrumentation and procedures for characterizing MIP films

The MIP film-coated Au glass slides were used for the MIP films characterization.

The polymer surfaces topography was examined using a MultiMode 8 AFM microscope equipped with a Nanoscope V controller, governed by ScanAsyst software from Bruker. Quality etched RTESPA-300 silicon tips with the spring constant of 40 N/m using the Tapping mode<sup>TM</sup> were applied to scan the films at high sensitivity. Under an optical microscope, some parts of the films were carefully removed with a Teflon<sup>TM</sup> spatula to estimate film thickness. Subsequently, the number of points on both sides of the film step (sufficiently far from a partially detached step front) formed that way was AFM imaged and averaged. Next, the step height was determined as the difference in average values of points on the step and its foot. This thickness determination was repeated for every scratched area on the Au-layered glass slide. Finally, the determined step heights were averaged, thus estimating film thickness.

The polymer topography and morphology were revealed using a Nova NanoSEM 450 microscope of FEI (USA).

The polymer surface elemental composition was examined using high-resolution XPS. This technique is vital in confirming imprinting and removing the target analyte from the MIP films. For that purpose, the elemental analysis was carried out using the PHI5000 VersaProbe-Scanning ESCA Microprobe instrument (ULVAC-PHI) at base pressure below  $5 \times 10^{-9}$  mbar. Monochromatic Al K $\alpha$  ( $h\nu = 1486.4$  eV) radiation was used, and the X-ray beam focused to 100- $\mu\text{m}$  diameter was scanned over a  $(250 \times 250)$   $\mu\text{m}^2$  sample surface at an operating power of 25 W (15 kV). Resultant XPS spectra were analyzed with CASA XPS software.

The polymer films were characterized and profiled using PM-IRRAS. This spectroscopy is vital in confirming the composition of MIP and NIP films before and after template extraction. For that purpose, the PM-IRRAS spectra of the films were recorded in the reflection mode with a Vertex 80 v spectrophotometer of Bruker equipped with a PMA50 module and a deuterated triglycine sulfate detector. The MIP film-coated Au-layered glass slide was mounted in a dedicated holder and investigated using the reflection mode at the  $83^\circ$  incident angle of the p-polarized light beam. The recorded spectra were scanned 1024 times and then averaged at a  $2\text{-cm}^{-1}$  resolution. Then, Opus 6.5 software was used to calculate the positions of the bands in the spectra recorded.



## *Chapter 3*

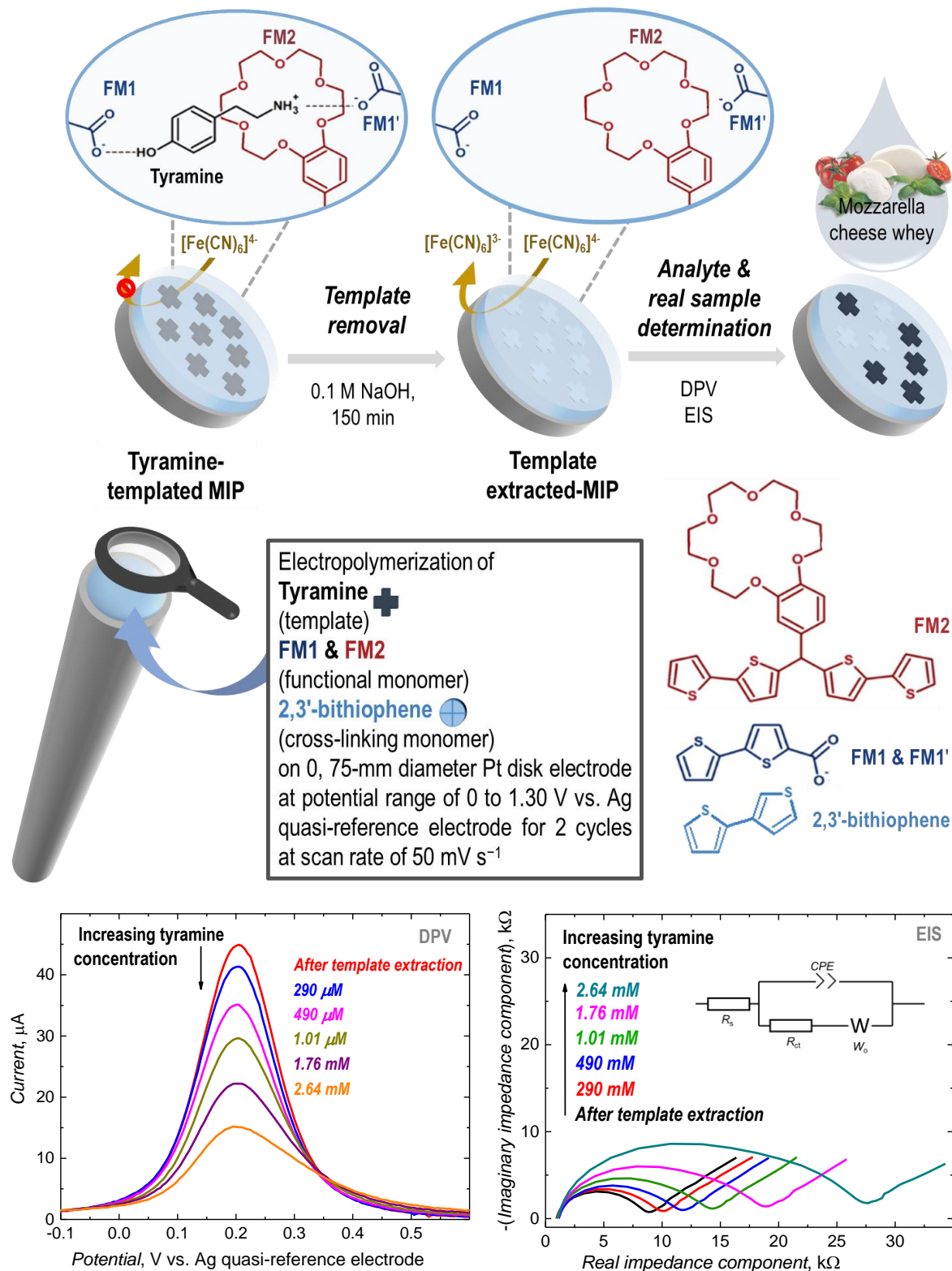
# *Electrochemical sensor for selective tyramine determination with a molecularly imprinted polymer film*

This chapter discusses the research work published in *Bioelectrochemistry*, **2021**, *138*, 107695.  
<https://doi.org/10.1016/j.bioelechem.2020.107695>

## Abstract

An electrochemical molecularly imprinted polymer (MIP) chemosensor was devised and tested for selective determination of tyramine. Smoking and fermentation of food products, such as meat, fish, poultry, cheese, etc., generates food toxins, including tyramine. Therefore, tyramine may serve as a biomarker of the rottenness of food products. Tyramine can exceptionally be dangerous for patients treated with monoamine oxidase (MAO) inhibitors as a large intake may lead to a 'cheese reaction,' namely, a dangerous hypertensive crisis. Currently, the chromatographic technique is used to determine tyramine in food matrices. This technique is expensive and time-consuming. Therefore, a fast and efficient electrochemical sensor was devised within the present study using tyramine-imprinted polythiophene films as selective recognition units. The chemosensor LOD at  $S/N = 3$ , in both DPV and EIS determinations using the  $\text{Fe}(\text{CN})_6^{4-}/\text{Fe}(\text{CN})_6^{3-}$  redox probe, was 159 and 168  $\mu\text{M}$  tyramine, respectively. The linear dynamic response range of the devised chemosensor was 290  $\mu\text{M}$  to 2,6 mM tyramine. The imprinting factor determined using DPV analysis was 5.6. The chemosensor was highly selective to common biological interferences, including glucose, urea, and creatinine.

## Graphical abstract



## 3.1 Introduction

The present chapter discusses simplified indirect tyramine electrochemical determination using an MIP chemosensor. For that, tyramine was imprinted in a derivatized conductive polythiophene film. The resulting MIP-tyramine film-coated electrodes were applied for selective tyramine determination using electrochemical transduction techniques combined with the so-called "gate effect."

## 3.2 Results and discussion

### 3.2.1 Functional monomers selection, electropolymerization, as well as sensitivity and selectivity of the MIP-1 chemosensor

The selection of the appropriate functional monomers is vital for successful imprinting. The reason is that functional monomers provide interaction patterns that allow MIP molecular cavities to recognize the target analyte molecule selectively. First of all, for successful imprinting, the selected monomers should form in solution with the template a pre-polymerization complex sufficiently stable to survive electropolymerization. Subsequently, the functional monomers would place themselves in the expected positions inside the imprinted cavities after complex copolymerization with a cross-linking monomer. Finally, removal of the template results in vacating the desired molecular cavities. Thus, the tyramine template complexation was first modeled with DFT to select the most promising functional monomers for further laboratory experiments.

An initial selection of the **FM1** monomer was driven by chemical intuition. This monomer was expected to form hydrogen bonds with either the hydroxyl or amino groups of the tyramine. Presumably, such weak bonds should be sufficient for template imprinting and subsequent removal. Therefore, **FM1**-tyramine complexes' structures were optimized, and their properties were studied using the DFT B3LYP functional and 3-21g(\*) basic quantum-chemical modeling. The DFT calculations suggested forming a stable **FM1**-tyramine complex at a molar ratio of 2:1 (Figure 3.2-1a). At this ratio, hydrogen bonding was predicted between the **FM1** monomer and tyramine's hydroxyl, acting as an acceptor (Figure 3.2-1b). Moreover, these calculations predicted the possible binding of the **FM1** monomer with the protonated primary amine group of tyramine (Figure 3.2-1b). The calculated Gibbs free energy change of

formation of the **FM1**-tyramine complex (at the 2:1 molar ratio) was appreciable, equalling to  $\Delta G = -180$  kJ/mol.

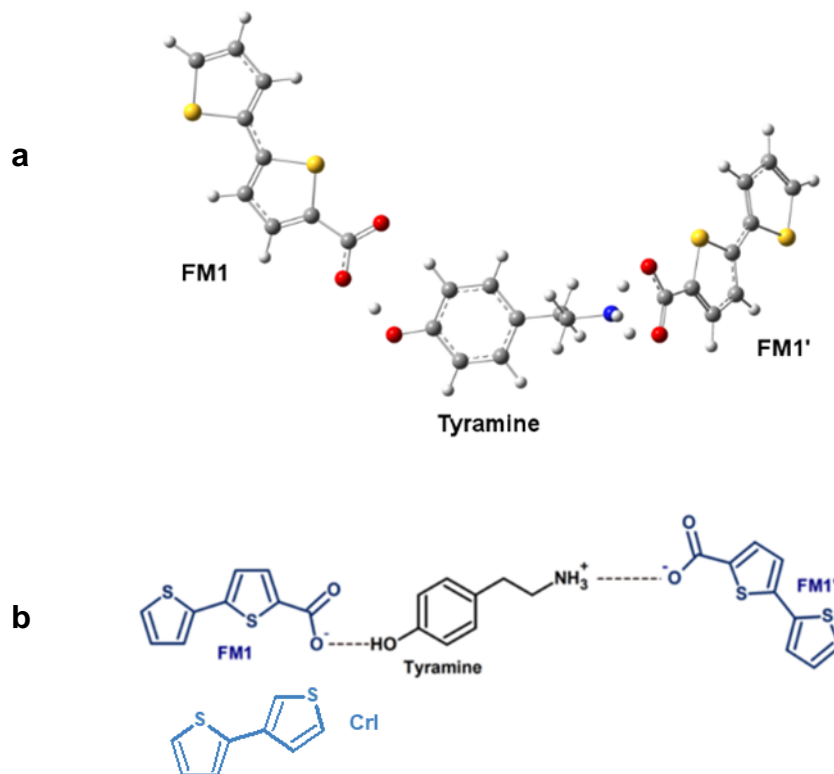


**Figure 3.2-1.** (a) DFT optimized structures with the B3LYP functional and the 3-21g(\*) basis set at room temperature and (b) structural formulas of the tyramine pre-polymerization complexes containing two monomer **FM1** molecules, one tyramine molecule, and one 2,3-bithiophene cross-linking molecule. The effect of the acetonitrile solvent was approximated with the PCM.

The pre-polymerization complexes of the **FM1**-tyramine in the acetonitrile solvent were electropolymerized in the presence of the 2,3-bithiophene cross-linking monomer under potentiodynamic conditions on the 0.75-mm diameter Pt electrodes to form a film of the molecularly imprinted polymer marked as **MIP-1**. The potential was scanned for five cycles from 0 to 1.30 V vs. Ag quasi-reference electrode (Figure 3.2-2a). The non-imprinted polymer (**NIP-1**) films were deposited under the same conditions but without the tyramine template (Figure 3.2-2b). During the **MIP-1** and **NIP-1** film deposition, an anodic peak at  $\sim 1.25$  V vs. Ag quasi-reference electrode was observed. This peak increased with each consecutive cycle. That indicates successful electropolymerization and deposition of a conducting polymer film.

Furthermore, a cathodic peak at 1.00 V vs. Ag quasi-reference electrode appearing in the second cycle indicates possible electroreduction of the thiophene radical cations generated during the initial anodic scan, confirming successful polymer film deposition. The CV and DPV experiments in the presence of the  $\text{Fe}(\text{CN})_6^{4-}/\text{Fe}(\text{CN})_6^{3-}$  redox probe proved electrode surface complete coating with the **MIP-1** film because the current after film deposition was negligible (Figure 3.2-2c and Figure 3.2-2d curve 1).

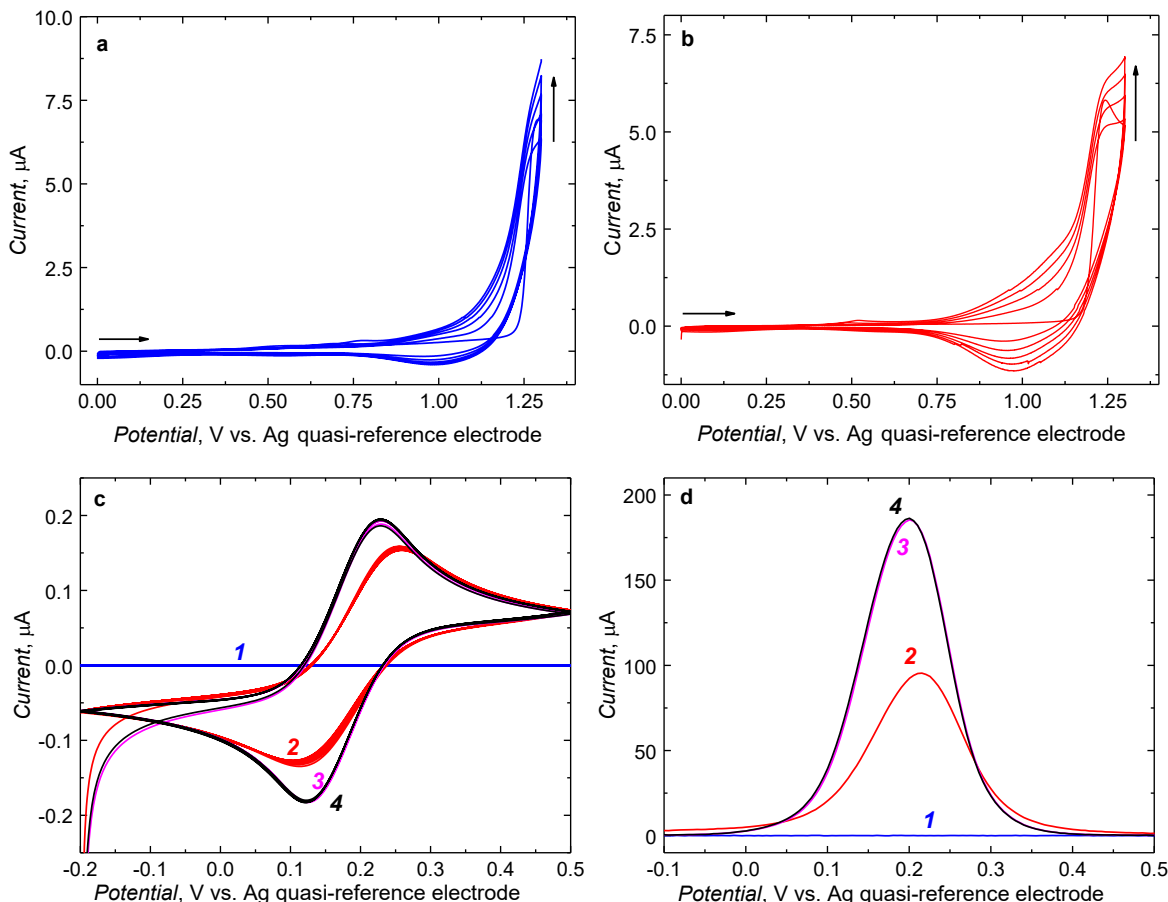


**Figure 3.2-2.** Current-potential curves recorded for deposition of the (a) **MIP-1** using a 50  $\mu\text{M}$  tyramine, 100  $\mu\text{M}$  FM1, 500  $\mu\text{M}$  2,3'-bithiophene, and 100 mM (TBA)ClO<sub>4</sub> acetonitrile solution (b) **NIP-1** films using a 100  $\mu\text{M}$  FM1, 500  $\mu\text{M}$  2,3'-bithiophene, and 100 mM (TBA)ClO<sub>4</sub> acetonitrile solution on 0.75-mm diameter Pt disk electrodes at potential ranging from 0 to 1.30 V vs. Ag quasi-reference electrode at a scan rate of 50 mV/s. (c) CV and (d) DPV curves recorded for 100 mM  $\text{K}_3[\text{Fe}(\text{CN})_6]$  and 100 mM  $\text{K}_4[\text{Fe}(\text{CN})_6]$  in PBS (pH = 7.4) for the **MIP-1** film-coated electrode (curve 1) before and after (curve 2) 30, (curve 3) 45, and (curve 4) 60 min of tyramine extraction with 0.1 M NaOH.

Subsequently, the tyramine template was extracted from the **MIP-1** film with 0.1 M NaOH under vigorous stirring for 30 to 60 min. After 45 min of extraction, a constant current of  $\sim 185 \mu\text{A}$  was reached (curve 3 in Figure 3.2-2d), indicating successful template removal.

Next, the **MIP-1** chemosensor was tested for its sensitivity to tyramine and selectivity against common interferences present in the human body (Figure 3.2-3). The DPV calibration plot for tyramine shows that the  $\text{Fe}(\text{CN})_6^{4-}/\text{Fe}(\text{CN})_6^{3-}$  DPV peak for the **MIP-1** chemosensor linearly decreases with the increase of the tyramine concentration (curve 1 in Figure 3.2-3). That proves that the **MIP-1** film is sensitive to tyramine in the concentration range of 2 to 7  $\mu\text{M}$ . Disadvantageously, however, those currents also decreased similarly for common interferences, including creatinine, urea, and glucose of the concentration range same as that of the tyramine analyte. Evidently, this chemosensor was not selective.

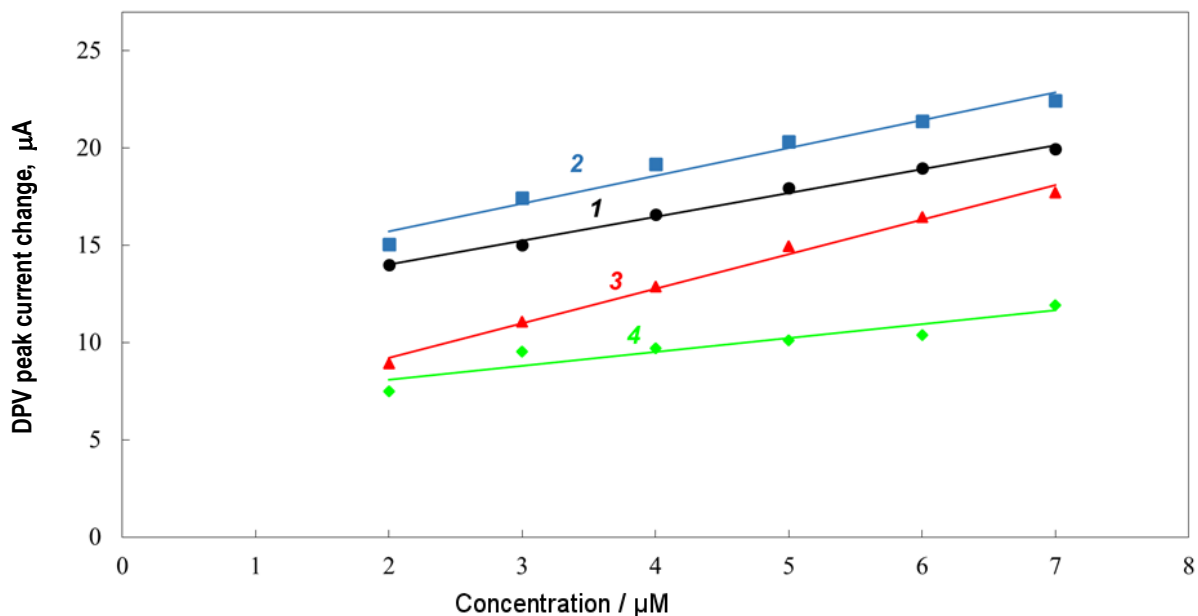


**Figure 3.2-3.** DPV calibration plots for the **MIP-1** film-coated electrode after tyramine extraction for (curve 1) tyramine, (curve 2) creatinine, (curve 3) urea, and (curve 4) glucose. All measurements were performed using the 0.75-mm diameter Pt disk electrode and 0.1 M  $\text{K}_3[\text{Fe}(\text{CN})_6]$  and 0.1 M  $\text{K}_4[\text{Fe}(\text{CN})_6]$  in 0.1 M PBS (pH = 7.4).

### 3.2.2 Functional monomers selection and electropolymerization of the MIP-2 chemosensor

To improve the selectivity of the chemosensor, the crown-ether-moiety-containing monomer, **FM2**, was selected as the second functional monomer to provide an additional interaction site for tyramine recognition. Structures of the **FM1**-tyramine-**FM2** complexes of the molar ratio of 2:1:1 were optimized, and their properties were examined using the DFT theory and basic quantum-chemical modeling (Figure 3.2-4a). The DFT calculations predicted that the **FM2** monomer would form a supramolecular complex with tyramine's protonated primary amine group (Figure 3.2-4b). Meanwhile, the positive charge of the tyramine's protonated primary amine group in the supramolecular complex would be neutralized by one molecule of the **FM1** monomer serving as the counter ion (Figure 3.2-4b). Moreover, these calculations forecast the formation of a hydrogen bond between one of the **FM1** molecules and tyramine's hydroxyl (Figure 3.2-4b). The calculated negative Gibbs free energy change accompanying the formation of the **FM1**-tyramine-**FM2** complex (at the 2:1:1 molar ratio) was much higher ( $\Delta G = -220$  kJ/mol) than the **FM1**-tyramine complex. A higher negative Gibbs free energy indicates the formation of very stable complexes, thus presumably leading to successful tyramine template imprinting and higher chemosensors selectivity.

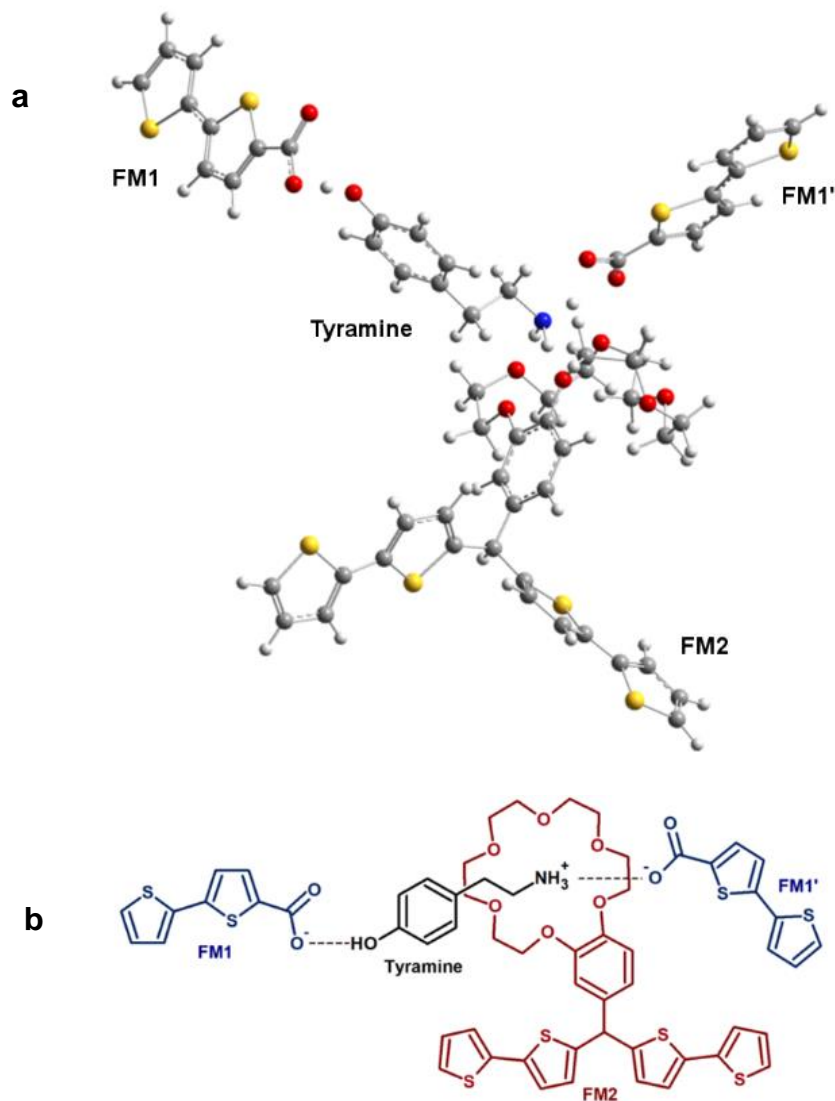


**Figure 3.2-4.** (a) DFT structure optimized with the B3LYP functional and the 3-21g(\*) basis set at room temperature and (b) structural formula of the **FM1**-tyramine-**FM2** pre-polymerization complex of the 2:1:1 molar ratio. The acetonitrile solvent effect was approximated with the PCM model.

The film of this polymer, marked as **MIP-2**, was deposited from the pre-polymerization **FM1**-tyramine-**FM2** complex solution under potentiodynamic conditions. **NIP-2** films were prepared under the same conditions except for the tyramine template absence. Initially, the **MIP-2** film was deposited on the electrode surface using five potential cycles (Figure 3.2-5a). However, the resulting film was relatively thick, making template extraction difficult (Figure 3.2-5b and 5c). Eventually, the extraction was unsuccessful after various attempts to alter the parameters, such as the extraction time and concentration of the extracting solution. The **MIP-**

2 film deposited using five cycles was not further studied. Therefore, the **MIP-2** and **NIP-2** films were deposited on the electrode surface using only two potential cycles, resulting in relatively thin films.

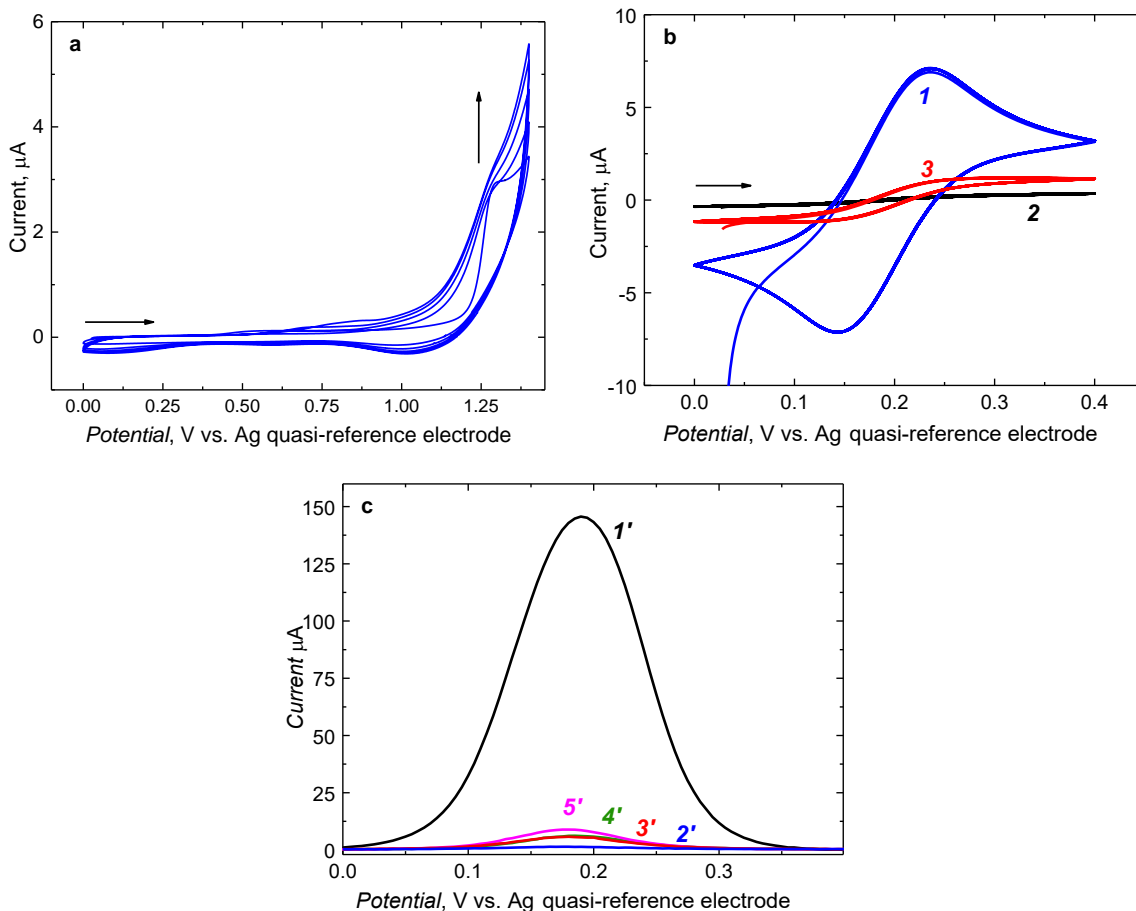


**Figure 3.2-5.** (a) Five-cycle potentiodynamic curve of deposition of the **MIP-2** film prepared using a 50  $\mu\text{M}$  tyramine, 100  $\mu\text{M}$  FM1, 50  $\mu\text{M}$  FM2, 500  $\mu\text{M}$  2,3'-bithiophene, and 100 mM (TBA)ClO<sub>4</sub> acetonitrile solution on the 0.75-mm Pt disk electrode for the potential ranging from 0 to 1.30 V vs. Ag quasi-reference electrode at a scan rate of 50 mV/s. (b) CV curves for 0.1 M K<sub>3</sub>[Fe(CN)<sub>6</sub>] and 0.1 M K<sub>4</sub>[Fe(CN)<sub>6</sub>] in PBS (pH = 7.4) on (curve 1) the bare Pt electrode, as well as the **MIP-2** film-coated Pt electrode (curve 2) before and (curve 3) after 150-min extraction in 10 M NaOH, and (d) DPV curves for 100 mM K<sub>3</sub>[Fe(CN)<sub>6</sub>] and 100 mM K<sub>4</sub>[Fe(CN)<sub>6</sub>] in 0.1 M PBS (pH = 7.4) recorded on (curve 1') the bare Pt electrode, as well as the MIP film-coated Pt electrode (curve 2') before and after (curve 3') 60, (curve 4') 80, and (curve 5') 150 min of tyramine template extraction in 10 M NaOH.

The shape of the potentiodynamic curve and the current value recorded for deposition of the **MIP-2** (Figure 3.2-6a) and **NIP-2** (Figure 3.2-6b) film resembled those for the deposition of the **MIP-1** (Figure 3.2-2a) and **NIP-1** (Figure 3.2-2b) films. However, anodic peaks were

slightly shifted positively (to 1.30 V vs. Ag quasi-reference electrode) compared to **MIP-1**, where the anodic peaks were at 1.25 V vs. Ag quasi-reference electrode.

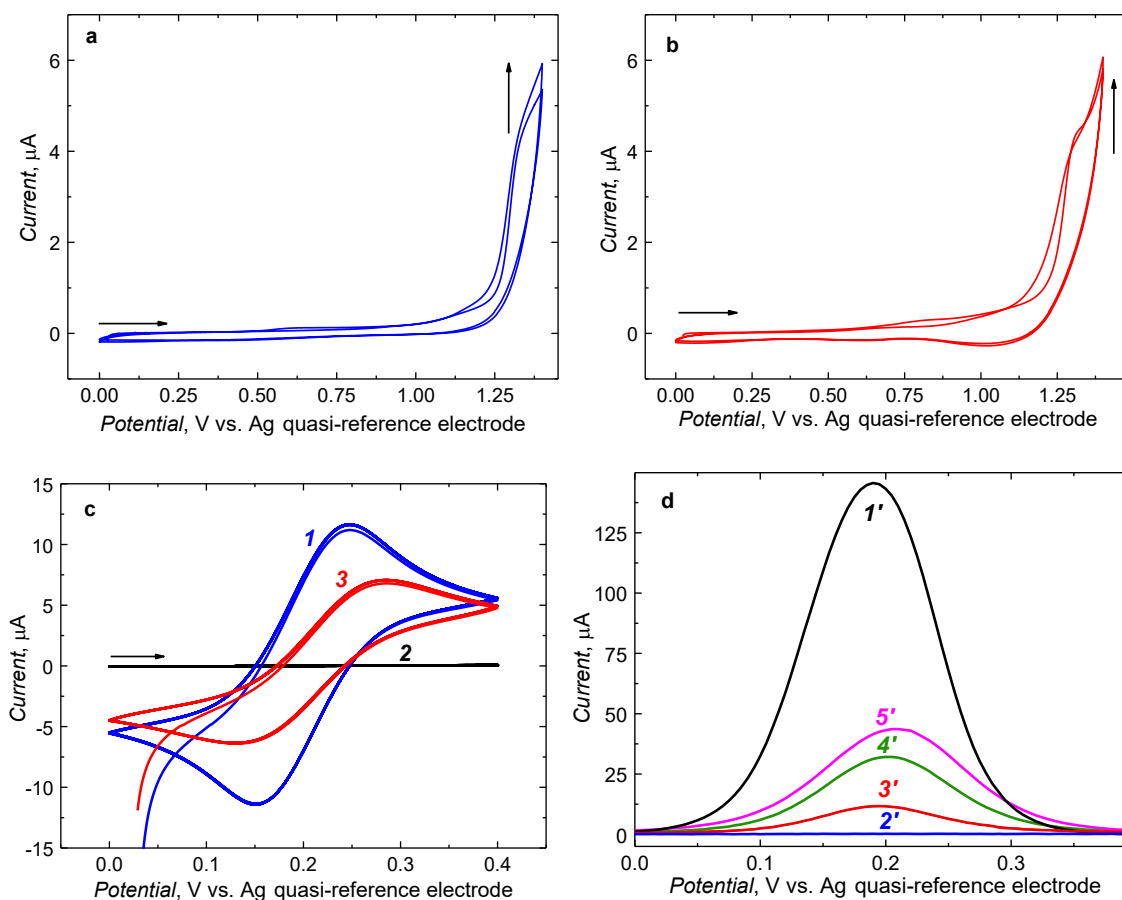


**Figure 3.2-6.** Two-cycle potentiodynamic curves recorded at 0,75-mm Pt disk electrode at scanning potential of 0 to 1.30 V vs. Ag quasi-reference electrode at a scan rate of 50 mV/s for (a) 50 μM tyramine, 100 μM FM1, 50 μM FM2, 500 μM 2,3'-bithiophene, and 100 mM (TBA)ClO<sub>4</sub> acetonitrile solution that lead to deposition of an **MIP-2** film and (b) 100 μM FM1, 50 μM FM2, 500 μM 2,3'-bithiophene, and 100 mM (TBA)ClO<sub>4</sub> acetonitrile solution that result in an **NIP-2** film. (c) CV curves for 0.1 M K<sub>3</sub>[Fe(CN)<sub>6</sub>] and 0.1 M K<sub>4</sub>[Fe(CN)<sub>6</sub>] in PBS (pH = 7.4) on (curve 1) the bare Pt electrode, as well as the **MIP-2** film-coated Pt electrode (curve 2) before and (curve 3) after 150-min tyramine template extraction in 0.1 M NaOH, and (d) DPV curves for 100 mM K<sub>3</sub>[Fe(CN)<sub>6</sub>] and 100 mM K<sub>4</sub>[Fe(CN)<sub>6</sub>] in 0.1 M PBS (pH = 7.4) recorded on (curve 1') the bare Pt electrode, as well as the **MIP-2** film-coated Pt electrode (curve 2') before and after (curve 3') 10, (curve 4') 60, and (curve 5') 150 min of extraction in 0.1 M NaOH.

This shift suggests forming a more stable pre-polymerization complex, predicted by the DFT calculation. The resulting **MIP-2** and **NIP-2** films were less conductive than the **MIP-1** and **NIP-1** films. The CV and DPV experiments demonstrated the successful film deposition and

complete blockage of the redox probe access to the electrode, although the films were deposited using only two potential cycles (Figure 3.2-6c curve 2 and Figure 3.2-6d curve 2'). Subsequently, the tyramine template was extracted from the MIP-2 film under vigorous stirring in 0.1 M NaOH for 10 to 150 min. Notably, the DPV peak reached a constant ( $\sim 45 \mu\text{A}$ ) value in the redox probe presence after 150 min template extraction with NaOH (Figure 3.2-6d curve 5'). After template extraction, the faradaic currents for the redox probe increased in both CV and DPV curves (Figure 3.2-6c curve 3 and Figure 3.2-6d curve 5'), confirming the presence of the molecular cavities.

### 3.2.3 MIP-2 and NIP-2 films characterizing

#### PM-IRRAS measurements

The PM-IRRAS measurements were performed to identify chemical bonds before and after tyramine template extraction. Results of these measurements are essential to evaluate the deposited film and to confirm cavity formation indirectly. Multiple bands in the region of 1440 to 1520  $\text{cm}^{-1}$  are seen for all deposited films. These are assigned to the thiophene aromatic ring C=C bond stretching (Figure 3.2-7).<sup>202</sup> A well-pronounced band between 1750 and 1700  $\text{cm}^{-1}$ , present in the spectra for all films, is due to C=O bond stretching. The C=O bands in spectra for all deposited films indicate that all monomers present in the pre-polymerization complex solution were successfully copolymerized and within the polymer film deposited on the electrode surface. Moreover, the C-H bond stretching vibration in aromatic and aliphatic moieties band is present in spectra for all films at  $\sim 3100$  and  $\sim 2900 \text{ cm}^{-1}$ .

The N-H stretching vibration band was expected to be present in the spectrum for the as-deposited **MIP-2** film because of the presence of the tyramine template in it. However, this band was absent. On the contrary, a low-intensity N-H stretching vibration band was present at  $\sim 3260 \text{ cm}^{-1}$  after tyramine extraction (spectrum 2 in Figure 3.2-7). This low intensity of the N-H stretching band is expected because the tyramine content in the deposited **MIP-2** film is relatively low compared to the content of the monomer. Moreover, the **MIP-2** film was deposited using only two potential cycles. Although this film was thin (see AFM film characterization) after two potentiodynamic cycles, it completely blocked the redox probe transport through the film (curve 2 in Figure 3.2-6c). As a result, the signal-to-noise ratio in

the PM-IRRAS spectrum for the **MIP-2** film is low, and therefore the N-H stretching vibration band is not seen just after film deposition.

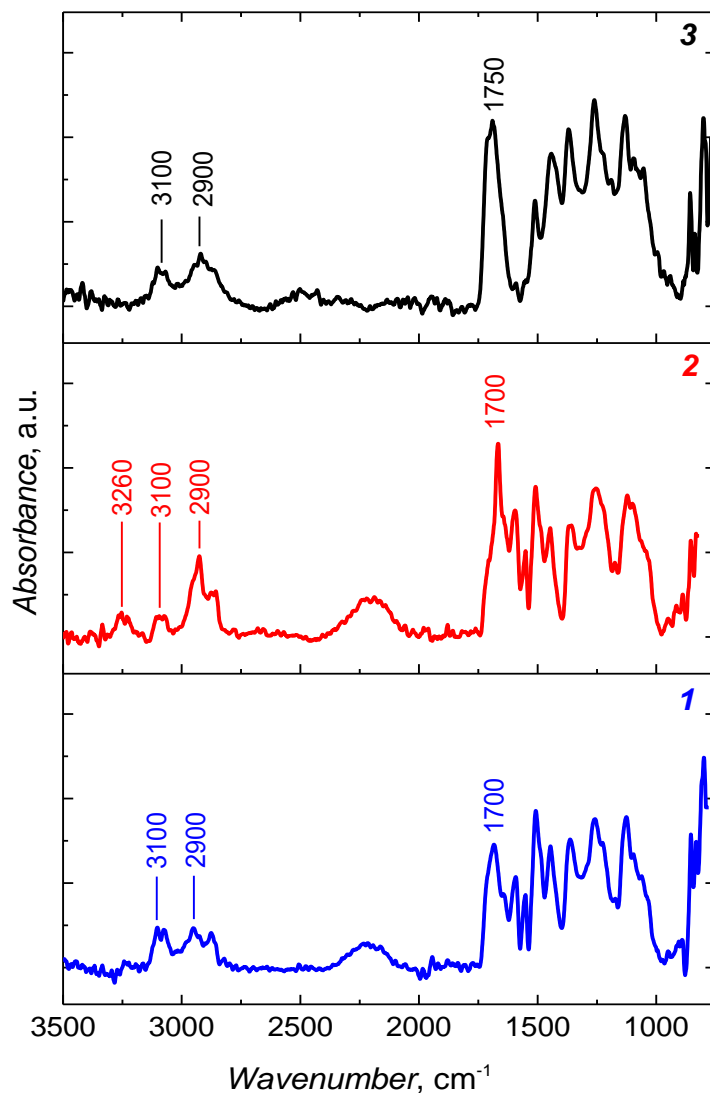


**Figure 3.2-7.** PM-IRRAS spectra for **MIP-2** film-coated electrodes (1) before and (2) after tyramine template extraction for 150 min in 0.1 M NaOH, and (3) the **NIP-2** film-coated electrode.

Furthermore, one can speculate that the formation of the supramolecular complex of the tyramine protonated primary amine group with the crown ether moiety of **FM2** may cause a shift of the N-H stretching vibration band to the wavenumber lower than expected because the N-H stretching vibration band for primary and secondary amines is positioned at 3200 to

3500  $\text{cm}^{-1}$ . Thus, it might be possible (or not) that the N-H stretching band overlaps with the C-H stretching band in the 3100 to 3000  $\text{cm}^{-1}$  region.

### **XPS measurements**

The XPS measurements were performed to determine the elemental composition of **MIP-2** and **NIP-2** films before and after tyramine template extraction. In XPS, the MIP film is probed at the 1 to 2 nm depth. Only the elemental surface composition and not polymer bulk can be determined at this depth. However, the elemental composition (even at the surface level) changes after chemical treatment, and the XPS is very sensitive to such changes. Therefore, the resultant XPS data are helpful to confirm both elemental changes after chemical treatment and template removal.

The XPS evaluated the content of four primary elements, namely, nitrogen, oxygen, carbon, and sulfur (Tables 3.2-1). Among them, the nitrogen content is the most significant. This content in the **MIP-2** film decreased substantially from 1.43 at.% just after deposition to 0.69 at.% after template extraction. The N-to-C ratio was calculated for the **MIP-2** film before and after template extraction (Table 3.2-2). The calculation revealed that the N-to-C ratio for the **MIP-2** film after extraction (0.0095) declined to less than half of its initial value (0.0207). There are two possible reasons for these significant changes in the relative nitrogen content, i.e., (i) tyramine removal or/and (ii) tetrabutylammonium cation entrapment. Moreover, tyramine was extracted from the **NIP-2** film in the same manner as from the **MIP-2** film to confirm these possibilities. For the **NIP-2** film, the XPS data revealed that the nitrogen content decreased only slightly after the extraction (Tables 3.2-1). Therefore, the decrease in the nitrogen content in the **MIP-2** film after extraction can be assigned to the tyramine template removal rather than the removal of the  $\text{TBA}^+$  cation.

The sulfur content in MIP films provides information about the polythiophene polymer backbone content. After tyramine extracting from the **MIP-2** film, the sulfur content slightly decreased to 8.2 at.% from its original value of 12.8 at.% determined immediately after polymerization. This decrease might be caused by using a strongly basic aqueous solution for the extraction. Presumably, this extraction caused rearrangement of the surface polymer chains so that the hydrophilic carboxyl groups and crown ether moieties were exposed to the solution, thus hiding the hydrophobic polythiophene backbone inside the polymer. Moreover, removing

oligomers and traces of unreacted monomers during the extraction could decrease the sulfur signal intensity.

**Table 3.2-1.** The XPS determined the element content of the **MIP-2** and **NIP-2** films.

Element	Element content, atomic percent			
	MIP-2 before template extraction	MIP-2 after template extraction	NIP-2 before template "extraction"	NIP-2 after template "extraction"
<b>O</b>	16.70	18.07	15.59	22.24
<b>N</b>	1.43	0.69	2.26	1.73
<b>C</b>	69.06	73.08	82.15	65.09
<b>S</b>	12.81	8.16	15.59	10.94

**Table 3.2-2.** The atomic percent ratio of nitrogen (N) to carbon (C) in the **MIP-2** and **NIP-2** films was determined with XPS before and after tyramine template extraction.

Polymer film	N-to-C atomic percent ratio	
	before extraction	after extraction
<b>MIP-2</b>	0.0207	0.0095
<b>NIP-2</b>	0.0275	0.0266

### AFM imaging

The MIP and NIP films were AFM imaged to determine their thickness, morphology, and topography. The determined thickness and nanomechanical parameters are shown in Table 3.2-3. An MIP film on the Au-layered glass slide electrode was first scratched, and those scratches were imaged to calculate the average thickness of the film. The films deposited using two potential cycles were expected to be thin. This expectation was supported by the AFM result, where the **MIP-2** and **NIP-2** thickness was 19 ( $\pm 2$ ) and 24 ( $\pm 3$ ) nm, respectively (Table 3.2-3). After tyramine template extraction, the **MIP-2** film thickness slightly decreased

to 16 ( $\pm 1$ ) nm, whereas the **NIP-2** film thickness remained almost the same, equalling 24 ( $\pm 2$ ) nm.

Moreover, surface roughness was evaluated for the **MIP-2** and **NIP-2** films. This roughness is a parameter describing surface irregularities. It is used to determine how smooth the film surface is. Moreover, this parameter determines the film deposition quality, which eventually helps adjust the deposition parameters to obtain the desired film smoothness depending on the preferred application. Furthermore, surface roughness is essential for characterizing both conducting and semiconducting polymer films. That is because it reflects the film surface area, which affects the mass transport through the polymer-solution interface, i.e., the analyte transport in this case.<sup>203</sup> The roughness of the **MIP-2** and **NIP-2** as-deposited films were 2.7 ( $\pm 0.3$ ) and 1.9 ( $\pm 0.2$ ) nm, respectively (Table 3.2-3). Apparently, the **MIP-2** film was rougher than the bare gold electrode surface and the **NIP-2** film. However, the **NIP-2** film roughness increased significantly after tyramine extraction, amounting to 2.7 ( $\pm 0.3$ ) nm, whereas the **MIP-2** film roughness decreased to 1.5 ( $\pm 0.1$ ) nm.

Additionally, other nanomechanical parameters, including Young's modulus and adhesion, were determined to confirm film deposition. The **MIP-2** and **NIP-2** film Young's modulus was  $\sim 6$  GPa, which corresponds to the value reported for the thiophene films.<sup>204</sup> However, this value is much lower than that for the bare gold, estimated to be 42 GPa. Young's modulus for the bare gold surface is only an estimation as the tip spring constant was not modified to measure highly rigid objects. Besides, Young's modulus decreased for both the **MIP-2** and **NIP-1** film after the extraction, indicating film 'softening.' Adhesion of the Si tip to the polymer film surface was in the range of 5 to 8 nN. This value is much lower than 20 nN for the bare gold electrode surface. This weaker adhesion is caused by opposite hydrophilic properties of the polythiophene film and the AFM Si tip, i.e., the former is hydrophobic, and the latter is hydrophilic, being coated with a few-nm-thick silicon oxide film.

The AFM images of **MIP-2** and **NIP-2** films are presented in Figure 3.2-8. These thin films' topography was highly influenced by the topography of the underlying gold surface. Circular grains with average diameters ranging from 40 to 70 nm were observed for all films. However, the morphology of grains varied for each film. For instance, the **MIP-2** and **NIP-2** as-deposited films were composed of uneven and unsymmetrical grains. The large and small

grains seemed fused in these films (Figure 3.2-8a and 8b), unlike the uniform and round grains in the bare gold electrode (Figure 3.2-8c).

**Table 3.2-3.** The **MIP-2** and **NIP-2** film morphological and nanomechanical parameters derived from AFM images.

Sample	Film thickness, nm	Film roughness, $R_a$ , nm	Young's modulus, GPa	Adhesion, nN
Bare gold electrode	NA	$1.7 \pm 0.2$	$42.0 \pm 1.5^a$	$20.0 \pm 9.0$
<b>MIP-2</b> before tyramine extraction	$19 \pm 2$	$2.7 \pm 0.3$	$6.3 \pm 0.1$	$6.5 \pm 1.4$
<b>MIP-2</b> after tyramine extraction	$16 \pm 1$	$1.5 \pm 0.1$	$4.0 \pm 1.7$	$5.2 \pm 0.8$
<b>NIP-2</b> before tyramine extraction	$24 \pm 3$	$1.9 \pm 0.2$	$6.0 \pm 0.5$	$5.7 \pm 1.5$
<b>NIP-2</b> after tyramine extraction	$24 \pm 2$	$2.7 \pm 0.3$	$2.2 \pm 0.2$	$8.4 \pm 2.3$

<sup>a</sup>This value is an estimate only because the tip spring constant value was not adjusted to image films as rigid as Au.

Furthermore, the **MIP-2** film morphology significantly changed after tyramine extraction (Figure 3.2-8a'). The **MIP-2** film grains appear more even and globular, resembling grains in the bare gold electrode. The estimated average grain diameter for the tyramine-extracted **MIP-2** film was 65 nm, higher than 49 nm for the bare gold electrode. The **MIP-2** morphology changes after extraction indicate removing the weaker bound films' parts. In contrast, the **NIP-2** film's grain morphology was slightly altered after the extraction. But overall, the grains retained the characteristics of the non-extracted **NIP-2** film (Figure 3.2-b'). Presumably, there are fewer (or no) weakly bound parts in the **NIP-2** films. This inference is supported by the value of adhesion of the **NIP-2** film to the gold support after tyramine extraction, which was 8.4 ( $\pm 2.3$ ) nN. This value was higher than the 5.2 ( $\pm 0.8$ ) nN value for the **MIP-2** film subjected to a similar treatment. The AFM imaging and nanomechanical studies further confirmed the successful polymer films deposition on the gold electrodes and the removal of the weakly bound parts of the **MIP-2** films.

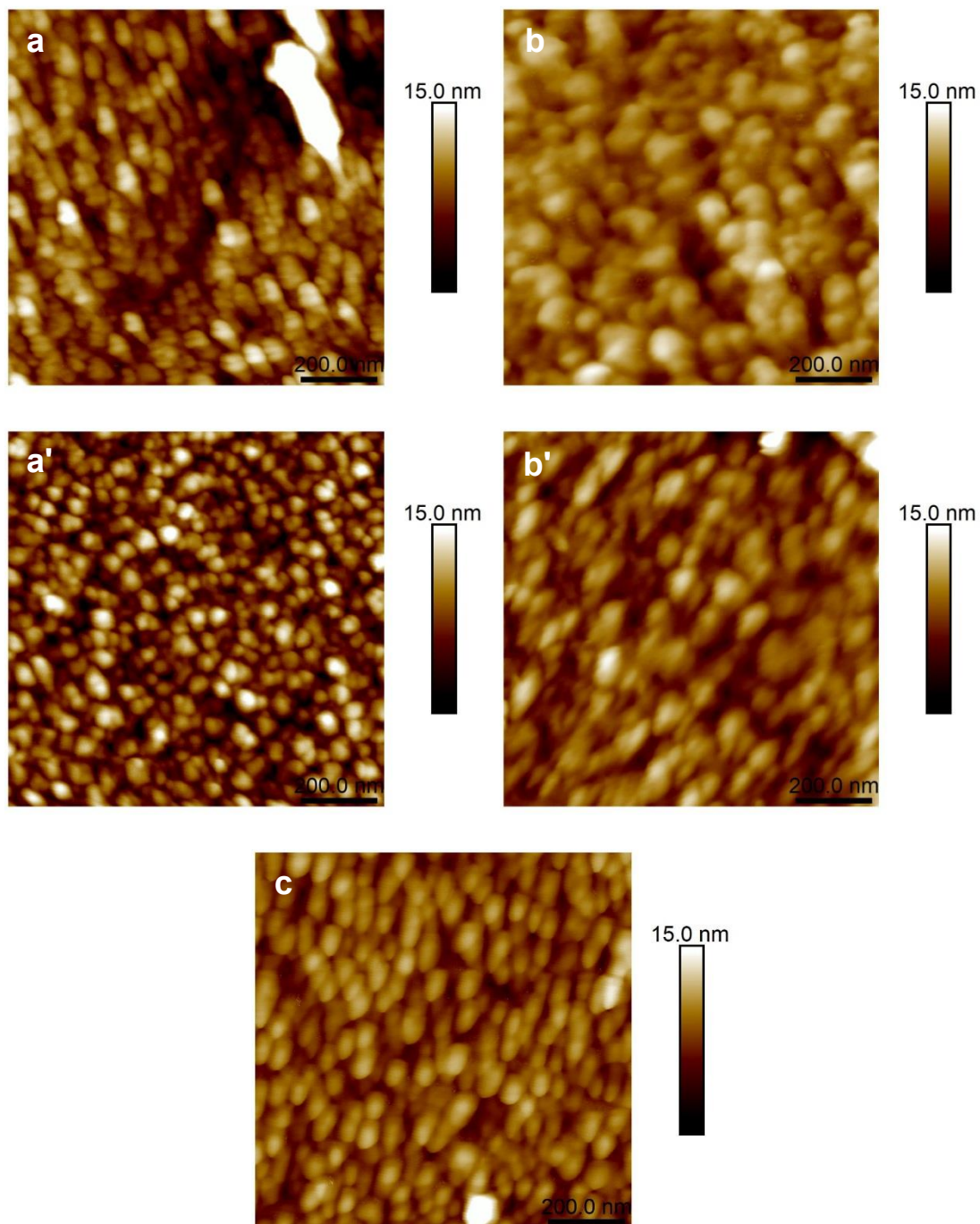


**Figure 3.2-8.** AFM images of the (a) and (a') **MIP-2** as well as (b) and (b') **NIP-2** film coated on (c) (glass slide)/Ti/Au; (a) and (b) before as well as (a') and (b') after tyramine extraction for 150 min in 0.1 M NaOH.

## SEM imaging

SEM imaging provided information about the film morphology. Figure 3.2-9 displays the results of the SEM imaging of the **MIP-2** and **NIP-2** films before and after extraction. It appeared that **MIP-2** and **NIP-2** films uniformly coated electrode surfaces after polymer deposition. No cracks nor pores were observed. No significant changes were found after tyramine extraction involving film chemical treatment with NaOH.

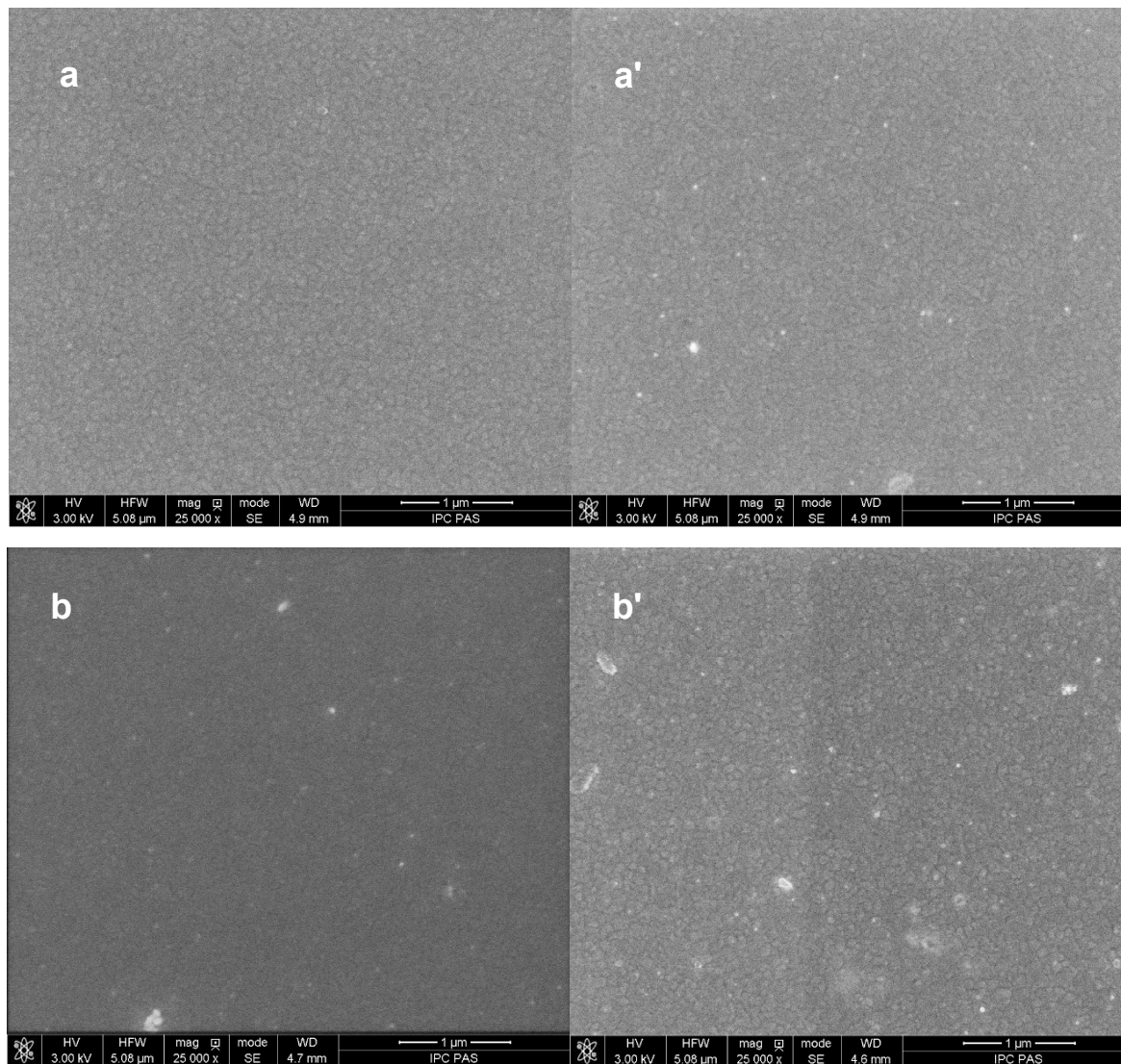


**Figure 3.2-9.** SEM images of (a and a') **MIP-2** and (b and b') **NIP-2** film-coated (glass slide)/Ti/Au electrodes; (a and b) before and (a' and b') after tyramine extraction for 150 min in 0.1 M NaOH.

### 3.2.4 Determining MIP-2 film-coated electrode's selectivity with DPV and EIS transduction

The prepared **MIP-2** film-coated electrodes deposited from the pre-polymerization complex solution containing **FM1**, **FM2**, and tyramine were applied for the DPV determination of tyramine. The  $\text{Fe}(\text{CN})_6^{4-}/\text{Fe}(\text{CN})_6^{3-}$  DPV peak for the **MIP-2** film coated electrode decreased with the increase of the tyramine concentration ranging from 290  $\mu\text{M}$  to 2.64 mM (Figure 3.2-10a). The DPV peak changes fulfilled the following linear regression equation;  $(I_{\text{DPV},0} - I_{\text{DPV},s}) [\mu\text{A}] = -0.67(\pm 0.71) [\mu\text{A}] + 13.39(\pm 0.86) [\mu\text{A}/\text{mM}] C_{\text{tyramine}}$ , [mM]. The correlation coefficient and the LOD at  $S/N = 3$  were  $R^2 = 0.9859$  and  $\text{LOD} = 159 \mu\text{M}$ , respectively. The control **NIP-2** film was also subjected to a similar experiment. The DPV peak decreased with the tyramine concentration increase for the **NIP-2** film-coated electrode as well. However, the DPV peak changes were not as significant (Figure 3.2-10b). The apparent imprinting factor, calculated as the ratio of slopes of the calibration plots constructed for **MIP-2** and **NIP-2** film-coated electrodes, was appreciable, equalling  $IF = 5.6$ . This high imprinting factor indeed confirms the successful imprinting of the tyramine template.

The **MIP-2** chemosensor selectivity to common biological interferences was examined (Figure 3.2-10c). Unlike the **MIP-1** chemosensor, the **MIP-2** chemosensor exhibited high selectivity towards creatinine, urea, and glucose. The calculated selectivity coefficient was 17.7 for creatinine, whereas the chemosensor's response to glucose and urea was negligible. Moreover, the selectivity of the **MIP-2** chemosensor to tyramine's structural analogs, such as L-tyrosine, adrenaline, and D-phenylalanine, was examined. At low concentrations, i.e., below 0.5 mM, the **MIP-2** chemosensor response to these three analogs resembled that to tyramine. However, at high concentrations, i.e., above 0.5 mM, the **MIP-2** chemosensor was more selective to these interferences. The calculated selectivity coefficients were 3.2, 3.8, and 3.6, respectively.

The EIS measurements were performed for the same solutions immediately after the DPV measurements to understand better mechanistic aspects of the chemosensor response. The resultant responses were used to construct Nyquist and Bode plots. For the **MIP-2** chemosensor, semicircles were well-defined in Nyquist plots. The semicircle diameter represents the charge transfer resistance,  $R_{\text{ct}}$ , of the faradaic process of the redox probe (Figure 3.2-11a).

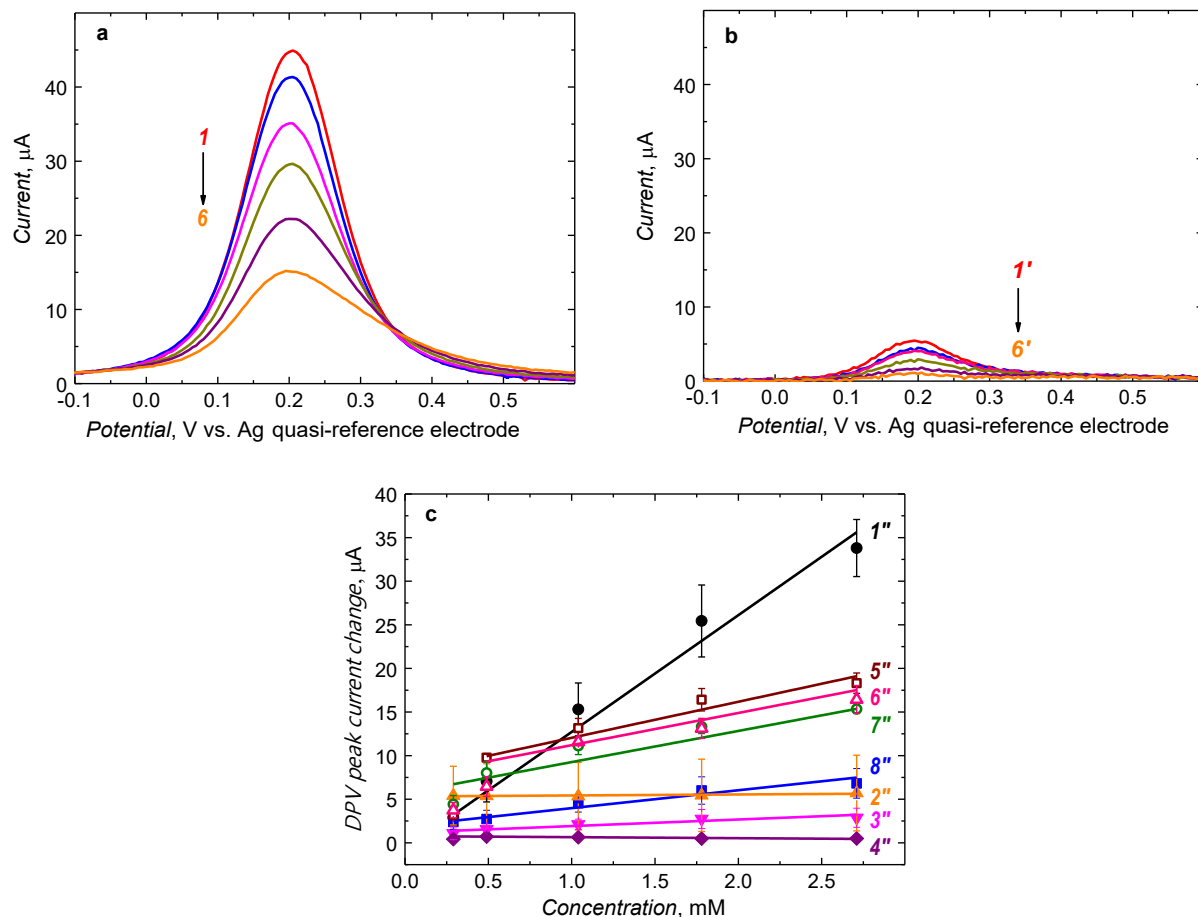


**Figure 3.2-10.** DPV curves recorded for (a) **MIP-2** and (b) **NIP-2** film-coated 0.75-mm diameter Pt disk electrodes (curves *1* and *1'*) after tyramine extraction and in the presence of (curves *2* and *2'*) 290  $\mu\text{M}$ , (curves *3* and *3'*) 490  $\mu\text{M}$ , (curves *4* and *4'*) 1.01 mM, (curves *5* and *5'*) 1.76 mM, or (curves *6* and *6'*) 2.64 mM tyramine in 0.1 M  $\text{K}_3[\text{Fe}(\text{CN})_6]$  and 0.1 M  $\text{K}_4[\text{Fe}(\text{CN})_6]$ , in 0.1 M PBS (pH = 7.4). (c) Calibration plots of DPV peak changes with the concentration change of (curves *1''* and *8''*) tyramine, (curve *2''*) glucose, (curve *3''*) creatinine, (curve *4''*) urea, (curve *5''*) L-tyrosine, (curve *6''*) adrenaline, and (curve *7''*) D-phenylalanine on the (curves *1''* – *7''*) **MIP-2** and (curve *5''*) **NIP-2** film coated electrode.

It increased with the increase of the tyramine concentration, indicating the increase of the charge transfer resistance. Moreover, the semicircles were significantly flattened at high tyramine concentrations. Most likely, the inhomogeneity of the electrode surfaces caused this effect. Moreover, the diffusion-controlled process, represented by the Warburg impedance, was observed in these plots in low-frequency ranges (above 10  $\text{k}\Omega$ ). Generally, the studied process is entirely diffusion-controlled if manifested by a straight line of the  $45^\circ$  slope in the low-frequency range. That means that the real impedance equals the imaginary component's

absolute value.<sup>205</sup> However, in these plots, these slopes were  $37 (\pm 2)^\circ$ , revealing the possibility of the **MIP-2** film influencing the redox probe diffusion.

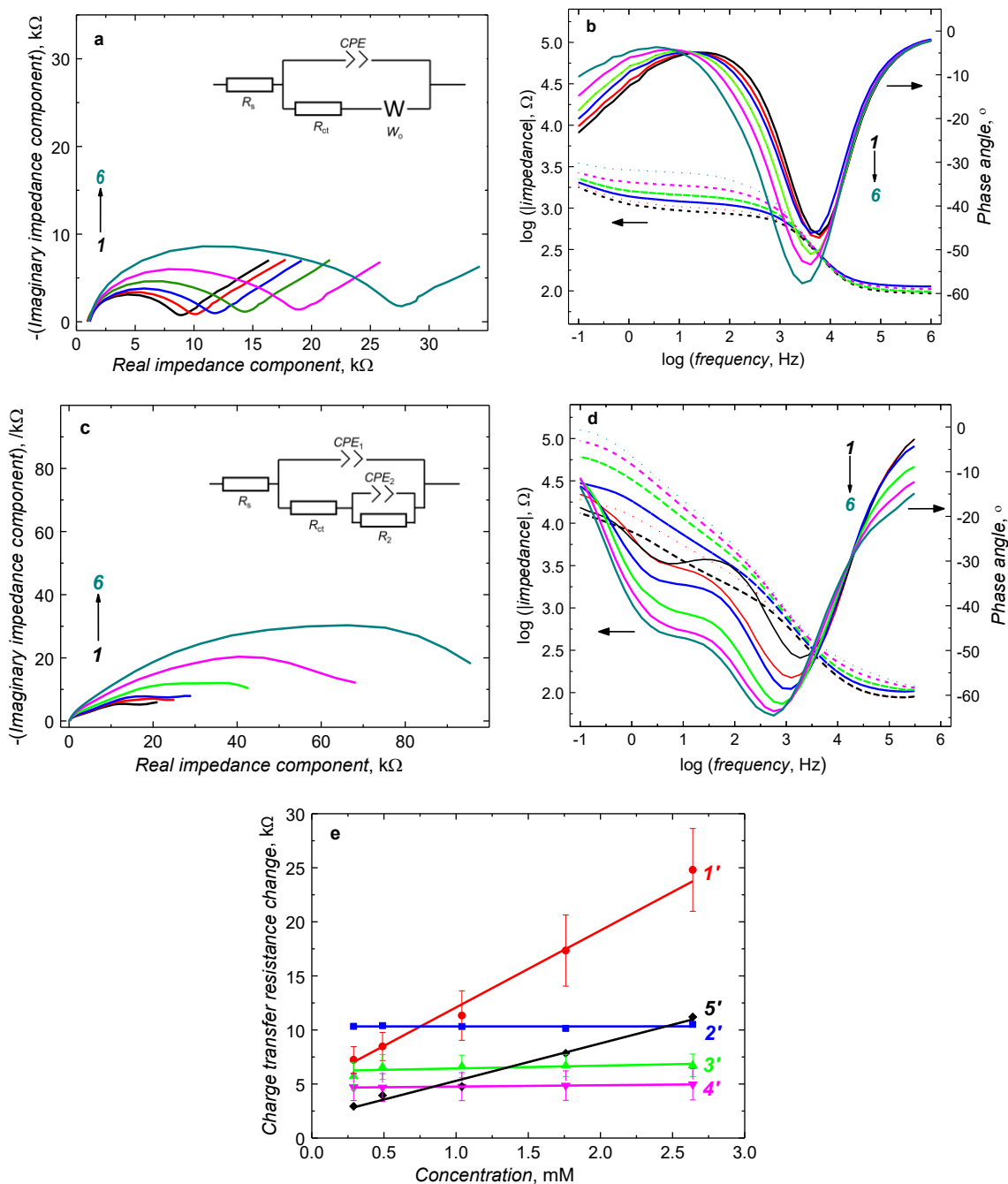


**Figure 3.2-11.** The (a and c) Nyquist and (b and d) Bode plots for 0.75-diameter Pt disk electrodes coated with the (a and b) **MIP-2** and (c and d) **NIP-2** film and immersed in 0.1 M  $\text{K}_3[\text{Fe}(\text{CN})_6]$  and 0.1 M  $\text{K}_4[\text{Fe}(\text{CN})_6]$ , in 0.1 M PBS (pH = 7.4). (Curve 1) after tyramine extraction, and then in the presence of (curve 2) 290  $\mu\text{M}$ , (curve 3) 490  $\mu\text{M}$ , (curve 4) 1.04

mM, (curve 5) 1.76 mM, and (curve 6) 2.64 mM tyramine. (e) Calibration plots of the charge transfer resistance change with the change of concentration of (curve 1') tyramine, (curve 2') urea, (curve 3') glucose, and (curve 4') creatinine on the tyramine-extracted **MIP-2** film coated electrode as well as (curve 5') tyramine on the **NIP-2** film coated electrode. Equivalent circuits fitted to the EIS spectra for (a, inset) **MIP-2** and (c, inset) **NIP-2** film-coated electrodes.

Furthermore, these lines remained unchanged in the presence of tyramine, suggesting that the diffusion-rate control for this system is independent of the tyramine concentration.<sup>206</sup> Therefore, the chemosensor's response did not originate from shrinking nor expanding the **MIP-2** film when it bound the analyte molecules in imprinted cavities. Instead, the changes in the **MIP-2** film's conductivity were the reasons for the chemosensor's response.<sup>118</sup> The Bode plots (Figure 3.2-11b), where only one peak was present in the frequency range of 1 to 10 kHz, support this inference. This peak corresponds to the faradaic process of the redox probe. The electrochemical system was approximated with a modified Randles-Ershler equivalent circuit,  $R_s + CPE / (R_{ct} + W_o)$ , where  $R_s$  is the solution resistance,  $R_{ct}$  is the charge transfer resistance,  $CPE$  is the constant phase element, and  $W_o$  is the Warburg impedance. A calibration plot (Figure 3.2-10e) was constructed based on the Nyquist plot responses. In this plot, the  $R_{ct}$  changes were linearly dependent on the tyramine concentration in the range of 290  $\mu$ M up to 2.64 mM. This plot obeyed the following linear regression equation.  $(R_{ct}) [k\Omega] = 4.97 (\pm 0.38) [k\Omega] + 7.11 (\pm 0.45) [k\Omega/mM] c_{\text{tyramine}} [mM]$ . At  $S/N = 3$ , the correlation coefficient and the LOD were  $R^2 = 0.9843$  and  $LOD = 168 \mu\text{M}$  tyramine. The calculated selectivity coefficient for creatinine was as high as 28, and the **MIP-2** chemosensor responded neither to the glucose nor urea concentrations changes.

A similar experiment was subjected to the **NIP-2** film-coated electrodes as well. Apparently, the EIS spectra for the **NIP-2** film (Figure 3.2-11c and 11d) differed from those recorded for the **MIP-2** film (Figure 3.2-11a and 11b). In the Nyquist plot for the **NIP-2** film, one full and one partial semicircle were present. Tiny full semicircles were generated at the beginning of the high-frequency range (Figure 3.2-11c). The curved lines that accompanied these parts of Nyquist plots formed merely partial semicircles. Those might have developed because the redox probe diffusion through the porous non-conductive **NIP-2** film was hindered.

Moreover, the partial semicircles' diameters increased with the tyramine concentration increase, suggesting that this system's diffusion-control process depends on the tyramine

concentration. Similarly, there were two peaks for the **NIP-2** film in the Bode plots (Figure 3.2-11d), one in a higher frequency range, similarly to the **MIP-2** film (Figure 3.2-11b), and the other in the frequency range of 1 to 10 Hz. The redox probe diffusion through the porous polymer film might be responsible for this second peak.

Presumably, the **MIP-2** and **NIP-2** film-coated electrodes exhibit different electrochemical response mechanisms. The "gate effect" mechanism is operative for the **NIP-2** film-coated electrode, where the redox probe diffuses to the electrode surface through a non-conductive porous thin polymer film for charge exchange.<sup>113</sup> Analytes ingress causes the film to expand or to shrink, thus leading to pore widenings and, that way, affecting the redox probe diffusion.<sup>206</sup> For this system, the Randles-Ershler equivalent circuit (Figure 3.2-11a, inset) did not fit well. Therefore, the circuit shown in Figure 3.2-11c was used to fit the spectra recorded for the **NIP-2** film-coated electrode.<sup>207,208,209</sup> The apparent imprinting factor,  $IF = 2.1$ , was calculated from the ratio of slopes of the  $R_{ct}$  changes of the **MIP-2** and **NIP-2** film-coated electrodes with the tyramine concentration changes. This low  $IF$  value is caused by the different fitting of the equivalent circuits to the Nyquist plots of the **MIP-2** and **NIP-2** film to determine the  $R_{ct}$  values. Thus, the reliability of the calculated  $IF$  is limited.

### 3.2.5 DPV determining tyramine in real samples using **MIP-2** chemosensor

The **MIP-2** chemosensor was applied for tyramine DPV determination in real samples of Mozzarella cheese whey. This determination is critical for examining the usefulness of the designed **MIP-2** chemosensor and highlighting possibilities of real-life applications. Tyramine concentrations used in its determinations in real samples (Figure 3.2-12a, curve 2'') were the same as those used in tyramine determinations in PBS solutions (Figure 3.2-10c, curve 1''). The Mozzarella cheese whey samples were spiked with tyramine. The 11.67  $\mu\text{A}/\text{mM}$  slope of the plot constructed for the PBS solution alone (Figure 3.2-12a, curve 1'') was similar to that of 11.67  $\mu\text{A}/\text{mM}$  for the PBS solution spiked with Mozzarella cheese whey (Figure 3.2-12a, curve 2''). However, the latter value is unreliable because the matrix effect was prominent. The signal for the solution containing the real sample was higher than for the blank PBS solution. Furthermore, the **MIP-2** film was saturated with tyramine above the 1-mM tyramine concentration. Therefore, the previously used linear calibration plot for tyramine

determination in the blank PBS solution appeared impractical for tyramine determination in the real sample.

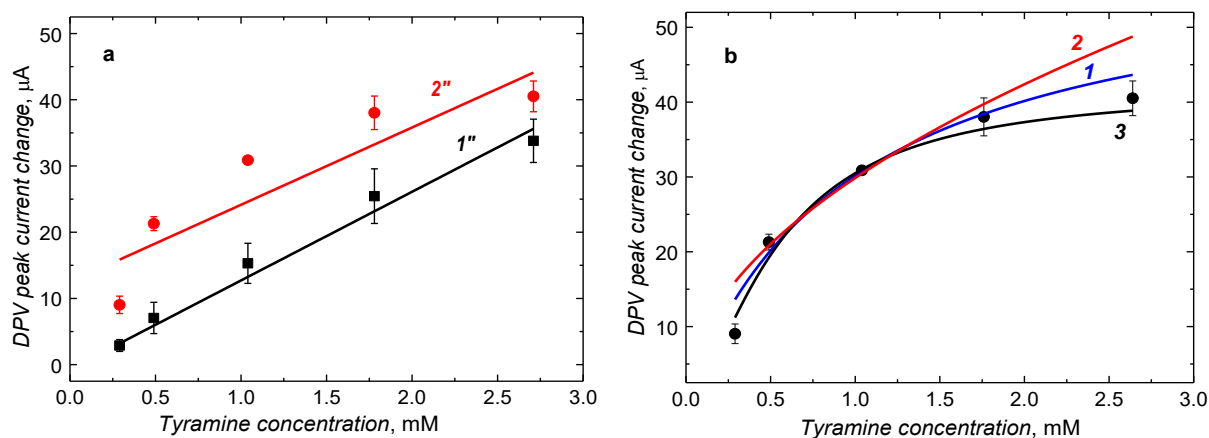


**Figure 3.2-12.** (a) Comparison of calibration plots and (b) Langmuir (curve 1), Freundlich (curve 2), and Langmuir-Freundlich (curve 3) isotherms fitted to the DPV peak current change with the tyramine concentration change in real samples of Mozzarella cheese whey. DPV measurements were performed for the tyramine-extracted **MIP-2** film-coated 0.75-mm diameter Pt disk electrodes using 0.1 M  $K_3[Fe(CN)_6]$  and 0.1 M  $K_4[Fe(CN)_6]$ , in (curve 1'') 0.1 M PBS (pH = 7.4) and (curve 2'') Mozzarella cheese whey diluted 100 times with 0.1 M PBS (pH = 7.4).

Instead, sorption isotherms were opted to determine tyramine using the **MIP-2** chemosensor response to the real samples tested. The Langmuir, Freundlich, and Langmuir-Freundlich isotherms, typically used to fit analytes and interferences sorption in MIPs, fitted the DPV data acquired herein (Figure 3.2-12b and Table 3.2-4).<sup>210</sup> Among these three isotherms, the Langmuir-Freundlich isotherm fit (Figure 3.2-12b, curve 3) was the best. Therefore, this isotherm was subsequently used to construct the calibration plot for tyramine determination in another Mozzarella Cheese whey samples batch. The recovery responses of the **MIP-2** chemosensor to the Mozzarella whey samples spiked with tyramine are presented in Table 3.2-5. The calculated tyramine recovery satisfactorily ranged from 84 to 115 at.%. That concludes that the chemosensor selectivity for tyramine determination in food samples is sufficiently high, although preliminary sample purification is recommended to avoid the matrix effect.

**Table 3.2-4.** Results of isotherm fitting to the DPV peak changes with the tyramine concentration changes in real samples of Mozzarella cheese whey measured with **MIP-2** film-coated 0.75-mm diameter Pt disk electrodes.

Isotherm	Isotherm equation	Fitted parameter			$R^2$
		$\Delta I_{DPV, \max}$ , $\mu A$	$K$ , $mM^{-1}$	$n$	
Langmuir	$\Delta I_{DPV} = \Delta I_{DPV, \max} \frac{K_L c_{\text{tyramine}}}{1 + K c_{\text{tyramine}}}$	60.0 ( $\pm 10.7$ )	1.01 <sup>a</sup> ( $\pm 0.366$ )	-	0.9555
Freundlich	$\Delta I_{DPV} = K_F c_{\text{tyramine}}^{\frac{1}{n}}$	-	29.86 <sup>b</sup> ( $\pm 1.00$ )	1.96 <sup>d</sup> ( $\pm 0.12$ )	0.8794
Langmuir-Freundlich	$\Delta I_{DPV} = \Delta I_{DPV, \max} \frac{(K_{LF} c_{\text{tyramine}})^n}{1 + (K_{LF} c_{\text{tyramine}})^n}$	41.9 ( $\pm 7.3$ )	1.84 <sup>c</sup> ( $\pm 0.478$ )	1.61 <sup>e</sup> (0.467)	0.9786

<sup>a</sup>  $K_L$  - Langmuir constant

<sup>b</sup>  $K_F$  - Freundlich constant

<sup>c</sup>  $K_{LF}$  - Langmuir-Freundlich constant

<sup>d</sup> Adsorption intensity

<sup>e</sup> Homogeneity factor

**Table 3.2-5.** Results of tyramine determination in Mozzarella whey samples with the **MIP-2** film-coated electrode using the Langmuir-Freundlich fitted isotherm as the calibration plot.

Sample No.	Concentration of added tyramine, mM	$\Delta I_{DPV}$ , $\mu A$	Calculated tyramine concentration, mM	Recovery, %
1	0.3	9.54 ( $\pm 2.64$ )	0.25 ( $\pm 0.10$ )	84.8 ( $\pm 33.9$ )
2	0.4	15.68 ( $\pm 2.86$ )	0.39 ( $\pm 0.11$ )	98.7 ( $\pm 26.8$ )
3	0.5	21.83 ( $\pm 3.62$ )	0.57 ( $\pm 0.13$ )	115.0 ( $\pm 25.1$ )
4	0.6	23.70 ( $\pm 0.76$ )	0.64 ( $\pm 0.05$ )	107.0 ( $\pm 7.6$ )

### 3.3 Conclusions

An electrochemical MIP chemosensor was devised, fabricated, and tested for selective tyramine determination. With DFT modeling, structures of the pre-polymerization complexes of the tyramine template with two different functional monomers, namely, **FM1** and **FM2**, were optimized. Two chemosensors, namely, **MIP-1** and **MIP-2**, were prepared from the pre-polymerization complex solution containing only **FM1** and both the **FM1** and **FM2** monomer, respectively. Although the former was not selective to common biological interferences, its sensitivity to tyramine was high. An additional monomer containing a crown ether moiety, **FM2**, was incorporated into the polymer to improve the chemosensor selectivity. The **FM2** monomer provided the **MIP-2** film an additional supramolecular interaction site for tyramine recognition, significantly enhancing chemosensor selectivity.

Moreover, the **MIP-2** film-coated electrode performance was superior to that of the **NIP-2** control. The calculated apparent imprinting factor for DPV was appreciable, equalling  $IF = 5.6$ , confirming successful tyramine imprinting. The  $IF$  calculated for EIS was 2.1. The two different fittings of the equivalent circuit to the EIS spectra for the **MIP-2** and **NIP-2** film result in such a low imprinting factor. Furthermore, the difference in the performance of the **MIP-2** and **NIP-2** film-coated electrodes found in the EIS measurements revealed the impact of the film nature, which eventually influenced the chemosensor response. The **MIP-2** film-coated electrode response change with the tyramine concentration change result from the film conductivity changes, whereas the "gate effect" was operative for **NIP-2** film-coated electrode.

The **MIP-2** chemosensor linear dynamic concentration range in DPV and EIS determinations, using the  $\text{Fe}(\text{CN})_6^{4-}/\text{Fe}(\text{CN})_6^{3-}$  redox probe, covered the micro- and millimolar tyramine concentration ranges. The LOD at  $S/N = 3$  for DPV and EIS determinations was 159 and 168  $\mu\text{M}$  tyramine, respectively. Finally, the prepared **MIP-2** film-coated electrode was applied to tyramine determination in Mozerella cheese whey to highlight the usefulness of the chemosensor for tyramine quantitation in a real sample. A pronounced matrix effect and the signal saturation for the **MIP-2** chemosensor were observed for tyramine concentrations exceeding 1 mM. Therefore, the Langmuir-Freundlich isotherm was proposed to fit the acquired DPV data and construct a calibration plot for tyramine in whey samples. The calculated from the constructed calibration plot, tyramine recovery was quite acceptable,

ranging from 84 to 115 at.%. The chemosensor selectivity was sufficiently high for tyramine determination in food samples.



## *Chapter 4*

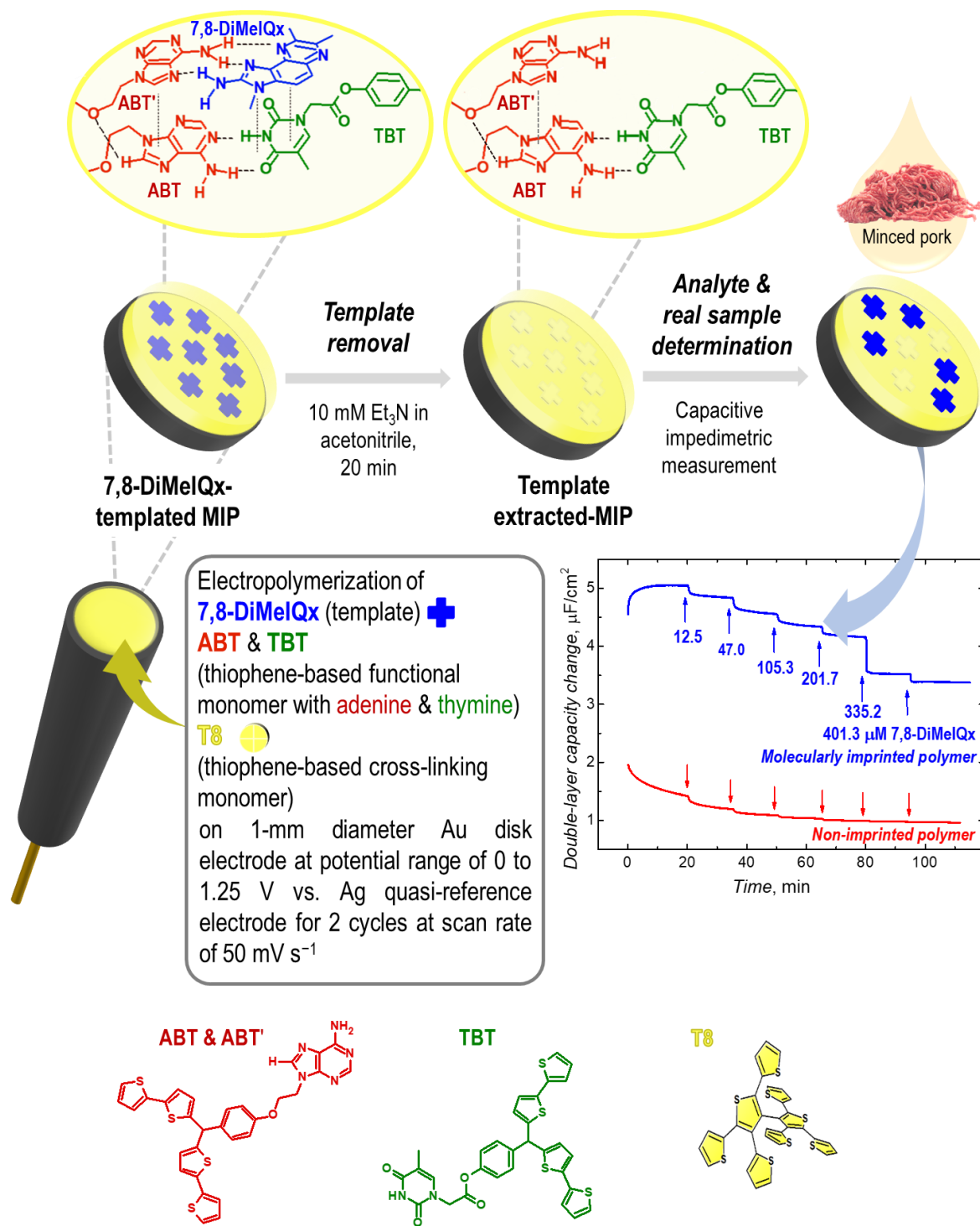
# *Selective impedimetric chemosensing of carcinogenic heterocyclic aromatic amine by dsDNA mimicking molecularly imprinted polymer film-coated electrodes*

This chapter discusses the research work published in *J. Agric. Food Chem.*, **2021**, *69*, 14689-14698. <https://doi.org/10.1021/acs.jafc.1c05084>.

## Abstract

A nucleobase-functionalized impedimetric molecularly imprinted polymer (MIP) sensor was devised and tested for selective determination of 2-amino-3,7,8-trimethyl-3*H*-imidazo[4,5-*f*]quinoxaline, **7,8-DiMeIQx**, quinoxaline heterocyclic aromatic amine (HAA). HAAs are formed when meat and fish are cooked, fried, or grilled at high temperatures. They are potent hazardous carcinogens. Although the HAAs are usually generated at low concentrations (~ng per g of a food sample), they effectively damage the DNA by intercalating or strand breaking, thus leading to cancer. Currently, HPLC is used for these toxins determination in food matrices. However, this technique is expensive, tedious, and time-consuming. Therefore, the HAAs were selectively determined within the present study by nucleobase-functionalized molecularly imprinted polymer as a chemosensor recognition unit. This chemosensor appeared suitable for a fast, simple, inexpensive, and reliable route to determine the HAAs in food matrices. Its linear dynamic concentration range extended from 47 to 400  $\mu\text{M}$  **7,8-DiMeIQx** with the LOD, determined by capacitance measurement, equalling 15.5  $\mu\text{M}$  at  $S/N = 3$ . The calculated apparent imprinting factor was appreciably high,  $IF = 8.5$ . Moreover, the chemosensor was highly selective to common biological interferences, including glucose, urea, and creatinine.

# Graphical abstract



## 4.1 Introduction

The present chapter discusses a simplified approach to determining quinoxaline heterocyclic aromatic amines (HAAs) using a nucleobase-functionalized MIP chemosensor by mimicking HAA's intercalation in a dsDNA strand. For that, the MIP film was prepared by potentiodynamic electropolymerization of a pre-polymerization complex of two adenine- and one thymine-substituted *bis*(2,2'-bithien-5-yl)methane functional monomer molecules with one **7,8-DiMeIQx** template molecule, in the presence of the 2,4,5,2',4',5'-hexa(thiophene-2-yl)-3,3'-bithiophene cross-linking monomer, in solution. The resulting MIP-**7,8-DiMeIQx** film-coated electrodes were applied to determine HAAs selectively using the "gate effect," studied with the DPV and EIS capacitance measurements.

## 4.2 Results and discussion

### 4.2.1 Functional monomers selection

The selection of suitable monomers is critical for successful preparing molecular cavities in MIPs that can mimic the **7,8-DiMeIQx** template binding to the double-stranded (dsDNA), similar to interactions characteristic of the HAA intercalation in the real dsDNA. For that, the **Abt** and **Tbt** functional monomers, respectively containing adenine and thymine moieties, were selected based on chemical initiation to the dsDNA mimic with an A-T nucleobase pair. Subsequently, the pre-polymerization complexes of the **7,8-DiMeIQx** template with selected functional monomers at different molar ratios were optimized using the DFT M06-2X functional with 6-31G\* basis set for quantum-chemical modeling. This modeling predicted the formation of stable **Abt-(7,8-DiMeIQx)** and **Tbt-(7,8-DiMeIQx)** complexes at the molar ratio of 1 : 1. The calculated Gibbs free energy change ( $\Delta G$ ) values of the complexes' formation were -46.2 and -34.4 kJ/mol, respectively. At the molar ratio of 1 : 1 : 1 and 2 : 1 : 1 for **Abt** : **7,8-DiMeIQx** : **Tbt**, the  $\Delta G$  values were -66.5 and -84.3 kJ/mol, respectively. These values indicated that the complex with the molar ratio of 2 : 1 : 1 was most stable.

Moreover, the  $\Delta G$  values for all optimized pre-polymerization complexes at different molar ratios are higher than that for the (Watson-Crick)-like **Abt-Tbt** complex (Table 4.2-1). That implies that the pre-polymerization complexes were more stable than the A-T nucleobase

pair of the double-stranded (dsDNA) itself, contributing to the possibility of successful imprinting and, thus, higher selectivity.

Furthermore, former research revealed that intercalators avidly bound to the dsDNA revealing high affinity if values of the complex stability constant,  $K_s$  were of the order of  $10^4 \text{ M}^{-1}$ .<sup>211</sup> Clearly, the interaction of the **7,8-DiMeIQx** template with **Abt** and **Tbt** functional monomers were strong (Table 4.2-1), especially at the molar ratio of **Abt** : **7,8-DiMeIQx** : **Tbt** equalling 2 : 1 : 1. These strong interactions ensure the stable pre-polymerization complex formation and possibly contribute to the successful imprinting of the **7,8-DiMeIQx** template. Therefore, the complex with the molar ratio of 2 : 1 : 1, called **Abt-Tbt/Abt-(7,8-DiMeIQx)**, was preferred for further examinations.

**Table 4.2-1.** The Gibbs free energy change ( $\Delta G$ ) accompanying the **Abt** and **Tbt** functional monomers pairing and forming complexes with the **7,8-DiMeIQx** template in acetonitrile, calculated using the DFT method at the M06-2x/6-31G\* level with the dispersion correction (D3).

Complex	$\Delta G$ , kJ/mol
<b>Abt-Tbt</b>	-26.4
<b>Tbt-(7,8-DiMeIQx)</b>	-34.4
<b>Abt-(7,8-DiMeIQx)</b>	-46.2
<b>Abt-(7,8-DiMeIQx)-Tbt</b>	-66.5
<b>Abt-Tbt/Abt-(7,8-DiMeIQx)</b>	-84.3

The **Abt-Tbt/Abt-(7,8-DiMeIQx)** complex structural formula is shown in Figure 4.2-1c and its DFT optimized structure in solution in Figure 4.2-2a. The DFT calculations predicted six hydrogen bonds and one  $\pi$ - $\pi$  stacking for this complex, contributing to a high negative  $\Delta G$  value. Then, the template molecule was removed from the structure-optimized **Abt-Tbt/Abt-(7,8-DiMeIQx)** complex (Figure 4.2-1c and 4.2-2b). At this stage, the terminal positions of *bis*(2,2'-bithien-5-yl)methane moieties were "frozen" to model interactions of the imprinted cavities with the **7,8-DiMeIQx** molecule. The DFT modeling predicted two stable conformations of the imprinted molecular cavity where one was ready for analyte recognition (Figure 4.2-1d and 4.2-2b), and the other was inactive (Figure 4.2-1e and 4.2-2c). The Gibbs

free energy of formation of the conformation capable of template binding was by 1.5 kJ/mol lower than that of the inactive conformation. With this behavior, the MIP film mimics allosteric molecular recognition in protein receptors.<sup>212</sup>

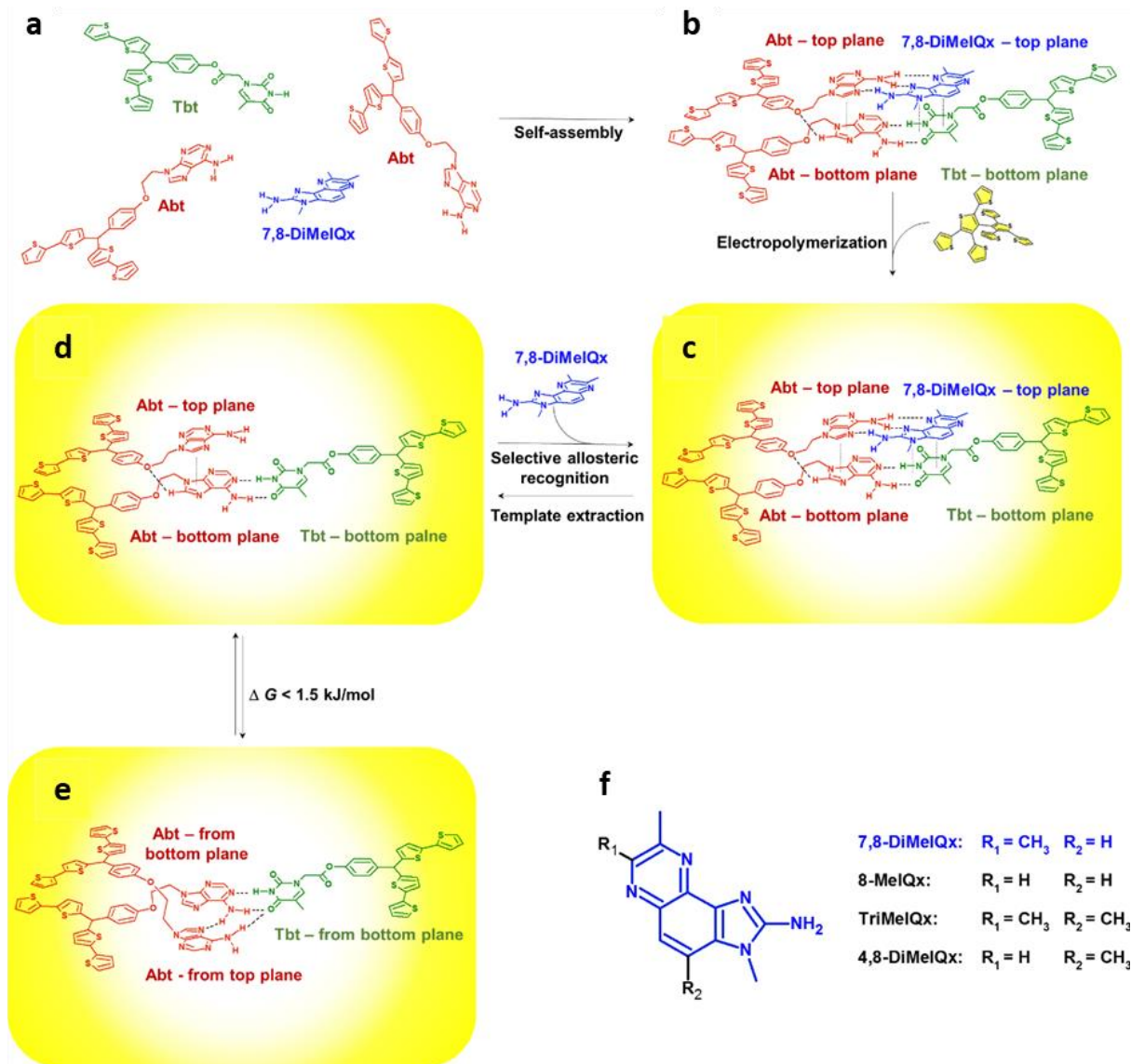


**Figure 4.2-1.** Structural formula of (a) functional monomers (**Abt**, **Tbt**) and the **7,8-DiMeIQx** template as well as of (b) the **Abt-Tbt/Abt-(7,8-DiMeIQx)** pre-polymerization complex and the imprinted molecular cavity in the MIP film (c) with the template molecule before and after extraction in two different conformations, vis., (d) one - ready for analyte recognition and (e) the other - inactive. (f) Structural formulas of the 2-amino-3,7,8-trimethyl-3*H*-imidazo[4,5-*f*]quinoxaline (**7,8-DiMeIQx**), and its close analogs, i.e., 2-amino-3,8-dimethylimidazo[4,5-*f*]quinoxaline (**8-MeIQx**), 2-amino-3,4,7,8-tetramethyl-3*H*-imidazo[4,5-*f*]quinoxaline (**TriMeIQx**), and 2-amino-3,4,8-trimethyl-3*H*-imidazo[4,5-*f*]quinoxaline, (**4,8-DiMeIQx**).

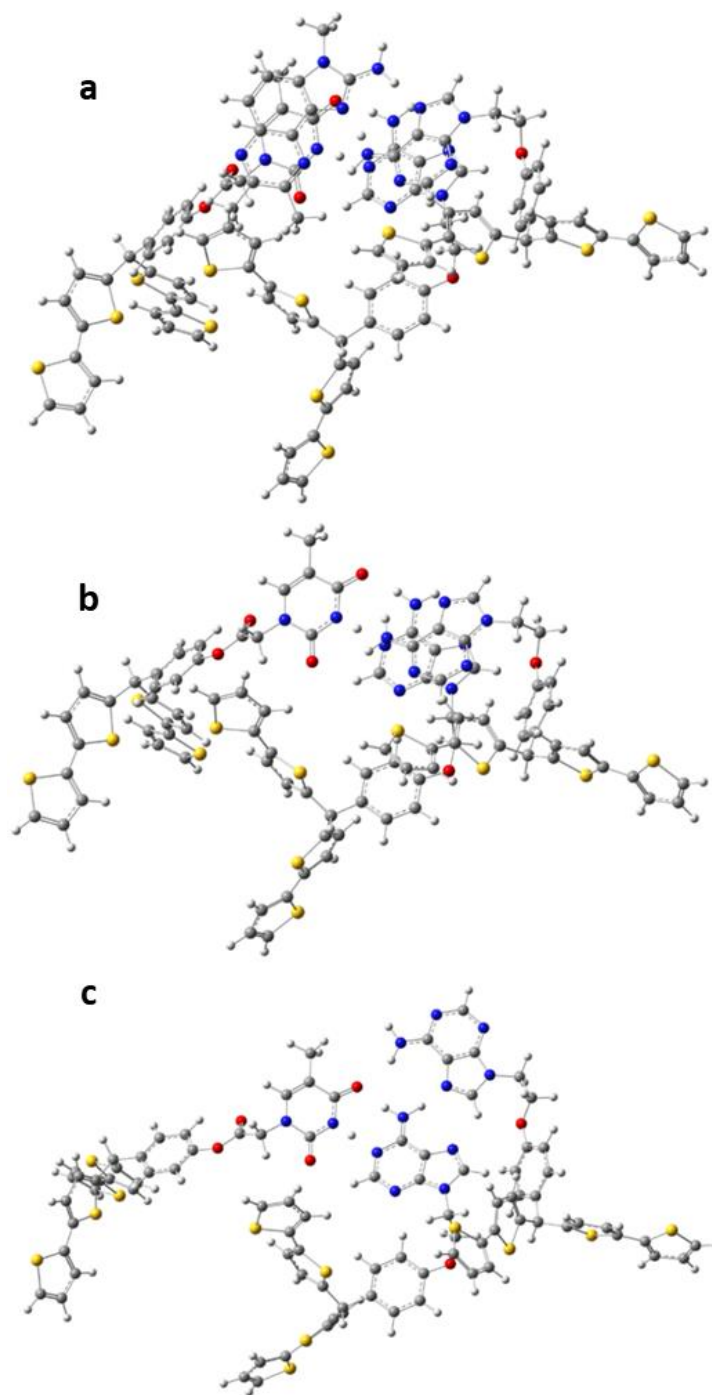


**Figure 4.2-2.** Structure of the DFT optimized at the M06-2X/6-31G\* level with the dispersion correction (D3) of (a) the **Abt-Tbt/Abt-(7,8-DiMeIQx)** pre-polymerization complex as well as the molecular cavity imprinted in the MIP with the template molecule removed in two conformations, i.e., (b) one - ready for analyte recognition and (c) the other - inactive.

#### 4.2.2 Pre-polymerization complex electropolymerizing and selectivity of the MIP chemosensor

The pre-polymerization **Abt-Tbt/Abt-(7,8-DiMeIQx)** complex in acetonitrile was electropolymerized using two potentiodynamic cycles between 0 and 1.25 vs. Ag quasi-reference electrode and simultaneously deposited, as the MIP film, on the 1-mm diameter Au electrode (Figure 4.2-3a, curve 1). The non-imprinted polymer (NIP) film was deposited under the same conditions but without the **7,8-DiMeIQx** template (Figure 4.2-3a, curve 2). A well-developed anodic peak at 0.85 V vs. Ag quasi-reference electrode was generated in the first cycle for the MIP film. The corresponding peak potential for the NIP film was slightly lower, equalling ~0.80 V vs. Ag quasi-reference electrode. Nevertheless, the peaks appeared at lower potentials in the second scan for both films. Stable **Abt-Tbt/Abt-(7,8-DiMeIQx)** complex formation might cause the difference in anodic peak potentials for MIP and NIP films.<sup>213</sup> Moreover, the NIP film appeared more compact than the MIP film as the monomer's faradic current significantly decreased in the second scan.

The DPV experiments for the 1 mM ferrocene redox probe in the acetonitrile solution supported the successful deposition of the polymer film on the electrode surface (Figure 4.2-4b, curve 2). The faradic current significantly decreased after the deposition, indicating that the electrode surface was blocked with the film deposited. Then, the **7,8-DiMeIQx** template was extracted with 0.1 mM NaOH under vigorous magnetic stirring for 20 min, resulting in a faradic current increase to ~15  $\mu$ A (Figure 4.2-4d, curve 3), which stood for successful **7,8-DiMeIQx** template removal.

Subsequently, the extracted MIP film-coated electrodes were applied for **7,8-DiMeIQx** determination. For that, DPV was combined with the "gate effect," similarly to our tyramine chemosensor. As expected, the DPV peak of the ferrocene redox probe in the acetonitrile solution depended on the **7,8-DiMeIQx** concentration (Figure 4.2-5a). With the **7,8-DiMeIQx** concentration increase, the DPV ferrocene peak significantly decreased. Moreover, this decrease was linear in the **7,8-DiMeIQx** concentration range of 2.5 to 12  $\mu$ M (Figure 4.2-5b line 1'). That confirmed that the MIP chemosensor was highly sensitive to the **7,8-DiMeIQx** analyte. The apparent imprinting factor, calculated from the slopes' ratio of the calibration plots for the MIP and NIP chemosensor's response in the presence **7,8-DiMeIQx**, was  $IF = 23$ .

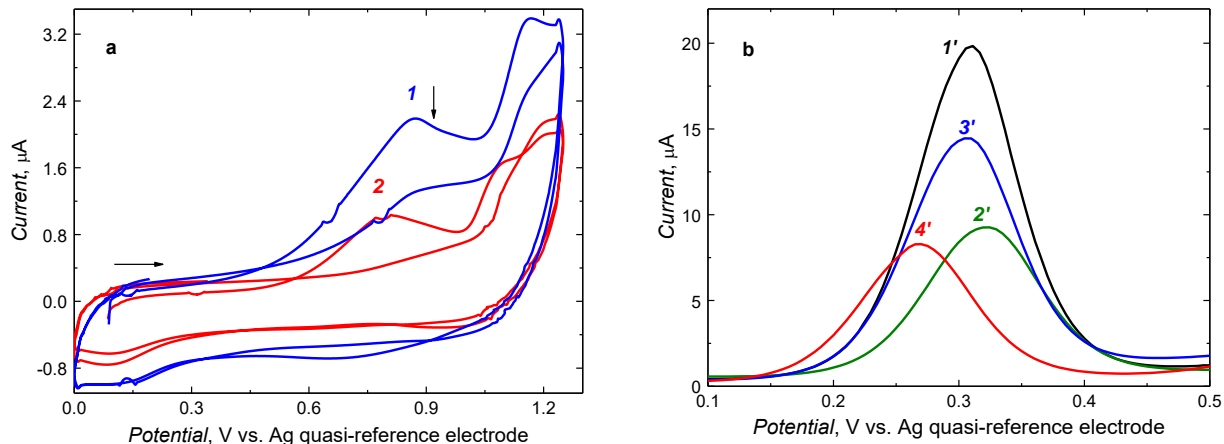


**Figure 4.2-3.** (a) Potentiodynamic two-cycle curves for (1) MIP and (2) NIP films depositions on 1-mm diameter Au disk electrodes from the acetonitrile solution of 20  $\mu\text{M}$  7,8-DiMeIQx, (for MIP only), 40  $\mu\text{M}$  Abt, 20  $\mu\text{M}$  Tbt, 40  $\mu\text{M}$  CrI, and 20 mM (TBA)ClO<sub>4</sub>, at a scan rate of 50 mV/s. (b) DPV curves recorded in the acetonitrile solution of 1 mM ferrocene, 0.1 M (TBA)ClO<sub>4</sub>, for the (1') bare Au electrode, and the MIP film-coated electrode (2') before and (3') after 20 min of 7,8-DiMeIQx extraction with 0.1 mM NaOH under vigorous stirring and (4') NIP film-coated electrode.

Despite this high imprinting factor, which substantiates the successful imprinting, this chemosensor was not selective to common biological interferences, vis., glucose, urea, and creatinine. Moreover, the repeatability of the NIP film-coated electrode's response in the 7,8-DiMeIQx analyte presence was low (indicated by the high error bars in Figure 4.2-4b, line 5').

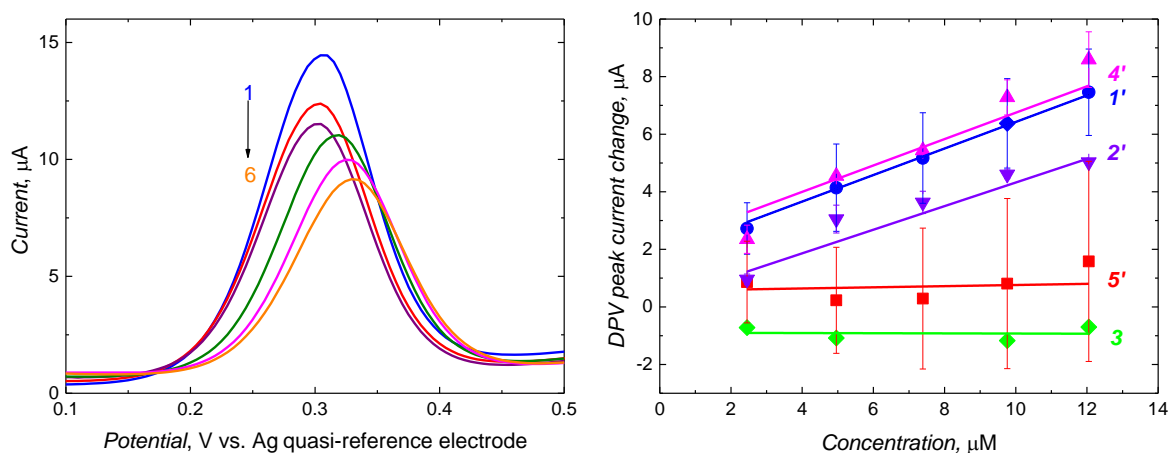


**Figure 4.2-4.** (a) DPV curves for (1) 0, (2) 2.5, (3) 5.0, (4) 7.4, (5) 9.8, and (6) 12  $\mu\text{M}$  7,8-DiMeIQx and (b) calibration plots for the MIP film-coated 1-mm diameter Au electrode for the acetonitrile solution of 1 mM ferrocene, 0.1 M (TBA)ClO<sub>4</sub>, after addition of the (curve 1') 7,8-DiMeIQx analyte, or interferences of (curve 2') glucose, (curve 3') urea, and (curve 4') tyramine.

The MIP chemosensor selectivity was improved by changing determination conditions. This change was necessary because the chemosensor was not selective in organic solvent solutions. Moreover, the polythiophene-based chemosensor for tyramine was selective in an aqueous solution such as PBS.<sup>214</sup> Therefore, the present sensing medium was changed from the acetonitrile solution to the PBS aqueous solution (pH = 7.4) of the 0.1 M  $K_3[Fe(CN)_6]$  and 0.1 M  $K_4[Fe(CN)_6]$  redox probe. The **7,8-DiMeIQx** analyte of known concentrations was applied for the MIP chemosensor operation, and the DPV responses were recorded. Unfortunately, the DPV signal change was insignificant in the 2.5 to 12  $\mu\text{M}$  **7,8-DiMeIQx** range (Figure 4.2-5). Presumably, the extraction with sodium hydroxide might have been too harsh and unsuitable for the prepared MIP film-coated electrode. Thus, these harsh conditions might have influenced the film integrity, which indirectly influenced the sensitivity of the template-extracted MIP film-coated electrode to the **7,8-DiMeIQx** analyte.

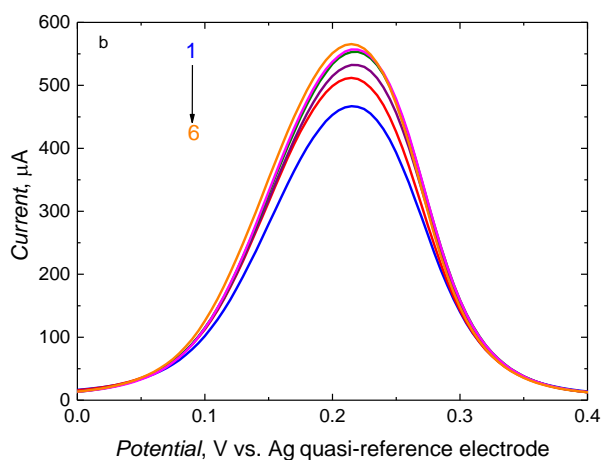


**Figure 4.2-5.** DPV curves for the MIP film-coated 1-mm diameter Au electrode for the 0.1 M  $K_3[Fe(CN)_6]$  and 0.1 M  $K_4[Fe(CN)_6]$  in PBS (pH = 7.4) after **7,8-DiMeIQx** analyte addition of the concentration of (1) 0, (2) 2.5, (3) 5.0, (4) 7.4, (5) 9.8, and (6) 12  $\mu\text{M}$ .

A milder extraction solvent has been opted to avoid any possible MIP film damage. The MIP and NIP film-coated electrodes were treated for 20 min with 10 mM triethylamine ( $\text{Et}_3\text{N}$ ) in acetonitrile (Figure 4.2-6a and 6b). Initially, the film-coated electrodes were rinsed with acetonitrile and then directly transferred to the PBS (pH = 7.4) containing  $[Fe(CN)_6]^{3-}/[Fe(CN)_6]^{4-}$  redox probe for the DPV measurement. However, changes in the DPV peak after this extraction treatment were insignificant (Figure 4.2-6a and 4.2-6b, curves 3 and 3', respectively) compared to previous experiments (Figure 4.2-3b). Often, the DPV peak current

differed from experiment to experiment. Moreover, consecutive **7,8-DiMeIQX** analyte addition to the working solution resulted in unrepeatable DPV peaks at the template-extracted MIP film-coated electrode. Therefore, before analyte addition, the MIP and NIP film-coated electrodes were soaked in the PBS (pH = 7.4) solution of the  $[\text{Fe}(\text{CN})_6]^{3-}/[\text{Fe}(\text{CN})_6]^{4-}$  redox probe for 60 min. This treatment is expected to allow the MIP film to swell, crucial for any electrochemical activity.<sup>215</sup> Expectedly, the DPV peak increased at both MIP and NIP film-coated electrodes after this extraction treatment (Figure 4.2-6a and 4.2-6b, curves 4 and 4', respectively). The chemosensor was applied to determine **7,8-DiMeIQX** using DPV.

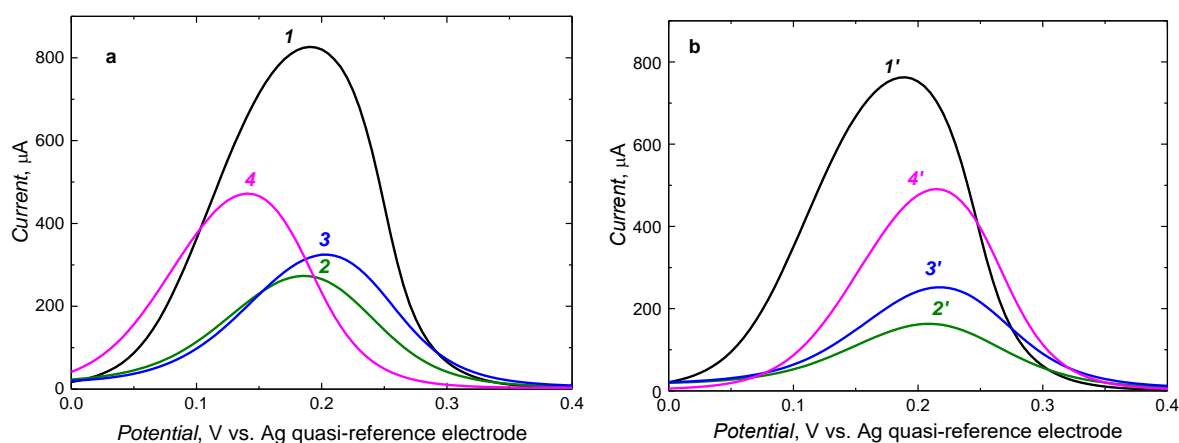


**Figure 4.2-6.** DPV curves for (a) MIP and (b) NIP film-coated electrodes in the 0.1 M  $\text{K}_3[\text{Fe}(\text{CN})_6]$  and 0.1 M  $\text{K}_4[\text{Fe}(\text{CN})_6]$  PBS (pH = 7.4) solution for the (curves 1 and 1') bare 1-mm Au electrode, and MIP and NIP film-coated electrodes (curves 2 and 2') before and (curves 3 and 3') after 20 min of **7,8-DiMeIQX** extraction with 10 mM  $\text{Et}_3\text{N}$  in acetonitrile under vigorous magnetic stirring, and then (curves 4 and 4') immersed in 0.1 M  $\text{K}_3[\text{Fe}(\text{CN})_6]$  and 0.1 M  $\text{K}_4[\text{Fe}(\text{CN})_6]$  in PBS (pH = 7.4) for 60 min after 2-min extraction.

In an aqueous solution, the MIP chemosensor was insensitive to the **7,8-DiMeIQX** analyte in a narrow 2.5 to 12  $\mu\text{M}$  concentration range (Figure 4.2-5). Hence, a broader range was applied (Figure 4.2-7a and 7b). The DPV peak for the  $[\text{Fe}(\text{CN})_6]^{3-}/[\text{Fe}(\text{CN})_6]^{4-}$  redox probe decreased with the **7,8-DiMeIQX** analyte concentration increase. However, the response was non-linear in the concentration range of 69.7 to 150.2  $\mu\text{M}$  (Figure 4.2-7c). Unfortunately, a similar response was also observed for the control NIP film. Thus, the imprinting could not be confirmed, in addition to the poor selectivity.

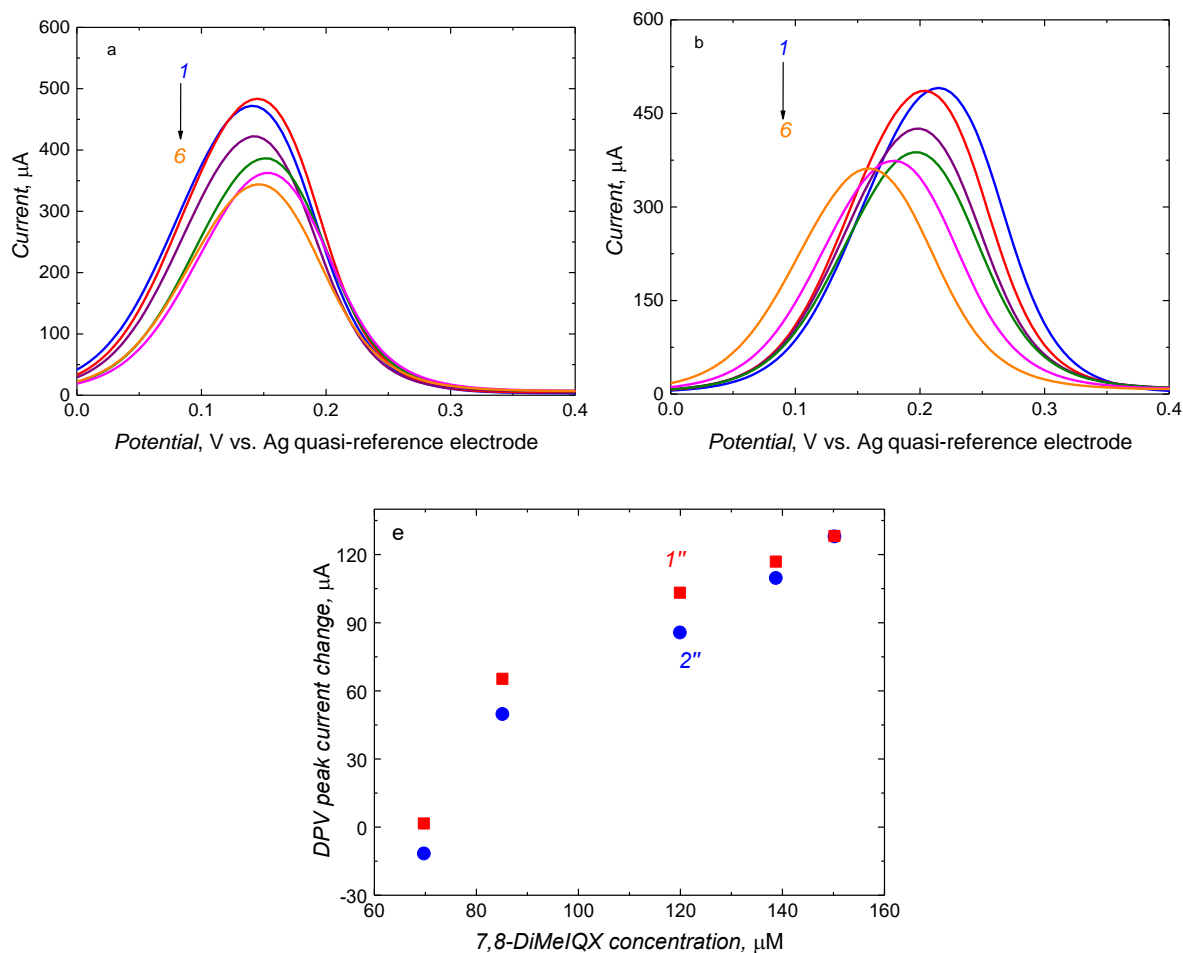


**Figure 4.2-7.** DPV curves for the (a) MIP and (b) NIP film-coated electrode after **7,8-DiMeIQX** addition to the test solution at the concentration of (curves 1 and 1') 0, (curves 2 and 2') 69.7, (curves 3 and 3') 85.1, (curves 4 and 4') 119.9, (curves 5 and 5') 138.7, and (curves 6 and 6') 150.2  $\mu\text{M}$ . (c) Calibration plots for the 0.1 M  $\text{K}_3[\text{Fe}(\text{CN})_6]$  and 0.1 M  $\text{K}_4[\text{Fe}(\text{CN})_6]$  in PBS (pH = 7.4) for the (curve 1'') MIP and (curve 2'') NIP film-coated electrode.

### 4.2.3 Electropolymerizing and electrochemical impedance spectroscopy parameters selecting for capacitive impedimetric MIP chemosensing

The MIP film-coated electrode performance in DPV studies of the "gate effect" was low despite multiple attempts to improve the selectivity. Hence, different transduction was in demand which would afford the required selectivity. So, the CI technique was opted to study the MIP film-coated electrode performance. For that, an MIP film was deposited on a 1-mm diameter Au disk electrode using a freshly prepared pre-polymerization **Abt-Tbt/Abt-(7,8-DiMeIQx)** complex solution to select appropriate parameters for CI measurements.

There were no changes in the MIP and NIP film-coated electrode deposition procedure. Therefore, the deposition of new films (Figure 4.2-8a) resembled previous depositions (Figure 4.2-3). However, the procedure of films treatment after the deposition was optimized to ensure film integrity. The newly deposited MIP and NIP film-coated electrodes were dried in air for 20 min, and then the **7,8-DiMeIQx** template was extracted with 10 mM Et<sub>3</sub>N in acetonitrile for 20 min (Figure 4.2-8b). After the extraction, the films were abundantly rinsed with acetonitrile and then dried in air for 20 min before DPV and EIS measurements (Figures 4.2-8a as well as 4.2-9a and 9b). After measurements with 0.1 M K<sub>3</sub>[Fe(CN)<sub>6</sub>] and 0.1 M K<sub>4</sub>[Fe(CN)<sub>6</sub>] in PBS (pH = 7.4), the film-coated electrodes were rinsed with water and then again dried in air for 20 min before transferring to the 10 mM KF solution. These additional steps were necessary to wash out any remaining residues of solvents and or redox probe on the film-coated electrodes and let the electrodes completely dry before transferring them between organic and aqueous solutions. These steps ensured films' stability and integrity in each measurement.

After 20-min **7,8-DiMeIQx** template extraction in 10 mM Et<sub>3</sub>N, the DPV peak at the MIP film-coated electrode stabilized at ~500  $\mu$ A (Figure 4.2-8b, curve 3'). This peak remained constant although the films were further extracted for up to 45 minutes (Figure 4.3-8b, curve 4'), demonstrating that the 20-min extraction was sufficient to remove all **7,8-DiMeIQx** from the MIP film. Moreover, the repeatability of these experiments was no longer an issue. Subsequently, the MIP film-coated electrodes were characterized by EIS. The EIS spectra were recorded in the 100 mHz to 200 kHz frequency range at the 10-mV ac amplitude. In this range, all required electrode processes proceeded. The diameter of the flattened semicircles in the Nyquist plot represents the charge transfer resistance,  $R_{ct}$  (Figure 4.2-9a). After extraction, this diameter decreased only slightly (Figure 4.2-9a, curve 2''), indicating a decrease in the  $R_{ct}$  because of the cavity formation. On the other hand, the Warburg diffusion, represented by straight lines in the low-frequency region, remained unchanged after template extraction. In the Bode plot (Figure 4.2-9b), with the frequency increase, the impedance pronouncedly decreased in the 0.1 to 10 Hz and 10 to 100 kHz range, and the phase angle slightly increased in the 0.1 to 10 Hz range and slightly decreased in the 1 to 10 kHz range remaining relatively constant in the 10 Hz to 1 kHz range.

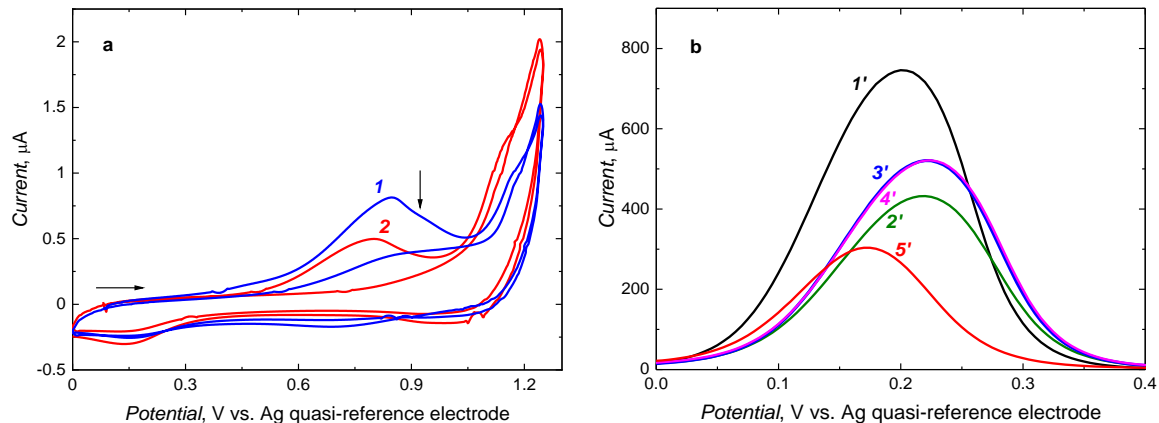


**Figure 4.2-8.** (a) Potentiodynamic curves for deposition on 1-mm diameter Au disk by electropolymerization at a scan rate of 50 mV/s of the film of (curve 1) MIP and (curve 2) NIP from the acetonitrile solution of 20  $\mu\text{M}$  **7,8-DiMeIQx** (for MIP only) 40  $\mu\text{M}$  **Abt**, 20  $\mu\text{M}$  **Tbt**, 40  $\mu\text{M}$  **CrI** and 20 mM (TBA)ClO<sub>4</sub>. (b) DPV curves for (curve 1') the bare electrode, and the electrode coated with the MIP film (curve 2') before and after **7,8-DiMeIQx** (curve 3') 20-min and (curve 4') 45-min extraction with 10 mM Et<sub>3</sub>N in acetonitrile, and (curve 5') coated with the NIP film in 0.1 M K<sub>3</sub>[Fe(CN)<sub>6</sub>] and 0.1 M K<sub>4</sub>[Fe(CN)<sub>6</sub>] in PBS (pH = 7.4).

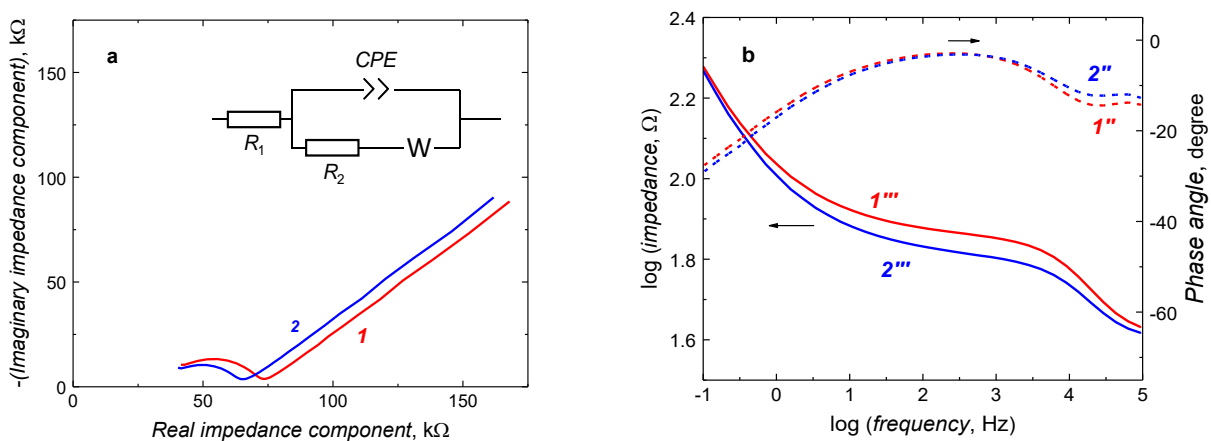


**Figure 4.2-9.** (a) Nyquist and (b) Bode plots of EIS spectra for MIP film-coated electrode (curves 1, 1', and 1'') before and (curves 2, 2'', and 2''') after **7,8-DiMeIQx** template extraction. The EIS measurements were performed using 0.1 M K<sub>3</sub>[Fe(CN)<sub>6</sub>] and 0.1 M K<sub>4</sub>[Fe(CN)<sub>6</sub>] in PBS (pH = 7.4).

Then, the EIS spectra for the MIP film-coated electrode in 10 mM KF at 0.21 V vs. Ag quasi-reference were recorded before and after template extraction and then after the **7,8-DiMeIQx** addition to reaching its 105.3  $\mu\text{M}$  concentration in the test solution (Figure 4.2-10a and 10b). This step was necessary to select a suitable frequency for CI measurements. There was no electrode process in the Nyquist plot at 0.21 V vs. Ag quasi-reference electrode (Figure

4.2-10a). Moreover, in the Bode plot, the phase angle changed significantly in the frequency range of 100 Hz to 10 kHz after **7,8-DiMeIQx** extraction (Figure 4.2-10b, curves 1'' and 2''). After adding **7,8-DiMeIQx** to reach its concentration of 105.3  $\mu\text{M}$  in the test solution, the phase angle returned to its original value, i.e., that before extraction, indicating analyte binding (Figure 4.2-10b, curve 3''). These phase angle changes revealed that the **7,8-DiMeIQx** molecule binding to the imprinted cavity caused the most pronounced changes in electrochemical double-layer capacity at 500 Hz. Therefore, this frequency was applied in subsequent studies of the MIP film-coated electrode selectivity using the CI technique.

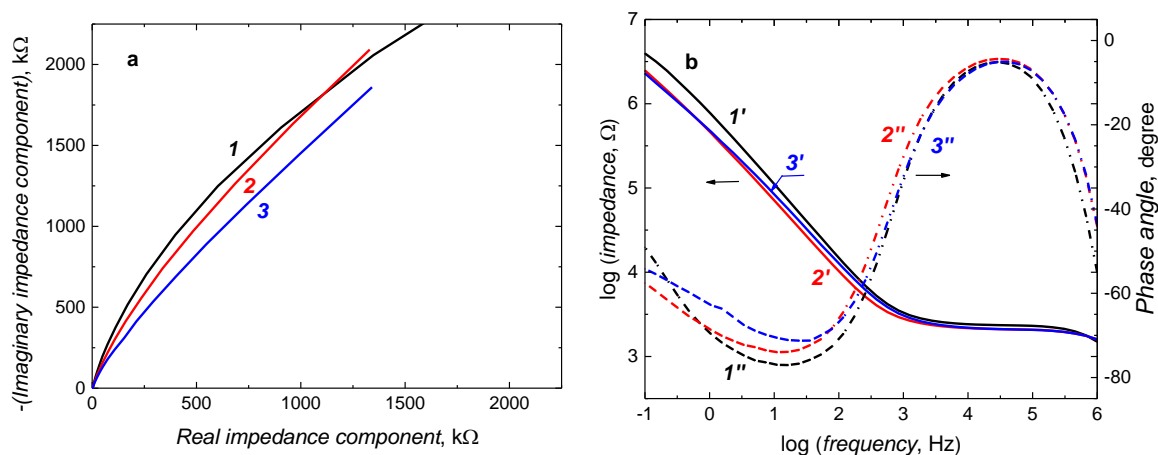


**Figure 4.2-10.** (a) Nyquist and (b) Bode plots of the EIS spectra recorded for the MIP film-coated electrodes (1, 1', and 1'') before and (2, 2', and 2'') after **7,8-DiMeIQx** template extraction, and (3, 3', and 3'') in 105.3  $\mu\text{M}$  **7,8-DiMeIQx**. The measurements were performed using 1-mm diameter Au disk electrode in 10 mM KF.

#### 4.2.4 Characterizing the MIP chemosensor

##### FTIR measurements

The FTIR measurements were performed to identify chemical bonds before and after template extraction, which helps evaluate MIP film deposition. The MIP film spectra, recorded before and after template extraction and the NIP film spectra (Figure 4.2-11), confirm film deposition. Bands at 1450 to 1500  $\text{cm}^{-1}$  associated with the thiophene aromatic ring C=C bond stretching are seen in spectra for all films. Interestingly, the MIP film after template extraction and the NIP film spectra exhibit certain similarities. A band between 1600 and 1700  $\text{cm}^{-1}$  is present for all deposited films, although it is most pronounced for the MIP film before extraction

(Figure 4.2-11, curve 1). This band may be attributed to C=C and C=N bonds' stretchings of the **7,8-DiMeIQx** template present in the polymer matrix after electropolymerization and successfully removed by extraction. Moreover, a pronounced band at  $\sim 2900\text{ cm}^{-1}$  for the MIP after extraction and NIP films may originate from the C-H bond stretching in aromatic and aliphatic moieties. Notably, the films were deposited using only two potentiodynamic cycles. That resulted in the deposition of thin films (see AFM characterization below). Therefore, the absorption signal was weak, which influenced the characterization of the deposited films.

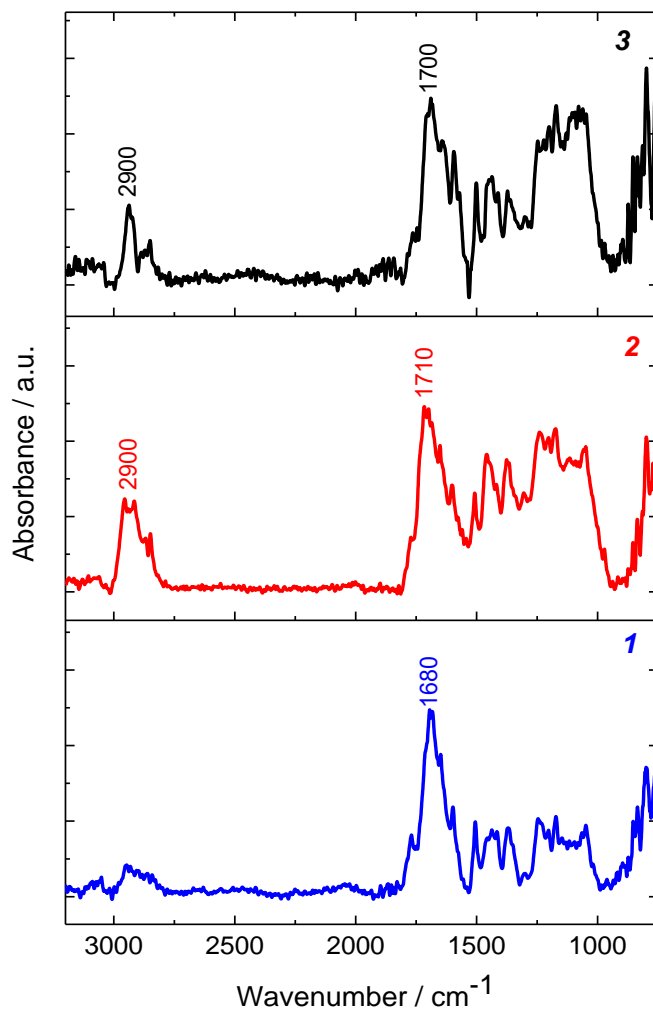


**Figure 4.2-11.** The FTIR spectra for Au-layered glass slides coated with an MIP film (curve 1) before and (curve 2) after template extraction, and (curve 3) an NIP film.

## XPS measurements

The XPS measurements were performed to determine the elemental composition of the deposited films before and after **7,8-DiMeIQx** template extraction, thus confirming this extraction. Unfortunately, besides carbon and nitrogen, no characteristic elements in the 7,8-DiMeIQx template could serve as internal probes. Therefore, it was impossible to confirm the presence of the **7,8-DiMeIQx** template after the electropolymerization and its absence after template extraction from the MIP film. The XPS spectroscopy evaluated the content of four primary elements, namely, oxygen, nitrogen, carbon, and sulfur (Table 4.2-2).

Among these elements, the nitrogen and oxygen contents are the most significant. The nitrogen content increased after extraction in the MIP film (Table 4.2-2). However, the nitrogen content remained the same before and after extracting treatment of the NIP film. On the other hand, the oxygen content in the MIP film slightly increased after template extraction. The calculated oxygen-to-nitrogen atom ratio for the MIP film before extraction slightly increased after the extraction (Table 4.2-3). This slight increase may confirm template extraction because of no oxygen in **7,8-DiMeIQx**. Furthermore, the oxygen-to-nitrogen atom ratio for the MIP film before extraction is slightly lower than that for both the film of MIP after extraction and NIP.

**Table 4.2-2.** The atom content of the MIP and NIP film determined with XPS.

Element	Element content, at.%			
	MIP before template extraction	MIP after template extraction	NIP before template "extraction"	NIP after template "extraction"
O	6.09	7.77	6.44	7.36
N	3.95	4.50	3.60	3.65
C	80.04	78.31	78.47	78.43
S	9.92	9.42	11.49	10.56

**Table 4.2-3.** The oxygen-to-nitrogen (O-to-N) atomic percent ratio in the MIP and NIP films determined with XPS before and after **7,8-DiMeIQx** template extraction.

Polymer film	O-to-N atomic percent ratio	
	before extraction	after extraction
MIP	1.54	1.73
NIP	1.79	2.02

### AFM imaging

The polymer films were imaged with AFM to determine their thickness, morphology, and topography (Figure 4.2-12a to 12d). Globular polymer grains fused into round flattened "pancake-like" structures are seen in all films. These structures' diameter varies from 40 to 120 nm. **7,8-DiMeIQx** template extraction did not affect the size and structure of these grains. Nanomechanical parameters determined for the films are compiled in Table 4.2-4. The film thickness was determined by uniformly scratching the film and then imaging those scratches. Expectedly, the films deposited using two potential cycles were thin (Table 4.2-4). After template extraction, the MIP film thickness slightly decreased. However, the NIP film thickness increased after the extraction. The changes caused by the **7,8-DiMeIQx** template extraction are too small to be considered.

Moreover, surface roughness was measured for all the films to determine the smoothness level of the film's surface. The MIP and NIP films appeared to be uniform, although some loosely bound grains are visible in both films (Figure 4.2-12a and 12c). The MIP film surface was less rough than the NIP film surface (Table 4.2-4). After extraction, the MIP film roughness increased, whereas the NIP film roughness decreased (Table 4.2-4). After extracting treatment of the NIP film, these roughness changes might originate from removing loosely bound grains. In the MIP film, the overall film roughness increased after template extraction. Moreover, these loosely bound grains might break into smaller pieces after extraction, thus increasing MIP film roughness. Generally, the AFM imaging and nanomechanical study confirmed the polymer films formation on the Au disk electrodes and the removal of the weakly bound parts present on the MIP and NIP films' surfaces during template extraction.

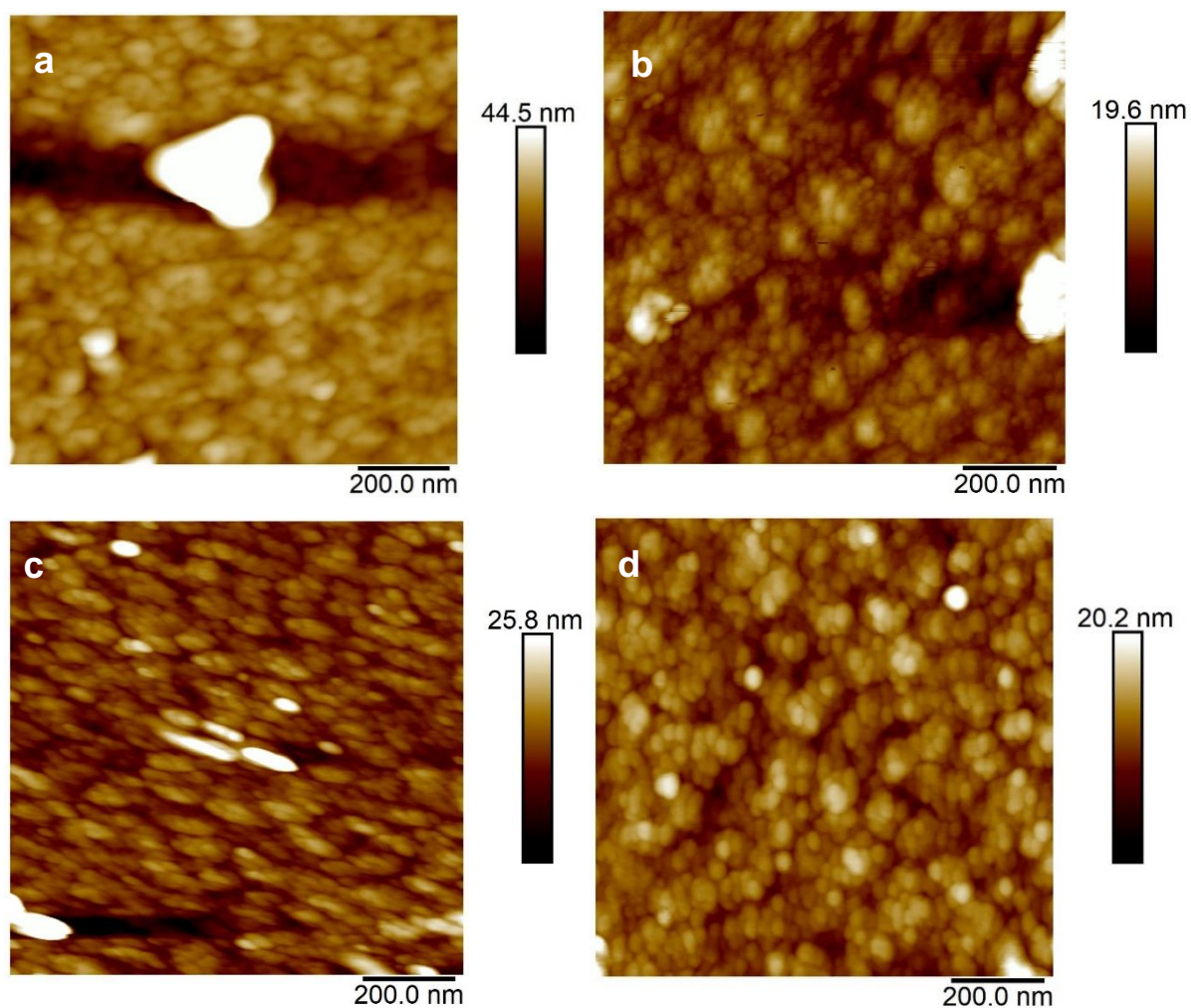


**Figure 4.3-12.** AFM images of the (a and b) MIP and (c and d) NIP films, (a and c) taken before and (b and d) after **7,8-DiMeIQx** template extraction.

**Table 4.2-4.** The MIP and NIP film properties determined by AFM imaging.

Film property	MIP before template extraction	MIP after template extraction	NIP before film rinsing	NIP after film rinsing
Thickness, nm	$9.4 \pm 3.0$	$7.5 \pm 1.2$	$8.4 \pm 1.9$	$12.0 \pm 2.6$
Roughness, $R_a$ , nm	$2.2 \pm 0.9$	$4.2 \pm 1.5$	$6.4 \pm 1.4$	$3.7 \pm 0.9$
Grain diameter, nm	$85.0 \pm 35.0$	$85.0 \pm 43.0$	$82.0 \pm 35.0$	$88.0 \pm 36.0$
Phase, degree	$111.0 \pm 1.0$	$23.3 \pm 0.4$	$19.4 \pm 0.9$	$4.9 \pm 0.1$

## SEM imaging

Polymer films were SEM imaged to acquire information about the films' morphology before and after template extraction (Figure 4.2-13). The MIP-2 and NIP-2 films uniformly coated electrode surfaces (Figure 4.2-13a and 13b, respectively). There were no significant changes after the NIP film extracting treatment. However, there were oddly-shaped holes in the MIP films after template extraction (Figure 4.2-13 a'). These holes might arise from partial film removal during the extraction and explain the low repeatability and selectivity of the MIP chemosensors in the redox probe presence, as reported in the literature.<sup>66</sup>

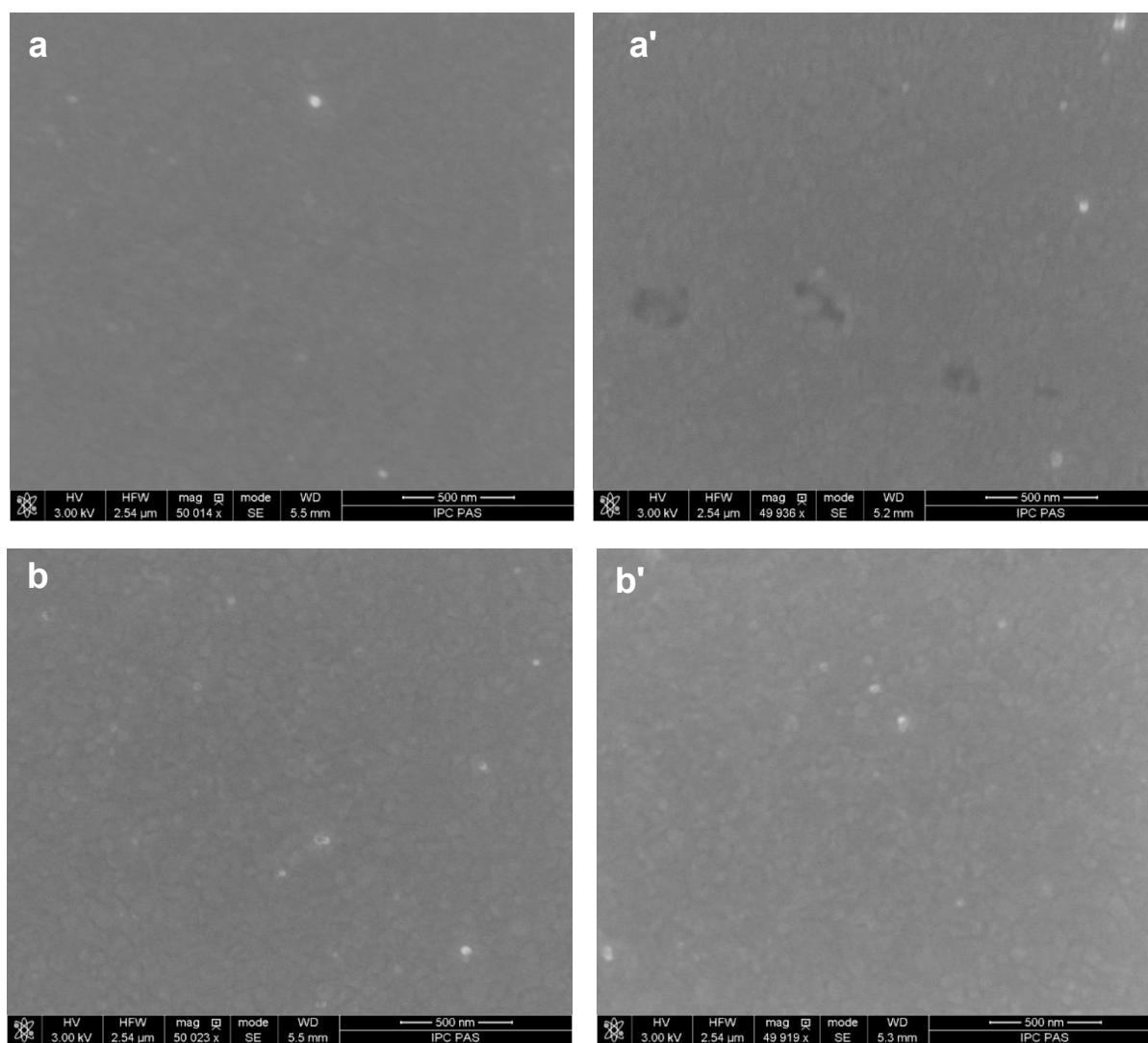


**Figure 4.3-13.** SEM images of the (a, a') MIP-2 and (b, b') NIP-2 film-coated (glass slide)/Ti/Au electrodes (a, b) before and (a', b') after **7,8-DiMeIQx** extraction for 150 min in 0.1 M NaOH.

#### 4.2.5 Selectivity of the capacitive impedimetric MIP chemosensor

The MIP film-coated electrode selectivity to common interferences was evaluated using CI under steady-state solution and FIA conditions at the 500-Hz frequency and 10-mV amplitude in 10 mM KF. A concentrated KF solution was selected as the supporting electrolyte solution for the CI determinations because KF is electroinactive, and its solutions afford sufficiently high solubility of interferences. The supporting electrolyte nature influence on the conductive polymer sensitivity has already been examined.<sup>161</sup> The K<sup>+</sup> and F<sup>-</sup> ions do not adsorb on electrodes, unlike ions of many other electrolytes. Therefore, KF is highly suitable for the CI measurements using an MIP chemosensor. Moreover, if the supporting electrolyte concentration is high, the electric double layer is thin (< 1 nm). Then, only a tiny fraction of the MIP film imprinted cavities are located sufficiently close to the electrode surface to influence double-layer capacity. In contrast, a low supporting electrolyte concentration develops a thick double layer, not preferred for CI sensing.<sup>216</sup>

The double-layer capacity change ( $\Delta C_{dl}$ ) with the analyte or interference concentration change was followed with EIS. First, **7,8-DiMeIQx** of known concentrations was determined with the bare 1-mm diameter Au disk electrode under steady-state conditions (Figure 4.2-14b). The  $\Delta C_{dl}$  linearly increased with the **7,8-DiMeIQx** concentration increase from 70 to 140  $\mu\text{M}$ . However, these results were scattered as denoted by high error bars, especially at high concentrations. Regardless, the  $\Delta C_{dl}$  for MIP and NIP films linearly decreased with the **7,8-DiMeIQx** concentration increase from 47 to 400  $\mu\text{M}$  (Figure 4.2-14a and 14c). This opposite response of the MIP and NIP film-coated electrodes to that of the bare 1-mm Au disk electrode resulted in a prominent apparent imprinting factor and selectivity of the CI chemosensor.

The MIP chemosensor response under steady-state conditions follows the linear regression equation of  $\Delta C_{dl} [\mu\text{F cm}^{-2} \mu\text{M}^{-1}] = -2.96 \times 10^{-1} (\pm 2.28 \times 10^{-2}) - 4.4 \times 10^{-3} (\pm 9.56 \times 10^{-5}) C_{7,8\text{-DiMeIQx}} [\mu\text{M}]$  with the regression coefficient of  $R^2 = 0.9986$ . The LOD, determined at  $S/N = 3$ , was 15.5  $\mu\text{M}$ . The apparent imprinting factor, calculated by dividing the calibration plot slope for the MIP and NIP film-coated electrode, was relatively high, equaling  $IF = 8.5$ . The MIP chemosensor selectivity to common biological interferences, namely, glucose, urea, and creatinine (Figure 3.3-10c), was 27.5, 9.7, and 43, respectively. Moreover, the chemosensor response to **8-MeIQx**, a close structural analog of the **7,8-DiMeIQx** analyte, was examined;

the chemosensor's response to this analyte was negligible. That additionally emphasizes a high MIP chemosensor selectivity to the interferences.

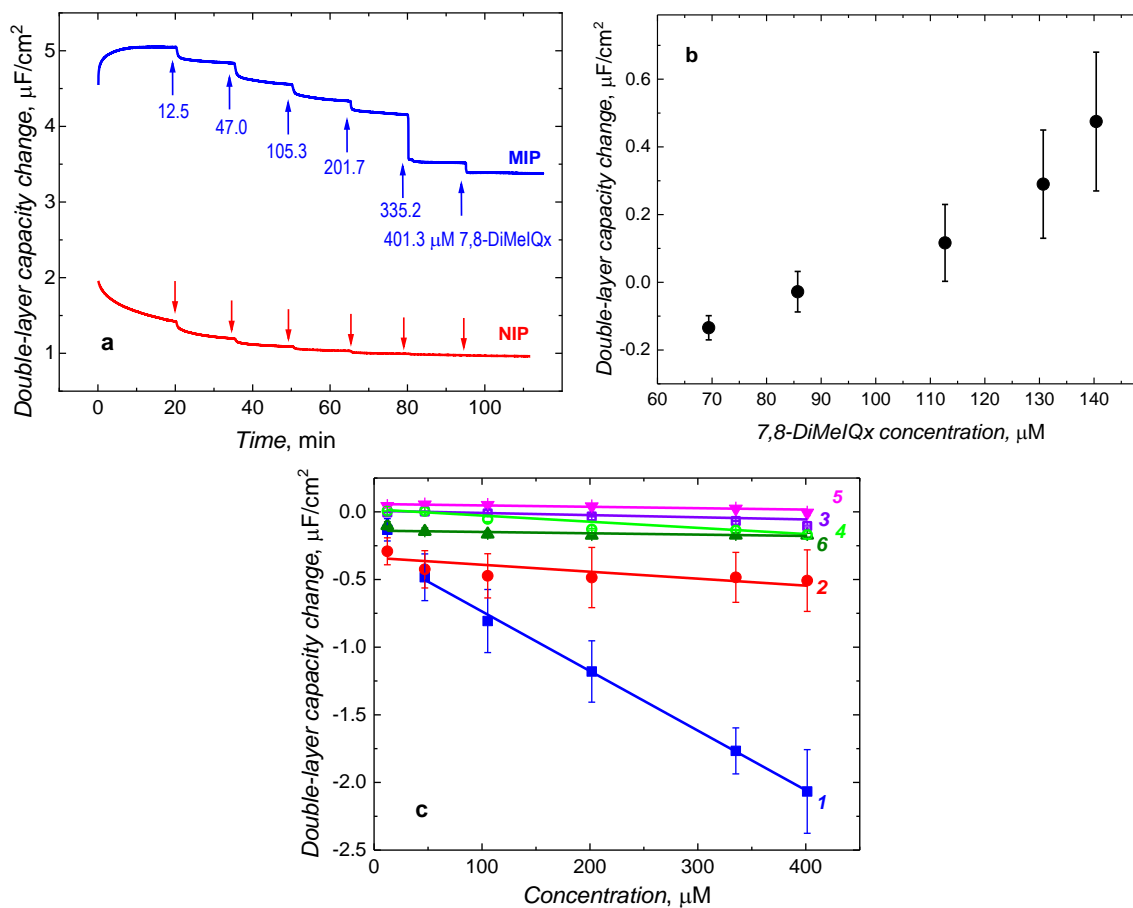


**Figure 4.2-14.** Double-layer capacity changes with time for the (a) MIP and NIP film-coated electrodes under steady-state solution conditions. Calibration plots constructed for double-layer capacity changes at the (b) bare Au electrode and (c) the Au electrode coated with the film of (curve 1) MIP and (curve 2) NIP with the concentration change of **7,8-DiMeIQx**, (curve 3) glucose, (curve 4) urea, (curve 5) creatinine, and (curve 6) **8-MeIQx**. The measurements were performed with a 1-mm diameter Au disk electrode using 10 mM KF at a 0.21 V vs. Ag quasi-reference electrode, 10-mV amplitude, and 500-Hz frequency. All data points for the calibration plots were recorded three times to calculate each point's average value and standard deviation.

Moreover, the MIP film-coated electrode sensitivity to **7,8-DiMeIQx** was studied under FIA conditions. First, the MIP and NIP films were deposited on 1-mm diameter Pt disk electrodes in a three-electrode glass cell under steady-state conditions. Then the **7,8-DiMeIQx** template was extracted from the polymer film-coated electrodes, similar to the procedure

discussed in Section 4.2.3 above. Next, the **7,8-DiMeIQx** analyte of known concentrations was determined under FIA conditions at the bare and polymer film-coated electrodes. The chemosensor's responses were recorded with EIS under optimized conditions of the  $50\text{-}\mu\text{L min}^{-1}$  flow rate of the  $10\text{ mM KF}$  carrier solution.

The double-layer capacity of MIP film-coated electrodes increased with the **7,8-DiMeIQx** concentration increase (Figure 4.2-15a), similar to that for the bare Au electrode measured under steady-state conditions (Figure 4.2-14b). Interestingly, the NIP film-coated electrode response was similar to that of the MIP film-coated electrode, although the peaks were higher, and the signal more slowly returned to its baseline for the latter. This result demonstrates that the control NIP film affinity to **7,8-DiMeIQx** is lower than that of the MIP film. Moreover, the peak shape (Figure 4.2-515a) was non-gaussian. That suggests that the overall time was too short for the system to reach the partition equilibrium, although the MIP film-coated electrode time of response to **7,8-DiMeIQx** was longer than that of the NIP film-coated control electrode. The peak was considerably smaller and broader at a lower flow rate, and the signal reached its baseline much slower (Figure 4.2-15b).

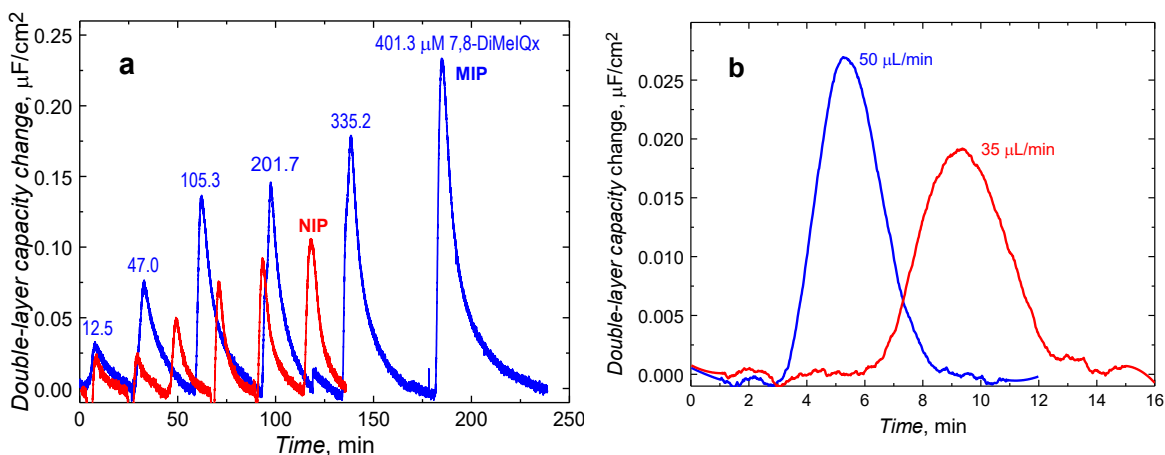


**Figure 4.2-15.** Double-layer capacity change with time for (a) the MIP and NIP film-coated electrodes after injection of solutions of **7,8-DiMeIQx** of concentrations indicated at each peak with a number and (b) two different flow rates indicated at each peak with a number. The measurements were performed with a 1-mm diameter Pt disk electrode using  $10\text{ mM KF}$ , at  $0.21\text{ V vs. Ag/AgCl}$ ,  $10\text{-mV}$  amplitude, and  $500\text{ Hz}$  frequency.

The calibration plot for the chemosensor's response to **7,8-DiMeIQx** in a broad, 1 to  $400\text{ }\mu\text{M}$  concentration range is shown in Figure 4.2-16a. The response was not linear in this range, and the MIP imprinted cavities seemed saturated above  $100\text{ }\mu\text{M}$  **7,8-DiMeIQx**.

Moreover, the NIP film-coated electrode and bare Pt electrode response to **7,8-DiMeIQx** were indistinguishable (Figure 4.2-16a, curves 2 and 3). Thus, it was impossible to determine the apparent imprinting factor for this concentration range. Instead, the data were fitted with the Langmuir-Freundlich isotherms, and indeed, the Langmuir-Freundlich isotherm fitted the data points for MIP film-coated electrode very well (Figure 4.2-16). The calculated isotherm parameters are compiled in Table 4.2-5. The homogeneity factor,  $n$ , describes the extent of the homogeneous distribution of molecular cavities in the polymer matrix. The  $n$  value for MIP film-coated electrodes was 0.67, significantly lower than those recorded for the bare and the NIP film-coated electrodes, equaling 0.85 and 0.90, respectively. This considerable difference in the  $n$  value suggests a possible involvement of two processes. One might be selective **7,8-DiMeIQx** sorption in the imprinted cavities and the other - non-specific **7,8-DiMeIQx** binding on the polymer surface.

Moreover, under FIA conditions, the calibration curve was linear only in a narrow concentration range of the pseudo-linear part of the Langmuir-Freundlich isotherm extending from 1 to 100  $\mu\text{M}$  **7,8-DiMeIQx** (Figure 4.2-16b). The CI chemosensor response obeyed the regression equation of  $\Delta C_{dl} [\mu\text{F cm}^{-2} \mu\text{M}^{-1}] = 2.21 \times 10^{-2} (\pm 1.23 \times 10^{-3}) + 1.19 \times 10^{-3} (\pm 5.44 \times 10^{-5}) C_{7,8\text{-DiMeIQx}} [\mu\text{M}]$  with the regression coefficient and the LOD at  $S/N = 3$  of  $R^2 = 0.994$  and  $\text{LOD} = 3.1 \mu\text{M}$ , respectively. The determined apparent imprinting factor was  $IF \approx 2.8$ , significantly lower than that determined under steady-state solution conditions.

This difference suggests that two different processes, one faster and one slower, might be operative at the MIP film-coated electrode. The faster process might involve the **7,8-DiMeIQx** binding on the film surface, causing the  $C_{dl}$  increase, as observed under FIA conditions. The other might involve the **7,8-DiMeIQx** sorption in molecular cavities located deeper in the film, which caused polymer shrinking or ion expelling. This action resulted in the  $C_{dl}$  decrease, as in the steady-state experiments. Moreover, the significantly broad chemosensor linear dynamic concentration range under steady-state conditions leads to two inferences. First, under steady-state solution conditions, there was a sufficiently long time available for the system to reach partition equilibrium, and second, the number of imprinted cavities engaged in the **7,8-DiMeIQx** binding was much higher than that under FIA conditions. Most likely, only the outer part of the MIP film participated in the analyte binding under the FIA conditions.

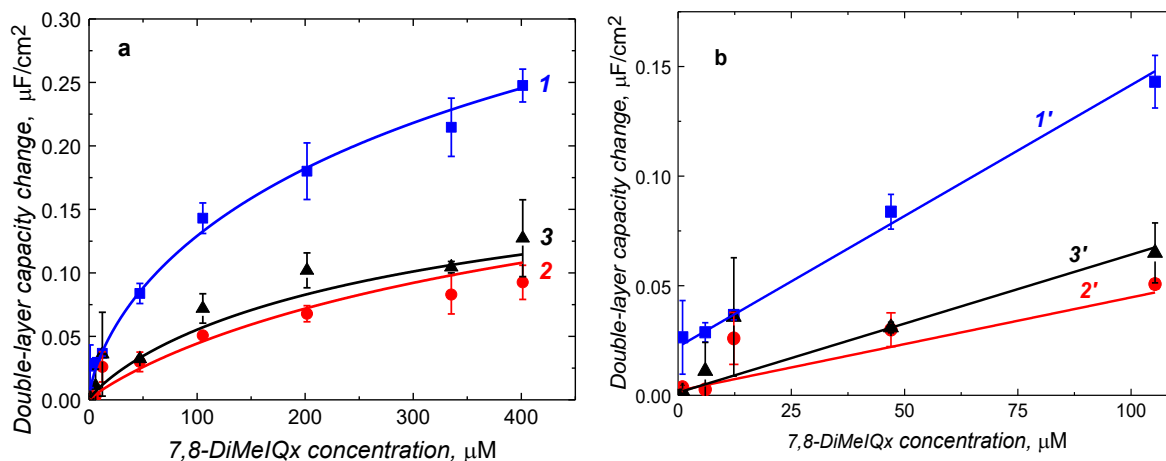


**Figure 4.2-16.** Calibration plots of the double-layer capacity change with the **7,8-DiMeIQx** concentration in (a) a broad and (b) narrow range for the (curves *1* and *1'*) MIP film-coated, (curves *2* and *2'*) NIP film-coated, or (curves *3* and *3'*) bare 1-mm diameter Pt disk electrode in 10 mM KF at 0.21 V vs. Ag/AgCl with the 10-mV amplitude, 500-Hz frequency, and a 50- $\mu\text{L min}^{-1}$  flow rate. All data points were recorded thrice to calculate each point's average value and standard deviation.

**Table 4.2-5.** Calculated parameters of the Langmuir-Freundlich isotherms.

Pt disk electrode	$\Delta C_{\text{DL,max}}$ , $\mu\text{F/cm}^2$	$K$ , $\mu\text{M}$	$n$	$R^2$
MIP film-coated	0.59 ( $\pm 0.29$ )	$1.49 \times 10^{-3}$ ( $\pm 1.86 \times 10^{-3}$ )	0.67 ( $\pm 0.08$ )	0.991
NIP film-coated	0.26 ( $\pm 0.68$ )	$1.73 \times 10^{-3}$ ( $\pm 7.32 \times 10^{-3}$ )	0.90 ( $\pm 0.29$ )	0.774
Bare	0.22 ( $\pm 0.093$ )	$2.82 \times 10^{-3}$ ( $\pm 2.74 \times 10^{-3}$ )	0.85 ( $\pm 0.15$ )	0.994

<sup>a</sup>The Langmuir-Freundlich isotherm equation,  $\Delta C_{\text{DL}} = \Delta C_{\text{DL,max}} \frac{(Kc)^n}{1+(Kc)^n}$ . Symbols  $\Delta C_{\text{DL,max}}$ ,  $K$ ,  $c$ , and  $n$  stand for the maximum double-layer capacity change, Langmuir-Freundlich constant, **7,8-DiMeIQx** concentration, and homogeneity factor, respectively.

#### 4.2.6 7,8-DiMeIQx determining in pork samples using the MIP chemosensor

The MIP chemosensor was applied for the **7,8-DiMeIQx** determination in real samples to highlight its practical applicability. For that, the pork meat extract, prepared following the procedure reported in Chapter 2, Section 2.3.5, above, was spiked with **7,8-DiMeIQx**, and then this heteroaromatic amine was determined under steady-state solution conditions using CI (Figure 4.2-17). The recovery of the MIP chemosensor responses to **7,8-DiMeIQx** in pork

meat extract is presented in Table 4.2-6. This recovery, quite appreciable, ranged from 90 to 110%. That concludes that the devised MIP chemosensor is suitable for the **7,8-DiMeIQx** determination in real food samples.

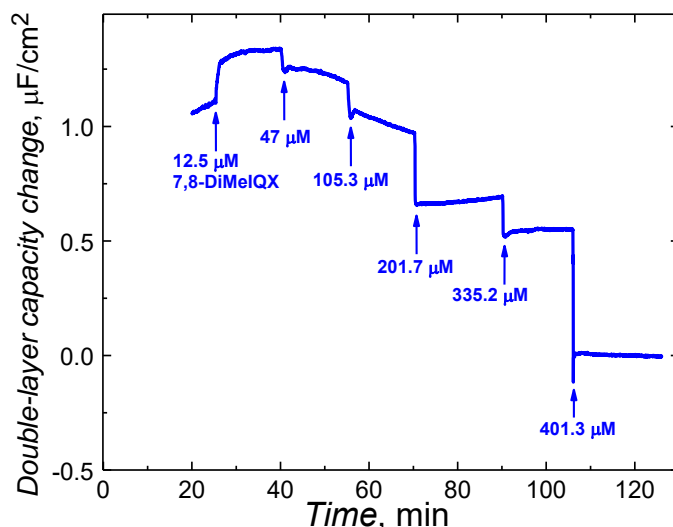


**Figure 4.2-17.** The double-layer capacity change with time for different **7,8-DiMeIQx** concentrations, indicated with numbers at each **7,8-DiMeIQx** solution injection, measured with the MIP film-coated electrode under steady-state conditions using a 1-mm diameter Au disk electrode, 10 mM KF, 0.21 V vs. Ag quasi-reference electrode, 10-mV ac potential amplitude, and 500 Hz frequency of the potential change.

**Table 4.2-6.** Capacitive impedimetry determined **7,8-DiMeIQx** in a pork meat extract.

Sample No.	Added <b>7,8-DiMeIQx</b> concentration, $\mu\text{M}$	Measured double-layer capacity change, $\text{nF cm}^{-2}$	Determined <b>7,8-DiMeIQx</b> concentration, $\mu\text{M}$	Recovery, %
1	47.0	-0.52 ( $\pm 0.27$ )	51.3 ( $\pm 4.9$ )	109.1 ( $\pm 10.4$ )
2	105.3	-0.84 ( $\pm 0.28$ )	124.1 ( $\pm 2.8$ )	117.8 ( $\pm 2.6$ )
3	201.7	-1.16 ( $\pm 0.18$ )	195.2 ( $\pm 27$ )	96.8 ( $\pm 13.4$ )
4	335.2	-1.51 ( $\pm 0.34$ )	276.9 ( $\pm 10.1$ )	82.6 ( $\pm 3.0$ )
5	401.3	-1.93 ( $\pm 0.35$ )	370.7 ( $\pm 12.9$ )	92.4 ( $\pm 3.2$ )

### 4.3 Conclusions

An MIP chemosensor for selective determination of **7,8-DiMeIQx** was devised, fabricated, and tested. This chemosensor construction and operation were inspired by the HAA's ability to intercalate dsDNA readily. The **Abt** and **Tbt** compounds were selected as functional monomers to mimic the (Watson-Crick) adenine-thymine dsDNA nucleobase pair. The DFT modeling was used to optimize the pre-polymerization complex structures of the **7,8-DiMeIQx** template with **Abt** and **Tbt** functional monomers in the solution. It predicted six hydrogen bonds and one  $\pi$ - $\pi$  stacking, which resulted in a high negative Gibbs free energy gain,  $\Delta G = -84.3$  kJ/mol calculated for the pre-polymerized complex formation with the molar ratio of **Abt** : **7,8-DiMeIQx** : **Tbt** equal to 2 : 1 : 1.

After the MIP film deposition by potentiodynamic electropolymerization and then template extraction, the MIP film-coated electrode was applied for **7,8-DiMeIQx** determination with DPV using the "gate effect." However, the MIP chemosensor performance was low despite multiple attempts to improve its selectivity. Therefore, a different transduction technique, namely, capacitive impedimetry, was chosen to investigate the MIP film-coated electrode selectivity to **7,8-DiMeIQx** under steady-state solution and FIA conditions. In the former, the performance of the MIP-2 film-coated electrode was superior to the control NIP film and highly selective towards interferences, namely, glucose, creatinine, urea, and 8-DiMeIQx. Moreover, the MIP chemosensor linear dynamic concentration range was broad, ranging from 47 to 400  $\mu\text{M}$  **7,8-DiMeIQx**. The LOD at  $S/N = 3$  was  $\text{LOD} = 15.5$   $\mu\text{M}$ , and the calculated apparent imprinting factor was appreciably high,  $IF = 8.5$ , confirming the **7,8-DiMeIQx** imprinting.

Interestingly, the dependence of the MIP chemosensor's double-layer capacity change with the **7,8-DiMeIQx** concentration change, measured under FIA conditions in the 1 to 400  $\mu\text{M}$  **7,8-DiMeIQx** concentration range, was non-linear. This dependence reached saturation for the **7,8-DiMeIQx** concentration exceeding 100  $\mu\text{M}$  **7,8-DiMeIQx**. Therefore, the dynamic concentration range was linear only for a narrow **7,8-DiMeIQx** concentration range of 1 to 100  $\mu\text{M}$ . Under FIA conditions, the LOD was 3.1  $\mu\text{M}$  at  $S/N = 3$ , and the apparent imprinting factor was  $IF = \sim 2.8$ , which is significantly lower than those determined under steady-state solution conditions. Most importantly, the double-layer capacity changes of the MIP film-

coated electrode under FIA conditions were opposite to those measured under steady-state solution conditions.

Presumably, two processes were involved in the **7,8-DiMeIQx** determination using the MIP film-coated electrode. The faster one might involve the **7,8-DiMeIQx** adsorption on the film surface, which caused the double-layer capacity increase, as observed under FIA conditions. The slower process presumably involved the **7,8-DiMeIQx** sorption in molecular cavities located deeper in the film, which caused the polymer to shrink or expel ions from the film, resulting in the double-layer capacity decrease observed in experiments under steady-state solution conditions.

The MIP film-coated electrode performance investigated under steady-state solution conditions was superior to that under FIA conditions. Thus, the former conditions were used to study the MIP chemosensor usefulness for **7,8-DiMeIQx** determination in real samples. The MIP film-coated electrode was applied for **7,8-DiMeIQx** quantization in the pork meat extract. The **7,8-DiMeIQx** recovery determined from the constructed calibration plot quite acceptably exceeded 80%. Therefore, the selectivity of the devised MIP chemosensor was sufficiently high for **7,8-DiMeIQx** determination in food samples.



## Chapter 5

### *Summary and future perspectives*

The food safety assessment is one of the essences of the modern food industry. Significant amounts of financial resources are spent on maintaining high-quality standards of food products. Two major factors contribute to this demand; (i) increased public awareness of safe food and (ii) a surge in quantity and variety of food pollutants due to globalization, industrialization, and population growth. For decades, chromatography coupled with mass spectrometry has been utilized to examine food products. Due to its high cost, measurement complexity, and long experiment time, electrochemical sensors in combination with MIPs recently opted for food analysis.

MIP-based electrochemical sensors are versatile as they can be devised for any food contaminant. It offers simplicity in sensor preparation and measurement, and cost-effectiveness. Moreover, these sensors exhibit a high affinity towards the target analytes due to their MIPs' recognition units, operating similarly to the lock-and-key mechanism of an enzyme and its substrate. Therefore, within the present research, we have devised, engineered, and tested chemosensors of high selectivity against tyramine and **7,8-DiMeIQx**, two cancer triggering food toxins using molecularly imprinted polythiophene derivatives' films.

Two tyramine-imprinted MIP films, namely, **MIP-1** and **MIP-2**, were electrochemically deposited on Pt electrodes using the pre-polymerization complex solution containing the tyramine template, thiophene-based functional monomers, i.e., **FM1** and **FM2**, and 2,3-bithiophene cross-linking monomer. The **MIP-1** was prepared using **FM1**, whereas **MIP-2** was prepared using both functional monomers. Afterward, the template was extracted from both MIPs with NaOH, exposing the imprinted cavities. The template-extracted MIP films were then used for DPV and EIS indirect tyramine determination in the presence of  $\text{Fe}(\text{CN})_6^{4-}/\text{Fe}(\text{CN})_6^{3-}$  redox couple.

**MIP-1** exhibited high sensitivity towards tyramine. Disadvantageously, however, the **MIP-1** chemosensor was unable to discriminate common interferences, including creatinine, urea, and glucose of the concentration range same as that of the tyramine analyte. Therefore, **FM2**, the crown-ether-moiety-containing monomer, was incorporated in **MIP-2** as a second

functional monomer to provide an additional interaction site for tyramine recognition and improve the chemosensor's selectivity. This chemosensor linearly responded to tyramine in the dynamic tyramine concentration range of 290  $\mu\text{M}$  to 2.64 mM. The LOD values at  $S/N = 3$  were 159 and 168  $\mu\text{M}$  tyramine using DPV and EIS, respectively. Fortunately, the **MIP-2** chemosensor exhibited high selectivity to the glucose, urea, and creatinine interferences. The calculated DPV determined apparent imprinting factor was  $IF = 5.6$ . The **MIP-2** film was meticulously characterized using PM-IRRAS and XPS as well as AFM and SEM.

Moreover, the **MIP-2** chemosensor was used to determine tyramine in Mozzarella cheese samples. The analyte recovery determined with DPV ranged from 84 to 115%, acceptable for tyramine determination in food samples. Overall, a simple procedure of tyramine determination from the perspective of sensor preparation and measurement at a low cost with high selectivity was developed using a MIP chemosensor.

A nucleobase-functionalized MIP was deposited on an Au electrode by potentiodynamic electropolymerization of a pre-polymerization complex of thiophene-based functional monomers bearing adenine and thymine, and the **7,8-DiMeIQx** template in the presence of the T8 cross-linking monomer. The **7,8-DiMeIQx** template was subsequently extracted from the MIP film resulting in exposure of the imprinted cavities. Then, the **7,8-DiMeIQx** analyte was determined indirectly using DPV in the presence of the ferrocene or  $\text{Fe}(\text{CN})_6^{4-}/\text{Fe}(\text{CN})_6^{3-}$  redox probe. Unfortunately, despite multiple attempts, the DPV investigation of the "gate effect" was unsuccessful for this MIP chemosensor. Thus, CI was opted to investigate the selectivity to **7,8-DiMeIQx** of the MIP chemosensor under steady-state and FIA conditions.

Fortunately, the MIP chemosensor linearly responded to **7,8-DiMeIQx** in a broad concentration range of 47 to 400  $\mu\text{M}$ , with the LOD of 15.5  $\mu\text{M}$  at  $S/N = 3$  under steady-state conditions. The MIP chemosensor discriminated against interferences, including glucose, creatinine, urea, and **8-DiMeIQx**. The calculated apparent imprinting factor was high,  $IF = 8.5$ . Interestingly, the same chemosensor applied under FIA conditions non-linearly responded to **7,8-DiMeIQx** in the concentration range of 1 to 400  $\mu\text{M}$ . It appeared that the chemosensor reached saturation at **7,8-DiMeIQx** concentrations exceeding 100  $\mu\text{M}$ . However, the response was linear in a narrow range of 1 to 100  $\mu\text{M}$  **7,8-DiMeIQx**. The apparent imprinting factor calculated for the FIA determinations was  $IF = \sim 2.8$  with the LOD of 3.1  $\mu\text{M}$  at  $S/N = 3$ .

Moreover, the **7,8-DiMeIQx**-templated MIP film was meticulously characterized using PM-IRRAS and XPS as well as AFM and SEM.

The chemosensor was applied for **7,8-DiMeIQx** determination in pork extract samples under steady-state conditions; the recovery exceeded 80%. Overall, a MIP-based electrochemical chemosensor was successfully designed by utilizing the ability of the HAA to intercalate the dsDNA. The prepared chemosensor was highly selective to **7,8-DiMeIQx** without using any redox probe.

The present thesis addresses MIPs devising, testing, and applying as recognizing units in electrochemical chemosensors. Therefore, the results may aid future research on developing chemosensors capable of detecting and determining more complex forms of food toxins and other contaminants with higher repeatability, selectivity, and stability. Moreover, it may help devise redox probe-free chemosensors and the "gate effect" aided chemosensing. Furthermore, the developed strategy of imprinting DNA fragments may serve as an alternative to DNA biosensors. This strategy may also aid the fabrication of robust DNA-like chemosensors for determining other compounds interacting with dsDNAs.

One of the significant challenges to address is the potential difficulty in determining toxins in food matrices because of interference of macromolecular matrix components, e.g., proteins. Unfortunately, these components may clog the chemosensor's surface, hindering the detection signal and lowering selectivity. Therefore, these components should be removed in a preliminary treatment of the food matrix before determining toxins with an MIP chemosensor.



# References

1. Alexander, C.; Andersson, H. S.; Andersson, L. I.; Ansell, R. J.; Kirsch, N.; Nicholls, I. A.; O'Mahony, J.; Whitcombe, M. J., Molecular imprinting science and technology: a survey of the literature for the years up to and including 2003. *J. Mol. Recogn.* **2006**, *19*, 106-80.
2. He, S.; Zhang, L.; Bai, S.; Yang, H.; Cui, Z.; Zhang, X.; Li, Y., Advances of molecularly imprinted polymers (MIP) and the application in drug delivery. *Eur. Polym. J.* **2021**, *143*, 110179.
3. Breinl, F.; Haurowitz, F., Chemische Untersuchung des Präzipitates aus Hämoglobin und Anti-Hämoglobin-Serum und Bemerkungen über die Natur der Antikörper. *Biol. Chem.* **1930**, *192*, 45-57.
4. (a) Pauling, L., A Theory of the Structure and Process of Formation of Antibodies\*. *J. Am. Chem. Soc.* **1940**, *62*, 2643-2657; (b) Liu, Z. X., Z.; Wang, D.; Yang, Y.; Duan, Y.; Ma, L.; Lin, T.; Liu, H., A Review on Molecularly Imprinted Polymers Preparation by Computational Simulation-Aided Methods. *Polymers (Basel)*. **2021**, *13*, 2657.
5. Dickey, F. H., Specific Adsorption *J. Phys. Chem.* **1955**, *59*, 695-707.
6. Fu, J.; Chen, L.; Lia, J.; Zhangac, Z., Current status and challenges of ion imprinting. *J. Mater. Chem. A* **2015**, *3*, 13598-13627.
7. Wulff, G. S., A.; Zabrocki, K., Enzyme-Analogue Build Polymer and Their Use For The Resolution of Racemates. *Tetrahedron Lett.* **1973**, *44*, 4329-433.
8. (a) Feroz, M.; Vadgama, P., Molecular Imprinted Polymer Modified Electrochemical Sensors for Small Drug Analysis: Progress to Practical Application. *Electroanalysis* **2020**, *32*, 2361-2386; (b) Arshady, R.; Mosbach, K., Synthesis of Substrate-selective Polymers by Host-Guest Polymerization. *Makromol. Chem* **1981**, *182*, 687-692.
9. K. Sreenivasan, R. S., Imparting Recognition Sites in Poly(HEMA) for Two Compounds Through Molecular Imprinting. *J. Appl. Polym. Sci.* **1998**, *71*, 1823-1826.
10. Enzyme and Their Substrate: Mode of Action. <https://plantlet.org/mode-of-action-enzymes-and-their-substrates/>.
11. Shafiee, A.; Ghadiri, E.; Kassis, J.; Pourhabibi Zarandi, N.; Atala, A., Biosensing Technologies for Medical Applications, Manufacturing, and Regenerative Medicine. *Curr. Stem Cell Rep.* **2018**, *4*, 105-115.
12. (a) Naresh, V.; Lee, N., A Review on Biosensors and Recent Development of Nanostructured Materials-Enabled Biosensors. *Sensors (Basel)*. **2021**, *21*, 1109; (b) Habimana, J. d. D.; Jian, J.; Sun, X., Minireview: Trends in Optical-Based Biosensors for Point-Of-Care Bacterial Pathogen Detection for Food Safety and Clinical Diagnostics. *Anal. Lett.* **2018**, *51*, 2933-2966; (c) Farzin, L.; Shamsipur, M.; Samandari, L.; Sheibani, S., Recent advances in designing nanomaterial-based biointerfaces for electrochemical biosensing cardiovascular biomarkers. *J. Pharm. Biomed. Anal.* **2018**, *161*, 344-376.
13. (a) Kryscio, D. R.; Peppas, N. A., Critical review and perspective of macromolecularly imprinted polymers. *Acta Biomater.* **2012**, *8*, 461-73; (b) Cross, T. A., M2 Proton Channel

from Influenza A: Example of Structural Sensitivity to Environment. In *Encyclopedia of Biophysics*, Roberts, G. C. K., Ed. Springer Berlin Heidelberg: Berlin, Heidelberg, 2013; pp 1321-1327.

14. Sharma, P. S.; Dabrowski, M.; D'Souza, F.; Kutner, W., Surface development of molecularly imprinted polymer films to enhance sensing signals. *TrAC, Trends Anal. Chem.* **2013**, *51*, 146-157.

15. Sarpong, K. A.; Xu, W.; Huang, W.; Yang, W., The Development of Molecularly Imprinted Polymers in the Clean-Up of Water Pollutants: A Review. *Am. J. Anal. Chem.* **2019**, *10*, 202-226.

16. Guo, P.; Zhang, J.; Chen, X.; Zhao, L., Preparation of dummy template-imprinted polymers for the rapid extraction of nonsteroidal anti-inflammatory drugs residues in aquatic environmental samples. *Biomed. Chromatogr.* **2018**, *32*, e4193.

17. Wang, X.; Yu, J.; Li, J.; Kang, Q.; Shen, D.; Chen, L., Quantum dots based imprinting fluorescent nanosensor for the selective and sensitive detection of phycocyanin: A general imprinting strategy toward proteins. *Sens. Actuators, B* **2018**, *255*, 268-274.

18. Nezhadali, A.; Es'haghia, E.; Khatibib, A., Selective extraction of progesterone hormones from environmental and biological samples using a polypyrrole molecularly imprinted polymer and determination by gas chromatography. *Anal. Methods* **2016**, *8*, 1813-1827.

19. You, M.; Yang, S.; Tang, W.; Zhang, F.; He, P., Molecularly imprinted polymers-based electrochemical DNA biosensor for the determination of BRCA-1 amplified by SiO<sub>2</sub>@Ag. *Biosens. Bioelectron.* **2018**, *112*, 72-78.

20. Zhao, W.; Zhang, R.; Xu, S.; Cai, J.; Zhu, X.; Zhu, Y.; Wei, W.; Liu, X.; Luo, J., Molecularly imprinted polymeric nanoparticles decorated with Au NPs for highly sensitive and selective glucose detection. *Biosens. Bioelectron.* **2018**, *100*, 497-503.

21. Zhang, C.; Cui, H.; Han, Y.; Yu, F.; Shi, X., Development of a biomimetic enzyme-linked immunosorbent assay based on molecularly imprinted polymers on paper for the detection of carbaryl. *Food Chem.* **2018**, *240*, 893-897.

22. Xiao, D.; Jiang, Y.; Bi, Y., Molecularly imprinted polymers for the detection of illegal drugs and additives: a review. *Mikrochim. Acta* **2018**, *185*, 247.

23. Chen, C.; Luo, J.; Li, C.; Ma, M.; Yu, W.; Shen, J.; Wang, Z., Molecularly Imprinted Polymer as an Antibody Substitution in Pseudo-immunoassays for Chemical Contaminants in Food and Environmental Samples. *J. Agric. Food Chem.* **2018**, *66*, 2561-2571.

24. Sikiti, P.; Msagati, T. A. M.; Mamba, B. B.; Mishra, A. K., Synthesis and characterization of molecularly imprinted polymers for the remediation of PCBs and dioxins in aqueous environments. *J. Environ. Health Sci. Eng.* **2014**, *12*, 82.

25. (a) Fu, X.; Yang, Q.; Zhou, Q.; Lin, Q.; Wang, C., Template-Monomer Interaction in Molecular Imprinting: Is the Strongest the Best? *Open J. Org. Polym. Mater.* **2015**, *05*, 58-68; (b) Hasanah, A. N.; Yulianti, A. B.; Rahayu, D., Selective Atenolol Determination in Blood Using Molecular Imprinted Polymer with Itaconic Acid as Functional Monomer. *Int. J. Appl. Pharm.* **2019**, *11*, 136.

26. Zarycz, M. N. C.; Guerra, F. C., NMR (1)H-Shielding Constants of Hydrogen-Bond Donor Reflect Manifestation of the Pauli Principle. *J. Phys. Chem. Lett.* **2018**, *9*, 3720-3724.
27. Fish, W. P.; Ferreira, J.; Sheardy, R. D.; Snow, N. H.; O'Brien, T. P., Rational Design of an Imprinted Polymer: Maximizing Selectivity by Optimizing the Monomer–Template Ratio for a Cinchonidine MIP, Prior to Polymerization, Using Microcalorimetry. *J. Liq. Chromatogr. Relat. Technol.* **2007**, *28*, 1-15.
28. (a) Dong, W.; Yan, M.; Zhang, M.; Liu, Z.; Li, Y., A computational and experimental investigation of the interaction between the template molecule and the functional monomer used in the molecularly imprinted polymer. *Anal. Chim. Acta* **2005**, *542*, 186-192; (b) Zhang, B.; Fan, X.; Zhao, D., Computer-Aided Design of Molecularly Imprinted Polymers for Simultaneous Detection of Clenbuterol and Its Metabolites. *Polymers (Basel)*. **2018**, *11*, 17.
29. Nicholls, I. A.; Adbo, K.; Andersson, H. S.; Andersson, P. O.; Ankarloo, J.; Hedin-Dahlströmb, J.; Jokela, P.; Karlsson, J. K.; Olofsson, L.; Rosengren, J.; Shoravi, S.; Svenson, J.; Wikman, S., Can we rationally design molecularly imprinted polymers? *Anal. Chim. Acta* **2001**, *435*, 9-18.
30. Hasanah, A. N.; Safitri, N.; Zulfa, A.; Neli, N.; Rahayu, D., Factors Affecting Preparation of Molecularly Imprinted Polymer and Methods on Finding Template-Monomer Interaction as the Key of Selective Properties of the Materials. *Molecules* **2021**, *26*, 5612.
31. Singh, M.; Singh, S.; Singh, S. P.; Patel, S. S., Recent advancement of carbon nanomaterials engrained molecular imprinted polymer for environmental matrix. *Trends Environ. Anal. Chem.* **2020**, *27*, e00092.
32. Mueller, A., A Note about Crosslinking Density in Imprinting Polymerization. *Molecules* **2021**, *26*, 5139.
33. Jianfeng, H.; Lan, L.; Guilan, Y.; Qinying, D., Preparation, characterization, and properties studies of quinine-imprinted polymer in the aqueous phase. *Front. Chem. China* **2006**, *2*, 211-216.
34. Alizadeh, T.; Atayi, K., Synthesis of nano-sized hydrogen phosphate-imprinted polymer in acetonitrile/water mixture and its use as a recognition element of hydrogen phosphate selective all solid-state potentiometric electrode. *J. Mol. Recognit.* **2018**, *31*, e2678.
35. Xiao, D.; Su, L.; Teng, Y.; Hao, J.; Bi, Y., Fluorescent nanomaterials combined with molecular imprinting polymer: synthesis, analytical applications, and challenges. *Microchim. Acta* **2020**, *187*, 399.
36. (a) Beltran, A.; Marce, R. M.; Cormack, P. A.; Borrull, F., Synthesis by precipitation polymerisation of molecularly imprinted polymer microspheres for the selective extraction of carbamazepine and oxcarbazepine from human urine. *J. Chromatogr. A* **2009**, *1216*, 2248-53; (b) Samah, N. A.; Sanchez-Martin, M. J.; Sebastian, R. M.; Valiente, M.; Lopez-Mesas, M., Molecularly imprinted polymer for the removal of diclofenac from water: Synthesis and characterization. *Sci. Total Environ.* **2018**, *631-632*, 1534-1543.
37. Yi, L. X.; Fang, R.; Chen, G. H., Molecularly imprinted solid-phase extraction in the analysis of agrochemicals. *J. Chromatogr. Sci.* **2013**, *51*, 608-18.

38. Kempe, H.; Kempe, M., Development and evaluation of spherical molecularly imprinted polymer beads. *Anal. Chem.* **2006**, *78*, 3659-66.
39. Zhao, G.; Liu, J.; Liu, M.; Han, X.; Peng, Y.; Tian, X.; Liu, J.; Zhang, S., Synthesis of Molecularly Imprinted Polymer via Emulsion Polymerization for Application in Solanesol Separation. *Appl. Sci.* **2020**, *10*, 2868.
40. Haginaka, J.; Tabo, H.; Matsunaga, H., Preparation of molecularly imprinted polymers for organophosphates and their application to the recognition of organophosphorus compounds and phosphopeptides. *Anal. Chim. Acta* **2012**, *748*, 1-8.
41. Miura, C.; Matsunaga, H.; Haginaka, J., Molecularly imprinted polymer for caffeic acid by precipitation polymerization and its application to extraction of caffeic acid and chlorogenic acid from *Eucommia ulmoides* leaves. *J. Pharm. Biomed. Anal.* **2016**, *127*, 32-8.
42. Kwaśniewska, K.; Gadzała-Kopciuch, R.; Buszewski, B., Magnetic molecular imprinted polymers as a tool for isolation and purification of biological samples. *Open Chem.* **2015**, *13*, 1228-1235.
43. Ozcan, A. A.; Say, R.; Denizli, A.; Ersöz, A., L-histidine imprinted synthetic receptor for biochromatography applications. *Anal. Chem.* **2006**, *78*, 7253-7258.
44. Hantash, J.; Bartlett, A.; Oldfield, P.; Denes, G.; O'Rielly, R.; Roudiere, D.; Menduni, S., Use of an on-line imprinted polymer pre-column, for the liquid chromatographic-UV absorbance determination of carbaryl and its metabolite in complex matrices. *J. Chromatogr. A* **2006**, *1125*, 104-11.
45. (a) Albernaz, V. L.; Bach, M.; Weber, A.; Southan, A.; Tovar, G. E. M., Active Ester Containing Surfmer for One-Stage Polymer Nanoparticle Surface Functionalization in Mini-Emulsion Polymerization. *Polymers (Basel)*. **2018**, *10*, 408; (b) Sun, Y.; Chen, J.; Li, Y.; Li, H.; Zhu, X.; Hu, Y.; Huang, S.; Li, J.; Zhong, S., Bio-inspired magnetic molecularly imprinted polymers based on Pickering emulsions for selective protein recognition. *New J. Chem.* **2016**, *40*, 8745-8752.
46. Refaat, D.; Aggour, M. G.; Farghali, A. A.; Mahajan, R.; Wiklander, J. G.; Nicholls, I. A.; Piletsky, S. A., Strategies for Molecular Imprinting and the Evolution of MIP Nanoparticles as Plastic Antibodies-Synthesis and Applications. *Int. J. Mol. Sci.* **2019**, *20*, 6304.
47. (a) Lu, X.-F.; Shi, Y.-F.; Lv, H.-L.; Fu, Y.-Y.; Ma, D.; Xue, W., Preparation and characterization of molecularly imprinted poly(hydroxyethyl methacrylate) microspheres for sustained release of gatifloxacin. *J. Mater. Sci.: Mater. Med.* **2014**, *25*, 1461-9; (b) Sun, L.; Guan, J.; Xu, Q.; Yang, X.; Wang, J.; Hu, X., Synthesis and Applications of Molecularly Imprinted Polymers Modified TiO<sub>2</sub> Nanomaterials: A Review. *Polymers (Basel)*. **2018**, *10*, 1248.
48. Jyoti; Gonzato, C.; Zolek, T.; Maciejewska, D.; Kutner, A.; Merlier, F.; Haupt, K.; Sharma, P. S.; Noworyta, K. R.; Kutner, W., Molecularly imprinted polymer nanoparticles-based electrochemical chemosensors for selective determination of cilostazol and its pharmacologically active primary metabolite in human plasma. *Biosens. Bioelectron.* **2021**, *193*, 113542.

49. El-Schich, Z.; Zhang, Y.; Feith, M.; Beyer, S.; Sternbæk, L.; Ohlsson, L.; Stollenwerk, M.; Wingren, A. G., Molecularly imprinted polymers in biological applications. *Biotechniques* **2020**, *69*, 406-419.
50. Xu, S.; Li, J.; Chen, L., Molecularly imprinted polymers by reversible addition-fragmentation chain transfer precipitation polymerization for preconcentration of atrazine in food matrices. *Talanta* **2011**, *85*, 282-9.
51. Bhogal, S.; Kaur, K.; Malik, A. K.; Sonne, C.; Lee, S. S.; Kim, K.-H., Core-shell structured molecularly imprinted materials for sensing applications. *TrAC, Trends Anal. Chem.* **2020**, *133*, 116043.
52. Braunecker, W. A.; Matyjaszewski, K., Controlled/living radical polymerization: Features, developments, and perspectives. *Prog. Polym. Sci.* **2007**, *32*, 93-146.
53. Cummins, W.; Duggan, P.; McLoughlin, P., A comparative study of the potential of acrylic and sol-gel polymers for molecular imprinting. *Anal. Chim. Acta* **2005**, *542*, 52-60.
54. Shang, L.; Liu, C.; Chen, B.; Hayashi, K., Development of molecularly imprinted sol-gel based LSPR sensor for detection of volatile *cis*-jasmone in plant. *Sens. Actuators, B* **2018**, *260*, 617-626.
55. Li, M.; Li, R.; Tan, J.; Jiang, Z. T., Titania-based molecularly imprinted polymer for sulfonic acid dyes prepared by sol-gel method. *Talanta* **2013**, *107*, 203-10.
56. Moein, M. M.; Abdel-Rehim, A.; Abdel-Rehim, M., Recent Applications of Molecularly Imprinted Sol-Gel Methodology in Sample Preparation. *Molecules* **2019**, *24*.
57. Adumitrăchioaie, A., Electrochemical Methods Based on Molecularly Imprinted Polymers for Drug Detection. A Review. *Int. J. Electrochem. Sci.* **2018**, *13*, 2556-2576.
58. Ming, W.; Wang, X.; Lu, W.; Zhang, Z.; Song, X.; Li, J.; Chen, L., Magnetic molecularly imprinted polymers for the fluorescent detection of trace 17 $\beta$ -estradiol in environmental water. *Sens. Actuators, B* **2017**, *238*, 1309-1315.
59. Lian, W.; Huang, J.; Yu, J.; Zhang, X.; Lin, Q.; He, X.; Xing, X.; Liu, S., A molecularly imprinted sensor based on  $\beta$ -cyclodextrin incorporated multiwalled carbon nanotube and gold nanoparticles-polyamide amine dendrimer nanocomposites combining with water-soluble chitosan derivative for the detection of chlortetracycline. *Food Control* **2012**, *26*, 620-627.
60. Wang, Y.; Zhou, J.; Zhang, B.; Tian, L.; Ali, Z.; Zhang, Q., Fabrication and characterization of glutathione-imprinted polymers on fibrous SiO<sub>2</sub> microspheres with high specific surface. *Chem. Eng. J.* **2017**, *327*, 932-940.
61. Liu, Y.; Shi, X. W.; Kim, E.; Robinson, L. M.; Nye, C. K.; Ghodssi, R.; Rubloff, G. W.; Bentley, W. E.; Payne, G. F., Chitosan to electroaddress biological components in lab-on-a-chip devices. *Carbohydr. Polym.* **2011**, *84*, 704-708.
62. Sharma, P. S.; Dabrowski, M.; Noworyta, K.; Huynh, T.-P.; Kc, C. B.; Sobczak, J. W.; Pieta, P.; D'Souza, F.; Kutner, W., Fullerene derived molecularly imprinted polymer for chemosensing of adenosine-5'-triphosphate (ATP). *Anal. Chim. Acta* **2014**, *844*, 61-9.

63. Sharma, P. S.; Pietrzyk-Le, A.; D'Souza, F.; Kutner, W., Electrochemically synthesized polymers in molecular imprinting for chemical sensing. *Anal. Bioanal. Chem.* **2012**, *402*, 3177-204.
64. Huynh, T.-P.; Sharma, P. S.; Sosnowska, M.; D'Souza, F.; Kutner, W., Functionalized polythiophenes: Recognition materials for chemosensors and biosensors of superior sensitivity, selectivity, and detectability. *Prog. Polym. Sci.* **2015**, *47*, 1-25.
65. Malitesta, C.; Losito, I.; Zambonin, P. G., Molecularly Imprinted Electrosynthesized Polymers: New Materials for Biomimetic Sensors. *Anal. Chem.* **1999**, *71*, 1366-1370.
66. Gajda, M.; Rybakiewicz, R.; Cieplak, M.; Żołek, T.; Maciejewska, D.; Gilant, E.; Rudzki, P. J.; Grab, K.; Kutner, A.; Borowicz, P.; Kutner, W.; Noworyta, K. R., Low-oxidation-potential thiophene-carbazole monomers for electro-oxidative molecular imprinting: Selective chemosensing of aripiprazole. *Biosens. Bioelectron.* **2020**, *169*, 112589.
67. Zembrzuska, D.; Kalecki, J.; Cieplak, M.; Lisowski, W.; Borowicz, P.; Noworyta, K.; Sharma, P. S., Electrochemically initiated co-polymerization of monomers of different oxidation potentials for molecular imprinting of electroactive analyte. *Sens. Actuators, B* **2019**, *298*, 126884.
68. (a) Chen, L.; Xu, S.; Li, J., Recent advances in molecular imprinting technology: current status, challenges and highlighted applications. *Chem. Soc. Rev.* **2011**, *40*, 2922-42; (b) Lu, H.; Tian, H.; Wang, C.; Xu, S., Designing and controlling the morphology of spherical molecularly imprinted polymers. *Mater. Adv.* **2020**, *1*, 2182-2201.
69. Hu, L.; Zhou, T.; Luo, D.; Feng, J.; Tao, Y.; Zhou, Y.; Mei, S., Bioaccumulation of tetrabromobisphenol A in a laboratory-based fish-water system based on selective magnetic molecularly imprinted solid-phase extraction. *Sci. Total Environ.* **2019**, *650*, 1356-1362.
70. Wu, Y.; Zhang, W.; Chen, Y.; Chen, Z., Electroosmotic pump-supported molecularly imprinted monolithic column for capillary chromatographic separation of nitrophenol isomers. *Electrophoresis* **2015**, *36*, 2881-7.
71. Marć, M.; Wiczorek, P. P., Application potential of dummy molecularly imprinted polymers as solid-phase extraction sorbents for determination of low-mass polybrominated diphenyl ethers in soil and sediment samples. *Microchem. J.* **2019**, *144*, 461-468.
72. Regal, P.; Díaz-Bao, M.; Barreiro, R.; Cepeda, A.; Fente, C., Application of molecularly imprinted polymers in food analysis: clean-up and chromatographic improvements. *Open Chem.* **2012**, *10*, 766-784.
73. Piletsky, S. A.; Turner, N. W.; Laitenberger, P., Molecularly imprinted polymers in clinical diagnostics-future potential and existing problems. *Med. Eng. Phys.* **2006**, *28*, 971-7.
74. (a) Han, S.; Su, L.; Zhai, M.; Ma, L.; Liu, S.; Teng, Y., A molecularly imprinted composite based on graphene oxide for targeted drug delivery to tumor cells. *J. Mater. Sci.* **2018**, *54*, 3331-3341; (b) Liu, R.; Poma, A., Advances in Molecularly Imprinted Polymers as Drug Delivery Systems. *Molecules* **2021**, *26*, 3589.
75. Wulff, G., Enzyme-like Catalysis by Molecularly Imprinted Polymers. *Chem. Rev.* **2002**, *102*, 1-28.

76. Kozitsina, A. N.; Svalova, T. S.; Malysheva, N. N.; Okhokhonin, A. V.; Vidrevich, M. B.; Brainina, K. Z., Sensors Based on Bio and Biomimetic Receptors in Medical Diagnostic, Environment, and Food Analysis. *Biosensors (Basel)*. **2018**, *8*, 35.
77. Vlatakis, G.; Andersson, L. I.; Müller, R.; Mosbach, K., Drug assay using antibody mimics made by molecular imprinting. *Nature* **1993**, *361*, 645-7.
78. Hutchins, R. S.; Bachas, L. G., Nitrate-Selective Electrode Developed by Electrochemically Mediated Imprinting/Doping of Polypyrrole. *Anal. Chem.* **1995**, *67*, 1654-1660.
79. Cui, B.; Liu, P.; Liu, X.; Liu, S.; Zhang, Z., Molecularly imprinted polymers for electrochemical detection and analysis: progress and perspectives. *J. Mater. Res. Technol.* **2020**, *9*, 12568-12584.
80. Nantasenamat, C.; Isarankura-Na-Ayudhya, C.; Naenna, T.; Prachayasittikul, V., Quantitative structure-imprinting factor relationship of molecularly imprinted polymers. *Biosens. Bioelectron.* **2007**, *22*, 3309-3317.
81. Mora-Granados, M.; González-Gómez, D.; Jeong, J. S.; Gallego-Picó, A., A Molecularly Imprinted Polymer for Selective Extraction of Phenolic Acids from Human Urine. *Appl. Sci.* **2021**, *11*, 1577.
82. Prabakaran, K.; Jandas, P. J.; Luo, J.; Fu, C.; Wei, Q., Molecularly imprinted poly(methacrylic acid) based QCM biosensor for selective determination of L-tryptophan. *Colloids Surf., A* **2021**, *611*, 125859.
83. El-Akaad, S.; Mohamed, M. A.; Abdelwahab, N. S.; Abdelaleem, E. A.; De Saeger, S.; Beloglazova, N., Capacitive sensor based on molecularly imprinted polymers for detection of the insecticide imidacloprid in water. *Sci. Rep.* **2020**, *10*, 14479.
84. Herrera-Chacón, A.; Cetó, X.; del Valle, M., Molecularly imprinted polymers - towards electrochemical sensors and electronic tongues. *Anal. Bioanal. Chem.* **2021**, *413*, 6117-6140.
85. Kalecki, J.; Cieplak, M.; Dąbrowski, M.; Lisowski, W.; Kuhn, A.; Sharma, P. S., Hexagonally Packed Macroporous Molecularly Imprinted Polymers for Chemosensing of Follicle-Stimulating Hormone Protein. *Sensors* **2020**, *5*, 118-126.
86. Vasapollo, G.; Sole, R. D.; Mergola, L.; Lazzoi, M. R.; Scardino, A.; Scorrano, S.; Mele, G., Molecularly imprinted polymers: present and future prospective. *Int. J. Mol. Sci.* **2011**, *12*, 5908-45.
87. (a) Guo, Z.; Florea, A.; Jiang, M.; Mei, Y.; Zhang, W.; Zhang, A.; Săndulescu, R.; Jaffrezic-Renault, N., Molecularly Imprinted Polymer/Metal-Organic Framework Based Chemical Sensors. *Coatings* **2016**, *6*, 42; (b) John, A.; Benny, L.; Cherian, A. R.; Narahari, S. Y.; Varghese, A.; Hegde, G., Electrochemical sensors using conducting polymer/noble metal nanoparticle nanocomposites for the detection of various analytes: a review. *J. Nanostruct. Chem.* **2021**, *11*, 1-31.
88. Elfadil, D.; Lamaoui, A.; Della Pelle, F.; Amine, A.; Compagnone, D., Molecularly Imprinted Polymers Combined with Electrochemical Sensors for Food Contaminants Analysis. *Molecules* **2021**, *26*.

89. (a) Di Stefano, V.; Avellone, G.; Bongiorno, D.; Cunsolo, V.; Muccilli, V.; Sforza, S.; Dossena, A.; Drahos, L.; Vekey, K., Applications of liquid chromatography-mass spectrometry for food analysis. *J. Chromatogr.* **2012**, *1259*, 74-85; (b) Li, Z.; Wang, J.; Chen, X.; Hu, S.; Gong, T.; Xian, Q., A novel molecularly imprinted polymer-solid phase extraction method coupled with high-performance liquid chromatography-tandem mass spectrometry for the determination of nitrosamines in water and beverage samples. *Food Chem.* **2019**, *292*, 267-274; (c) Aghoutane, Y.; Diouf, A.; Osterlund, L.; Bouchikhi, B.; El Bari, N., Development of a molecularly imprinted polymer electrochemical sensor and its application for sensitive detection and determination of malathion in olive fruits and oils. *Bioelectrochemistry* **2020**, *132*, 107404.
90. Mohd Ali, M.; Hashim, N.; Aziz, S. A.; Lasekan, O., Emerging non-destructive thermal imaging technique coupled with chemometrics on quality and safety inspection in food and agriculture. *Trends Food Sci. Technol.* **2020**, *105*, 176-185.
91. Cao, Y.; Feng, T.; Xu, J.; Xue, C., Recent advances of molecularly imprinted polymer-based sensors in the detection of food safety hazard factors. *Biosens. Bioelectron.* **2019**, *141*, 111447.
92. Maduraiveeran, G.; Sasidharan, M.; Ganesan, V., Electrochemical sensor and biosensor platforms based on advanced nanomaterials for biological and biomedical applications. *Biosens. Bioelectron.* **2018**, *103*, 113-129.
93. Vasilescu, A.; Nunes, G.; Hayat, A.; Latif, U.; Marty, J. L., Electrochemical Affinity Biosensors Based on Disposable Screen-Printed Electrodes for Detection of Food Allergens. *Sensors (Basel)*. **2016**, *16*, 1863.
94. Leibl, N.; Haupt, K.; Gonzato, C.; Duma, L., Molecularly Imprinted Polymers for Chemical Sensing: A Tutorial Review. *Chemosensors* **2021**, *9*, 123.
95. Arreguin-Campos, R.; Jimenez-Monroy, K. L.; Dilien, H.; Cleij, T. J.; Grinsven, v. B.; Eersels, K., Imprinted Polymers as Synthetic Receptors in Sensors for Food Safety. *Biosensors (Basel)*. **2021**, *11*, 46.
96. Blanco-López, M. C.; Lobo-Castañón, M. J.; Miranda-Ordieres, A. J.; Tuñón-Blanco, P., Electrochemical sensors based on molecularly imprinted polymers. *TrAC, Trends Anal. Chem.* **2004**, *23*, 36-48.
97. Liang, R.; Zhang, R.; Qin, W., Potentiometric sensor based on molecularly imprinted polymer for determination of melamine in milk. *Sens. Actuators, B* **2009**, *141*, 544-550.
98. Franklin, R. K.; Martin, S. M.; Strong, T. D.; Brown, R. B., Chemical and Biological Systems: Chemical Sensing Systems for Liquids. In *ReferenceModule in Materials and Materials Engineering* Elsevier: 2016.
99. Zhang, M.; Zhao, H. T.; Xie, T. J.; Yang, X.; Dong, A. J.; Zhang, H.; Wang, J.; Wang, Z. Y., Molecularly imprinted polymer on graphene surface for selective and sensitive electrochemical sensing imidacloprid. *Sens. Actuators, B* **2017**, *252*, 991-1002.
100. Hassan, A. H. A.; Sappia, L.; Moura, S. L.; Ali, F. H. M.; Moselhy, W. A.; Sotomayor, M.; Pividori, M. I., Biomimetic magnetic sensor for electrochemical determination of scombrotoxin in fish. *Talanta* **2019**, *194*, 997-1004.

101. Liu, Z.; Zhang, Y.; Feng, J.; Han, Q.; Wei, Q., Ni(OH)<sub>2</sub> nanoarrays based molecularly imprinted polymer electrochemical sensor for sensitive detection of sulfapyridine. *Sens. Actuators, B* **2019**, *287*, 551-556.
102. Capoferri, D.; Del Carlo, M.; Ntshongontshi, N.; Iwuoha, E. I.; Sergi, M.; Di Ottavio, F.; Compagnone, D., MIP-MEPS based sensing strategy for the selective assay of dimethoate. Application to wheat flour samples. *Talanta* **2017**, *174*, 599-604.
103. Ben Aissa, A.; Herrera-Chacon, A.; Pupin, R. R.; Sotomayor, M.; Pividori, M. I., Magnetic molecularly imprinted polymer for the isolation and detection of biotin and biotinylated biomolecules. *Biosens. Bioelectron.* **2017**, *88*, 101-108.
104. Gaudin, V., Chapter 11 - Receptor-based electrochemical biosensors for the detection of contaminants in food products. In *Electrochemical Biosensors*, Ensafi, A. A., Ed. Elsevier: 2019; pp 307-365.
105. Lian, W.; Liu, S.; Yu, J.; Li, J.; Cui, M.; Xu, W.; Huang, J., Electrochemical sensor using neomycin-imprinted film as recognition element based on chitosan-silver nanoparticles/graphene-multiwalled carbon nanotubes composites modified electrode. *Biosens. Bioelectron.* **2013**, *44*, 70-6.
106. Meng, X.; Guo, W.; Qin, X.; Liu, Y.; Zhu, X.; Pei, M.; Wang, L., A molecularly imprinted electrochemical sensor based on gold nanoparticles and multiwalled carbon nanotube-chitosan for the detection of tryptamine. *RSC Adv.* **2014**, *4*, 38649-38654.
107. Shamsipur, M.; Moradi, N.; Pashabadi, A., Coupled electrochemical-chemical procedure used in construction of molecularly imprinted polymer-based electrode: a highly sensitive impedimetric melamine sensor. *J. Solid State Electrochem.* **2017**, *22*, 169-180.
108. Sergeeva, T. A.; Piletsky, S. A.; Brovko, A. A.; Slinchenko, E. A.; Sergeeva, L. M.; El'skaya, A. V., Selective recognition of atrazine by molecularly imprinted polymer membranes. Development of conductometric sensor for herbicides detection. *Anal. Chim. Acta* **1999**, *392*, 105-111.
109. Shirzadmehr, A.; Afkhami, A.; Madrakian, T., A new nano-composite potentiometric sensor containing an Hg<sup>2+</sup> ion-imprinted polymer for the trace determination of mercury ions in different matrices. *J. Mol. Liq.* **2015**, *204*, 227-235.
110. Cui, M.; Liu, S.; Lian, W.; Li, J.; Xu, W.; Huang, J., A molecularly-imprinted electrochemical sensor based on a graphene-Prussian blue composite-modified glassy carbon electrode for the detection of butylated hydroxyanisole in foodstuffs. *Analyst* **2013**, *138*, 5949-5955.
111. Yin, Z.-Z.; Cheng, S.-W.; Xu, L.-B.; Liu, H.-Y.; Huang, K.; Li, L.; Zhai, Y.-Y.; Zeng, Y.-B.; Liu, H.-Q.; Shao, Y.; Zhang, Z.-L.; Lu, Y.-X., Highly sensitive and selective sensor for sunset yellow based on molecularly imprinted polydopamine-coated multi-walled carbon nanotubes. *Biosens. Bioelectron.* **2018**, *100*, 565-570.
112. Li, Y.; Liu, Y.; Yang, Y.; Yu, F.; Liu, J.; Song, H.; Liu, J.; Tang, H.; Ye, B.-C.; Sun, Z., Novel Electrochemical Sensing Platform Based on a Molecularly Imprinted Polymer Decorated 3D Nanoporous Nickel Skeleton for Ultrasensitive and Selective Determination of Metronidazole. *ACS Appl. Mater. Interfaces* **2015**, *7*, 15474-15480.

113. Yoshimi, Y.; Ohdaira, R.; Iiyama, C.; Sakai, K., “Gate Effect” of thin layer of molecularly-imprinted poly(methacrylic acid-co-ethyleneglycol dimethacrylate). *Sens. Actuators, B* **2001**, *73*, 49-53.
114. Sharma, P. S.; Garcia-Cruz, A.; Cieplak, M.; Noworyta, K. R.; Kutner, W., “Gate Effect” in molecularly imprinted polymers: the current state of understanding. *Curr. Opin. in Electrochem.* **2019**, *16*, 50-56.
115. Yoshimi, Y.; Narimatsu, A.; Nakayama, K.; Sekine, S.; Hattori, K.; Sakai, K., Development of an enzyme-free glucose sensor using the “gate effect” of a molecularly imprinted polymer. *J. Artif. Organs* **2009**, *12*, 264-70.
116. Munawar, H.; Garcia-Cruz, A.; Majewska, M.; Karim, K.; Kutner, W.; Piletsky, S. A., Electrochemical determination of fumonisin B1 using a chemosensor with a recognition unit comprising molecularly imprinted polymer nanoparticles. *Sens. Actuators, B* **2020**, *321*, 128552.
117. Lach, P.; Cieplak, M.; Noworyta, K. R.; Pieta, P.; Lisowski, W.; Kalecki, J.; Chitta, R.; D’Souza, F.; Kutner, W.; Sharma, P. S., Self-reporting molecularly imprinted polymer with the covalently immobilized ferrocene redox probe for selective electrochemical sensing of p-synephrine. *Sens. Actuators, B* **2021**, *344*, 130276.
118. Lach, P.; Cieplak, M.; Majewska, M.; Noworyta, K. R.; Sharma, P. S.; Kutner, W., “Gate Effect” in p-Synephrine Electrochemical Sensing with a Molecularly Imprinted Polymer and Redox Probes. *Anal. Chem.* **2019**, *91*, 7546-7553.
119. Yang, L.; Zhao, F.; Zeng, B., Electrochemical determination of eugenol using a three-dimensional molecularly imprinted poly (p-aminothiophenol-co-p-aminobenzoic acids) film modified electrode. *Electrochim. Acta* **2016**, *210*, 293-300.
120. Monoamine Oxidase Inhibitors (MAOI) –Mechanism of Action |Psychopharmacology | Clinical Application. <https://psychscenehub.com/psychinsights/maoi-psychopharmacology/>.
121. Youdim, M. B. H.; Edmondson, D.; Tipton, K. F., The therapeutic potential of monoamine oxidase inhibitors. *Nat. Rev. Neurosci.* **2006**, *7*, 295-309.
122. Sathyanarayana Rao, T. S.; Yeragani, V. K., Hypertensive crisis and cheese. *Indian J. Psychiatry* **2009**, *51*, 65-66.
123. Dhakal, S.; Macreadie, I., Tyramine and Amyloid Beta 42: A Toxic Synergy. *Biomedicines* **2020**, *8*, 145.
124. Meal ideas and menus: Avoiding high-tyramine foods made easy. <http://www.chrisbojrabmd.com/downloads/files/MAOI%20Diet%20and%20Menu%20Book.pdf>.
125. Gatti, R.; Lotti, C.; Morigi, R.; Andreani, A., Determination of octopamine and tyramine traces in dietary supplements and phytoextracts by high-performance liquid chromatography after derivatization with 2,5-dimethyl-1H-pyrrole-3,4-dicarbaldehyde. *J. Chromatogr. A* **2012**, *1220*, 92-100.
126. Koh, A. H. W.; Chess-Williams, R.; Lohning, A. E., HPLC-UV-QDa analysis of Citrus aurantium-labelled pre-workout supplements suggest only a minority contain the plant extract. *J. Pharm. Biomed. Anal.* **2021**, *193*, 113746.

127. Atta, N. F.; Hamed, M. M.; Abdel-Mageed, A. M., Computational investigation and synthesis of a sol-gel imprinted material for sensing application of some biologically active molecules. *Anal. Chim. Acta* **2010**, *667*, 63-70.
128. Atta, N. F.; Abdel-Mageed, A. M., Smart electrochemical sensor for some neurotransmitters using imprinted sol-gel films. *Talanta* **2009**, *80*, 511-518.
129. Zhang, D.; Liu, H.; Geng, W.; Wang, Y., A dual-function molecularly imprinted optopolymer based on quantum dots-grafted covalent-organic frameworks for the sensitive detection of tyramine in fermented meat products. *Food Chem.* **2019**, *277*, 639-645.
130. Huang, J.; Xing, X.; Zhang, X.; He, X.; Lin, Q.; Lian, W.; Zhu, H., A molecularly imprinted electrochemical sensor based on multiwalled carbon nanotube-gold nanoparticle composites and chitosan for the detection of tyramine. *Food Res. Int.* **2011**, *44*, 276-281.
131. Lee, J.-D.; Hong, J.-I., Two-dimensional sensor array for discrimination of amines. *Tetrahedron Lett.* **2013**, *54*, 2890-2893.
132. Luliński, P.; Sobiech, M.; Żołek, T.; Maciejewska, D., A separation of tyramine on a 2-(4-methoxyphenyl)ethylamine imprinted polymer: An answer from theoretical and experimental studies. *Talanta* **2014**, *129*, 155-164.
133. Li, Y.; Hsieh, C.-H.; Lai, C.-W.; Chang, Y.-F.; Chan, H.-Y.; Tsai, C.-F.; Ho, J.-a. A.; Wu, L.-c., Tyramine detection using PEDOT:PSS/AuNPs/1-methyl-4-mercaptopyridine modified screen-printed carbon electrode with molecularly imprinted polymer solid-phase extraction. *Biosens. Bioelectron.* **2017**, *87*, 142-149.
134. Li, Y.; Hsieh, C.-H.; Lai, C.-W.; Chang, Y.-F.; Chan, H.-Y.; Tsai, C.-F.; Ho, J.-a. A.; Wu, L.-c., Tyramine detection using PEDOT:PSS/AuNPs/1-methyl-4-mercaptopyridine modified screen-printed carbon electrode with molecularly imprinted polymer solid phase extraction. *Biosens. Bioelectron.* **2017**, *87*, 142-149.
135. Liu, M.; Zhang, B.; Zhang, M.; Hu, X.; Chen, W.; Fang, G.; Wang, S., A dual-recognition molecularly imprinted electrochemiluminescence sensor based on g-C<sub>3</sub>N<sub>4</sub> nanosheets sensitized by electrodeposited rGO-COOH for sensitive and selective detection of tyramine. *Sens. Actuators, B* **2020**, *311*, 127901.
136. Jiang, J.; Lin, X.; Ding, D.; Diao, G., Graphitic-phase carbon nitride-based electrochemiluminescence sensing analyses: recent advances and perspectives. *RSC Adv.* **2018**, *8*, 19369-19380.
137. Qiao, D.; Zhang, Z.; Wang, L.; Sheng, W.; Deng, Q.; Wang, S., In-situ preparation of molecularly imprinted fluorescent sensing test strips for on-site detection of tyramine in vinegar. *Microchem. J.* **2021**, *160*, 105638.
138. Skog, K. I.; Johansson, M. A.; Jägerstad, M. I., Carcinogenic heterocyclic amines in model systems and cooked foods: a review on formation, occurrence and intake. *Food Chem. Toxicol.* **1998**, *36*, 879-96.
139. Dong, H.; Xian, Y.; Li, H.; Bai, W.; Zeng, X., Potential carcinogenic heterocyclic aromatic amines (HAAs) in foodstuffs: Formation, extraction, analytical methods, and mitigation strategies. *Compr. Rev. Food Sci. Food Saf.* **2020**, *19*, 365-404.

140. Murkovic, M., Analysis of heterocyclic aromatic amines. *Anal. Bioanal. Chem.* **2007**, *389*, 139-46.
141. Casal, S.; Mendes, E.; Fernandes, J. O.; Oliveira, M. B.; Ferreira, M. A., Analysis of heterocyclic aromatic amines in foods by gas chromatography-mass spectrometry as their tert.-butyldimethylsilyl derivatives. *J. Chromatogr. A* **2004**, *1040*, 105-14.
142. Nadeem, H. R.; Akhtar, S.; Ismail, T.; Sestili, P.; Lorenzo, J. M.; Ranjha, M.; Jooste, L.; Hano, C.; Aadil, R. M., Heterocyclic Aromatic Amines in Meat: Formation, Isolation, Risk Assessment, and Inhibitory Effect of Plant Extracts. *Foods* **2021**, *10*, 1466.
143. Barzegar, F.; Kamankesh, M.; Mohammadi, A., Heterocyclic aromatic amines in cooked food: A review on formation, health risk-toxicology, and their analytical techniques. *Food Chem.* **2019**, *280*, 240-254.
144. Gibis, M., Heterocyclic Aromatic Amines in Cooked Meat Products: Causes, Formation, Occurrence, and Risk Assessment. *Compr. Rev. Food Sci. Food Saf.* **2016**, *15*, 269-302.
145. Boer, D. R.; Canals, A.; Coll, M., DNA-binding drugs caught in action: the latest 3D pictures of drug-DNA complexes. *Dalton Trans.* **2009**, *21*, 399-414.
146. Elmquist, C. E.; Wang, F.; Stover, J. S.; Stone, M. P.; Rizzo, C. J., Conformational differences of the C8-deoxyguanosine adduct of 2-amino-3-methylimidazo[4,5-f]quinoline (IQ) within the NarI recognition sequence. *Chem. Res. Toxicol.* **2007**, *20*, 445-54.
147. Kim, D.; Guengerich, F. P., Cytochrome P450 activation of arylamines and heterocyclic amines. *Annu. Rev. Pharmacol. Toxicol.* **2005**, *45*, 27-49.
148. Schut, H. A. J.; Snyderwine, E. G., DNA adducts of heterocyclic amine food mutagens: implications for mutagenesis and carcinogenesis. *Carcinogenesis* **1999**, *20*, 353-368.
149. Dong, H.; Xian, Y.; Li, H.; Wu, Y.; Bai, W.; Zeng, X., Analysis of heterocyclic aromatic amine profiles in Chinese traditional bacon and sausage based on ultrahigh-performance liquid chromatography-quadrupole-Orbitrap high-resolution mass spectrometry (UHPLC-Q-Orbitrap-HRMS). *Food Chem.* **2020**, *310*, 125937.
150. Wu, Y.; Chen, L.; Xian, Y.; Hou, X.; Liang, M.; Dong, H.; Chen, J., Quantitative analysis of fourteen heterocyclic aromatic amines in bakery products by a modified QuEChERS method coupled to ultra-high performance liquid chromatography-tandem mass spectrometry (UHPLC-MS/MS). *Food Chem.* **2019**, *298*, 125048.
151. Manful, C. F.; Vidal, N. P.; Pham, T. H.; Nadeem, M.; Wheeler, E.; Hamilton, M. C.; Doody, K. M.; Thomas, R. H., Rapid determination of heterocyclic amines in ruminant meats using accelerated solvent extraction and ultra-high performance liquid chromatography-mass spectrometry. *MethodsX* **2019**, *6*, 2686-2697.
152. Cayuela, A.; Soriano, M. L.; Valcárcel, M., Strong luminescence of carbon dots induced by acetone passivation: efficient sensor for a rapid analysis of two different pollutants. *Anal. Chim. Acta* **2013**, *804*, 246-51.
153. López, C.; Zougagh, M.; Algarra, M.; Rodríguez-Castellón, E.; Campos, B. B.; Esteves da Silva, J. C.; Jiménez-Jiménez, J.; Ríos, A., Microwave-assisted synthesis of carbon dots and its potential as analysis of four heterocyclic aromatic amines. *Talanta* **2015**, *132*, 845-50.

154. Frandsen, H.; Frederiksen, H.; Alexander, J., 2-Amino-1-methyl-6-(5-hydroxy-)phenylimidazo[4,5-*b*]pyridine (5-OH-PhIP), a biomarker for the genotoxic dose of the heterocyclic amine, 2-amino-1-methyl-6-phenylimidazo[4,5-*b*]pyridine (PhIP). *Food Chem. Toxicol.* **2002**, *40*, 1125-30.
155. Nawaz, N.; Abu Bakar, N. K.; Muhammad Ekramul Mahmud, H. N.; Jamaludin, N. S., Molecularly imprinted polymers-based DNA biosensors. *Anal. Biochem.* **2021**, *630*, 114328.
156. Slinchenko, O.; Rachkov, A.; Miyachi, H.; Ogiso, M.; Minoura, N., Imprinted polymer layer for recognizing double-stranded DNA. *Biosens. Bioelectron.* **2004**, *20*, 1091-7.
157. Ogiso, M.; Minoura, N.; Shinbo, T.; Shimizu, T., DNA detection system using molecularly imprinted polymer as the gel matrix in electrophoresis. *Biosens. Bioelectron.* **2007**, *22*, 1974-81.
158. Bartold, K.; Pietrzyk-Le, A.; Huynh, T.-P.; Iskierko, Z.; Sosnowska, M.; Noworyta, K.; Lisowski, W.; Sannicolo, F.; Cauteruccio, S.; Licandro, E.; D'Souza, F.; Kutner, W., Programmed Transfer of Sequence Information into a Molecularly Imprinted Polymer for Hexakis(2,2'-bithien-5-yl) DNA Analogue Formation toward Single-Nucleotide-Polymorphism Detection. *ACS Appl. Mater. Interfaces* **2017**, *9*, 3948-3958.
159. Huynh, T.-P.; Pieta, P.; D'Souza, F.; Kutner, W., Molecularly imprinted polymer for recognition of 5-fluorouracil by RNA-type nucleobase pairing. *Anal. Chem.* **2013**, *85*, 8304-12.
160. Sharma, P. S.; Wojnarowicz, A.; Sosnowska, M.; Benincori, T.; Noworyta, K.; D'Souza, F.; Kutner, W., Potentiometric chemosensor for neopterin, a cancer biomarker, using an electrochemically synthesized molecularly imprinted polymer as the recognition unit. *Biosens. Bioelectron.* **2016**, *77*, 565-72.
161. Huynh, T.-P.; Wojnarowicz, A.; Sosnowska, M.; Srebnik, S.; Benincori, T.; Sannicolo, F.; D'Souza, F.; Kutner, W., Cytosine derivatized bis(2,2'-bithienyl)methane molecularly imprinted polymer for selective recognition of 6-thioguanine, an antitumor drug. *Biosens. Bioelectron.* **2015**, *70*, 153-60.
162. Chen, S.; Liu, Y.; Chen, J., Heterogeneous electron transfer at nanoscopic electrodes: importance of electronic structures and electric double layers. *Chem. Soc. Rev.* **2014**, *43*, 5372-5386.
163. Bertrand, M. J., *Handbook of Instrumental Techniques for Analytical Chemistry*. American Chemical Society: 1998; Vol. 120, p 6633.
164. Choudhary, Y. S.; Jothi, L.; Nageswaran, G., Chapter 2 Electrochemical Characterization. In *Spectroscopic Methods for Nanomaterials Characterization*, 1st ed.; Sabu Thomas, R. T., Ajesh K Zachariah, Raghvendra Kumar Mishra, Ed. Elsevier: 2017; pp 19-54.
165. Tanimoto, S.; Ichimura, A., Discrimination of Inner- and Outer-Sphere Electrode Reactions by Cyclic Voltammetry Experiments. *J. Chem. Educ* **2013**, *90*, 778-781.
166. Bilal, S., Cyclic Voltammetry. In *Encyclopedia of Applied Electrochemistry* [Online] 1st ed.; Springer: 2014; pp. 285-289.
167. Brown, J. H., Development and Use of a Cyclic Voltammetry Simulator To Introduce Undergraduate Students to Electrochemical Simulations. *J. Chem. Educ* **2015**, *92*, 1490-1496.

168. Thompson, R. Q., Encyclopedia of Analytical Science, Second Edition (Worsfold, Paul; Tonshend, Alan; Poole, Colin). American Chemical Society: 2005; Vol. 82, p 1313.
169. Mabbott, G. A., An introduction to cyclic voltammetry. *J. Chem. Educ* **1983**, *60*, 697.
170. Leech, M. C.; Lam, K., A practical guide to electrosynthesis. *Nat. Rev. Chem.* **2022**.
171. Lu, J.-Y.; Yu, Y.-S.; Chen, T.-B.; Chang, C.-F.; Tamulevičius, S.; Erts, D.; Wu, K. C.-W.; Gu, Y., Fabrication of an Extremely Cheap Poly(3,4-ethylenedioxythiophene) Modified Pencil Lead Electrode for Effective Hydroquinone Sensing. *Polymers (Basel)*. **2021**, *13*, 343.
172. Pereira, R. G. a. C. M., Electroanalytical Techniques and Instrumentation in Food Analysis. In *Handbook of Food Analysis Instruments*, 1st ed.; Otlés, S., Ed. CRC Press: Boca Raton, 2008; pp 379-402.
173. Bard, A. J.; Faulkner, L. R., *Electrochemical Methods: Fundamentals and Applications*. 2nd ed.; Wiley: 2001; p 864.
174. Drake, K. F.; Van Duyne, R. P.; Bond, A. M., Cyclic differential pulse voltammetry: A versatile instrumental approach using a computerized system. *J. Electroanal. Chem. Interfacial Electrochem.* **1978**, *89*, 231-246.
175. Street, J. J.; Peterson, W. M., Anodic Stripping Voltammetry and Differential Pulse Polarography. In *Methods of Soil Analysis*, 1983; pp 133-148.
176. Iskierko, Z.; Sharma, P. S.; Bartold, K.; Pietrzyk-Le, A.; Noworyta, K.; Kutner, W., Molecularly imprinted polymers for separating and sensing of macromolecular compounds and microorganisms. *Biotechnol. Adv.* **2016**, *34*, 30-46.
177. Randviir, E. P.; Banks, C. E., Electrochemical impedance spectroscopy: an overview of bioanalytical applications. *Anal. Methods* **2013**, *5*, 1098-1115.
178. Scott, K., Electrochemical principles and characterization of bioelectrochemical systems. In *Microbial Electrochemical and Fuel Cells*, Scott, K.; Yu, E. H., Eds. Woodhead Publishing: Boston, 2016; pp 29-66.
179. Lisdat, F.; Schäfer, D., The use of electrochemical impedance spectroscopy for biosensing. *Anal. Bioanal. Chem.* **2008**, *391*, 1555.
180. Chang, B. Y.; Park, S. M., Electrochemical impedance spectroscopy. *Annu. Rev. Anal. Chem.* **2010**, *3*, 207-29.
181. Marti, O.; Drake, B.; Hansma, P. K., Atomic force microscopy of liquid-covered surfaces: "Atomic resolution images." *Appl. Phys. Lett.* **1987**, *51*, 484-486.
182. Jung, S.-H.; Park, D.; Park, J. H.; Kim, Y.-M.; Ha, K.-S., Molecular imaging of membrane proteins and microfilaments using atomic force microscopy. *Exp. Mol. Med.* **2010**, *42*, 597-605.
183. Babaei Gavan, K.; Van der Drift, E. W. J. M.; Venstra, W. J.; Zuiddam, M. R.; Van der Zant, H. S. J., Effect of undercut on the resonant behaviour of silicon nitride cantilevers. *J. Micromech. Microeng.* **2009**, *19*, 035003.
184. Veerapandian, M.; Kyusik, Y., Study of Atomic Force Microscopy in Pharmaceutical and Biopharmaceutical Interactions - A Mini-Review. *Curr. Pharm. Anal.* **2009**, *5*, 256-268.

185. Liu Y., B. C., Nie H., Hui D., Mei J., Lau W., Atomic Force Microscopy for Characterizing Nanocomposites. . In *Carbon-related Materials in Recognition of Nobel Lectures by Prof. Akira Suzuki in ICCE.*, Satoru Kaneko, P. M., Tamio Endo, Tetsuo Tsuchiya, Katsuhisa Tanaka, Masahiro Yoshimura, David Hui, Ed. Springer, Cham: 2017; pp 421-442.
186. Mohammed, A.; Abdullah, A. In *Scanning electron microscopy (SEM): a review*, Proceedings of International Conference on Hydraulics and Pneumatics–Hervex, Băile Govora, Romania, Băile Govora, Romania, 2018.
187. Zhang, R.; Ulery, B. D., Synthetic Vaccine Characterization and Design. *J. Bionanosci.* **2018**, *12*, 1-11.
188. Shah, F. A.; Ruscsák, K.; Palmquist, A., 50 years of scanning electron microscopy of bone—a comprehensive overview of the important discoveries made and insights gained into bone material properties in health, disease, and taphonomy. *Bone Res.* **2019**, *7*, 15.
189. Aziz, M., Ismail, A.F., X-Ray Photoelectron Spectroscopy (XPS). In *Membrane Characterization*, Nidal Hilal, A. I., Takeshi Matsuura, Darren Oatley-Radcliffe, Ed. Elsevier: 2017; p 458.
190. Baer, D. R.; Thevuthasan, S., Chapter 16 - Characterization of Thin Films and Coatings. In *Handbook of Deposition Technologies for Films and Coatings (Third Edition)*, Martin, P. M., Ed. William Andrew Publishing: Boston, 2010; pp 749-864.
191. (a) X-Ray Photoelectron Spectroscopy (XPS). <https://www.ifw-dresden.de/ifw-institutes/ikm/micronano-structures/methods/xps>; (b) Photoelectron spectrometer, ESCALAB Mk II by Vacuum Generators. [https://jacobs.physik.uni-saarland.de/home/index.php?page=steinbeiss/home\\_cms\\_steinbeissdet3-1&navi=service](https://jacobs.physik.uni-saarland.de/home/index.php?page=steinbeiss/home_cms_steinbeissdet3-1&navi=service).
192. Wu, L.; Jiang, X., Infrared Spectroscopy for Studying Plasma Membranes. In *Membrane Biophysics: New Insights and Methods*, Li, H. W. G., Ed. Springer, Singapore: 2018; pp 319-354.
193. Titus, D.; James Jebaseelan Samuel, E.; Roopan, S. M., Chapter 12 - Nanoparticle characterization techniques. In *Green Synthesis, Characterization and Applications of Nanoparticles*, Shukla, A. K.; Irvani, S., Eds. Elsevier: 2019; pp 303-319.
194. Chen, Y.; Zou, C.; Mastalerz, M.; Hu, S.; Gasaway, C.; Tao, X., Applications of Micro-Fourier Transform Infrared Spectroscopy (FTIR) in the Geological Sciences—A Review. *Int. J. Mol. Sci.* **2015**, *16*, 30223-30250.
195. (a) Monyoncho, E. A.; Zamlynny, V.; Woo, T. K.; Baranova, E. A., The utility of polarization modulation infrared reflection absorption spectroscopy (PM-IRRAS) in surface and in situ studies: new data processing and presentation approach. *Analyst* **2018**, *143*, 2563-2573; (b) Steiner, G.; Sablinskas, V.; Seidel, W.; Salzer, R., PM-IRRAS mapping of ultrathin molecular films with high spatial resolution. *Anal. Bioanal. Chem.* **2009**, *395*, 1641.
196. Kestell, J. D.; Mudiyansele, K.; Ye, X.; Nam, C. Y.; Stacchiola, D.; Sadowski, J.; Boscoboinik, J. A., Stand-alone polarization-modulation infrared reflection absorption spectroscopy instrument optimized for the study of catalytic processes at elevated pressures. *Rev. Sci. Instrum.* **2017**, *88*, 105109.

197. Boujday, S.; de la Chapelle, M. L.; Srajer, J.; Knoll, W., Enhanced Vibrational Spectroscopies as Tools for Small Molecule Biosensing. *Sensors (Basel)*. **2015**, *15*, 21239-64.
198. Zawisza, I.; Wittstock, G.; Boukherroub, R.; Szunerits, S., Polarization modulation infrared reflection absorption spectroscopy investigations of thin silica films deposited on gold. 2. Structural analysis of a 1,2-dimyristoyl-sn-glycero-3-phosphocholine bilayer. *Langmuir*. **2008**, *24*, 3922-9.
199. Frisch, M. J.; Trucks, G. W.; Schlegel, H. B.; Scuseria, G. E.; Robb, M. A.; Cheeseman, J. R.; Scalmani, G.; Barone, V.; Petersson, G. A.; Nakatsuji, H.; Li, X.; Caricato, M.; Marenich, A. V.; Bloino, J.; Janesko, B. G.; Gomperts, R.; Mennucci, B.; Hratchian, H. P.; Ortiz, J. V.; Izmaylov, A. F.; Sonnenberg, J. L.; Williams; Ding, F.; Lipparini, F.; Egidi, F.; Goings, J.; Peng, B.; Petrone, A.; Henderson, T.; Ranasinghe, D.; Zakrzewski, V. G.; Gao, J.; Rega, N.; Zheng, G.; Liang, W.; Hada, M.; Ehara, M.; Toyota, K.; Fukuda, R.; Hasegawa, J.; Ishida, M.; Nakajima, T.; Honda, Y.; Kitao, O.; Nakai, H.; Vreven, T.; Throssell, K.; Montgomery Jr., J. A.; Peralta, J. E.; Ogliaro, F.; Bearpark, M. J.; Heyd, J. J.; Brothers, E. N.; Kudin, K. N.; Staroverov, V. N.; Keith, T. A.; Kobayashi, R.; Normand, J.; Raghavachari, K.; Rendell, A. P.; Burant, J. C.; Iyengar, S. S.; Tomasi, J.; Cossi, M.; Millam, J. M.; Klene, M.; Adamo, C.; Cammi, R.; Ochterski, J. W.; Martin, R. L.; Morokuma, K.; Farkas, O.; Foresman, J. B.; Fox, D. J. *Gaussian 16 Rev. C.01*, Wallingford, CT, 2016.
200. Yang, Y. K.; Fang, G. Z.; Liu, G. Y.; Pan, M. F.; Wang, X. M.; Kong, L. J.; He, X. L.; Wang, S., Electrochemical sensor based on molecularly imprinted polymer film via sol-gel technology and multi-walled carbon nanotubes-chitosan functional layer for sensitive determination of quinoxaline-2-carboxylic acid. *Biosens. Bioelectron.* **2013**, *47*, 475-481.
201. Soucaze-Guillous, B.; Kutner, W., Flow characteristics of a versatile wall-jet or radial-flow thin-layer large-volume cell for electrochemical detection in flow-through analytical systems. *Electroanalysis* **1997**, *9*, 32-39.
202. Ryu, H. W.; Kim, Y. S.; Kim, J. H.; Cheong, I. W., Direct synthetic route for water-dispersible polythiophene nanoparticles via surfactant-free oxidative polymerization. *Polymer* **2014**, *55*, 806-812.
203. Jung, Y.; Kline, R. J.; Fischer, D. A.; Lin, E. K.; Heeney, M.; McCulloch, I.; DeLongchamp, D. M., The Effect of Interfacial Roughness on the Thin Film Morphology and Charge Transport of High-Performance Polythiophenes. *Adv. Funct. Mater.* **2008**, *18*, 742-750.
204. (a) Pérez Madrigal, M. M.; Giannotti, M. I.; Oncins, G.; Franco, L.; Armelin, E.; Puiggali, J.; Sanz, F.; del Valle, L. J.; Alemán, C., Bioactive nanomembranes of semiconductor polythiophene and thermoplastic polyurethane: thermal, nanostructural and nanomechanical properties. *Polym. Chem.* **2013**, *4*, 568-583; (b) Tahk, D.; Lee, H. H.; Khang, D.-Y., Elastic Moduli of Organic Electronic Materials by the Buckling Method. *Macromolecules* **2009**, *42*, 7079-7083.
205. Nguyen, T. Q.; Breitkopf, C., Determination of Diffusion Coefficients Using Impedance Spectroscopy Data. *J. Electrochem. Soc.* **2018**, *165*, E826-E831.
206. Alizadeh, T.; Akhoundian, M.; Ganjali, M. R., A ferrocene/imprinted polymer nanomaterial-modified carbon paste electrode as a new generation of gate effect-based voltammetric sensor. *New J. Chem.* **2018**, *42*, 4719-4727.

207. Leuaa, P.; Priyadarshani, D.; Tripathi, A. K.; Neergat, M., Internal and External Transport of Redox Species across the Porous Thin-Film Electrode/Electrolyte Interface. *J. Phys. Chem. C* **2019**, *123*, 21440-21447.
208. Bisquert, J.; Garcia-Belmonte, G.; Fabregat-Santiago, F.; Bueno, P. R., Theoretical models for ac impedance of finite diffusion layers exhibiting low-frequency dispersion. *J. Electroanal. Chem.* **1999**, *475*, 152-163.
209. (a) Omanovic, S.; Roscoe, S. G., Electrochemical Studies of the Adsorption Behavior of Bovine Serum Albumin on Stainless Steel. *Langmuir*. **1999**, *15*, 8315-8321; (b) Omanovic, S.; Roscoe, S. G., Interfacial Behavior of beta-Lactoglobulin at a Stainless Steel Surface: An Electrochemical Impedance Spectroscopy Study. *J. Colloid Interface Sci.* **2000**, *227*, 452-460.
210. (a) Umpleby, R. J.; Baxter, S. C.; Chen, Y.; Shah, R. N.; Shimizu, K. D., Characterization of Molecularly Imprinted Polymers with the Langmuir–Freundlich Isotherm. *Anal. Chem.* **2001**, *73*, 4584-4591; (b) Turiel, E.; Perez-Conde, C.; Martin-Esteban, A., Assessment of the cross-reactivity and binding sites characterisation of a propazine-imprinted polymer using the Langmuir-Freundlich isotherm. *Analyst* **2003**, *128*, 137-141; (c) Bisquert, J.; Garcia-Belmonte, G.; Fabregat-Santiago, F.; Bueno, P. R., Theoretical models for ac impedance of finite diffusion layers exhibiting low frequency dispersion. *J. Electroanal. Chem.* **1999**, *475*, 152-163; (d) Jeppu, G. P.; Clement, T. P., A modified Langmuir-Freundlich isotherm model for simulating pH-dependent adsorption effects. *J. Contam. Hydrol.* **2012**, *129-130*, 46-53.
211. Cao, Y.; He, X. W., Studies of interaction between safranin T and double-helix DNA by spectral methods. *Spectrochim. Acta, Part A* **1998**, *54*, 883-892.
212. Monod, J.; Wyman, J.; Changeux, J. P., On the nature of allosteric transitions: A plausible model. *J. Mol. Biol.* **1965**, *12*, 88-118.
213. Ashworth, C.; Frisch, G., Complexation equilibria of indium in aqueous chloride, sulfate and nitrate solutions: An electrochemical investigation. *J. Solution Chem.* **2017**, *46*, 1928-1940.
214. Ayerdurai, V.; Cieplak, M.; Noworyta, K. R.; Gajda, M.; Ziminska, A.; Sosnowska, M.; Piechowska, J.; Borowicz, P.; Lisowski, W.; Shao, S.; D'Souza, F.; Kutner, W., Electrochemical sensor for selective tyramine determination, amplified by a molecularly imprinted polymer film. *Bioelectrochemistry* **2021**, *138*, 107695.
215. Tatsuma, T.; Hioki, Y.; Oyama, N., Dependence of swelling behaviour and electrochemical activity of water-soluble polythiophene films on the nature of the electrolyte. *J. Electroanal. Chem.* **1995**, *396*, 371-376.
216. Sharma, P. S.; Iskierko, Z.; Noworyta, K.; Cieplak, M.; Borowicz, P.; Lisowski, W.; D'Souza, F.; Kutner, W., Synthesis and application of a “plastic antibody” in electrochemical microfluidic platform for oxytocin determination. *Biosens. Bioelectron.* **2018**, *100*, 251-258.



Biblioteka Instytutu Chemii Fizycznej PAN

**F-B.553/22**



**10000000109205**